

IJAMB

International Journal of Advances in Medical Biotechnology

TRIBUTE

Jorge Vicente Lopes da Silva

Scientist of Renato Archer Information Technology Center

Additive Manufacturing Pioneer in Latin America



Vol. 6 N.2, 2024

Special editor: Rodrigo A. Rezende
Figure credit: CTI Renato Archer
Cover design: T. Mariano

Jorge Vicente Lopes da Silva – Scientific Researcher and Friend

There are texts that are easy to write and then there are others that have such an emotional significance that are much harder. I was invited to write about Jorge Vicente Lopes da Silva, a Brazilian researcher that had and continues to have a worldwide impact in the scientific, academic and industrial domain. He had a significant scientific contribution worldwide, but his greatest impact was the friendships that he created with everyone that had the opportunity of meeting him.

At the end of his career, he was the Director of Renato Archer Information Technology Center (CTI). He obtained his Ph.D. degree in Chemical Engineering, and MSc and BSc degrees in Electrical Engineering. He was a senior researcher of the Renato Archer Information Technology Center (CTI) since 1988, a Brazilian research centre from the Science, Technology, Innovation and Communications Ministry. He coordinated the Robotics Division at CTI for some years and in 1997 he created and coordinated the Tridimensional Technologies Research Group at the same centre, being a pioneer in this area in Brazil. Under his supervision the team developed applications and research projects with funding agencies, industry and universities in Brazil and abroad. He was a member of many scientific committees and invited speaker of many relevant conferences in the area of Additive Manufacturing. He was member of the editorial board and referee of dozens of journals. He was also a member of national and international research networks in the healthcare area like the Science and Technology National Institutes (INCT) for Biofabrication, INCT for Regenerative Medicine, and in the Brazilian Institute for Neuroscience and Neurotechnology (BRAINN). He also coordinated projects in the area of tissue engineering and healthcare with the most relevant Brazilian funding agencies like FINEP, FAPESP and CNPq and Ministry of Health. The laboratory that he created become involved in additive manufacturing, CAD and BioCAD modelling, medical imaging, and computer simulation for medical applications. He cooperated with more than 300 hospitals in Brazil and some others abroad. As a result of his work, computer tools were developed in special the software InVesalius for medical imaging, which are currently in use in 150 countries as an open-source solution. He cooperated with many universities supervising or co-supervising master and PhD thesis.

According to the Scopus platform, he published 163 documents that resulted in 2686 citations and an h-index of 27. Whereas according to ORCID, he published 154 documents and according to Frontiers Media SA he published 220 publications. The numbers are very notorious in spite of their variation between platforms, but his impact is much more relevant. He inspired researchers in both the academic and industrial community worldwide. For instance, he participated as a jury member in PhD defences worldwide, illustrating his significance and recognition within the scientific community.

Just to illustrate a slight glimpse and relevance of his work, the last papers that he published present the following abstracts:

- Recent advances in additive manufacturing (AM) offer transformative potential for designing and fabricating implantable medical devices. AM provides key advantages over traditional manufacturing, such as high customizability, the ability to create complex geometries, good dimensional accuracy, reduced material waste, and a cleaner production environment. Integrating structural design optimization (SDO) techniques, like Topology, Shape, and Size Optimization, with AM enhances device functionality and performance. Lattice structures and AI/ML applications further improve surface roughness, biocompatibility, and adaptability. Research focuses on reducing stress shielding, enhancing osseointegration, and personalizing implants. The review provides a detailed classification of optimization methods, with each approach scrutinized for its unique contribution to overcoming specific challenges in medical implant design, thus leading to more advanced, effective, and patient-oriented implantable devices (DOI: <https://doi.org/10.3389/fmech.2024.1353108>)

- Integration between the phases of computer-based guided dental implant surgery can be used to optimize oral rehabilitation. Two new surgical guides prepared by using the 3D metal and polymer printing technology are presented for immediate implant loading and definitive fixed prosthesis construction in flapless dental implant surgery. Nine implants and 2 fixed prostheses were installed in 2 completely edentulous adult patients by using a metalopolymer surgical guide with a metal central bar attached to a polymer seal or a metal guide. Virtual planning was used to design the 3D printed surgical guides, which were then constructed by using selective laser sintering (SLM) and selective laser melting (SLS). The 3D printed surgical guides oriented the surgical placement of the implants and were welded to the abutments and attached to the denture framework. The technique allowed implants and prostheses to be installed on the same day. DOI: <https://doi.org/10.1016/j.prosdent.2022.05.034>

From the abstracts presented above, it is possible to observe that not only he focused on the latest technologies and their advances and innovations but also focused on issues related to health in order to improve the well-being of everyone worldwide.

In spite of his departure, his research and publications will still serve as inspiration and reference for many years to come, contributing to the continuous growth of knowledge.

Besides his work and contributions, those that had the opportunity to meet him, had the opportunity to meet a joyful and friendly person always prompt to discuss any topic and assist and guide those who were willing to work in the field of additive manufacturing related to medical applications.

On his departure from, many were the kind words from researchers in several social media platform that he touched worldwide. For instance, Professor Paulo Bártolo, Director of the Singapore Centre for 3D Printing, Nanyang Technological University, states:

"Jorge was a fantastic person with impressive energy and a way of being that touched all of us in a special way. Jorge will remain with us, in our memories and in our thoughts."

In the academic field, writing a scientific paper is accessible when one has all the correct data, but in this case, writing about someone that had a significant impact in one's life in all domains, both scientific and personal, is much more meaningful. In summary, I'm especially grateful of having had the opportunity of knowing him. Not only did he aid my academic career but also, he was a dear friend.

"With your departure my dear friend, the world will be poorer for it."

Henrique de Amorim Almeida
Associate Professor of the Mechanical Engineering Department,
School of Technology and Management,
Polytechnic Institute of Leiria
Portugal

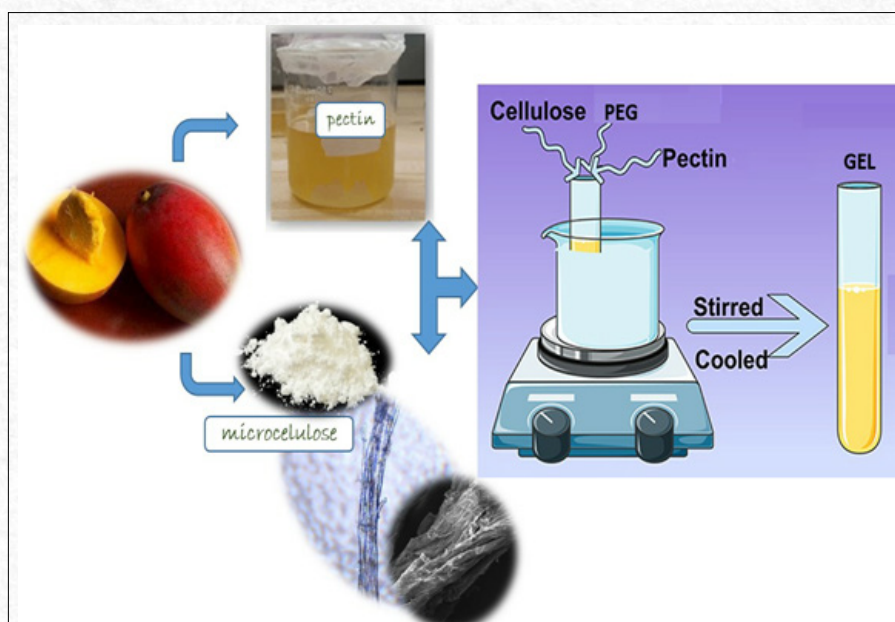


Development of gels composed of pectin/microcellulose from mango and peg for biotechnological applications

M.H. Ferraresi¹; V.M.M. Colturato¹; B.D. Neto¹; I.D. Coutinho²; L.A. Dutra³; A. Dametto⁴; W. R. Lustril¹; R.M. Nascimento de Assunção⁵; M.R. Costa Iemma¹; M.C.A.Ferreira Rezende^{6*}; M.A. Sabino⁷; H.S. Barud¹; R.A. Rezende^{1*}

Received: October 2024; Accepted: December 2024.

*Corresponding author: E-mail address: rarezende@uniara.edu.br



Abstract: Based on the concept of circular economy, waste from vegetable sources, mango between them, are reused and can be extracted some biomolecules as pectin and cellulose to be used in biotechnological applications, also for cosmetic industry, even use as biomaterials. In this context, the thermal, morphological, and rheological characterization of pure biopolymers and blends as gel was carried out to analyze their potential to produce membranes, scaffolds or bioprinted structures. FTIR analysis was performed demonstrating similar behaviors and groupings between the studied materials. The crystallinity index and amorphous areas obtained by XRD assay. Furthermore, other analysis performed was concerning the degree of polymerization according to the viscosity of the samples demonstrating the flow time of the polymers. After characterizing the polymers, formulations of gels combined mango pectin, mango microcellulose and vegetable microcellulose with wood sources were produced through calorimetry, scanning electron microscope (SEM), and rheology analyses. PEG was added with the purpose of improving the rheological properties and compatibility between the phases of these gels. We conclude through the characterization of these materials the viability in the production of structures for biotechnological applications as scaffolds in the medical areas between others.

Keywords: Pectin. Microcellulose. Gels. Rheology. Mango. Biotechnological Applications.

¹Postgraduate Program in Biotechnology in Regenerative Medicine and Medicinal Chemistry, University of Araraquara (Uniar), Araraquara-SP, Brazil.

²Natcrom Sustainable Solutions, Araraquara-SP, Brazil.

³Institute of Chemistry of Araraquara, Araraquara-SP, Brazil.

⁴BioSmart Nanotechnology, Araraquara-SP, Brazil.

⁵Federal University of Uberlândia, Faculdades de Ciências Integradas do Pontal, Ituiutaba-MG, Brazil.

⁶3D BioEng, Avenida J. Fernandes Mattos, 311, 80 Distrito Industrial, 14808-162, Araraquara-SP, Brazil.

⁷Universidad Simón Bolívar, Caracas, Venezuela.

Introduction

Mango is a tropical fruit highly valued worldwide for its flavor, aroma, and nutritional value. Pectin and cellulose are two compounds or by-products found in mango that have gelling properties. Pectin is a water-soluble fiber widely used to thicken and stabilize food and pharmaceutical agents. Cellulose, in turn, is a water-insoluble fiber that has the ability to absorb water and form a firm gel.¹

Brazil's valorization of mango by-products to produce biotechnological products is still a little-explored area, but there are some studies and initiatives in this direction. Some examples include mango residue extracts (peel, seed, and residual pulp) with bioactive compounds; they can produce bioethanol through fermentation²; the enzymes present in mango residues can be used in industrial biomass hydrolysis processes³. Cellulose fibers can be used as raw material for paper production⁴; they can be used as a source of nutrients in organic fertilizers, etc.⁵ It is still necessary to invest in research and development in this area to explore the full potential of these mango by-products.

But, in general, based on the scientific literature some research has been reported related to gels combining pectin and cellulose and derivatives. A case about improving the texture and consistency of food products, in addition to providing functional properties to the final product.⁶ In addition, these gels can also be used in pharmaceutical products, such as controlled drug delivery systems.⁷ Additionally, due to their biocompatible and bioactive properties, pectin and cellulose are considered promising materials for tissue engineering.⁸

In the case of hydrogels, which are materials with high water content and mechanical properties similar to those of biological tissues, mango pectin and microcellulose gels could be used in the production of hydrogels through various techniques, such as, for example, chemical gelation or physics, which can also lead to thinking about the fabrication of 3D scaffolds that are structures that provide mechanical support for cell growth and can be produced using these hydrogels.⁹

Based on the concept of circular economy, residues from vegetable sources, particularly from mangoes, can be explored, and pectin and cellulose microfibers can be extracted to be used as biomaterials.¹⁰

In this sense, this work aims at developing gels mixing pectin and mango microcellulose including a modifying phase (polyethylene glycol PEG) to improve the rheological behavior and proceed with their characterization.

Materials and Methods

Mango pectin (PECM) samples were provided by

NATCROM P&D ("<https://naticrom.com/>") and sized using the Polymix® PX-IG 2000 Impact Grinder Kinematica ball mill available from BIOSMART Nanotechnology LTDA ("<https://www.biosmartnano.com/>") for 5 minutes at frequencies of 20 Hz, resulting in powdered (PECM) particles. Dissolutions and gels of (PECM) in distilled water were made using the ratio of PECM:distilled H₂O for dissolution of 15% m/v; remaining in agitation for 30 minutes for complete homogenization.

The mango microcellulose (MCM) samples were provided by the company NATCROM P&D ("<https://www.naticrom.com/>").¹¹ They were extracted through the hydrolysis of AHP (Alkaline Hydrogen Peroxide) to eliminate hemicellulose and samples lignin. After hydrolysis, the samples were ultrasonicated for 1, 2, 3 hours in a 1% H₂O₂ solution with a low frequency ultrasound processor (20 kHz).

Drops of H₂SO₄ were added to the suspension (pH 5.0) and vigorously mixed using vortex mixer for 2 min to avoid agglomeration of disintegrated fibers avoiding possible equipment corrosion – subsequently lyophilized.¹²

The plant microcellulose (MCV) samples were provided by the Biopolmat laboratory at the University of Araraquara (UNIARA); being this MCV obtained through renewable and sustainable bases with reuse of wood fibers and used as a comparison material in relation to the extracted MCM. This MCV material was produced and donated by the Brazilian company Suzano.¹³

Polyethylene glycol-400 (PEG) use as dispersant and rheological helper was from Sigma Aldrich.

Characterization of pectin and microcellulose phases

Fourier transform infrared spectroscopy (FTIR)

In order to verify the chemical structure of the neat polymers PECM, MCM, MCV to be used to obtain the gels, the analysis was performed using an Agilent Cary 630 FTIR-ATR benchtop spectrometer with 64 scans (4500 cm⁻¹ to 500 cm⁻¹), resolution of 4 cm⁻¹, present in the LABQUIM laboratory located at the University of Araraquara – UNIARA.

Degree of polymerization (DP)

Given the characteristics of gels obtained by mixing polysaccharide phases, it is important to know the size of the molecules. The degree of polymerization of the microcelluloses and pectin was obtained according to TAPPI standard T 2300 m-94: Viscosity of pulp (capillary viscometer method, 2013)¹⁴ using the transparent Cannon-Fenske viscometer n°150.14 500 mg of each sample separately and added to 50 ml of distilled water, followed by homogenization in magnetic stirring

at 400 rpm/min for 5-min at room temperature. After this time, 50 ml of Ethylenediamine Cupric solution were added with hydrogen bath and taken again to magnetic stirring for 2 hours at 400 rpm/min. After the stirring time, for each case, 7 ml of the mixture were placed in the viscometer and inserted in a water bath at a temperature of 25 °C for 5-min. They carried out measurements of the flow times in triplicate and the average obtained was used to calculate the degree of polymerization according to the calculations proposed by Andritsou et al.¹⁵

X-Ray Diffraction

It is important to have information about the morphology of the materials, especially when the properties of the gels can reflect their composition related to the phases in the biocomposite material. X-ray diffraction (XRD) was performed using a Shimadzu model XRD-6000 diffractometer, operating at a power of 40 kV with 40 mA of current and CuK α radiation ($\lambda = 1.54148 \text{ \AA}$), in the angular range of 2θ from 5 to 40°, sweep speed of 2°/min and angular step of 0.02°. The samples submitted to XRD were: PECM, MCM, and MCV. The experiment was carried out at the Institute of Exact and Natural Sciences at the Federal University of Uberlândia, Campus Pontal, Ituiutaba, MG-Brazil.

TG curves

The SDT Q600 equipment from the company TA Instruments, present in the Biopolmat laboratory of the University of Araraquara – UNIARA, was used to carry out the thermogravimetric analysis (TG). Samples around 20 mg and 25 mg were heated at 10 °C/min into an alumina crucible from 30 °C to 700 °C, under a nitrogen atmosphere (30 mL/min flow rate).

Scanning Electron Microscopy – SEM

In the case of the PECM and MCM sample, it was also observed by optical microscopy (using a conventional four-lens binocular biological microscope by Olen) only with the aim of having evidence of the micrometric character before being observed by SEM.

In order to know the dimension or magnitude of the MCM and MCV microcellulose, the scanning electron microscopy (SEM) images were obtained using "Electronic microscope with field emission pistol - FEG-SEM Tescan model Mira 3 XMU with e-lithography beam and with EDS 60mm Bruker". QUANTAX EDS Bruker 60 mm with XFlash® energy dispersive X-ray detector and Espirit software. Located at the Center for Information Technology (CTI) Renato Archer, in Campinas, SP.

Cytotoxicity

Cell viability tests were carried out at Lecer

laboratory of the University of Araraquara. The MTT (3-(4,5-dimethylthiazol-2yl)-2,5-diphenyl tetrazoline bromide) assay was adopted. On the MTT assay, when there is the incubation with fibroblastic cells, the substrate is broken down by mitochondria, where the carbon dioxide emitted by the cells reacts with the MTT and it is transformed from a yellow compound into a dark blue compound (formazan) providing information on viable cells.¹⁶

For cytotoxicity evaluation, the culture medium of L929 cells grown in 24-well plate (1×10^4 /well) was removed and a volume of 200 μ l of conditioned medium was added. Cells were cultivated in the presence of different concentrations of conditioned media for each material (100, 50 and 25%) and the plate kept in an oven at 37° C with 5% CO₂ saturation for 24 hours. Subsequently, conditioned medium was removed and added 50 μ l/well of the MTT solution (5mg/ml) in PBSIX. After incubating the plate for 4 hours in oven at 37° C with 5% CO₂ saturation, the MTT solution was removed and the formazan crystals were solubilized in DMSO for absorbance reading at a wavelength of 570nm, in a Spectra Max Gemini XS plate reader (Molecular Devices).

Preparation and characterization of gels

Gels were prepared by combining mango pectin PECM, mango microcellulose MCM, plant (wood) microcellulose MCV with specific concentrations of each material (see table 1). The samples were incorporated using a mechanical mixer present at the Biopolmat lab, for 5-min and 500-rpm. Prior to this mixture, the samples of MCM and MCV were subjected to oxidation with hydrogen peroxide (commercial) to improve solubility with water, time 1 hour with magnetic stirring.

Two gel samples were prepared with a percentage of polyethylene glycol (PEG), improving the compatibility between the phases and possibly improving the gels' rheological behavior.

Table 1 - Concentrations (m/v) of the phases used to prepare the gels.

Gel (PEC/MC)	% PECM(*)	% MCM	% MCV	% PEG
(PECM ^{15%} MCM ^{1%})	15	1	0	0
(PECM ^{15%} MCM ^{2%})	15	two	0	0
(PECM ^{15%} MCV ^{1%})	15	0	1	0
(PECM ^{15%} MCV ^{2%})	15	0	two	0
(PECM ^{15%} MCM ^{1%} PEG ^{5%})	15	1	0	5
(PECM ^{15%} MCV ^{1%} PEG ^{5%})	15	0	1	5

(*) 10, 15 and 20% m/v solutions were prepared, but the 10% solutions were too dilute, and the 20% solution was very viscous and lumpy, so 15% m/v was selected.

FTIR-ATR spectra

The components of the chemical group of the gels were identified by Fourier Transform Infrared Spectroscopy (FTIR) in Attenuated Total Reflectance mode (FTIR-ATR) located at the CTI Renato Archer Information Technology Center, in Campinas, SP. FTIR spectra were measured in the range of 4000–400 cm⁻¹ with a resolution of 4 cm⁻¹ on a spectrometer (PerkinElmer, Spectrum GX, USA).

Rheology Analysis

The rheology analyzes were carried out in the Biopolmat lab in the University of Araraquara – UNIA-RA, using the TA Instruments ARI500ex 8B3689 rheometer at room temperature 25°C, 10.Orad/s; 0.01 to 100%. Shear rate 0.01 to 100.0. The geometry used was a parallel plate of 40.0mm Peltier plate Sandblasted.

SEM

Scanning electron microscopy (SEM) were performed as described in point 2.1.5 above. But in the case of gels, after mixing, they were placed on a glass plate to form films by drying (solvent casting or slow evaporation of the solvent) and at room temperature, to then be finally metalized and observed by SEM.

Results and Discussion

Characterization of the base polysaccharides of the gels: PECM, MCM, MCV

Thesamples of PECM, MCM, and MCV submitted to FTIR-ATR analysis allow identifying the possible

vibrations of the characteristic functional groups for each one of these polysaccharides (pectin and cellulose), thus these main bands can be observed in Figure 1. Particularly PECM shows its initial band at 1000 cm⁻¹ corresponding to COC functional groups. Another band behavior between 2800 cm⁻¹ and 3000 cm⁻¹ corresponding to the CH group. Another band at 3300 cm⁻¹ corresponding to the OH group, corroborating the structural formula of pectin. In the analysis of the MCM wavenumber was obtained at 1000 cm⁻¹ corresponding to the COC group, and the band at 1300 cm⁻¹ corresponding to the CH group, the band at 1500 cm⁻¹ corresponding to the C=C group. Another band at 2800 cm⁻¹ corresponding to the CH group and the band at 3300 cm⁻¹ corresponding to intramolecular hydrogen bonds in cellulose OH. The MCV analysis demonstrated similar behavior with mango microcellulose which is fully expected, thus showing the 1750 cm⁻¹ band approximately corresponding to the vibrations of the acetyl group and hemicellulose ester or carboxylic group.

Research carried out obtained similar cellulose functional groups and observed C=O groups in esters, CO in ethers, CH3 functional groups, and OH hydroxyl groups. Peaks around the 1505 cm⁻¹ and 1512 cm⁻¹ bands, attributed to the CC stretch, and the 1737 cm⁻¹ band associated with the C=O stretch was also observed, the peaks in the 2900-2800 cm⁻¹ region associated to CH stretching. The band in the region from 3900 cm⁻¹ to 3300 cm⁻¹ attributed to the OH group thus corroborating with the bands found in this research and compared with the cited bands.¹⁷⁻¹⁹

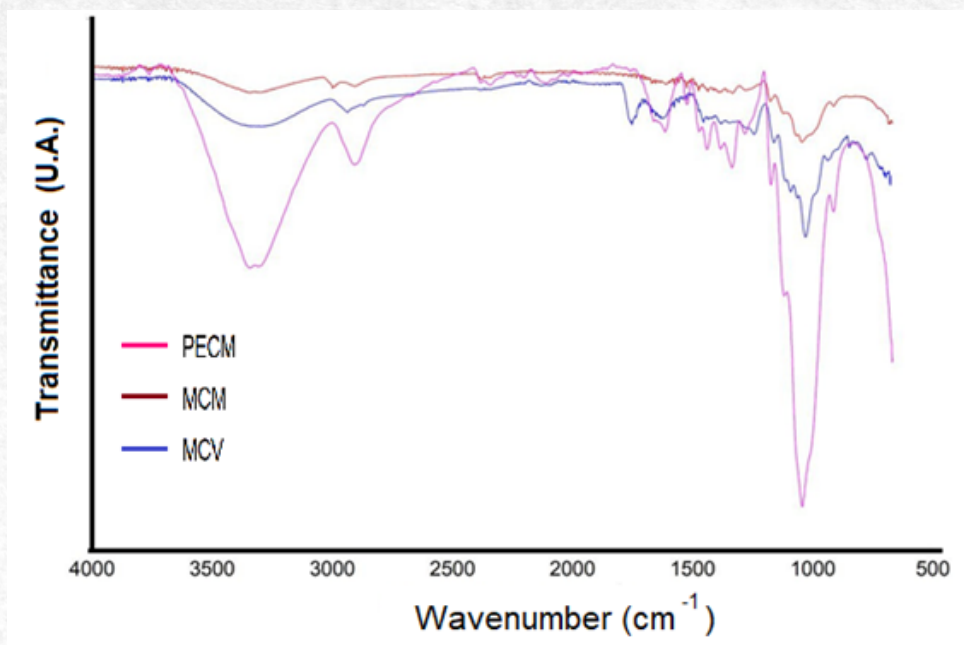
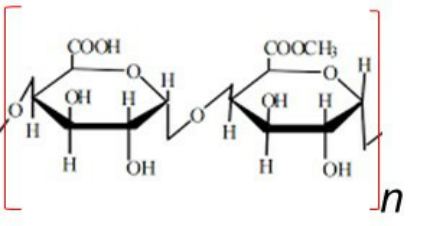
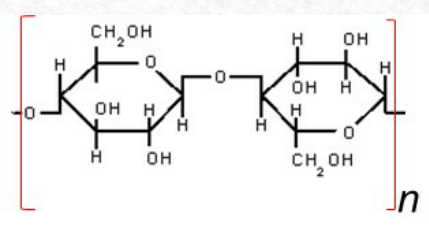
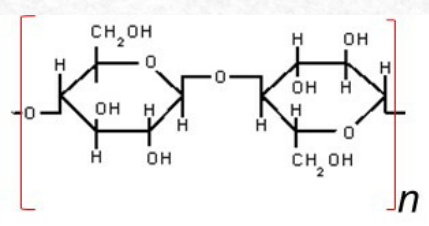


Figure 1 – FTIR of the analyzed samples PECM, MCM, and MCV.

After the chemical structure of the components of the gels has been verified by spectroscopy, it is important to also verify the molecular size of these polysaccharides.²⁰ Other results of these calculations were based on the literature and are shown in Table 1.¹

The results of the degree of polymerization (n) and the consideration of the molecular structure of the repetitive unit allow, through the molecular formula, to estimate a molar mass value of the polysaccharides studied in this research.

Table 1 – Degree of polymerization of pectin, microcellulose, mango cellulose microfibers and vegetal (wood) microcellulose samples.

Sample	Average Flow Time (s)	Degree of polymerization (n)	Molecular formula of the unit Monomeric	Molecular mass calculated (g/mol)*
PECM	175	436	 Pectin structure (FM= C ₁₃ O ₁₂ H ₁₈)	≈ 1.6 x 10 ⁵
MCM	79	194	 Cellulose structure (FM= C ₁₂ O ₁₀ H ₂₀)	≈ 6.3 x 10 ³
MCV	1501	2000	 Cellulose structure (FM= C ₁₂ O ₁₀ H ₂₀)	≈ 6.4 x 10 ⁵

(*) KDa = 103 g/mol

In the case of pectin, there are reports in the scientific literature showing that the molar mass varies between 50-150 KDa, and more specifically there are reports that show values between (154-250) KDa for fruits such as grapefruit²¹, and enter (164-247) KDa for orange²², and for pectin extracted from mango peel there are reports that give approximate results between 20-22 KDa²³. In the case of cellulose, regardless of its size on the micrometer scale, it will be the extraction process that will allow defining the molecular size. In this case, it was observed how the MCM has a molar mass almost 100 times less than that of the MCV, given that the latter would be extracted at an industrial level (given its commercial provider) and on the contrary in the case of the MCM that the extraction would be done at laboratory level, it is possible that the differences between these protocols lead to this structural difference between MCM and MCV. In general, the scientific literature reports results between 300-550 KDa for cellulose extracted from wood and other natural sources.²⁴

According to XRD results, there are several methods in the literature for calculating crystallinity indexes for natural and synthetic polymers²⁵. Figure 2 shows the XRD-diffractogram of cellulose and pectin biopolymers with peaks of moderate intensity between 10° and 20° and peaks of greater intensity between 20° and 30° from mango cellulose showing characteristic behavior cellulose and low-intensity peaks for amorphous pectin demonstrating a typical region of non-crystallize pectin.²⁶ Peaks around 35° to 70° could be attribute to some partially hydrolyze cellulose chains. The calculation results of the

crystalline and amorphous areas are also shown in the table into the Figure 2.

The literature has shown crystallinity indexes for corn husk cellulose microfibers, between 53% and 47%; microcellulose and cellulose microfibers derived from cassava are around 49%. The degree of crystallinity of commercial citrus pectin is equivalent to 17%. The values for MCM and MCV are a little below those reported in the literature. Still, it may be considering the different drying processes of each sample, which allows the reorganization of the chains, thus generating other crystallinity indices and a higher amorphous degree. In the case of pectin, the values found here coincide with those reported.^{19,27,28}

TG/DTG curves, Figure 3, of PECM, MCM, and MCV allow us to observe the determining temperatures for the mass degradation of the materials submitted to analysis.

TG/DTG curves for PECM indicate that degradation temperature starts around 200 °C and shows the mass loss in three steps up to almost zero up to 700 °C. DTG presents degradation peaks at 268 and 302 °C. TG/DTG curves for MCM and MCV show similar thermal stability with degradation starting around 250 °C and a correspondent peak in DTG curves between 306 and 322 °C; the thermal decomposition process for celluloses is almost similar, except that the MCV shows a higher percentage of carbonaceous residue up to 700 °C. Notably, until the beginning of degradation, the materials present a loss of approximately 6-10% of moisture in the temperature range close to 100-120 °C.

The images obtained by optical microscopy and

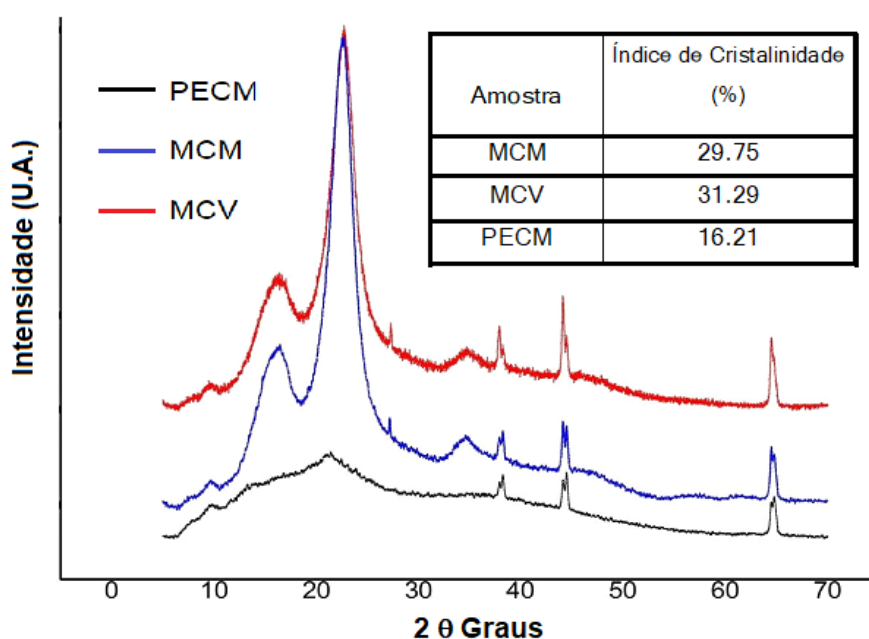


Figure 2 – XRD of MCM and MCV microcelluloses and mango pectin. Calculated values of the crystallinity index of each phase to formulate the gels.

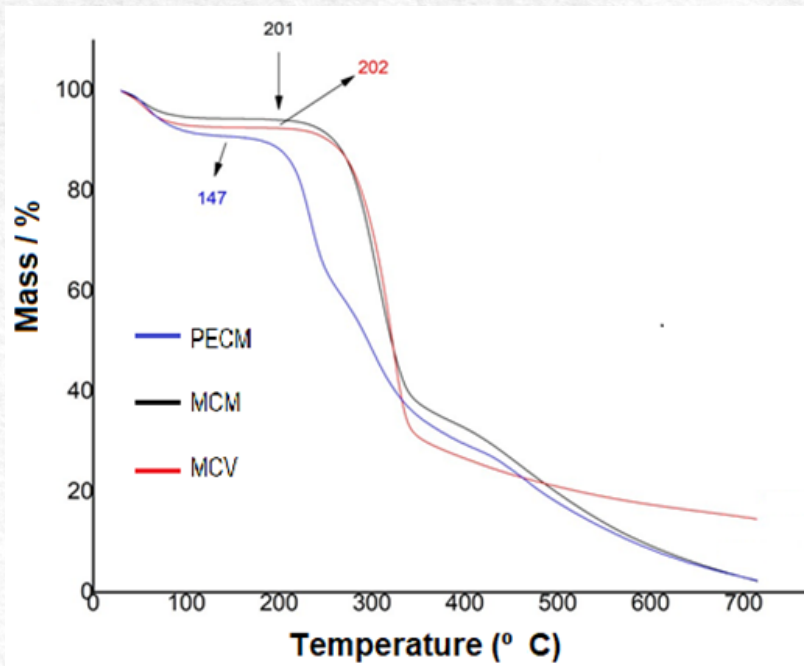


Figure 3 – TG/DTG curves for PECM, MCM, MCV.

SEM are summarized in Figure 4; demonstrating an irregular but homogeneous surface with a fibrillar character. The dimensions of the fiber diameter correspond to the micrometric scale, which is expected according to the extraction process. According to the scale of the images, it is possible to observe some fragmented irregularities of the cellulose, which could be attributed to oxidation

caused by hydrogen peroxide. Actions of hydrogen peroxide on the cellulose of the green coconut shell were observed significant changes in the surface of the cellulose making it more irregular and fragmented than the cellulose without treatment with peroxide^{29,30}.

Figure 5 shows the morphological characteristics and dimensions of the fibers that make up the

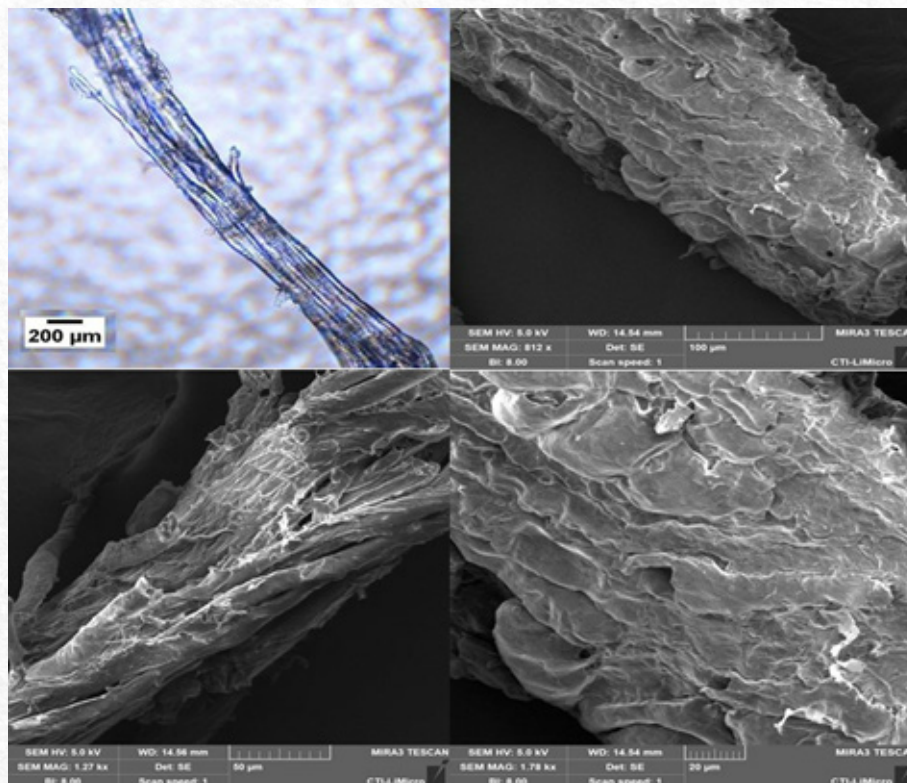


Figure 4 - SEM micrographs of the MCM sample that will be used in the preparation of pectin gels. There is evidence by optical microscopy that allows verifying the fibrillar character of the cellulose, which is characteristic of this material.

MCV. MCV shows characteristics similar to MCM, regardless of the extraction process and also its molar mass. MCV also has some surface and fragmented irregularities; this could be attributed to oxidation caused by hydrogen hydroxide.

Finally, pectin, given its character as a fluid and low-viscosity material, forms a film during the drying process so that it can be observed by SEM. The images show that the material owns certain surface irregularities. These irregularities and size of PECM particles can be viewed by the optical microscopy images (Figure 6).

For cytotoxicity, the method used was the reduction of the MTT(3-(4,5-dimethylthiazol-2-yl)-2,5 diphenyltetrazolium bromide), which consists of analyzing the conversion of MTT (soluble) into formazan crystals (insoluble form) by the action of mitochondrial dehydrogenase enzymes. The absorbance results were represented as percentage of cell viability in relation to the control group (100%), treated and plotted in the GraphPad Prism software as

can be viewed in Figure 7.

According to these results obtained, all materials showed non-cytotoxic behavior in 25%, 50% and 100% conditioned media. So these results can open a window to think about these gels as biomaterials for biomedical applications.

Similar results were found in other studies found in the literature analyzed the cytotoxic effect of cotton cellulose fibers on human dental pulp stem cells, obtaining cell proliferation and viability using the MTT assay in 96-well plates, at concentrations of (0.1; 1; 10; 50; 100 $\mu\text{g mL}^{-1}$) for 24 and 48 h. The authors point out that there was no cytotoxic behavior in any of the tested concentrations. Another study analyzed the cytotoxic effect of cellulose from sugarcane bagasse. Cytotoxicity assays were conducted with the exposure of 929 cells of the NCTC clone to the extract obtained from a sample of the membrane kept in contact for 24 hours in a culture medium DMEM; the authors obtained non-cytotoxic behavior in all analyzes^{31,32}.

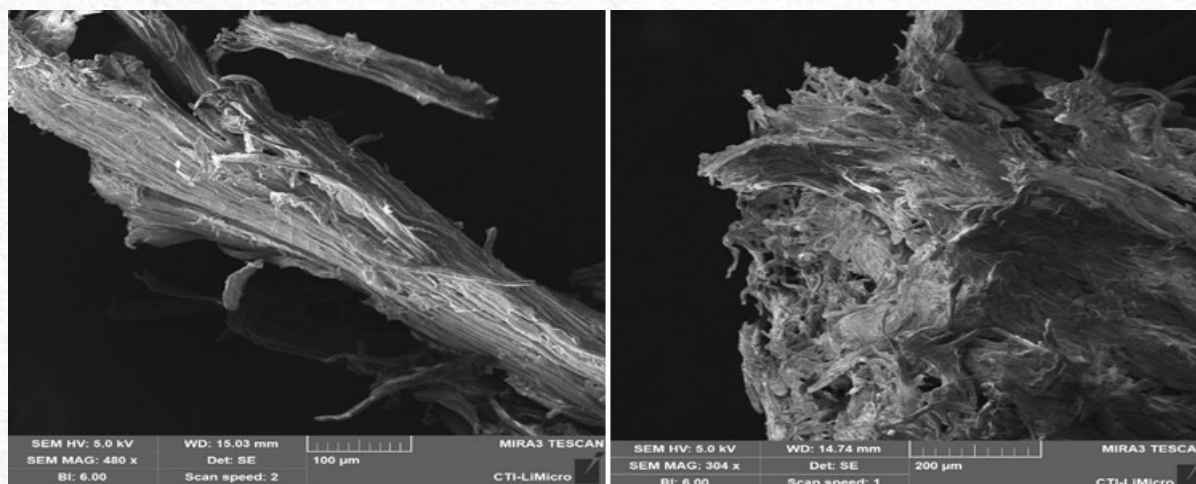


Figure 5 - SEM micrographs of the MCV sample that was use in the preparation of pectin gels.

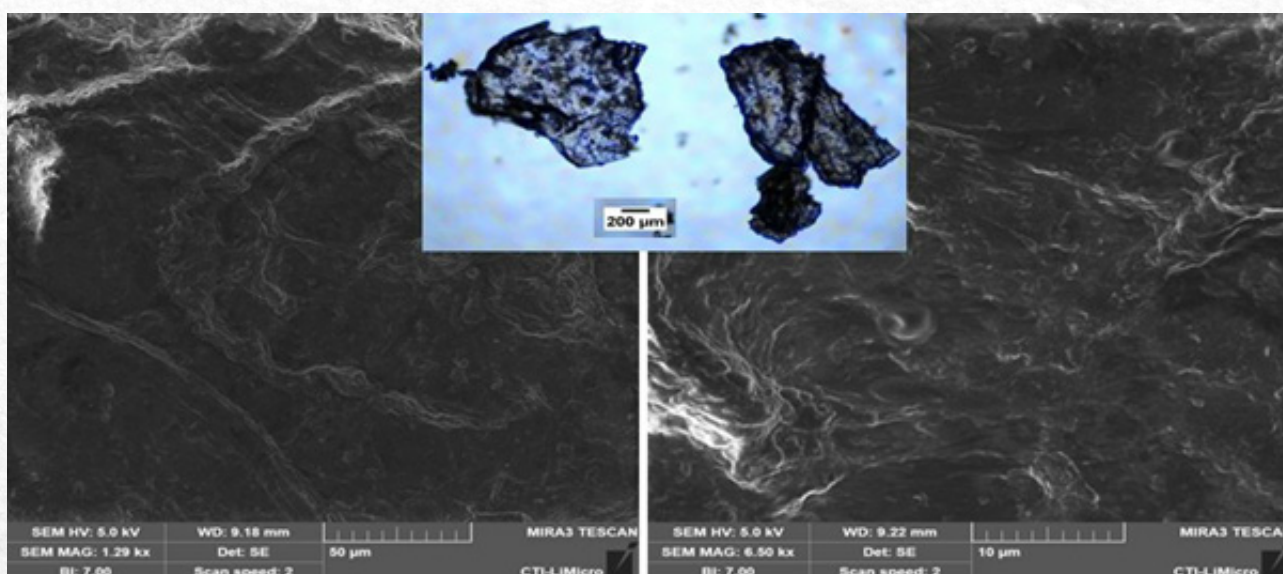


Figure 6 - Optical microscopy and SEM micrographs of the pectin sample.

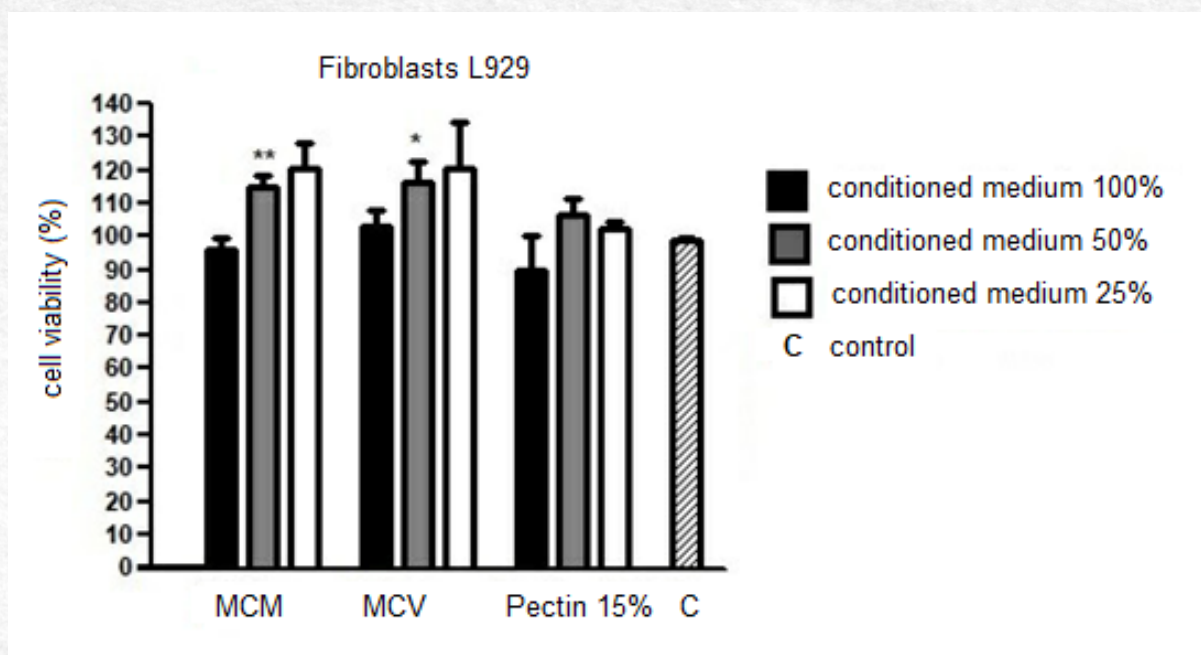


Figure 7 – Cytotoxicity analysis of MCM, MCV, PECM samples.

About the characterization of pectin/microcellulose gels

Pectin and cellulose gels have a wide potential for biotechnological applications, in areas such as food formulation, cosmetics and pharmaceuticals, bioremediation, packaging, and agronomy. These pectin and cellulose gels can exhibit physical properties that make them ideal to produce hydrogels and 3D scaffolds for tissue engineering. Their biocompatibility and ability to form emulsified systems also make them promising to produce materials with possibilities for use in additive manufacturing. Furthermore, studies have demonstrated that it is possible to modify the rheological properties of these gels through the addition of polymers such as PEG (polyethylene glycol), as previously mentioned what can further improve the rheological properties of these gels.

After production, the gels from mango pectin, mango cellulose and vegetal microcellulose were characterized using FTIR, TG, SEM and rheology analyses.

The results of the infrared spectroscopy of the PECM, MCM, MCV gels are presented in Figure 8, that all the curves presented similar behavior. Only seven bands are listed in the spectrometers of the gels, 1000, 1200, 1500, 1600, 1700, 2900 and 3300 cm^{-1} , which refers to the same bands of the materials when analyzed individually. The materials were incorporated and there was no negative interaction between them, since similar functional groups are found in each gel. In addition, opinions from some reports found in the literature the functional groups found are COC, CO, CH, C=O and OH.^{18,19}

TG/DTG curves for gels, Figure 9, show similar

thermal behaviors. The mass loss up to 100°C can be attribute to water evaporation, followed by the gel thermal degradation from 201°C with corresponding peaks DTG in 250 and 330-350°C. At 700°C is observe residues around 20-30%. According to the literature, the degradation of the chain polymeric pectin and the final degradation with the temperature at 330°C demonstrating the degradation of cellulose according to the literature.^{6,17}

Pectin gels report pectin degradation temperature between 230°C and 250°C with approximate mass loss between 53%. Furthermore, pectin and chitosan gels show pectin degradation between 220°C and 280°C with mass loss between 50% and 65% corroborating with studies found in the literature.^{33,34,35}

To characterize the surface of the gels developed based on pectin, mango microcellulose and vegetal microcellulose, scanning electron microscopy (SEM) analyzes were carried out at different magnifications to visualize the structures and morphology of the gels or blends. For this, a film was formed, which after drying, it was possible to be observed by SEM. The morphologies are shown in the micrographs of figures.¹⁰⁻¹⁵

In general, the SEM micrographs allow observing the homogenization of the gel, in addition to some fragments of granules of each type of microcellulose that were dispersed in the pectin (Figures 10-13). In these same images, at different magnifications, a smooth and compact uniform structure was observed between the dispersed phase and the matrix without major defects. Furthermore, the figures also show some elongated fibers that correspond to the microfibrils of mango or vegetal cellulose, which are well disperse and made some

compatibility by the presence of PEG due to the addition of this polymer in the formulation of the gels (Figures 14 and 15). It is noteworthy that only the two gels with PEG in their composition showed this dispersion behavior, and it could be stated that the PEG phase substantially improves the dispersion of microcellulose fibers.³⁶

Research with pectin hydrogels, starch and cellulose microfibers, had similar results in scanning electron microscopy, finding starch and pectin granules, which means that this dispersed phase within the matrix does not completely disaggregate due to the effect of the mixer.³⁴

The homogeneity of hydrogels with PEG is a result of their power of miscibility, hydrophilicity, and formation of a better interphase with the polymeric chain through PEC/MC hydrogen bonds. Studies claim that the addition of PEG in hydrogels causes a relaxation of tensions arising from the long chain, making them more elastic and denser.^{37,38} The latter can be proven by the results of the rheology of the gels, which are presented ahead.

So, the samples were submitted to rheology analysis to verify the viscoelastic capacity of the produced gels which means understanding the proportion as fluid and elastic solid behavior simultaneously. The elastic fraction of the deformation appears due to variations in the angle and the bonding distance between the atoms of the polymeric chain. The plastic fraction occurs due to the friction between the polymeric chains.³⁹

In general, pectin/cellulose gels are hydrocolloid gels compound formed by pectin and cellulose fibers. In this case the dispersed phase is microcellulose fibers. The behavior of the storage modulus versus tension in these gels is affected by the interaction between the pectin and cellulose components and could also be affected by the size of the microfibers.⁴⁰

In Figure 16, it can be observed that the gels present a pseudoplastic behavior at low shear rate, characteristic of gels that can be used in extrusion or bioextrusion processes. But after the increase in the shear rate, it seems that what predominates would be the majority phase of the PECM that generates a Newtonian behavior, however the microcellulose fibers, regardless of their origin, do not participate in the definition of the rheological behavior. For these gels, it is therefore important to consider only the shear values that allow them to have the required behavior for extrusion or bioextrusion processes.

Figure 17 shows the behavior of the storage modulus or elastic modulus versus the shear stress (within the range of pseudoplastic behavior in transition with Newtonian behavior). It is possible to see that at low strains, the gel storage modulus of

pectin/cellulose behaves in a linear elastic manner, like that of pectin gels. However, the addition of cellulose fibers should cause the gel to exhibit a more pronounced non-linear viscoelastic behavior, expecting an increase in the storage modulus as strain increases. In this case it is observed that the presence of PEG produces (at low deformation) a slight increase in the value of the modulus G' and as the deformation continues to increase and appreciable a behavior with a tendency to decrease the elasticity of the material, that is, cellulose fibers can limit gel deformation, leading to a less pronounced plateau in the storage modulus. This can result in a gel that is more rigid and resistant to deformation than a pectin gel without cellulose fibers. The presence of PEG seems to help maintain the elasticity of the gels where this polymeric phase is present.

The loss modulus is a measure of the energy dissipated by the gel during deformation and is related to the viscous or damping behavior of the gel. In pectin/cellulose gels, the loss modulus normally increases as much stress increases, as the gel undergoes more deformation and energy is dissipated, as seen in figure 18. For strains below 5%, i.e. for at low strains, the modulus loss can be relatively low, indicating a relatively low degree of power dissipation. However, as the stress increases, the cellulose fibers start to interact with the pectin molecules, leading to a more pronounced non-linear viscoelastic behavior and an increase in the loss modulus, as happens here for strains between 5-10%.

Finally, in Figure 19, it seems that fiber size and molecular mass play an important role, given that gels formulated with MCV have a more pronounced behavior as a solid material than in the case of gels formulated with MCM. Again, it is appreciated that the presence of PEG really helps the gels perform more optimally, as expected. Here it seems that fiber size and molecular mass play an important role, given that gels formulated with MCV have a more pronounced behavior as a solid material than in the case of gels formulated with MCM. Again, it is appreciated that the presence of PEG really helps the gels perform more optimally, as expected.

A study published in 2019 evaluated the influence of pectin and cellulose concentration on the rheology of mango gels. The researchers observed that the addition of cellulose increased the viscosity of the gel, while the addition of pectin resulted in a weaker gel. Furthermore, the combination of pectin and cellulose led to a gel with a more uniform texture and less susceptible to syneresis during storage.⁴¹

Another study published in 2019 investigated

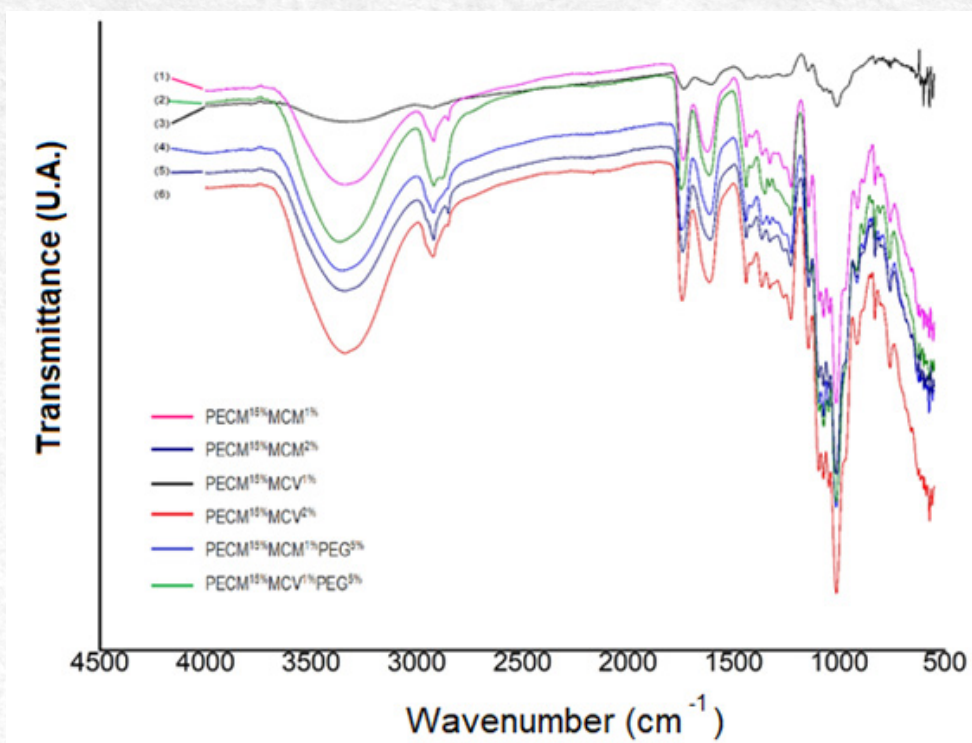


Figure 8 – FTIR spectra of PECM/MCM, PECM/MCV and PECM/MCM/PEG gels.

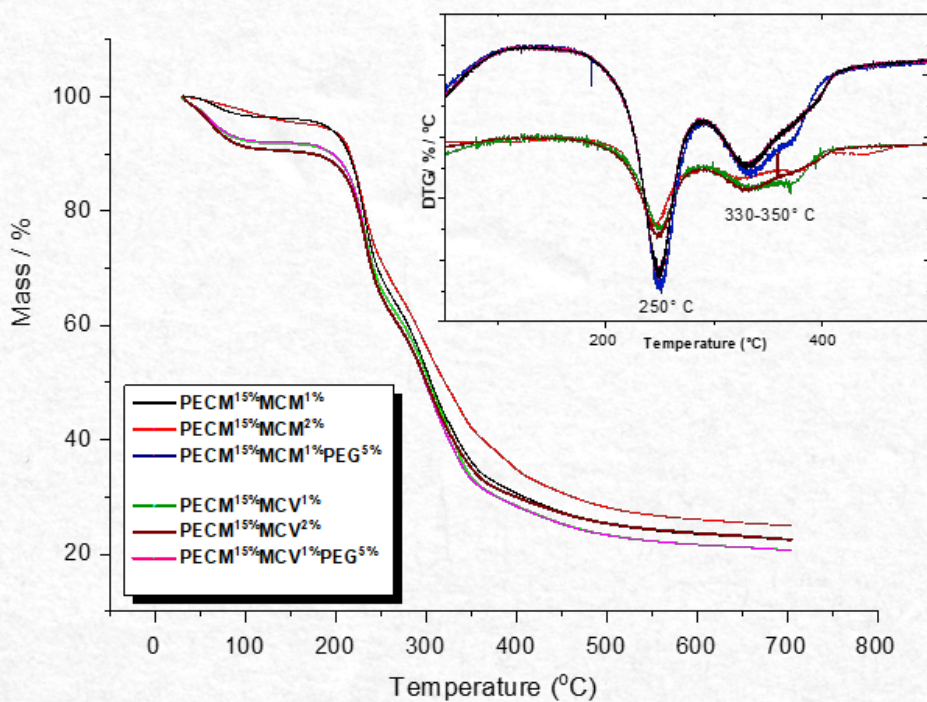


Figure 9 – TG/DTG curves for gels formulations.

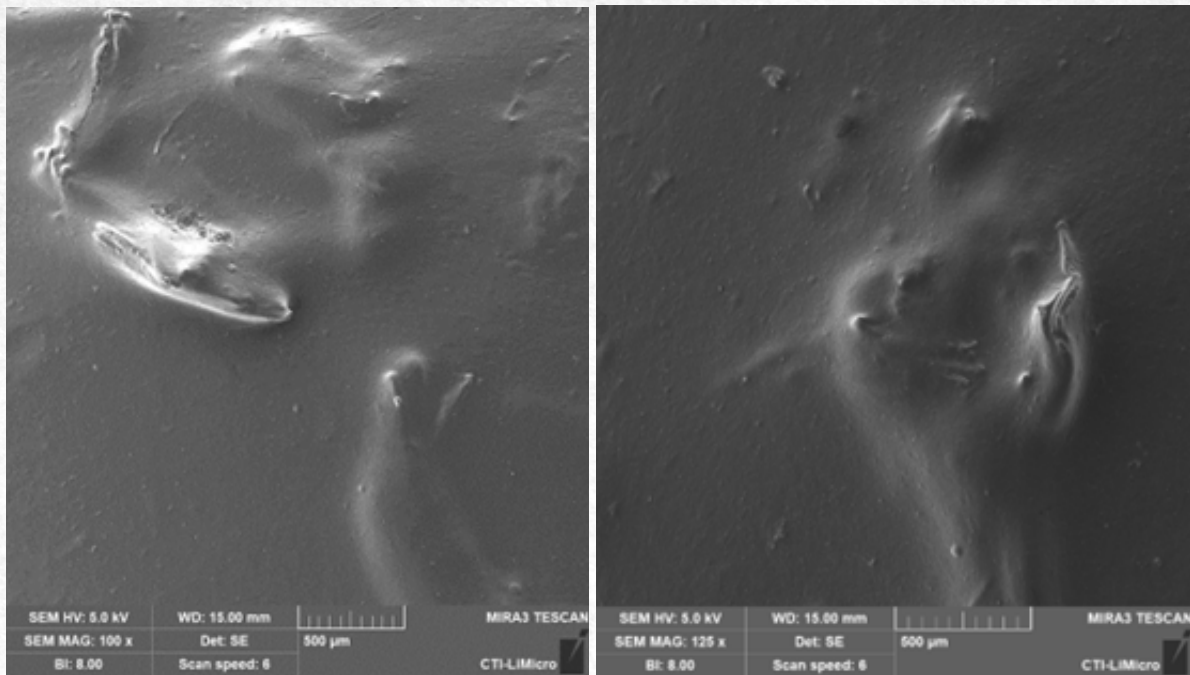


Figure 10 – SEM micrographs of the 1% PECT/MCM gel.

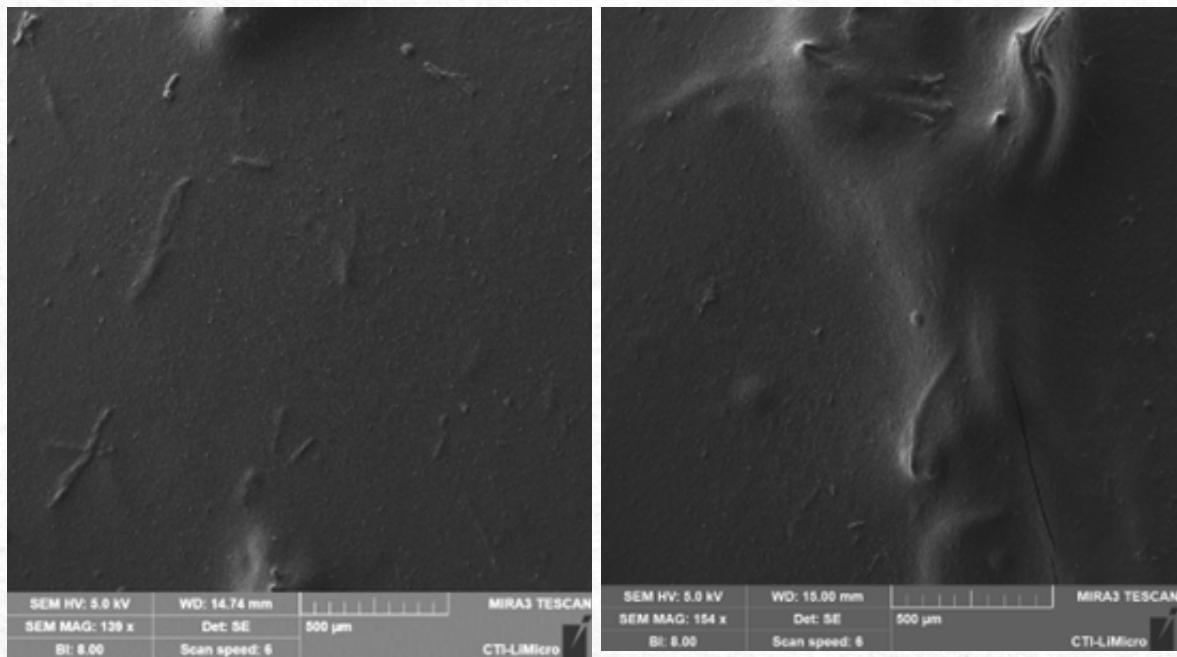


Figure 11 – SEM micrographs of the 2% PECT/MCM gel.

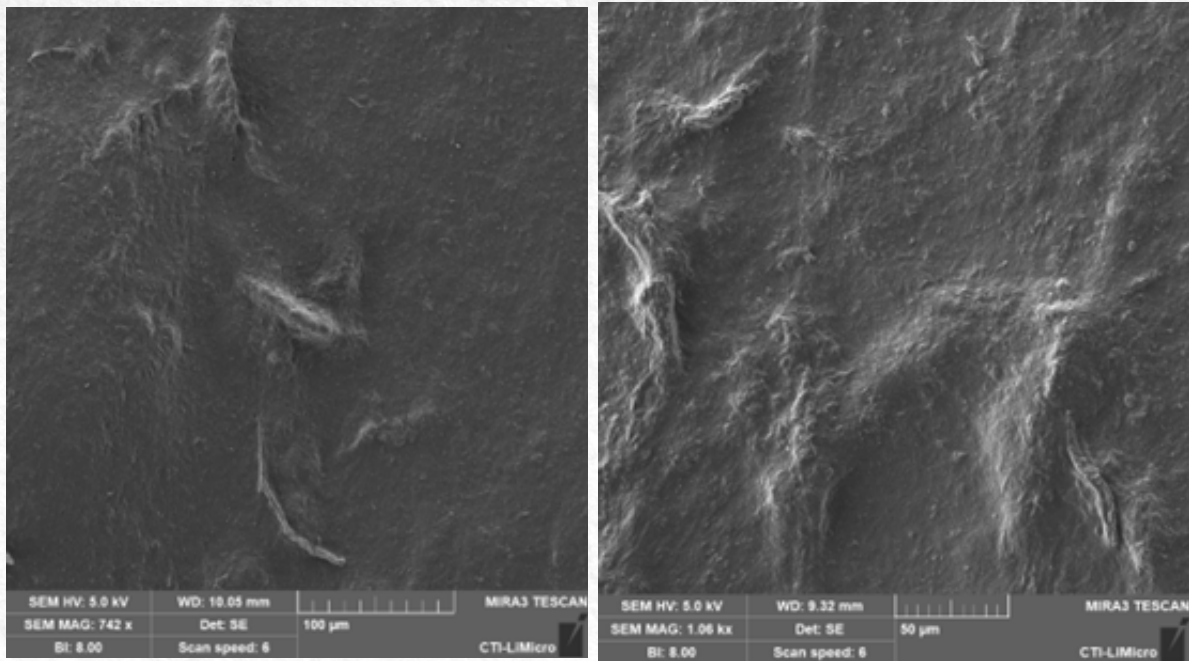


Figure 12 – SEM micrographs of the 1% PECT/MCV gel.

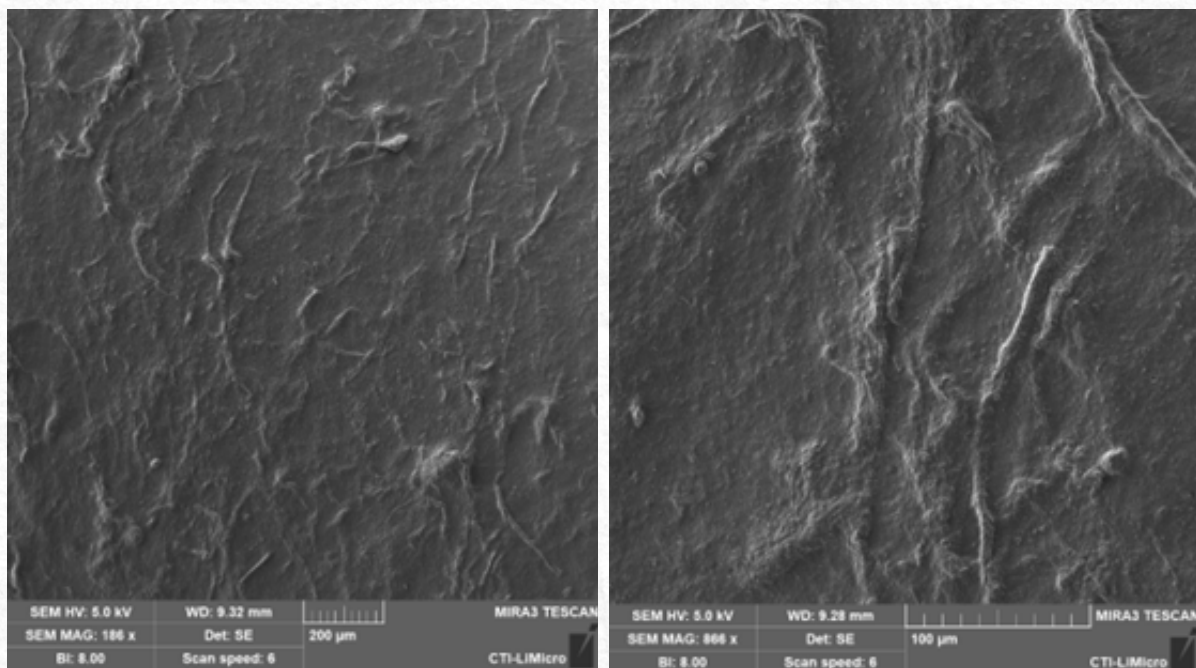


Figure 13 – SEM micrographs of the 2% PECT/MCV gel.

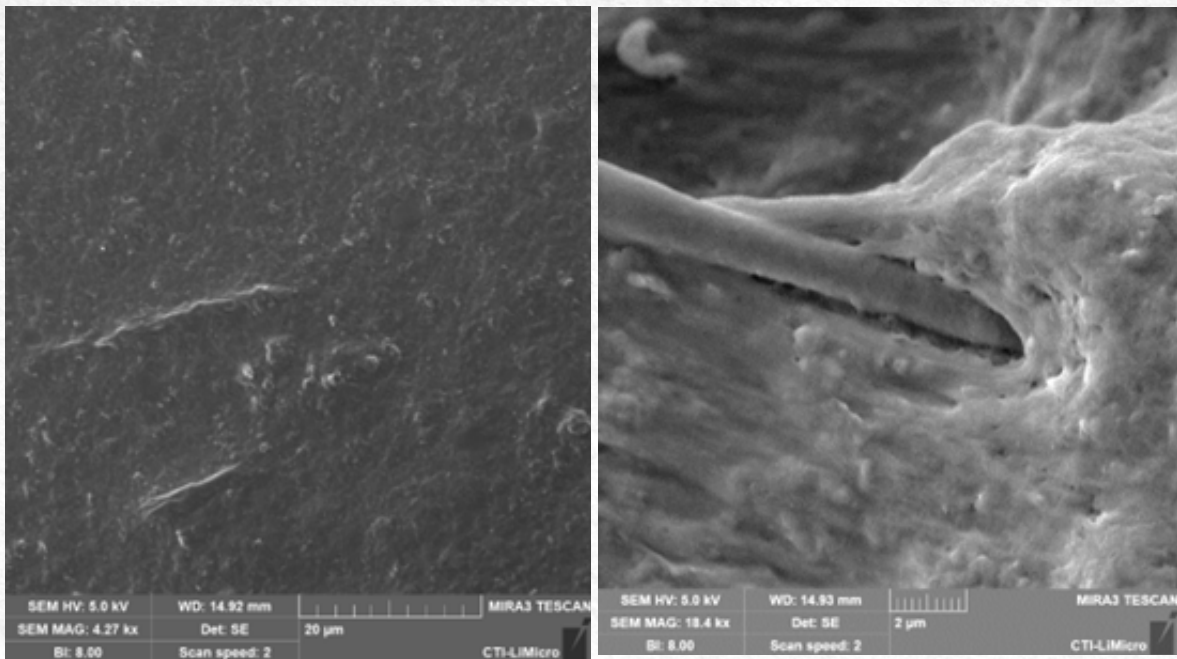


Figure 14 – SEM micrographs of the PECT/MCM(1%)/PEG(5%) gel.

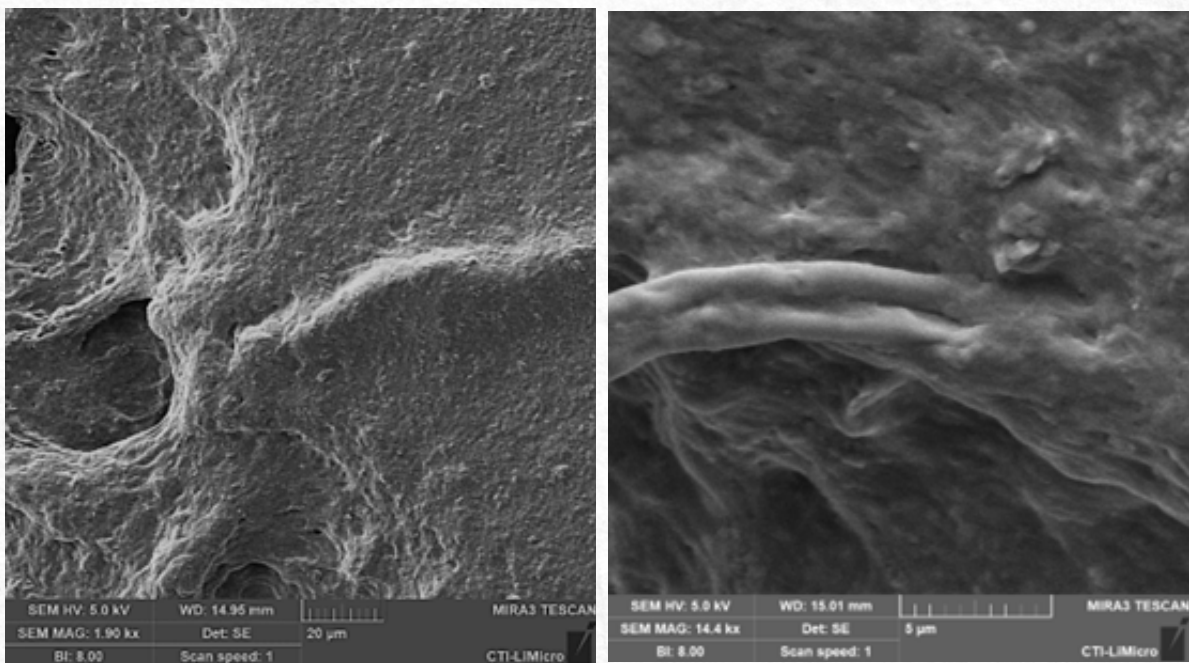


Figure 15 – SEM micrographs of the PECT/MCV(1%)/PEG(5%) gel.

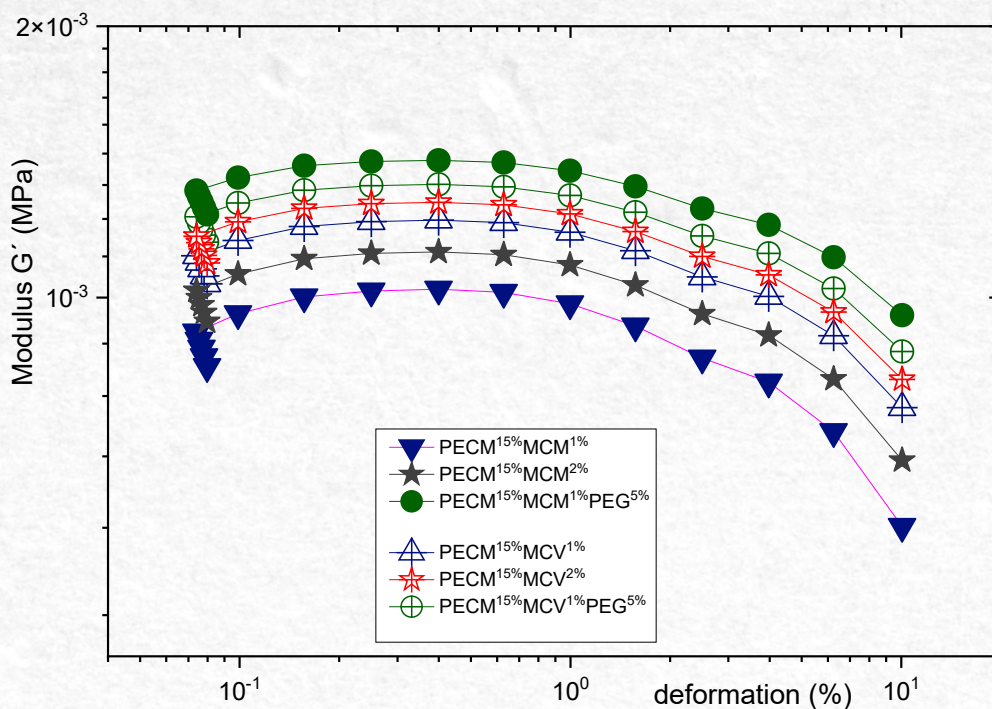


Figure 17 - Variations of G' as a function of pectin and microcellulose gels deformation, also with the PEG phase.

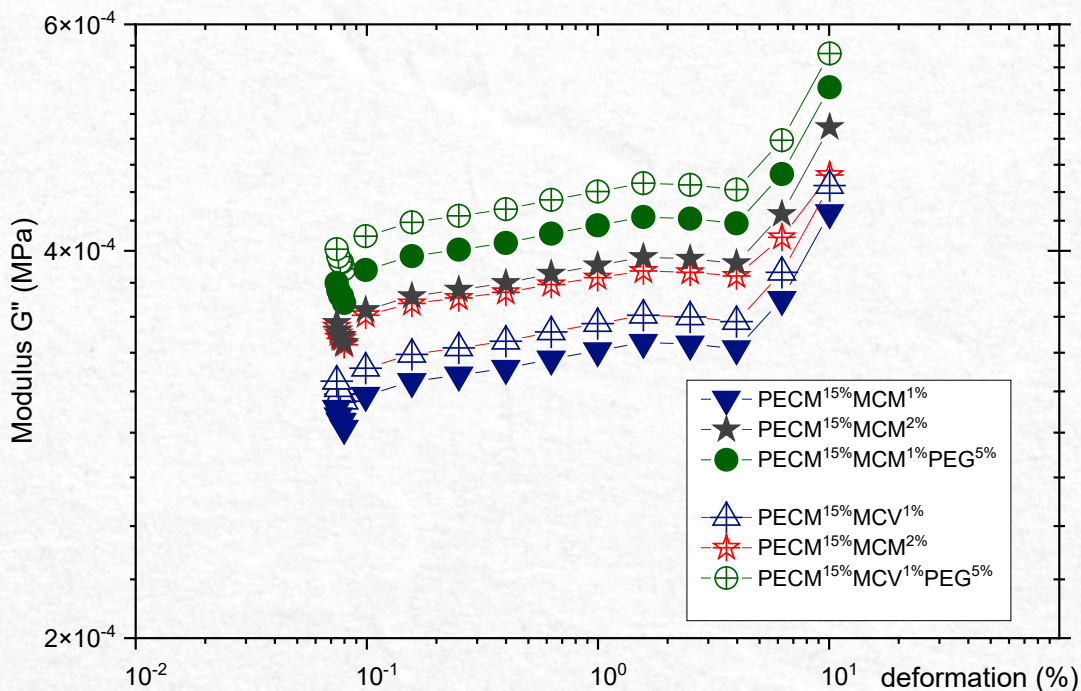


Figure 18 - Variations of G'' as a function of strain for pectin and microcellulose gels, also with the PEG phase.

the rheology of mango pectin and cellulose gels. The researchers observed that adding cellulose to pectin resulted in an increase in gel viscosity and strength. Furthermore, the addition of cellulose also led to a decrease in syneresis (liquid release) during gel storage. It was concluded that blend pectin and cellulose can be an interesting option for the development of fruit gels with improved rheological characteristics.⁴²

A third study, published in 2018 in the International Journal of Biological Macromolecules, investigated the rheology of pectin and cellulose gels derived from mangoes and other fruits. The researchers observed that the addition of cellulose increased the viscosity of the gel, while the addition of pectin resulted in a weaker, less elastic gel. Furthermore, the study reported that the combination of pectin and cellulose can result in a gel with a more uniform texture and less susceptible to syneresis during storage.⁴³

Finally, a study published in 2020 in the International Journal of Biological Macromolecules investigated the effect of adding PEG on the rheology of pectin and cellulose gels derived from mango. The researchers observed that the addition of PEG resulted in an increase in elasticity and a decrease in gel rigidity, without significantly affecting viscosity. Furthermore, the addition of PEG also led to a decrease in syneresis during gel storage.⁴⁴

Another research published in 2019 in the journal Carbohydrate Polymers investigated the influence of adding PEG on the rheology of apple-derived pectin and cellulose gels. The researchers observed that the addition of PEG resulted in an increase in gel viscosity, without significantly affecting elasticity and rigidity. Furthermore, the combination of PEG with other rheology modifying agents resulted in gels with even further improved rheological properties.⁴⁵

Conclusion

Therefore, the use of gels composed of pectin and cellulose from mango can be a promising option for the development of new products for the biotechnological area which includes food, pharmaceutical and biomedical sector, given their functional properties and possible health benefits and even for the clothing and footwear industries.

Pectin and cellulose gels have unique rheological properties that are influenced by the interaction between the two phases and the incorporation of PEG in some formulations. The addition of cellulose fibers can improve the mechanical properties of pectin gels, leading to more pronounced nonlinear viscoelastic behavior with a more rapid increase

in storage modulus as strain increases. It could be thought that cellulose fibers can act as physical crosslinks within the gel network, increasing its stiffness and strength, as demonstrated by rheological analyses.

In this sense, the storage modulus of pectin/microcellulose gels is a key rheological property that characterizes their stiffness and strength. The addition of MCM and MCV fibers increases the storage modulus of pectin gels, leading to a more pronounced non-linear viscoelastic behavior with a faster increase in the storage modulus as strain increases, and exhibiting a pseudoplastic behavior when analyzed the viscosity. In this case, the behavior of the modulus loss in these gels increases with increasing stress, indicating a greater degree of energy dissipation.

The inclusion of Polyethylene glycol (PEG) further improves the properties of the gels. PEG is a polymer soluble in water and in the pectin solution and can act as a plasticizer, reducing the rigidity and increasing the deformability of the gel. The addition of PEG can also improve the water holding capacity of the gel and increase its stability over time.

Pectin/microcellulose gels can have numerous biotechnological applications due to their unique rheological properties analyzed in this research, in addition to their biocompatibility. They could be used as thickeners, stabilizers, and gelling agents. Furthermore, they could be used in pharmaceuticals, cosmetics and biotechnology for drug delivery, wound healing and possibly in tissue engineering applications.

As prospects for this type of gels can focus on the development of new formulations and methods to produce these pectin/microcellulose gels with specific properties to meet particular requirements of these different applications. For example, the concentration and orientation of cellulose fibers can be optimized to achieve specific mechanical and rheological properties. Furthermore, the addition of other natural or synthetic polymers, such as chitosan or polyvinyl alcohol, can be investigated to further modify the properties of the gels.

Acknowledgment

Our sincere tribute and gratitude to scientist and friend Dr. Jorge Vicente Lopes da Silva for his pioneering work and contribution to the areas of additive manufacturing and biofabrication.

To Capes for supporting PROSUP-CAPES to the PPGB-MRQM Program at the University of Araraquara (Uniará). To FAPESP for the support, especially the Visiting Researcher Dr. M. Sabino at CTI Renato Archer, scholarship (Process 2021/13949-5). Centelha project ((Processes 2022/14860-0

(Centelha PIPE Fapesp), 2022/16520-2 (Centelha PIPE Finep), 2023 /02784-0 (BCO Centelha Scholarship)).

References

- [1]. Nasrollahzadeh M, Sajjadi M, Iravani S, Varma RS. Starch, cellulose, pectin, gum, alginate, chitin and chitosan derived (nano)materials for sustainable water treatment: A review. *Carbohydrate Polymers*. 2021 Jan;251:116986.
- [2]. Torres-León C, Rojas R, Serna-Cock L, Belmares-Cerda R, Aguilar CN. Extraction of antioxidants from mango seed kernel: Optimization assisted by microwave. *Food and Bioproducts Processing* [Internet]. 2017 Sep 1 [cited 2020 Dec 4];105:188–96. Available from: <https://www.sciencedirect.com/science/article/abs/pii/S0960308517300901>
- [3]. Mahadevan Tarrsini, Qi Hwa Ng, Yi Peng Teoh, Siew Hoong Shuit, Zhong Xian Ooi, Balakrishnan Kunsundari. Structural and composition modification of Harum Manis mango (*Mangifera indica*) leaves via chemical pretreatment for bioethanol production. *Biomass Conversion and Biorefinery*. 2021 Mar 30;13(5):3987–99.
- [4]. Ngoc Duc Vu, Trung Quang Tran, Van Muoi Nguyen. Process of making rice paper from mango puree. *Materials Today: Proceedings*. 2023 Apr 1.
- [5]. Arbos KA, Stevani PC, Castanha R de F. Antimicrobial activity, antioxidant and content of phenolic compounds in peel and kernel of mango fruits. *Ceres Magazine*. 2013 Apr;60(2):161–5.
- [6]. Abitbol T, Mijlkovic A, Malafronte L, Stevanic JS, Larson PT, Lopez-Sanchez P. Cellulose nanocrystal/low methoxyl pectin gels produced by internal ionotropic gelation. *Carbohydrate Polymers*. 2020 Nov;117345.
- [7]. Wang S, Meng Y, Li J, Liu J, Liu Z, Li D. A novel and simple oral colon-specific drug delivery system based on the pectin/modified nano-carbon sphere nanocomposite gel films. 2020 Aug 1;157:170–6.
- [8]. Tortorella S, Inzalaco G, Dapporto F, Maturi M, Letizia Sambri, Veronica Vetri Buratti, et al. Biocompatible pectin-based hybrid hydrogels for tissue engineering applications. *New Journal of Chemistry*. 2021 Jan 1;45(47):22386–95.
- [9]. Cernencu AI, Lungu A, Stancu IC, Serafim A, Heggset E, Syverud K, et al. Bioinspired 3D printable pectin-nanocellulose ink formulations. *Carbohydrate Polymers*. 2019 Sep;220:12–21.
- [10]. Bostancı NS, Büyüksungur S, Hasirci N, Tezcaner A. Potential of pectin for biomedical applications: a comprehensive review. *Journal of Biomaterials Science, Polymer Edition*. 2022 Jun 24;1–35.
- [11]. Natcrom Sustainable Solutions, Av. Jorge Fernandes de São Mattos, 311 - BOX 03 - 8° Industrial District, Araraquara-SP, Brazil, 14808-154, isadcoutinho@gmail.com , Tel .: +55 16 997699125
- [12]. Shahi N, Min B, Sapkota B, Rangari VK. Eco-Friendly Cellulose Nanofiber Extraction from Sugarcane Bagasse and Film Fabrication. *Sustainability*. 2020 Jul 27;12(15):6015.
- [13]. Suzano - Home [Internet]. Suzano.com.br. 2021. Available from: [https://www.suzano.com.br/Technical Association of the Pulp & Paper Industry Inc. \[Internet\]. www.tappi.org. \[cited 2023 Aug 28\]. Available from: http://www.tappi.org](https://www.suzano.com.br/Technical Association of the Pulp & Paper Industry Inc. [Internet]. www.tappi.org. [cited 2023 Aug 28]. Available from: http://www.tappi.org)
- [14]. Andritsou V, de Melo EM, Tsouko E, Ladakis D, Maragkoudaki S, Koutinas AA, et al. Synthesis and Characterization of Bacterial Cellulose from Citrus-Based Sustainable Resources. *ACS Omega*. 2018 Aug 31;3(8):10365–73.
- [15]. Stockert JC, Horobin RW, Colombo LL, Blázquez-Castro A. Tetrazolium salts and formazan products in Cell Biology: Viability assessment, fluorescence imaging, and labeling perspectives. *Acta Histochemica* [Internet]. 2018 Apr [cited 2019 Dec 6];120(3):159–67. Available from: <https://www.ufmt.br/ppgcs/images/uploads/editais/papers2019/Linha3/Tetrazolium-saltsandformazanproductsinCellBiologyViabilityassessmentfluorescenceimagingandlabelingperspectives>
- [16]. Machinsky, K. DV et al. Synthesis and characterization of cellulose acetate polymer. Currently, the search for alternatives to preserve the environment and add value to industrial and urban waste is increasing significantly. The conversion of ligated residues. n. October, 2018.
- [17]. Sousa, ALN et al. Chemical modification of pectin from red melon (*Cucumis melo* VAR. *acidulus*). *New Chemistry*, v. 40, no. 5, p. 554–560, 2017.
- [18]. Oliveira Souza L. Rheological and morphological characterization of cocoa husk nanocellulose for application in the development of biodegradable films. 2021;
- [19]. Du, B., Nie, S., Peng, F., Yang, Y., & Xu, B. (2022). A narrative review on conformational structure characterization of natural polysaccharides. *Food Frontiers*, 3(4), 631-640.
- [20]. Bagherian H, Zokaee Ashtiani F, Fouladitajar A, Mohatashamy M. Comparisons between conventional, microwave- and ultrasound-assisted methods for extraction of pectin from grapefruit. *Chemical Engineering and Processing: Process Intensification*. 2011 Nov;50 (11-12):1237–43.
- [21]. Zhou J, Wu Y, Shen Z. Viscous-flow properties and viscosity-average molecular mass of orange peel pectin. *Journal of Central South University of Technology*. 2008 Sep;15(51):520–4.
- [22]. Jamsazzadeh Kermani Z, Shpigelman A, Kyomugasho C, Van Buggenhout S, Ramezani M, Van Loey AM, et al. The impact of extraction with a chelating agent under acidic conditions on the cell wall polymers of mango peel. *Food Chemistry* [Internet]. 2014

- Oct 15 [cited 2020 Nov 30];161:199–207. Available from: <https://www.sciencedirect.com/science/article/pii/S0308814614005342>
- [23]. Ryoya Hiraoki, Ono Y, Saito T, Akira Isogai. Molecular Mass and Molecular-Mass Distribution of TEMPO-Oxidized Celluloses and TEMPO-Oxidized Cellulose Nanofibrils. *Biomacromolecules*. 2015 Jan 26;16(2):675–81.
- [24]. Carolino Ads. Estimation of the percentage of crystallinity of semi-crystalline aniline-derived polymers through x-ray diffraction patterns. 2017;
- [25]. Wathoni N, Yuan Shan C, Yi Shan W, Rostinawati T, Indradi RB, Pratiwi R, et al. Characterization and antioxidant activity of pectin from Indonesian mangosteen (*Garcinia mangostana* L.) rind. *Heliyon* [Internet]. 2019 Aug 1 [cited 2020 Mar 15];5(8):e02299. Available from: <https://www.sciencedirect.com/science/article/pii/S2405844019359596>
- [26]. Travalini AP, Prestes E, Pinheiro LA, Demiate IM. High crystallinity nanocellulose extracted from cassava bagasse fiber. 2016;
- [27]. Giosafatto, C. Valeria L., et al. "Characterization of Citrus pectin edible films containing transglutaminase-modified phaseolin." *Carbohydrate Polymers* 106 (2014): 200-208.
- [28]. Araujo CKC. Evaluation of the influence of chemical and biological surfactants on the enzymatic hydrolysis of green coconut shell after acid/alkaline pre-treatment and with alkaline hydrogen peroxide. 2016.
- [29]. Zanette R, Almeida LBF, Almeida CG, Oliveira CR, Humberto M, Munk M. In vitro cytotoxicity analysis of cotton cellulose nanofibers. 2017.
- [30]. Souza EE. Synthesis and characterization of regenerated cellulose membranes from cellulose extracted from sugarcane bagasse for the production of cuprophane. 2009.
- [31]. Paramasivan, Balasubramanian. "Microwave assisted carbonization and activation of biochar for energy-environment nexus: A review." *Chemosphere* 286 (2022): 131631.
- [32]. Kiruthika, S., et al. "Conducting biopolymer electrolyte based on pectin with magnesium chloride salt for magnesium battery application." *Polymer Bulletin* 77 (2020): 6299-6317.
- [33]. Okonkwo, Clinton E., et al. "Application of biogels for bioactives delivery: Recent developments and future research insights." *Applied Food Research* (2022): 100238.
- [34]. Ferrarezi, Márcia Maria Favaro, et al. "Poly(ethylene glycol) as a compatibilizer for poly (lactic acid)/thermoplastic starch blends." *Journal of Polymers and the Environment* 21 (2013): 151-159.
- [35]. Warren Cr, Adams Ma. Internal conductance does not scale with photosynthetic capacity: implications for carbon isotope discrimination and the economics of water and nitrogen use in photosynthesis. *Plant, Cell and Environment*. 2006 Feb;29(2):192–201.
- [36]. Victory MS. Characterization of hyaluronic acid gels cross-linked with polyethylene glycol diglycidyl ether and butanediol diglycidyl ether with indications in dentistry. 2020 Aug 6;
- [37]. Canevarolo Jr.S. *Polymer Science - A basic text for technologists and engineers*. 2006;139–68.
- [38]. Ciriminna R, Fidalgo A, Scurria A, Ilharco LM, Pagliaro M. Pectin: New science and forthcoming applications of the most valued hydrocolloid. *Food Hydrocolloids*. 2022 Jun;127:107483.
- [39]. Deng Z, Pan Y, Chen W, Chen W, Yun Y, Zhong Q, et al. Effects of cultivar and growth region on the structural, emulsifying and rheological characteristic of mango peel pectin. *Food Hydrocolloids*. 2020 Jun;103:105707
- [40]. Shayla Fernanda Barbieri, Sarah, Andrea Caroline Ruthes, Lúcia C, Nicole Cristine Kerkhoven, Silva, et al. Pectins from the pulp of gabioba (*Campomanesia xanthocarpa* Berg): Structural characterization and rheological behavior. *Carbohydrate Polymers*. 2019 Jun 15;214:250–8.
- [41]. Barbieri, S. F., da Costa Amaral, S., Ruthes, A. C., de Oliveira Petkowicz, C. L., Kerkhoven, N. C., da Silva, E. R. A., & Silveira, J. L. M. (2019). Pectins from the pulp of gabioba (*Campomanesia xanthocarpa* Berg): Structural characterization and rheological behavior. *Carbohydrate polymers*, 214, 250-258.
- [42]. Nascimento Oliveira A, de Almeida Paula D, Basílio de Oliveira E, Henriques Saraiva S, Stringheta PC, Mota Ramos A. Optimization of pectin extraction from Ubá mango peel through surface response methodology. *International Journal of Biological Macromolecules*. 2018 Jul;113:395–402.
- [43]. Ke J, Jiang GF, Shen G, Wu H, Liu Y, Zhang Z. Optimization, characterization and rheological behavior study of pectin extracted from chayote (*Sechium edule*) using ultrasound assisted method. *International Journal of Biological Macromolecules*. 2020 Mar 1;147:688–98.
- [44]. Patova OA, Smirnov VV, Golovchenko VV, Vityazev FV, Shashkov AS, Popov SV. Structural, rheological and antioxidant properties of pectins from *Equisetum arvense* L. and *Equisetum sylvaticum* L. *Carbohydrate Polymers*. 2019 Apr; 209:239–49.

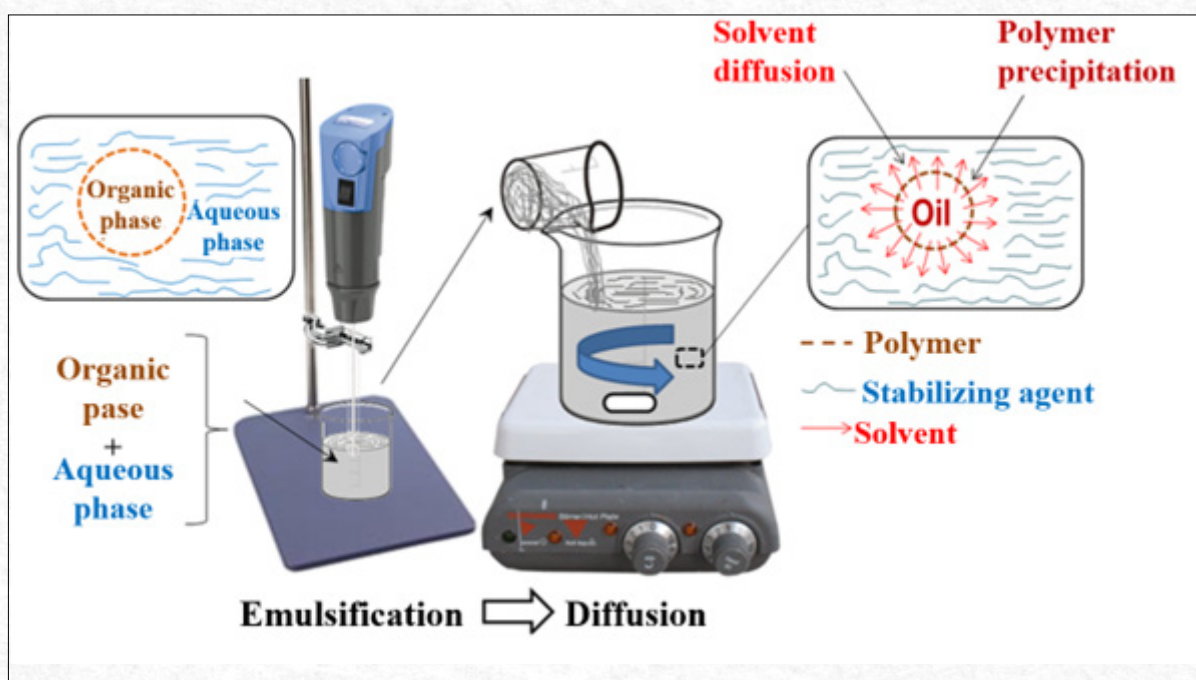


Encapsulation and controlled release of 1,4-naphthoquinone in PDLA nanoparticles: design, biological efficacy, and cancer targeting

K.González^{1,2*}; E.Del Carpio^{2*}; G.González^{3,4};
M.L.Serrano²; J.V.L. Da Silva⁵; M.A. Sabino^{5,6}

*Corresponding author: E-mail address: karina.gonzalez@ucv.ve; *edgar.delcarpio@ucv.ve

Received: October 2024; Accepted: December 2024.



Abstract: Drug release can be controlled by encapsulating active compounds in polymeric vehicles. Using nanotechnology, pharmaceutical drug delivery systems can be controlled and precise. The aim of this work is to obtain and characterize biocompatible micro and nanoparticulate systems based on a poly(D-lactic acid) matrix (PDLA) to study the controlled release of 1,4-naphthoquinone, which has reported anticancer activity. Scanning electron microscopy revealed spherical particles with an average size of 347 nm and 86% in the nanometer range. The encapsulation efficiency was 98.3%, as assessed by UV-visible spectroscopy. The hydrolytic degradation over 11 weeks showed controlled release of naphthoquinone at different pH conditions: 20.98% in alkaline, 19.69% in physiological, 18.83% in strongly acidic, and 16.70% in slightly acidic conditions. The enhanced release at alkaline pH suggests potential anticancer activity in colorectal cancer, benefiting treatment by releasing the drug to the affected area. Molecular docking studies on COX-2 confirmed these results, showing 1,4-naphthoquinone interacts with key amino acids (ALA202, THR206, HIS207) in the active site, modifying the prostaglandin chain which is crucial for the enzyme's function. The results show that this system has a high potentiality for use for pharmacological applications in colorectal cancer, as 1,4-naphthoquinone exhibits electronic properties.

Keywords: Controlled release. PDLA. 1,4-naphthoquinone. Micro and nanoparticles. Anticancer activity. Molecular docking.

¹Polymer Laboratory. Chemistry Center "Dr. Gabriel Chuchani." Venezuelan Institute of Scientific Research, Venezuela.

²Unit of Medicinal Chemistry. Faculty of Pharmacy. School "Dr. Jesus Maria Bianco." Central University of Venezuela. Caracas, Venezuela.

³School of Physics and Nanotechnology, Yachay Tech University. Ecuador.

⁴Center for Materials Engineering and Nanotechnology, Materials Laboratory. Venezuelan Institute of Scientific Research. Edo Miranda, Venezuela.

⁵Renato Archer Technology and Information Center, CTI. Campinas, SP, Brazil.

⁶B³IDA Group. Department of Chemistry. Simón Bolívar University. Edo Miranda, Venezuela.

Introduction

Controlled drug release is a very useful technique in pharmaceutical sciences, since it allows the drug to be released gradually and sustained in the body^{1,2}. Several mechanisms can accomplish this, including controlled diffusion, degradation of the encapsulating material, or response to specific stimuli (pH, temperature, enzymes)^{1,2}. Encapsulation is one of the primary strategies for controlling drug release, as an encapsulated drug has a number of benefits over other forms of administration and has been referred to as a modified drug release form³⁻⁶.

A key goal of medicinal chemistry is to improve the way in which active ingredients (such as biomolecules, drugs, etc.) are transported and released, thereby reducing side effects and improving therapeutic effects. As understanding of the pathophysiology of diseases and their cellular mechanisms is gained, drug delivery systems are customized in order to achieve optimal therapeutic effectiveness. The controlled drug release strategy allows the decrease of side effects, improve oral bioavailability, sustain the effect of drugs or genes in a selected tissue, increase the solubility of drugs for intravascular delivery and to improve the stability of therapeutic agents against enzymatic degradation by nucleases and proteases, especially in the case of drugs containing proteins, peptides, or nucleic acids^{3,7}.

From a pharmaceutical perspective, micro- and polymeric nanoparticles have the advantage of encapsulating lipophilic or hydrophilic substances at a high level. Moreover, they are used as vectors for the controlled release of proteins, peptides, vaccines, genes, and growth factors, among others, and in applications for a variety of therapies, including anticancer therapy⁸⁻¹⁰.

In the case of cancer therapy, the strategies adopted based on the use of micro- and nanoparticles have focused on two different mechanisms: A passive targeting strategy or vehiculization, and an active targeting strategy⁸. Passive targeting consists of the transport of micro-nanosystems through intracellular spaces into the tumor interstitium and their subsequent accumulation in these tissues. Active targeting refers to the active orientation of the micro-nanoparticles, and not just a simple accumulation in the tumor tissues, motivated by their marked specificity towards the target cells⁸. According to literature, the following biocompatible vehicles have been used to encapsulate drugs or biomolecules within particle matrixes: poly(L-lactic acid) (PLLA)⁹, poly(D-lactic acid) (PDLA)^{9,11,12}, polyethylene glycol (PEG)¹³, polyalkyl cyanoacrylate (PACA)¹⁴, poly-ε-caprolactone (PCL)¹⁵, poly(hydroxybutyrate-co-hydroxyvalerate) (PHBV)¹⁶, among others¹⁷. There are also polymethacrylates that react physicochemically to chan-

ges in pH, such as Eudragit^{®18}, which can be used to enhance oral drug bioavailability. Likewise, copolymers have been used, through the pegylation technique, being reported: PEG-PCL, PEG-PLA, among others^{19,20}. Nanocapsules have also been prepared using copolymers formed by varying the composition of their monomeric units of lactic acid/glycolic acid (PLGA)²¹⁻²³.

Poly(lactic acid)lactic acid, PLA, is an aliphatic polyester that have two stereoisomers PLLA and PDLA. The PDLA stereoisomer is amorphous and has been reported to decompose into non-toxic by-products through simple hydrolysis of the main ester chain in an aqueous environment, ultimately this degradation produces lactic acid which can be metabolized through the Krebs cycle into water and carbon dioxide[24]. These characteristics make PDLA safe for use in tissue engineering applications and can be applied for the encapsulation and controlled drug released due to its ability to protect the drug from photodegradation and pH changes²⁴⁻²⁶.

Micro-nanoparticles have been produced using many methods based on different physical-chemical principles. Some of these methods are nanoprecipitation, emulsion diffusion, double emulsification, emulsion-coacervation, polymer coating, layering, etc.^{27,28}. The present research was conducted using the microemulsification technique^{29,30}, which is a modification of the original emulsion-diffusion process used by our research group. In most cases, polymeric particle sizes of nanometers³¹⁻³⁴, have been obtained, along with encapsulation values exceeding 90%^{11,35-37}.

In terms of drugs, this work highlights the use of the active compound naphthoquinone, which has been reported to have a wide range of derivatives with biological activities, especially against some cancer cell lines^{38,39}. Combined with their low toxicity, segments of these compounds have been proposed as potential cancer chemotherapeutics³⁸.

According to reports, chitosan membranes have been developed for the controlled release of 1,4-naphthoquinone to treat oncologic skin cancer wounds⁴⁰. In vitro studies have demonstrated its cytotoxic potential in colon cancer, human breast cancer, hepatocellular cancer, leukemia and human melanoma cells, producing induction of oxidative stress, apoptosis and cell membrane damage in these cell lines^{41,42}. Based on the results of these studies, this research is focused on evaluating the effects of PDLA micro- and nanoparticles released under controlled conditions³⁵.

As one of the most prevalent types of cancer in the world, colon-rectal cancer is one of the leading causes of morbidity and mortality. Approximately 10% of all cancer cases are caused by this disease,

and it is the second leading cause of cancer-related death. According to the World Health Organization (WHO), more than 1.9 million new cases of colorectal cancer and more than 930,000 deaths due to this disease were reported in 2020⁴³.

In colorectal cancer, many enzymes are overexpressed and represent potential targets of action. In this regard, it has been shown that the metabolism of arachidonic acid, a polyunsaturated fatty acid, either by the cyclooxygenase (COX) pathway or by the lipoxygenase (LOX) pathway, generates a series of proinflammatory substances called eicosanoids including prostaglandins, thromboxanes, leukotrienes⁴⁴. COX-2, in particular, plays a crucial role in inflammation and pain. Overexpression of cyclooxygenase-2 has been associated with several diseases, including colon cancer, where it can promote tumor growth and angiogenesis⁴⁵.

Studies have shown that colonic epithelial cells overexpressing the COX-2 gene resist apoptosis and exhibit altered adhesion and angiogenic properties. These findings suggest that COX-2 may be involved in colorectal cancer progression. Furthermore, COX-2 is elevated in 40% of colon adenomas and 90% of colon carcinomas, but not in normal colonic epithelium. Using human colon carcinoma cell lines, COX-2 has been shown to induce local immunosuppression by increasing prostaglandin E₂, a potent inhibitor of T-lymphocyte proliferation, which allows colon cancer cells to escape host immune defenses^{46,47}. Clinical studies have found that COX-2 selective nonsteroidal anti-inflammatory drugs (NSAIDs) have exhibited potent action in the treatment of colorectal cancer by inhibiting the cyclooxygenase enzyme, since they have the ability to reduce inflammation and pain without the side effects associated with nonselective NSAIDs, they are more effective as chemotherapeutic agents⁴⁸.

The use of *in silico* techniques in medicinal chemistry, such as molecular docking, to study the interaction of 1,4-naphthoquinone with enzymes overexpressed in colon cancer provides valuable information on the biochemical mechanisms that may influence its anticancer activity^[50]. These enzymes, involved in drug detoxification and metabolism processes, may modify the bioavailability and efficacy of the compound. By performing docking simulations, it is possible to identify the preferential binding sites and evaluate how structural modifications of naphthoquinone could optimize its interaction with these enzymes, potentially improving its therapeutic profile. By performing docking simulations, it is possible to identify the preferential binding sites and evaluate how structural modifications of naphthoquinone could optimize its interaction with these enzymes, potentially improving its therapeutic profile. Our goal was to evaluate the interaction

between 1,4-naphthoquinone and COX-2 enzyme by molecular docking analysis in order to correlate its previously reported anticancer activity^{[21], [22]} with its interaction with this enzyme. Additionally, our study focused on colon rectal cancer because the controlled release results obtained at alkaline pH, which corresponds to intestinal pH were higher⁴⁹.

Therefore, the objective of this study was to encapsulate 1,4-naphthoquinone in PDLA polymeric micro-nanoparticulate systems and release the drug selectively, as well as to correlate the biological activity of 1,4-naphthoquinone by molecular docking using the COX-2 enzyme.

Methodology

Reagents

1,4-naphthoquinone (C₁₀H₆O₂; molecular mass: 158.15 g/mol, 97% CAS No. 130-15-4 from Sigma-Aldrich) was used. For encapsulation, poly(D-Lactic acid) (PDLA), molecular mass ≈ 91102 g/mol, NatureWork USA, was used as a polymer. Polyvinyl Alcohol (PVA) (C₂H₄O)_n, molecular mass ≈ 9.5x10⁴ g/mol, CAS No. 9002-89-5, Himedia, was available. Deionized water, chloroform (CHCl₃; molecular mass: 119.38 g/mol, CAS No. 67-66-3, 99.5% purity from Sigma-Aldrich). All reagents were supplied without further purification. The materials were supplied by the Organic Chemistry Laboratory, B⁵IDA Group, Universidad Simón Bolívar.

Preparation of PDLA micro-nanoparticles by microemulsification

The methodology employed for the preparation of micro- and nanoparticles is presented below^{29,30}: A 100 mL solution of 0.025% m/v polyvinyl alcohol (PVA) in water was prepared. An additional 5.0 mL of a solution containing 1,4-naphthoquinone at 0.18% m/v in CHCl₃ and PDLA polymer solution at 1% m/v in CHCl₃ was added to this solution. The polymer solution with the 1,4-naphthoquinone was added using a micropipette. A finned reactor was used as a vessel and an ultradisperser was included. The reactor was immersed in ultrasound equipment for 120 min. After the process, the emulsion was left under continuous agitation for 24 hours to remove chloroform by evaporation. The resulting suspension was centrifuged. The precipitated particles were washed with deionized water to remove any PVA that may have remained on their surface. The wash water was retained to determine the percentage of encapsulation. Finally, the particles were lyophilized and prepared for characterization (See Figure 1).

Feasibility assay. Reduction of 3-(4,5-dimethylthiazol-2-yl)-5-(3-carboxymethoxyphenyl)-2-(4-sulfophenyl)-2H-tetrazolium salt (MTS) for PDLA micro-nanoparticles.

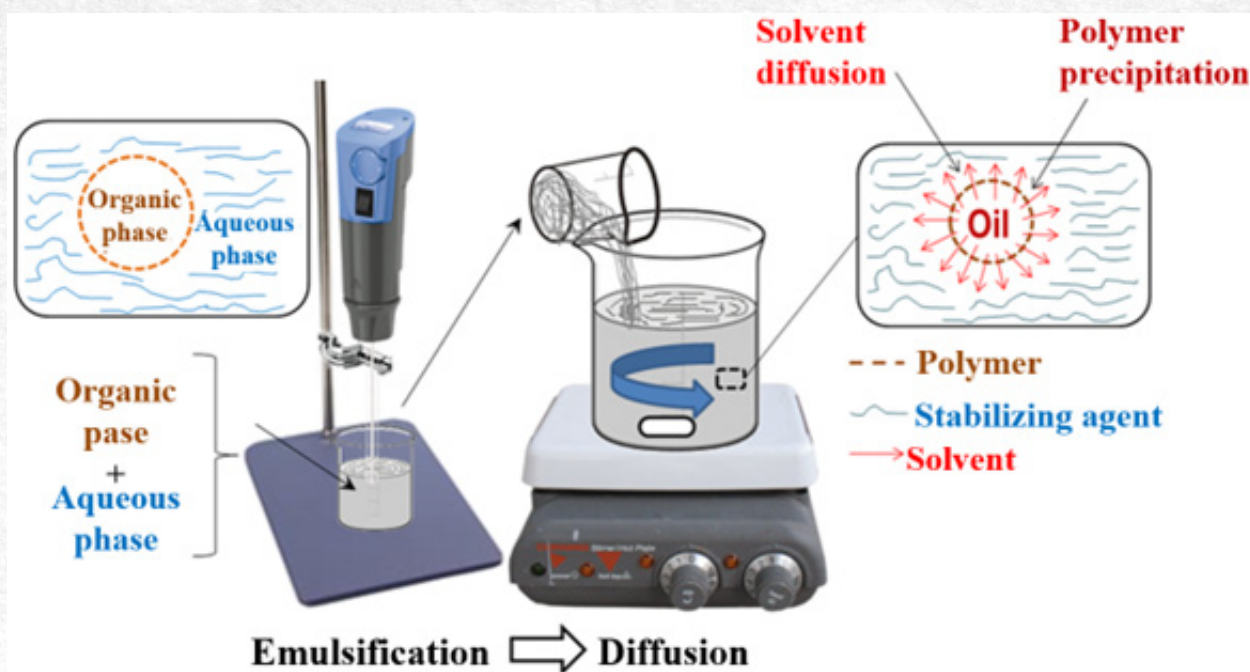


Figure 1 - Preparation of micro- and nanoparticles by emulsion-diffusion method.

PDLA polyester has been reported not to be cytotoxic [24], however, given the preparation method, it was necessary to evaluate the possible cytotoxicity of PDLA micro-nanoparticles without encapsulation. An *in vitro* cell survival study was previously performed, in MCF-7 breast cancer cells and NIH-3T3 murine fibroblasts, a colorimetric assay has been established for the metabolic reduction of MTS (reducing MTS to the tetrazolium salt [3-(4,5-dimethylthiazol-2-yl)-5-(3-carboxymethoxyphenyl)-2-(4-sulfophenyl)-2H-tetrazolium]) in formazan, and measuring the production of formazan at 550 nm⁵⁰.

To perform this, MCF-7 breast tumor cells and non-tumorigenic NIH-3T3 fibroblast cells were cultured at a density of 5x10³ cells per well in 96-well CELLSTAR® plates along with 100µL of DMEM medium supplemented with 15% SFB Gibco®, and left in incubation for 24 hours for adherence of the cells to the plate. Subsequently, the culture medium was removed and 90µL of the medium was added along with 10µL of the PDLA micro-nanoparticles at 1000 ppm concentration such that the concentration of the micro-nanoparticles in each well was 100 ppm. They were incubated at 37°C for 24, 48 and 72 hours, and at the end of this time 20µL of MTS CellTiter 96® Aqueous One Solution Cell Proliferation Assay G358A Promega® were added, waited 4 hours and the plates were read at 550 nm using the Autobio PHOMO® ELISA plate reader. As a positive control, cisplatin⁵¹ was used at different concentrations (0.5-100 µM). The assays were performed in triplicate.

Determination of encapsulation efficiency by UV-Visible Spectroscopy (UV-Vis)

The encapsulation efficiency of the compounds was determined indirectly from the quantification of the 1,4-naphthoquinone present in the washing water obtained after the encapsulation process in the micro and nanoparticles.

In this sense, an extraction of the derivatives contained in the washing water was carried out.

The organic solvent used in this experiment was chloroform, which promoted a liquid-liquid extraction and a saturated solution of NaCl. To determine the radiation absorption capacity of the compound obtained, the organic phase was dried using a rotary evaporator, and the compound obtained was diluted with DMSO to a volume of 2.0 mL. The calibration curves corresponding to the compounds were made, plotting the absorbance as a function of the concentration of each derivative. In order to determine encapsulation efficiency, 1,4-naphthoquinone absorption wavelength of 336nm according to equation (Eq.1)⁵²:

$$\% \text{ Encapsulation} = \frac{\text{Amount of encapsulated compound}}{\text{Initial amount of the compound in the system}} \times 100\% \text{ (Eq.1)}$$

UV-Vis controlled release assay by hydrolytic degradation at different pH conditions.

A hydrolytic degradation assay of polymeric micro-nanoparticles of 1,4-naphthoquinone was performed at different pH conditions, for this purpose:

a.- 10 mg of 1,4-naphthoquinone micro-nanoparticles in PDLA were placed in four centrifuge tubes at different conditions: acidic (1 ≤ pH ≤ 2), slightly acidic (pH ≈ 6), physiological (pH=7.4) and alkaline (pH=9). This model was made in virtue of being able to observe the different degradation conditions of these particles in pH that could occur in different

parts of the human body, for example, strongly acid gastric pH^[55], physiological pH in blood^[56], slightly acid pH in certain tumor conditions^[8] and slightly alkaline pH in the intestinal medium^[55].

b.- The assay was carried out for 12 weeks at 25 °C, during which the following extraction procedure was performed: the samples were centrifuged and a liquid-liquid extraction was performed in CHCl₃ and filtered with anhydrous MgSO₄.

c.- Each sample was brought to a volume of 2.00 mL for subsequent UV reading at the wavelength of maximum absorption ($\lambda=336\text{nm}$)^[52].

Characterization by Scanning Electron Microscopy

The PDLA micro-nanoparticles of 1,4-naphthoquinone, previously lyophilized, were observed using a JEOL JSM 6460 scanning electron microscope at 15 kV, previously, the samples were placed in a sample holder and coated with gold using a Balzers-SCD-030 Sputter-coater.

Molecular Docking Studies of 1,4-Naphthoquinone

For molecular docking studies the coordinates of Cyclooxygenase-2 (COX-2) were obtained from

the Protein Data Bank (PDBid: 5F1A). The PDB file of the enzyme was optimized by removing water molecules and co-crystallized ligands. The enzyme was energetically minimized in Swiss-PdbViewer (SPDBV) using GROMOS96 as the force field. Structural validation of the energetically minimized COX-2 was performed by Verify 3D using ERRAT, PROSA-WEB and ProCheck tools. Once the crystal structure of the receptor was validated, Molecular Docking studies were performed using AutoDock Vina and a ligand library consisting of 1,4-naphthoquinone (PubChem CID = 8530) and selective inhibitors (Parecoxib, PubChem CID = 119828; Sulindac, PubChem CID = 1548887; Rofecoxib, PubChem CID = 5090, Celecoxib; PubChem CID = 2662) and nonselective Cox-2 (Indomethacin, PubChem CID = 3715. All ligands were downloaded from PubChem in .sdf format and converted into .pdbqt formats to study molecular docking. Molecular docking studies were performed in quintuplicate. The results were prioritized according to the predicted binding free energy in kcal/mol. The molecular structure of the ligands used in the molecular docking studies is presented in Figure 2.

Results and Discussion

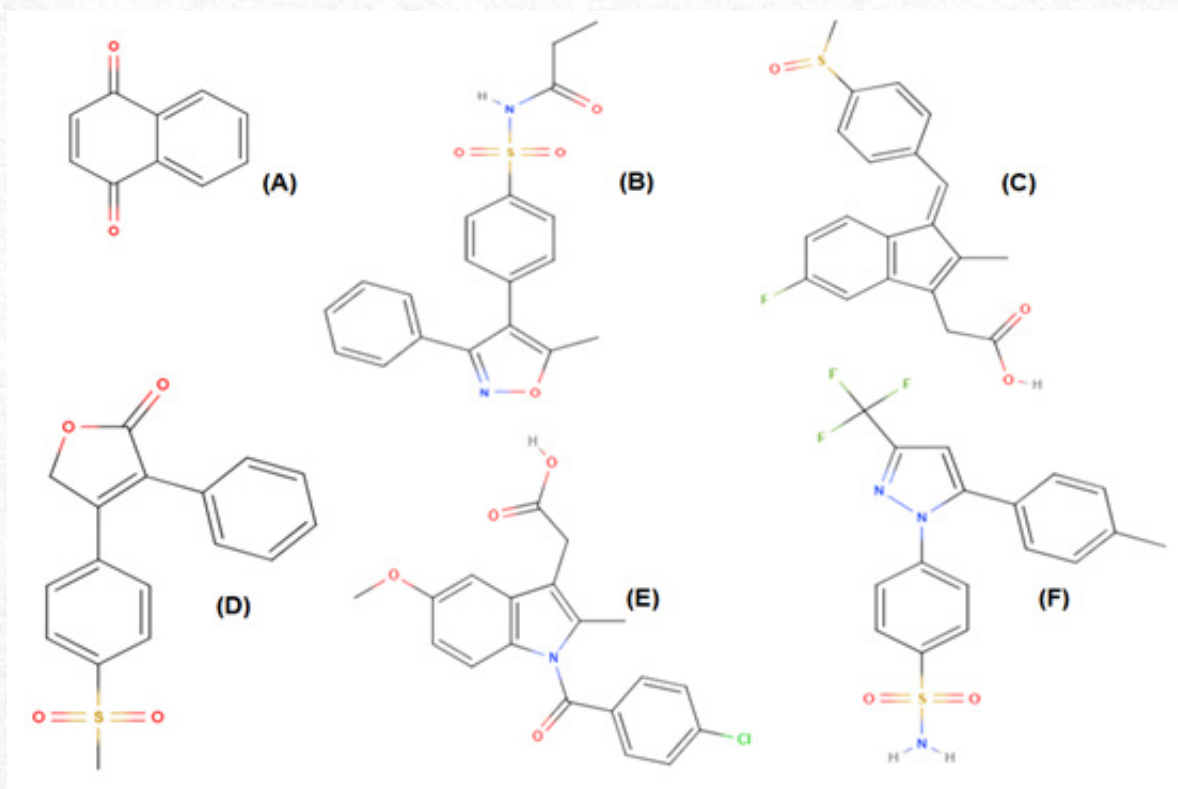


Figure 2 - Molecular structure of ligands and inhibitors used in molecular docking studies. 1,4-Naphthoquinone (A), Parecoxib (B), Sulindac (C), Rofecoxib (D), Indomethacin (E) and Celecoxib (F).

Encapsulation of 1,4-naphthoquinone in biocompatible polymeric micro-nanoparticles of PDLA by microemulsification

A previous analysis of the structure of 1,4-naphthoquinone and the polymer in which it was encapsulated, PDLA, indicates hydrogen bridge interactions can occur between the hydroxyl group

and the carbonyl group of PDLA and the carbonyl group of 1,4-naphthoquinone as shown in Figure 3. Moreover, 1,4-naphthoquinone is a flat aromatic molecule that can form a hydrophobic pocket during the formation of micro-nanoparticles.

Determination of encapsulation efficiency by UV-

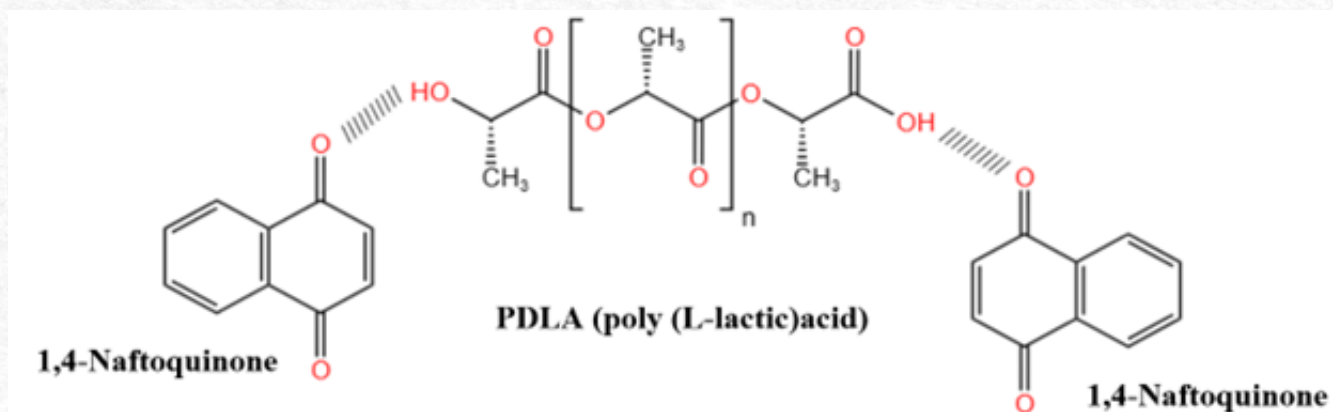


Figure 3 - Interactions between 1,4-naphthoquinone and PDLA polymer.

-Visible Spectroscopy

The value obtained for the encapsulation efficiency of 1,4-naphthoquinone in PDLA micro-nanoparticles is shown in Table 1. Based on the literature, the nanoprecipitation, emulsion-diffusion and layer-by-layer methods give the best results for

the encapsulation of micro-nanoparticles (80% or more)^{27,28}. A high percentage of encapsulation was obtained in this case, which is more than expected based on the literature.

Table 1 - Encapsulation efficiency of naphthoquinone in PDLA micro-nanoparticles.

Sample of 1,4-naphthoquinone/PDLA micro-nanoparticles	Added amount of compound	Encapsulated quantity	% Encapsulation
1,4-naphthoquinone	9 mg	8,8 mg	(98, 3 ± 0,2)%

Characterization by Scanning Electron Microscopy

Scanning microscopy was used to determine the morphology of the micro and nanoparticles. Figure 4 shows the SEM images of the particles obtained without encapsulation, while Figure 5 shows the particles with the naphthoquinone encapsulated. As can be seen, the encapsulation process does not affect the morphology of the particles. Based on the microscopy results, the following average particle size distribution value was obtained for the 1,4-naphthoquinone micro-nanoparticles encapsulated (χ) in PDLA: $\chi = (347 \pm 10)$ nm. A symmetrical morphology of spherical particles and a particle size in the micro and nanometer range is observed presenting a higher percentage (86.12 %) in the nanometer scale, with adequate size dispersion and morphology which is favorable for the purposes of controlled release^{31-33,53-57}.

It is unclear what the particles look like inside, but based on the method used to obtain them, it is expected that they are similar to micronanospheres, that is, they are of the matrix type, in which drugs are dispersed within the particles, absorbed mostly on the surface of the spherical particles or encapsulated within the polymeric structures [11]. Based on our observations, the release of micro-nanoparticles prepared by emulsion-diffusion and emulsion-coacervation methods is faster⁹.

Cell viability assay: Metabolic reduction of

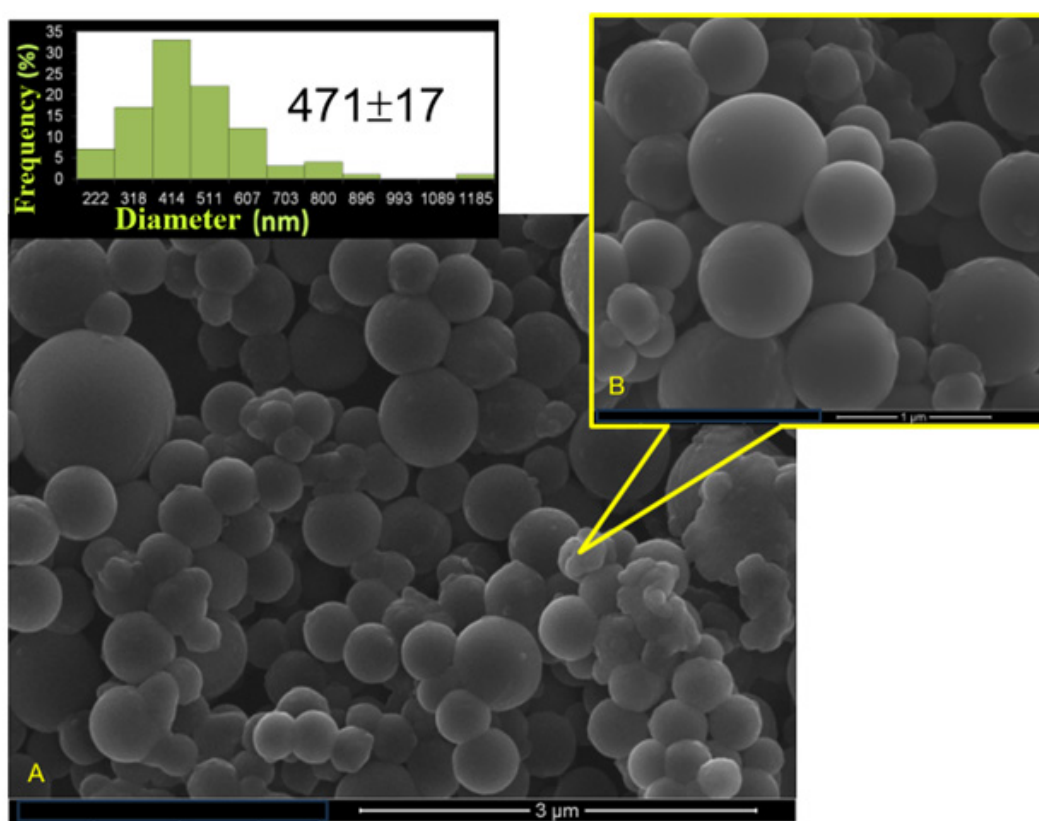


Figure 4 - SEM images: A) View of micro- and nanoparticles of PDLA. B) Details of the morphology.

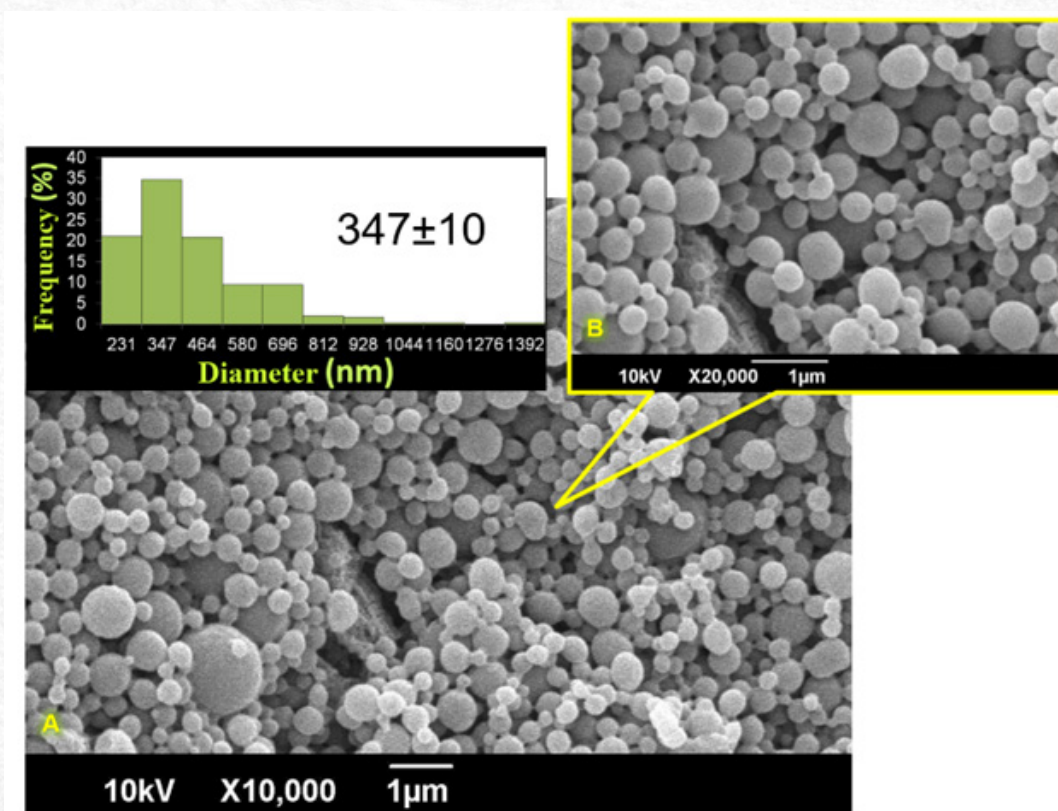


Figure 5 - SEM images: A) View of 1,4-naphthoquinone micro-nanoparticles encapsulated in PDLA. B) Details of the morphology.

3-(4,5-dimethylthiazol-2-yl)-5-(3-carboxymethoxyphenyl)-2-(4-sulfophenyl)-2H-tetrazolium salt (MTS)

The MTS cytotoxicity assay showed that at the maximum tested concentration of 100 ppm of the PLDA micro and nanoparticles did not show appreciable cell toxicity as they induced less than 5% cell death, in MCF-7 type breast cancer cells and in NIH-3T3 murine fibroblasts⁵⁰.

Release assay of 1,4-naphthoquinone in PDLA polymeric micro and nanoparticles by degradation test at different pH conditions

A degradation assay of the polymeric micro and nanoparticles was performed at different pH conditions and for 12 weeks at 25 °C: acidic (1 ≤ pH ≤ 2), slightly acidic (pH ≈ 6), physiological (pH=7.4) and alkaline (pH=9) pH in order to be able to observe the different degradation conditions at pH of different parts of the human body, e.g. strongly acidic gastric pH, physiological pH in blood, slightly acidic pH in certain tumor conditions and slightly alkaline pH in the intestinal medium. The graph obtained from the 1,4-naphthoquinone release assay of PDLA polymeric micro and nanoparticles at different pH conditions is shown below in Figure 6.

As can be seen in the graph, at different pH conditions in the hydrolytic degradation of the PDLA micro and nanoparticles, a controlled release of 1,4-naphthoquinone was achieved for up to eleven weeks. It is observed that, at physiological pH, SBF medium, the peak is reached at the first week and remains constant until about the fifth week and

then rises; in alkaline medium the peak of release is reached at the second week and remains in constant ascent with respect to all other release profiles.

In slightly acidic medium, the release reaches a peak at week three, stabilizes until week five, and then increases further, finally in acidic medium the peak is reached at the second week and remains constant until about the fifth week and then rises.

The *in vitro* release process of an active substance from micro and nanoparticles depends on a variety of factors, such as the concentration and physicochemical characteristics of the active substance (in particular its solubility and oil/water partition coefficient); the nature, degradability, molecular mass and concentration of the polymer; the *in vitro* release test conditions (pH of the medium, temperature, contact time, among others) and the conditions of the preparation method⁹.

Micro and nanoparticles obtained by emulsion-diffusion methods are biphasic systems with an initial rapid release phase followed by a second slower release phase. Bursting is caused by desorption of active substances from micro and nanoparticle surfaces or by degradation of thin polymeric membranes. This behavior apparently exhibits zero-order kinetics⁹.

The second phase corresponds to the diffusion of the drug molecules from the inner compartment, the core of the reservoir, to the outer phase. This diffusion process seems to be determined by: the drug partition coefficient, the drug-polymer interactions and the surfactant concentration⁹.

This process does not appear to be limited by

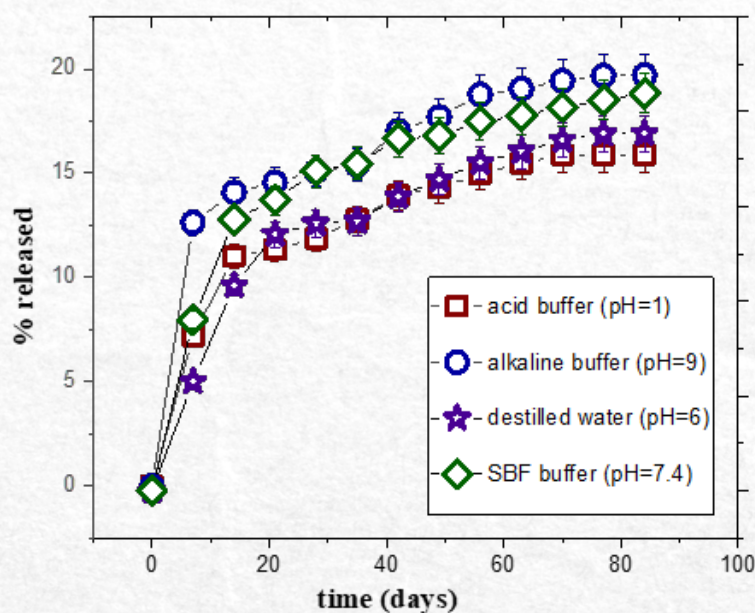


Figure 6 - % Released 1,4-naphthoquinone from PDLA micro-nanoparticles over time.

the rate of drug diffusion through the thin polymer barrier. The amount of polymer used can reduce the release rate significantly, and in such cases, erosion may facilitate drug release²⁸ by hydrolytic degradation, in this case.

In general, biodegradable polymers contain labile ester and anhydride bonds that are prone to hydrolysis⁶⁷, in the case of PDLA the hydrolysis-prone ester bond is observed. Polymers degrade hydrolytically when they come into contact with an aqueous medium, and depending on the pH of the medium, different degradation mechanisms occur. Upon penetration of water, the matrix swells, hydrogen bonds are broken, molecules are hydrated, and finally the unstable bonds are hydrolyzed. Hydrolysis may break functional groups on both the main chain and side chains^{68,69}.

Likewise, degradation of semicrystalline polymers occurs in two stages: i.) The first stage consists of the entry of water into the amorphous regions with random hydrolytic cleavage of labile bonds, such as ester bonds; ii.) Degradation of most amorphous regions marks the beginning of the second stage⁶⁷.

Having a good understanding of the degradation mechanism of polymeric materials offers the advantage of being able to predict its behavior and modify it accordingly. Therefore, several pH conditions were evaluated in the present assay. It is observed that at different pH conditions the hydrolytic degradation of the PDLA micro and nanoparticles exhibit kinetics that resembles zero order and that alkaline conditions accelerate the

degradation and therefore the release is favored, having the highest percentage of release being 20.98 %, followed by physiological medium at 19.69 %, strongly acid medium at 18.83% and slightly acid medium at 16.70%. There is evidence in the literature indicating that PLA degradation is favored at basic pH⁷⁰, which is in accordance with our results. Hydrolysis may be releasing lower molecular weight PLA chains and oligomers as degradation products. Consequently, hydrolytic degradation is favored from the inside out⁶⁹.

Acidic mediums have low degradation compared to basic mediums, possibly because amorphous zones and fragmented chains are predominantly attacked and do not diffuse into the medium until they become too small or diffuse in a negligible amount⁶⁹. From Figures 7 and 8, it can be seen that in basic media the mechanism occurs in fewer steps, which may influence the degradation rate, since the reaction takes place directly, largely because in the basic medium there is a strong base and nucleophile such as the hydroxyl ion (OH⁻) that is capable of directly attacking the acyl group, starting the hydrolysis process. Under acidic conditions, this situation does not occur, as activation of the acyl group under acid catalysis is required before the hydrolysis process can begin, giving rise to more stages, resulting in a wider variety of degradation by-products, however, the degradation process is slowed down even though primarily carboxylic acid groups and chain-terminal alcohols are obtained at the end⁷¹⁻⁷⁴.

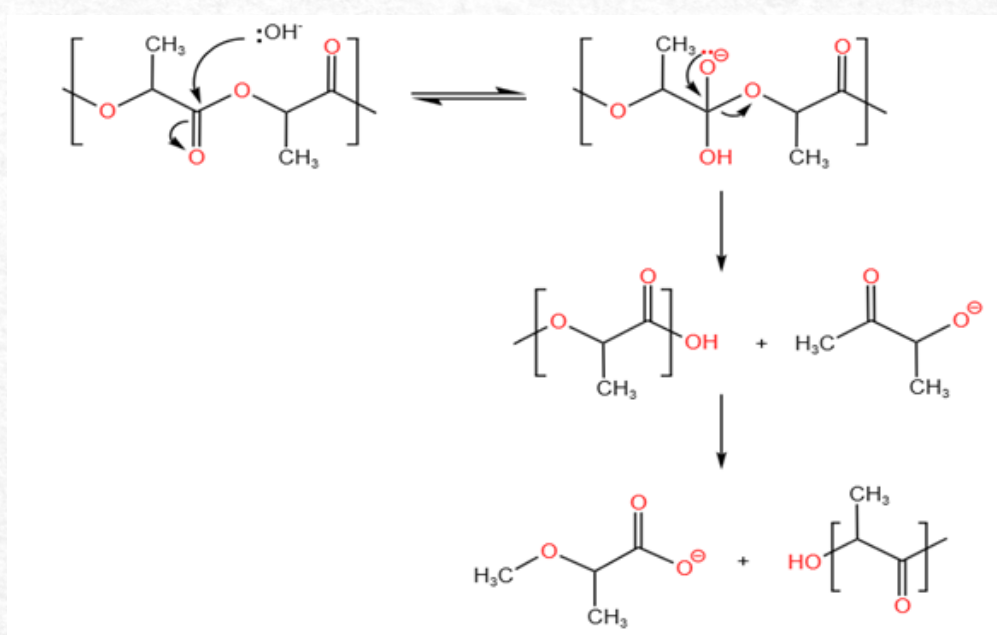


Figure 7 - Proposed mechanism of PDLA degradation by basic hydrolysis. Modified from references⁷¹⁻⁷⁴.

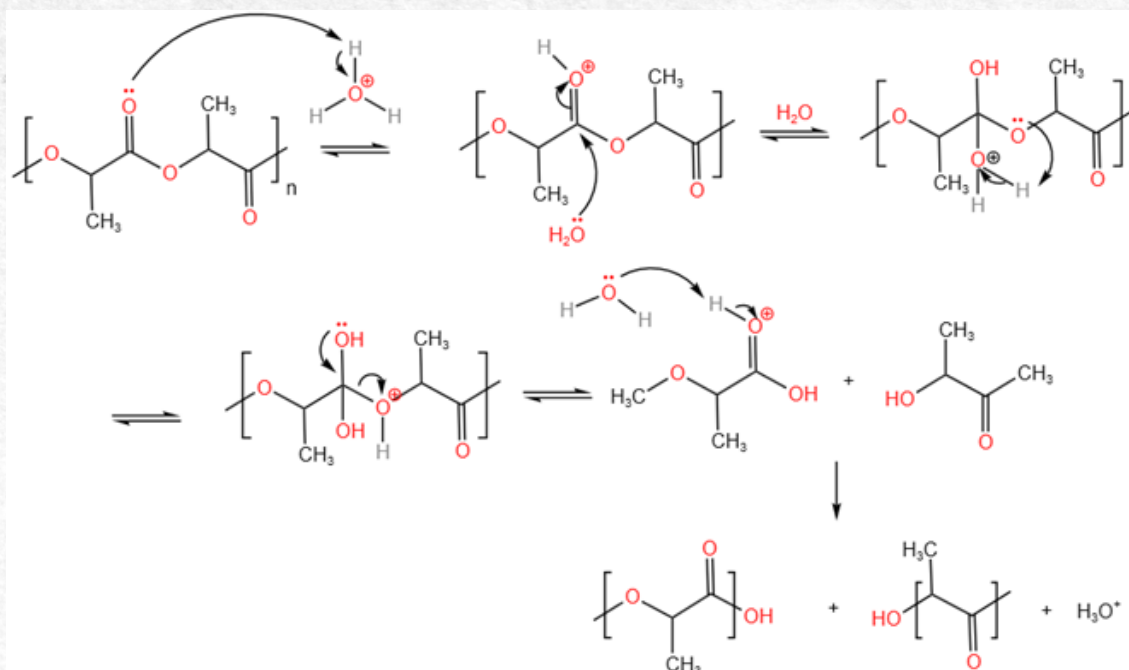


Figure 8 - Proposed mechanism of PDLA degradation by acid hydrolysis. Modified from references⁷¹⁻⁷⁴.

Hence, this study demonstrated that the hydrolytic degradation of polymeric micro and nanonanoparticles during 12 weeks at 25 °C under different pH conditions, demonstrated controlled release of naphthoquinone at different pH conditions over a period of 11 weeks, which is crucial for potential applications in colorectal cancer treatment. Different pH levels, including acidic, slightly acidic, physiological, and alkaline conditions, mimic the gastrointestinal tract and tumour microenvironments. Based on their release patterns, the PDLA micro and nanoparticles have demonstrated a high degree of efficiency in delivering 1,4-naphthoquinone, especially in the alkaline conditions found in the small intestine, where the release rate was highest (20.98%). This is noteworthy, since the small intestine is an important site of drug absorption, and the controlled release of 1,4-naphthoquinone in this region might enhance its therapeutic efficacy against colorectal cancer. The release profiles at different pH levels may also be relevant to the tumour microenvironment, where pH levels can vary significantly. By using PDLA micro and nanoparticles to release 1,4-naphthoquinone in a pH-dependent manner, the drug's anticancer properties may be enhanced and exploited to target specific regions of the tumour. PDLA micro and nanoparticles are a promising drug delivery system for the treatment of colorectal cancer, based on these findings.

Molecular Docking Studies

A docking study was conducted on

1,4-naphthoquinone to assess its potential therapeutic effects on colorectal cancer. At alkaline pH, 1,4-naphthoquinone was released more efficiently, suggesting better absorption in the small intestine. The incidence of colorectal cancer is the third highest in the world and is more prevalent in older individuals and people of all ages⁷⁵.

A potential therapeutic target has been identified as Cyclooxygenase-2 (COX-2) due to its role in promoting tumor growth, angiogenesis (the formation of new blood vessels that feed tumors) and inhibiting apoptosis (programmed cell death)⁷⁶. According to previous clinical studies, non-steroidal anti-inflammatory drugs (NSAIDs) are effective in treating colorectal cancer by inhibiting the enzyme cyclooxygenase. Further research concluded that cyclooxygenase-2 (COX-2) gene inhibitors are most effective for chemotherapy treatment⁷⁷. By inhibiting COX-2, selective cyclooxygenase-2 (COX-2) inhibitors, better known as coxibs, can reduce inflammation, pain, cancer cell proliferation, and new blood vessel formation, all of which can slow tumor growth without affecting the gastric protective effect provided by COX-1^{76,78}. These compounds work by blocking the action of COX-2, an enzyme that is overexpressed in inflamed tissues and in certain types of cancer, such as colorectal cancer^{76,78}. The most effective when used in conjunction with COX-2 inhibitors such as Parecoxib, Sulindac, Rofecoxib, and Celecoxib^{77,79}.

Molecular docking was performed by first downloading the COX-2 enzyme (PDBid: 5F1A) from the Protein Data Bank (<https://www.rcsb.org/>

structure/5F1A) and energetically minimizing it in order to: a) relax the structural stresses presented by inducing forced crystallization experimentally of the enzyme, providing a more realistic and stable conformation of the receptor⁸⁰, b) an energetically minimized receptor structure allows better prediction of the ligand-receptor interaction. This is essential to obtain accurate results in terms of binding affinity and ligand orientation⁸¹, and c) minimization facilitates ligand accommodation in receptor active sites, which improves interaction^{80,81}.

As soon as the enzyme was minimized, it was validated using three different tools (ERRAT⁵⁶, Prosa-Web⁵⁷, and ProCheck⁵⁸) to analyze the quality of the receptor structure. Resulting in an Overall Quality Factor of 97.026 in ERRAT, a Z-Score of -8.62 in Prosa-Web⁵⁷, and a total of 89.5% of residues in favorable zones according to the Ramachandran Plot reported in ProCheck⁵⁸ (for additional information please refer to the supplementary material).

Co-crystallized ligand was used as a positive control to verify that the selected box contained the essential amino acids of the active site. Certain amino acids, such as Ala202, Thr206, His 207, Val291, Pro441, Ala443, Val444, Lys446, Ser448 and Ala450, play crucial roles in the binding process of COX-2^{77,82}. A library of six ligands was run, including 1,4-naphthoquinone, selective COX-2 inhibitors (Parecoxib, Sulindac, Rofecoxib, Celecoxib) and non-selective COX-2 inhibitors (Indomethacin). The results of the quintuplicate molecular docking studies are presented in Table 2.

Based on the results presented in Table 2, it appears that, Parecoxib (-9.70 Kcal/mol) is the selective COX-2 inhibitor that presents the lowest binding energy and consequently; higher interaction with COX-2. Despite its weaker affinity for COX-2 (-7.32 Kcal/mol) than other COX-2 inhibitors, 1,4-naphthoquinone may be useful when moderate inhibition is desired.

By inhibiting COX-2 and regulating inflammatory prostaglandin production, 1,4-naphthoquinone could reduce inflammation and relieve pain, as it interacts with essential amino acids in the COX-2 active site such as ALA-202 (via π -alkyl interactions), THR-206 (via hydrogen bridge-type interactions), HIS-207 (via π donor-hydrogen bond) and HIS-386 (via π - π stacked interactions). Figure 9A shows the pocket of 1,4-naphthoquinone in COX-2 constructed using ICM Mol-Soft; Figure 9B presents the 2D interaction diagram generated in Discovery Studio for the best pose 1,4-naphthoquinone; Figure 9C, the selective COX-2 inhibitor parecoxib (gray color) and 1,4-naphthoquinone (yellow color) are shown overlaid to indicate that both ligands reside in the same active site. Parecoxib, however, being a more voluminous ligand, extends more in the active site, resulting in a greater complementarity with the cavity, and hence having a higher affinity and greater inhibitory activity.

Despite its rather simple molecular structure consisting of two rings (one aromatic and one aliphatic), 1,4-naphthoquinone has been shown to moderately inhibit COX-2, acting as a chemotherapeutic in colorectal cancer.

Furthermore, 1,4-naphthoquinone can serve as a starting point for chemical synthesis of other ligands and is in principle a potential lead compound as it does not violate the Lipinski rules calculated by SwissADME^{83w} (<http://www.swissadme.ch/index.php>) (see supplementary material). Based on *in silico* studies, three new ligands were proposed, introducing hydroxyl and methoxide groups around the aromatic ring to improve hydrogen bonding and lipophilicity. The small changes resulted in a significant increase in inhibitory capacity for COX-2, which increased affinity energy by 0.48 Kcal/mol (5-methoxy-1,4-naphthoquinone), making it more effective as a chemotherapeutic agent (Figure 10).

Table 2 - Ligand-receptor interaction energy (COX-2) obtained through molecular docking studies.

	Run 1	Run 2	Run 3	Run 4	Run 5	Average	Desvest
Ligand	Affinity Energy (Kcal/mol)	Affinity Energy (Kcal/mol)	Affinity Energy (Kcal/mol)	Affinity Energy (Kcal/mol)	Affinity Energy (Kcal/mol)	(Kcal/mol)	(Kcal/mol)
Parecoxib	-9.70	-9.70	-9.60	-9.80	-9.70	-9.70	0.07
Celecoxib	-9.40	-9.50	-9.40	-9.40	-9.50	-9.44	0.05
Sulindac	-9.10	-9.00	-9.00	-9.00	-9.00	-9.02	0.04
Indomethacin	-8.80	-8.81	-8.80	-8.79	-8.81	-8.80	0.01
Rofecoxib	-8.70	-8.70	-8.60	-8.70	-8.60	-8.66	0.05
1,4-Naphthoquinone	-7.30	-7.30	-7.40	-7.30	-7.30	-7.32	0.04

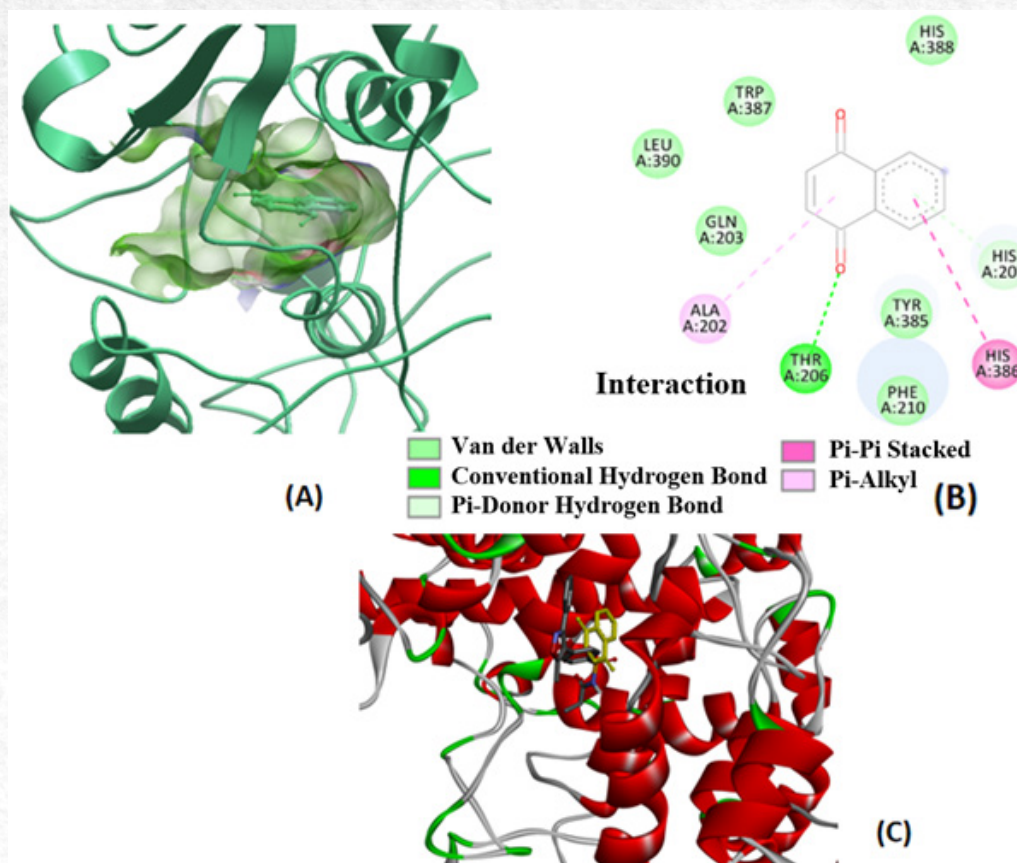


Figure 9 - 1,4-Naphthoquinone-COX-2 interaction pocket (A). 2D ligand-receptor interaction diagram (B). Overlap of Parecoxib (grey) and 1,4-naphthoquinone (yellow) in the active site (C).

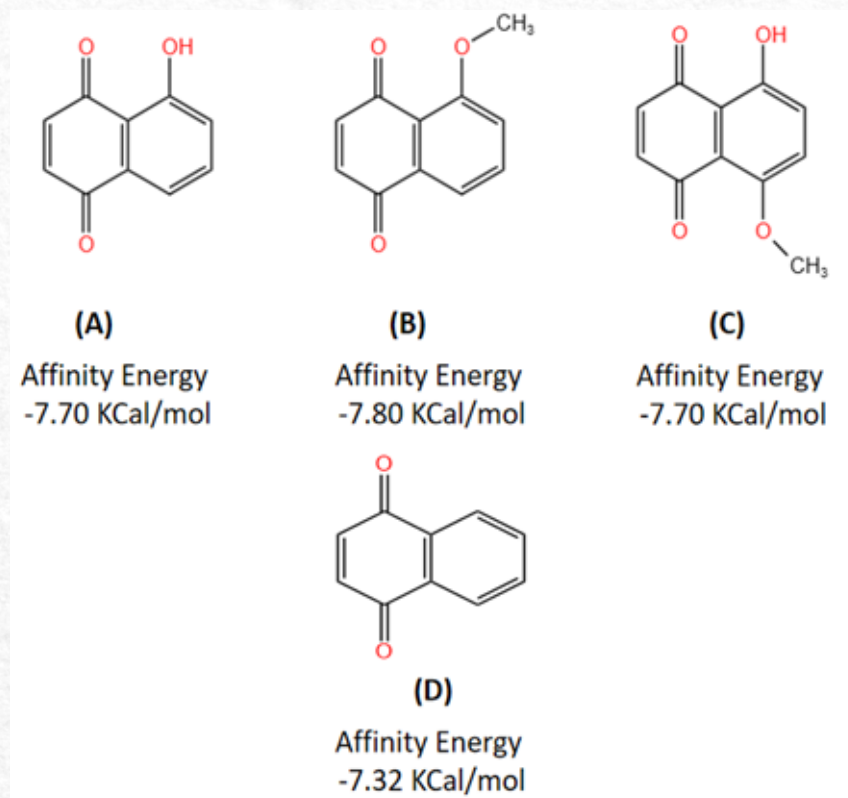


Figure 10 - Increase in affinity energy of modified 1,4-Naphthoquinone ligands. 5-hydroxy-1,4-naphthoquinone (A), 5-methoxy-1,4-naphthoquinone (B), 5-hydroxy-8-methoxy 1,4-naphthoquinone (C), 1,4-naphthoquinone (D).

Conclusions

A remarkable 98.3% encapsulation rate was achieved for 1,4-naphthoquinone in PDLA micro and nanoparticles. MTS assays conducted on MCF-7 breast cancer cells and NIH-3T3 murine fibroblasts demonstrated that the PDLA polymeric micro and nanoparticles were not toxic at concentrations up to 100 ppm. A controlled release assay revealed that alkaline conditions accelerated the degradation of micro and nanoparticles, resulting in a higher release percentage. Under the tested conditions, the system maintained a controlled release for eleven weeks. PDLA based drug delivery systems have significant potential for pharmacological applications, particularly for treating colorectal cancer. Molecular docking studies have demonstrated that 1,4-naphthoquinone can inhibit COX-2 by altering the mechanism of prostaglandin production which is valuable for developing novel anti-inflammatory drugs, exhibiting potential chemotherapeutic activity. Alone or combined with other inhibitors, 1,4-naphthoquinone could be a valuable chemotherapeutic agent, inhibiting COX-2, a key enzyme in colorectal cancer. PDLA micro and nanoparticles encapsulated with 1,4-naphthoquinone offer a promising approach for achieving controlled drug release in the treatment of colorectal cancer. By delivering drugs in a sustained and targeted manner, the system may be able to enhance therapeutic efficacy and reduce side effects. Future research should focus on *in vivo* studies to evaluate the efficacy and safety of PDLA based drug delivery systems. Furthermore, combining therapies and optimizing micro and nanoparticle encapsulation and design could improve drug delivery efficiency and effectiveness. This study underscores the potential of PDLA based drug delivery systems to revolutionize cancer treatment, particularly in colorectal cancer. Developing these systems will lead to improved therapeutic outcomes and more effective and personalized cancer therapies.

Acknowledgments

This article is dedicated to honoring the memory of Dr. Jorge Vicente Lopes da Silva, he passed away before the submission of this study, and who was an important pillar for the B⁵IDA research group at Universidad Simón Bolívar (USB) and for his invaluable collaboration throughout; including his contributions to the conceptualization and visualization of this research.

The authors would like to thank: Lic. Gleen Rodríguez at the Surface Lab of Lab E of USB for the preparation and observation of samples by SEM. To Dr. Juan Rodríguez of the

Cell Biology Lab. at USB for performing the cell viability assays. Lic. Damaris Soto from Center for Materials Engineering and Nanotechnology of the Venezuelan Institute of Scientific Research (IVIC) for supporting the UV-visible assays. CNPq-Brazil PCI program (process #300933/2024-0) for the financial support. And finally, express gratitude to the Fondo Nacional de Ciencia Tecnología e Innovación (FONACIT) for the funding received from projects # 2022OPGP125 and 2023PGP99.

References

- [1]. Zárate-Hernández, E., Hernández-Esquivel, R. A. & Pérez-Urizar, J. T. Microcapsules and microspheres: A vision to integral characterization and applications for biotechnological drugs delivery. *CienciaUAT* 15, (2021).
- [2]. Puccetti, M., Pariano, M., Schoubben, A., Giovagnoli, S. & Ricci, M. Biologics, theranostics, and personalized medicine in drug delivery systems. *Pharmacol. Res.* 201, (2024).
- [3]. Villafuerte-Robles, L. *Nanotecnología Farmacéutica. Razón y Palabra* 68, 1–20 (2009).
- [4]. Chapters, G. et al. Revisions to USP 30-NF 25 , First Supplement. (2011). USP XXXVIII NF XXXII.
- [5]. Liaqat, S. et al. Doxorubicin encapsulated blend of sitagliptin-lignin polymeric drug delivery system for effective combination therapy against cancer. *Int. J. Biol. Macromol.* 269, 132146 (2024).
- [6]. Kita, K. & Dittrich, C. Drug delivery vehicles with improved encapsulation efficiency: Taking advantage of specific drug-carrier interactions. *Expert Opin. Drug Deliv.* 8, 329–342 (2011).
- [7]. Lollo, G. Nanocápsulas de poliaminoácidos para la liberación selectiva de fármacos antitumorales. 346 (2012).
- [8]. Thauvin, C., Schwarz, B., Delie, F. & Allémann, E. Functionalized PLA polymers to control loading and/or release properties of drug-loaded nanoparticles. *Int. J. Pharm.* 548, 771–777 (2018).
- [9]. Kanaoujiya, R., Kumar Sahu, D., Behera, K., Kumar Singh, S. & Srivastava, S. Biomedical application of polymer based nanomaterials: Vaccines & drugs. *Mater. Today Proc.* (2023). doi:10.1016/j.matpr.2023.03.824
- [10]. González R, K. N., González, G., Rodríguez, J., Marques, Kruzakaya Vázquez, A. S. & Sabino, M. A. Encapsulación de derivados de sulfanil – sulfonil chalconas en sistemas micro/nanoparticulados poliméricos de PDLA con aplicación de liberación controlada. *Mater. Simulación Procesos Ind. y Nanotecnología JIFI-EAI*, (2018).
- [11]. González, K. N., González, G. & Sabino, M. A. Preparation of micro and nanoparticulated systems

- based in degradable polyesters for encapsulation of hirudin and delivery. *Acta Microsc.* 32, 29–38 (2023).
- [12]. Lee, J. Y., Bae, K. H., Kim, J. S., Nam, Y. S. & Park, T. G. Intracellular delivery of paclitaxel using oil-free, shell cross-linked HSA - Multi-armed PEG nanocapsules. *Biomaterials* 32, 8635–8644 (2011).
- [13]. Alhareth, K., Vauthier, C., Gueutin, C., Ponchel, G. & Moussa, F. HPLC quantification of doxorubicin in plasma and tissues of rats treated with doxorubicin loaded poly(alkylcyanoacrylate) nanoparticles. *J. Chromatogr. B Anal. Technol. Biomed. Life Sci.* 887–888, 128–132 (2012).
- [14]. Oliveira, A. I., Pinho, C., Fonte, P., Sarmiento, B. & Dias, A. C. P. Development, characterization, antioxidant and hepatoprotective properties of poly(ϵ -caprolactone) nanoparticles loaded with a neuroprotective fraction of *Hypericum perforatum*. *Int. J. Biol. Macromol.* 110, 185–196 (2018).
- [15]. Puppi, D., Braccini, S., Ranaudo, A. & Chiellini, F. Poly(3-hydroxybutyrate-co-3-hydroxyhexanoate) scaffolds with tunable macro- and microstructural features by additive manufacturing. *J. Biotechnol.* 308, 96–107 (2020).
- [16]. Karlsson, J., Vaughan, H. J. & Green, J. J. Biodegradable Polymeric Nanoparticles for Therapeutic Cancer Treatments. *Annu. Rev. Chem. Biomol. Eng.* 9, 105–127 (2018).
- [17]. Tian, S. et al. Controlled drug delivery for glaucoma therapy using montmorillonite/Eudragit microspheres as an ion-exchange carrier. *Int. J. Nanomedicine* 13, 415–428 (2018).
- [18]. Nosrati, H., Adinehvand, R., Manjili, H. K., Rostamizadeh, K. & Danafar, H. Synthesis, characterization, and kinetic release study of methotrexate loaded mPEG–PCL polymersomes for inhibition of MCF-7 breast cancer cell line. *Pharm. Dev. Technol.* 24, 89–98 (2019).
- [19]. Pan, L., Zhou, J., Ju, F. & Zhu, H. Intranasal delivery of α -asarone to the brain with lactoferrin-modified mPEG-PLA nanoparticles prepared by premix membrane emulsification. *Drug Deliv. Transl. Res.* 8, 83–96 (2018).
- [20]. Saez, V., Hernández, J. R. & Peniche, C. Las microesferas como sistemas de liberación controlada de péptidos y proteínas. *Biotechnol. Apl.* 24, 98–107 (2007).
- [21]. Moraes, C. M., Paula, E. De, Rosa, A. H. & Fraceto, L. F. Physicochemical stability of poly(lactide-co-glycolide) nanocapsules containing the local anesthetic bupivacaine. *J. Braz. Chem. Soc.* 21, 995–1000 (2010).
- [22]. Budama-Kilinc, Y. et al. Novel NAC-loaded poly(lactide-co-glycolide acid) nanoparticles for cataract treatment: Preparation, characterization, evaluation of structure, cytotoxicity, and molecular docking studies. *PeerJ* 2018, (2018).
- [23]. Hubbell, J. Biomaterials in tissue engineering. *Biotechnology* 565–76 (1995).
- [24]. Wang, S., Tan, M., Zhong, Z., Chen, M. & Wang, Y. Nanotechnologies for Curcumin: An Ancient Puzzler Meets Modern Solutions. *J. Nanomater.* 2011, 8 (2011).
- [25]. Yasukawa, T., Tabata, Y., Kimura, H. & Ogura, Y. Recent Advances in Intraocular Drug Delivery Systems. *Recent Pat. Drug Deliv. Formul.* 5, 1–10 (2011).
- [26]. Yu, B. et al. Morphology and internal structure control over PLA microspheres by compounding PLLA and PDLA and effects on drug release behavior. *Colloids Surfaces B Biointerfaces* 172, 105–112 (2018).
- [27]. Mora-Huertas, C. E., Fessi, H. & Elaissari, A. Polymer-based nanocapsules for drug delivery. *Int. J. Pharm.* 385, 113–142 (2010).
- [28]. Crucho, C. I. C. & Barros, M. T. Polymeric nanoparticles: A study on the preparation variables and characterization methods. *Mater. Sci. Eng. C* 80, 771–784 (2017).
- [29]. Vanderhoff, J., Mohamed, S. & Ugelstad, J. Polymer Emulsification Process.
- [30]. Vanderhoof, J., Vitkuske, F. & Bradford, E. Uniform Particle Size Latexes *. *J. Polym. Sci.* 20, 225–234 (1956).
- [31]. Lockman, P. R., Mumper, R. J., Khan, M. A. & Allen, D. D. Nanoparticle technology for drug delivery across the blood-brain barrier. *Drug Dev. Ind. Pharm.* 28, 1–13 (2002).
- [32]. Brigger, I., Dubernet, C. & Couvreur, P. Nanoparticles in cancer therapy and diagnosis. *Adv Drug Deliv Rev* 54, 631–651 (2002).
- [33]. Palma, E. et al. Antileishmanial activity of amphotericin B-loaded-PLGA nanoparticles: An overview. *Materials (Basel)*. 11, (2018).
- [34]. González, K. et al. In vitro anti-trypanosomal activity of 3-(aryl)-6-piperazinyl,2,4-triazolo[3,4- a] phthalazines-loaded ultrathin polymeric particles: effect of polymer type and particle size. *RSC Pharm.* (2024). doi:10.1039/d3pm00002h
- [35]. Karina Noreica, G. R. Síntesis y desarrollo de sistemas micro y nanoestructurados para la liberación controlada de fármacos. (Universidad Central de Venezuela, 2022).
- [36]. Marcano, Y. C. & Sabino, M. A. G. Chemical modification of alginate with L-cysteine to extend its use in drug delivery systems. *Cellul. Chem. Technol.* 52, 559–567 (2018).
- [37]. López, L., Leyva, E., La, G. de & Cruz, R. Las naftoquinonas : más que pigmentos naturales. *Rev. Mex. ciencias Farm.* 42, 1–17 (2011).
- [38]. Wang, S. H. et al. Synthesis and biological evaluation of lipophilic 1,4-naphthoquinone derivatives against human cancer cell lines. *Molecules* 20, 11994–12015 (2015).

- [39].Tomaz, A. F. et al. Ionically crosslinked chitosan membranes used as drug carriers for cancer therapy application. *Materials (Basel)*. 11, 1–18 (2018).
- [40].Kumar, D., Gihar, S., Shrivash, M. K., Kumar, P. & Kundu, P. P. A review on the synthesis of graft copolymers of chitosan and their potential applications. *Int. J. Biol. Macromol.* 163, 2097–2112 (2020).
- [41].Klaus, V. et al. 1,4-Naphthoquinones as inducers of oxidative damage and stress signaling in HaCaT human keratinocytes. *Arch. Biochem. Biophys.* 496, 93–100 (2010).
- [42].OMS. Cáncer colorrectal. (2023). Available at: <https://www.who.int/es/news-room/fact-sheets/detail/colorectal-cancer>. [accessed 4 June 2024]
- [43].Soumaoro, L. T. et al. Expression of 5-lipoxygenase in human colorectal cancer. *World J. Gastroenterol.* 12, 6355–6360 (2006).
- [44].Jin, K., Qian, C., Lin, J. & Liu, B. Cyclooxygenase-2-Prostaglandin E2 pathway: A key player in tumor-associated immune cells. *Front. Oncol.* 13, 1–10 (2023).
- [45].Gómez Estrada, H. A., González Ruiz, K. N. & Medina, J. D. Actividad antiinflamatoria de productos naturales. *Bol. Latinoam. y del Caribe Plantas Med. y Aromat.* 10, 182–217 (2011).
- [46].Gonzalez-Angulo, A. M., Fuloria, J. & Prakash, O. Cyclooxygenase 2 inhibitors and colon cancer. *Ochsner J.* 4, 176–179 (2002).
- [47].Yadav, M. et al. Structure-Based Virtual Screening, Molecular Docking, Molecular Dynamics Simulation and Pharmacokinetic modelling of Cyclooxygenase-2 (COX-2) inhibitor for the clinical treatment of Colorectal Cancer. *Mol. Simul.* 1081–1101 (2022). doi:<https://doi.org/10.1080/08927022.2022.2068799>
- [48].Abdelaziz, A. A. S. et al. Molecular docking and Anticancer Activity of Some Synthesized 1,4- naphthoquinone Derivatives against Human Cancer Cell Line. *J. Mol. Struct.* 1275, 134702 (2023).
- [49].Mosmann, T. Rapid colorimetric assay for cellular growth and survival: Application to proliferation and cytotoxicity assays. *J. Immunol. Methods* 65, 55–63 (1983).
- [50].Quispe, M. A. et al. Actividad citotóxica de *Physalis peruviana* (aguaymanto) en cultivos celulares de adenocarcinoma colorrectal, próstata y leucemia mieloide crónica. *Rev. Gastroenterol. del Perú.* 29, 239–46 (2009).
- [51].García F, P. T. Propiedades opticas de Naftoquinonas N-Fenil sustituidas. (Universidad Nacional Autónoma de México, 2007).
- [52].Garcia, M. Disturbios del estado ácido-básico en el paciente crítico. *Acta Med Per* 28, 46–55 (2011).
- [53].Hanna. ¿Cuáles son los niveles de pH del cuerpo humano? (2022). Available at: <https://www.hannainst.es/blog/1533/cuales-son-los-niveles-de-ph-del-cuerpo-human>.
- [54].Guex, N., Peitsch, M. C. & Schwede, T. Automated comparative protein structure modeling with SWISS-MODEL and Swiss-PdbViewer: A historical perspective. *Electrophoresis* 30, 162–173 (2009).
- [55].Colovos, C. & Yeates, T. O. Verification of protein structures: Patterns of nonbonded atomic interactions. *Protein Sci.* 2, 1511–1519 (1993).
- [56].Wiederstein, M. & Sippl, M. J. ProSA-web: Interactive web service for the recognition of errors in three-dimensional structures of proteins. *Nucleic Acids Res.* 35, 407–410 (2007).
- [57].Laskowski, R. A., MacArthur, M. W., Moss, D. S. & Thornton, J. M. PROCHECK: a program to check the stereochemical quality of protein structures. *J. Appl. Crystallogr.* 26, 283–291 (1993).
- [58].Trott, O. & Olson, A. Software News and Updates Gabedit — A Graphical User Interface for Computational Chemistry Softwares. *J. Comput. Chem.* 32, 174–182 (2012).
- [59].Eberhardt, J., Santos-Martins, D., Tillack, A. F. & Forli, S. AutoDock Vina 1.2.0: New Docking Methods, Expanded Force Field, and Python Bindings. *J. Chem. Inf. Model.* 61, 3891–3898 (2021).
- [60].Kim, S. et al. PubChem in 2021: New data content and improved web interfaces. *Nucleic Acids Res.* 49, D1388–D1395 (2021).
- [61].Madej, M., Kurowska, N. & Strzalka-Mroziak, B. Polymeric Nanoparticles—Tools in a Drug Delivery System in Selected Cancer Therapies. *Applied Sciences (Switzerland)* 12, (2022).
- [62].Perumal, S. Polymer Nanoparticles Synthesis and Applications. *Polymers (Basel)*. 14, 5449 (2022).
- [63].Zielinska, A. et al. Polymeric Nanoparticles: Production, Characterization, Toxicology and Ecotoxicology. *Molecules* 25, (2020).
- [64].Ramalho, M. J. & Pereira, M. C. Preparation and Characterization of Polymeric Nanoparticles: An Interdisciplinary Experiment. *J. Chem. Educ.* 93, 1446–1451 (2016).
- [65].Muhamad, I. I., Selvakumaran, S., Asmak, N. & Lazim, M. Designing Polymeric Nanoparticles for Targeted Drug Delivery System.
- [66].Yao, F. & Weiyuan, J. Drug Release Kinetics and Transport Mechanisms of Non- degradable and Degradable Polymeric Delivery Systems. *Expert Opin Drug Deliv.* 7, 429–444. (2010).
- [67].Vieira, A. C., Guedes, R. M. & Marques, A. T. Development of ligament tissue biodegradable devices: A review. *J. Biomech.* 42, 2421–2430 (2009).
- [68].Sabino, M. A., Morales, D., Ronca, G. & Feijoo, L. Estudio de la Degradación Hidrolítica de un Copolíme-

- ro Biodegradable. *Acta Científica Venez.* 54, 18–27 (2003).
- [69]. Scaffaro, R., Lopresti, F. & Botta, L. Preparation, characterization and hydrolytic degradation of PLA/PCL co-mingled nanofibrous mats prepared via dual-jet electrospinning. *Eur. Polym. J.* 96, 266–277 (2017).
- [70]. Elsayy, M. A., Kim, K. H., Park, J. W. & Deep, A. Hydrolytic degradation of polylactic acid (PLA) and its composites. *Renew. Sustain. Energy Rev.* 79, 1346–1352 (2017).
- [71]. Zaaba, N. F. & Jaafar, M. A review on degradation mechanisms of polylactic acid: Hydrolytic, photodegradative, microbial, and enzymatic degradation. *Polym. Eng. Sci.* 60, 2061–2075 (2020).
- [72]. Hurtado, L. & Sabino, M. Estudio del Proceso de Liberación de una Chalcona presente en Estructuras para Aplicaciones Biomédicas. (Universidad Simón Bolívar, 2018).
- [73]. Törmälä, P., Pohjonen, T. & Rokkanen, P. Bioabsorbable polymers: Materials technology and surgical applications. *Proc. Inst. Mech. Eng. Part H J. Eng. Med.* 212, 101–111 (1998).
- [74]. WHO. Cancer. (2022). <https://www.who.int/news-room/fact-sheets/detail/cancer> [accessed 7 October 2024].
- [75]. Castells, A., Rodríguez-Moranta, F. & Soriano, A. Implicación de ciclooxigenasa 2 en el cáncer : utilidad de los coxib. *Rev Esp Reum.* 30, 386–92 (2003).
- [76]. Dannenberg, A. et al. Cyclo-oxygenase 2: A pharmacological target for the prevention of cancer. *Lancet Oncol* 2, 544–551 (2001).
- [77]. Ruilope, L. & Coca, A. Inhibidores selectivos de la ciclooxigenasa-2 (Coxibs) y morbilidad cardiovascular. *Med. Clin. (Barc.)* 118, 219–221 (2022).
- [78]. Tsujii, M., Kawano, S. & Dubois, R. N. Cyclooxygenase-2 expression in human colon cancer cells increases metastatic potential. *Proc. Natl. Acad. Sci. U. S. A.* 94, 3336–3340 (1997).
- [79]. Ballón, W. & Grados, R. Acomplamiento molecular: criterios prácticos para la selección de ligandos biológicamente activos e identificación de nuevos blancos terapéuticos. *Rev.Cs.Farm. y Bioq* 7, 1–18 (2019).
- [80]. Stanzione, F., Giangreco, I. & Cole, J. Use of molecular docking computational tools in drug discovery. *Prog. Med. Chem.* 60, 273–343 (2021).
- [81]. Ikram, M. et al. Synthesis, molecular docking evaluation for LOX and COX-2 inhibition and determination of in-vivo analgesic potentials of aurone derivatives. *Heliyon* 10, e29658 (2024).
- [82]. Daina, A., Michielin, O. & Zoete, V. SwissADME: A free web tool to evaluate pharmacokinetics, drug-likeness and medicinal chemistry friendliness of small molecules. *Sci. Rep.* 7, 1–13 (2017).

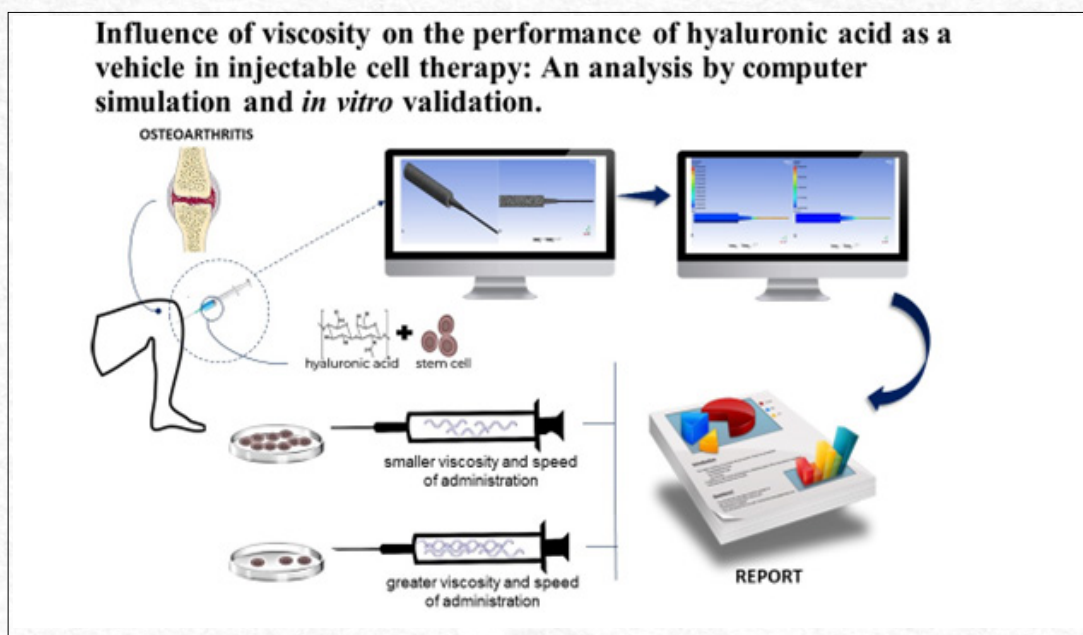


Influence of viscosity and velocity of administration on the performance of hyaluronic acid as a vehicle for bioprinting and injectable cell therapy: a computer simulation approach and *in vitro* validation

G.F.A. Terciotti¹; E. Trovatti¹; J.A. Nogueira²; J.V.L. Silva²; R.A. Rezende¹; P.Y. Noritomi²; A.C. Amaral^{*1}

*Corresponding author: E-mail address: acamaral@uniara.edu.br

Received: October 2024; Accepted: December 2024.



Abstract: Background: Hyaluronic acid (HA) is a natural polymer widely used as a vehicle in injectable cell therapy for the treatment of arthropathies. Objective: To estimate, through computational simulations and *in vitro* validation, the influence of HA's physicochemical properties and administration speed on the shear stress generated in the syringe/needle system, as well as the associated risk to cell viability during administration. Methods: The influence of viscosity was evaluated by considering the rheological parameters corresponding to HA concentrations of 6, 8, 10, 12, and 15 mg/mL. For assessing the impact of administration speed, values representative of the typical speed range used in clinical procedures were considered. Simulations were used to estimate shear stress as a function of administration speed for each viscosity level. Results: The findings revealed a directly proportional relationship between viscosity and administration speed with the magnitude of shear stress. Notably, the highest viscosity formulation, when administered at the fastest speed, reached "critical values" of shear stress associated with mechanical damage to cell membranes and cell death. Conversely, lower viscosity HA exhibited reduced stress levels, indicating it as the potentially preferred formulation for injectable cell therapy. The *in vitro* cell culture assays corroborated the computational simulation results. Conclusions: The administration of HA demonstrates a viscosity- and speed-dependent effect on shear stress, which should be carefully considered for its application in bioprinting and injectable cell therapies.

Keywords: Hyaluronic Acid. Regenerative Medicine. Cell and Tissue Transplant Based Therapy. Computer Simulation. Stem Cells. Bioprinting.

¹University of Araraquara, Araraquara, SP, Brazil.

²Center of Information Technology Renato Archer, Campinas, SP, Brazil.

Introduction

Hyaluronic acid (HA) is a biopolymer that forms a key component of the extracellular matrix in various tissues of the human body and serves as a fundamental constituent of synovial fluid within synovial joints^[1]. Structurally, it is an anionic, non-sulfated glycosaminoglycan that consists of repeating disaccharide units of N-acetyl-D-glucosamine and D-glucuronic acid, linked by alternating β -1,4 and β -1,3 glycosidic bonds^[2,3]. Due to its high biocompatibility, biodegradability, non-toxicity, and low immunogenicity, HA has gained significant attention over the past decade as a superior biomaterial in diverse fields such as orthopedics, dermatology, aesthetics, tissue engineering, and drug delivery^[2,4,5,6,7].

Given its safety profile and proven therapeutic efficacy, particularly in intra-articular viscosupplementation for osteoarthritis, HA has been increasingly used as a preferred carrier in clinical research focused on injectable cell therapy (ICT)^[8,9,10]. Specifically, it is employed to deliver mesenchymal stem cells (MSCs) as part of regenerative medicine strategies aimed at treating musculoskeletal pathologies of both traumatic and degenerative origins^[3,5,11].

Despite the highly promising preliminary therapeutic outcomes, ongoing ICT research is focused on optimizing cellular parameters and administration procedures to maximize therapeutic benefits^[11,12]. Among the critical factors for the success of cell therapy is the availability of a sufficient quantity of healthy and functional MSCs at the repair site. To address this, researchers are actively investigating optimal cell concentrations tailored to specific MSC sources and target pathological conditions. Equally important, though currently less explored, is the need to define parameters related to the carrier vehicle and the procedure itself for ICT administration^[13,14].

While HA is widely used as the preferred vehicle for MSC-based ICT, there remains a lack of consistent scientific evidence clarifying its influence on these cells, both during and after the injection procedure. Existing studies, though not specifically focused on ICT applications, indicate that high molecular weight HA may exert modulatory effects on cultured cells. This includes modulation on cell viability, cell proliferation and/or the stimulation of biomolecule release involved in immunomodulation, neovascularization and regeneration within the microenvironment^[6,9]. Beyond its potential direct cellular effects, the impact of HA's physicochemical properties on the mechanical environment during ICT administration is still unknown. Such factors could influence cell integrity and potentially compromise therapeutic

efficacy. Therefore, this study aims to investigate the influence of HA viscosity, when used as a vehicle in ICT, on cell viability during the administration process. Given the characteristics of the injectable delivery method, the administration speed was also considered a crucial technical variable.

The use of computer simulation has been more and more adopted for analyzing different scenarios and predicting the behavior of some process or some specific variable. Normally, computer simulations are performed after strategical simplification in the model including variables and conditions of interest. Despite it, this tool application is very cheap and avoids waste of time and resources for reaching important conclusions and decisions before a real stuff is indeed implemented^[15-18].

Materials and methods

Computational Simulation of the Influence of Hyaluronic Acid Viscosity

The initial step involved developing a virtual model to enable computational simulation experiments aimed at determining the influence of varying hyaluronic acid (HA) viscosity and administration speed on shear stress levels affecting the administered cells. The simulation analysis focused on evaluating HA flow behavior within the syringe/needle assembly during administration.

Obtaining the Geometry and 3D Mesh of Elements

The model was initially designed using computer-aided design software, Rhinoceros[®] 5.0, based on the geometry of the syringe and needle components of an injection device. This allowed for an accurate reproduction of the syringe body, tip, barrel, and needle shaft. The geometric parameters were provided by DMC Equipamentos LTDA. Specifically, the dimensions used in the analysis corresponded to a 2 mL syringe ($\varnothing = 8.65$ mm; length = 64.4 mm) and a 22G 25 x 7 needle (Injex company[®]). These dimensions are consistent with the administration device accompanying the bioproduct Opus Joint[®], which comprises non-animal-origin HA and is used for intra-articular viscosupplementation in osteoarthritis patients.

After establishing the geometry of the syringe and needle components in a virtual environment, a triangular mesh was generated using Ansys/CFX[®] 18.2 software. The mesh for the inner wall of the syringe/needle assembly contained the smallest elements (Figure 1), enabling more refined analysis in regions with the highest predicted shear stress levels.

The size of the mesh elements was dependent on the geometry's dimensions. Generally, it is recommended to have at least three elements

along the smallest area of interest to ensure a robust simulation. Figure 2 illustrates the variation in size and number of elements in regions where the geometry changes abruptly, particularly around the syringe nozzle, barrel, and needle shaft. The

regions corresponding to the barrel and needle shaft featured the smallest elements, enhancing detail in the analysis of these critical areas, where the highest shear stress levels were anticipated during HA flow.

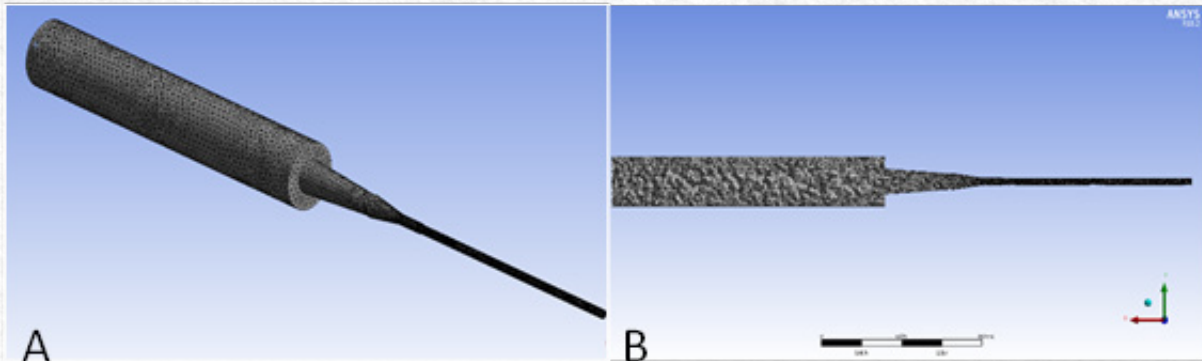


Figure 1 - Image of the external (A) and internal (B) mesh of the syringe/needle assembly geometry.

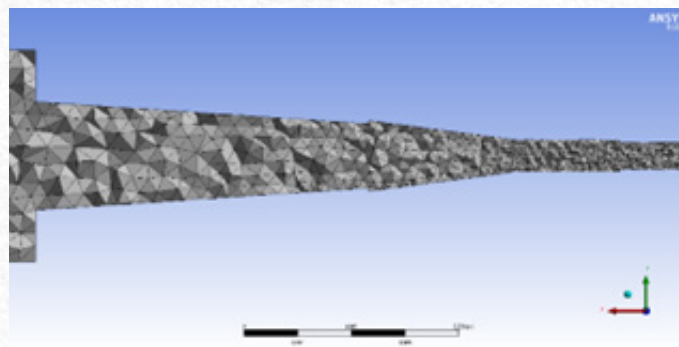


Figure 2 - Highlighting of the mesh refinement in regions corresponding to the syringe nozzle and needle rod.

Production and Establishment of Rheological Parameters for Different HA Formulations

To simulate the influence of HA viscosity, the rheological parameters of various HA formulations were established. One of the formulations analyzed was Opus Joint[®] itself. Based on its concentration, four additional formulations with varying concentrations were prepared, resulting in a 5-point scale with concentrations of 6, 8, 10, 12, and 15 mg/mL. The rheological parameters for each formulation were provided by DMC Equipamentos. However, specific values and other physicochemical characteristics are not disclosed due to confidentiality agreements with the manufacturer.

HA is classified as a viscoelastic fluid, capable of exhibiting the elastic properties of a solid (approximated using Hooke's Law) as well as the viscosity of a fluid. Depending on the applied stress, it displays both viscous and plastic behaviors simultaneously. Due to its viscoelastic nature, shear stress is reduced by its elastic properties. However, for the

purposes of this study, the fluid was treated as a non-Newtonian fluid to simulate critical conditions without attenuating viscous forces.

Unlike Newtonian fluids, the viscosity of non-Newtonian fluids is not proportional to shear stress and changes throughout the flow. This change can be modeled mathematically, and for this study, the power-law model was used, represented by the following equation:

$$\tau = K \left(\frac{du}{dy} \right)^{n-1}$$

Where: τ is the shear stress, K is the fluid consistency index, $\frac{du}{dy}$ is the strain rate and n is the power index.

This model was selected because the viscosity vs. shear stress graphs obtained from rheological analyses were consistent with the behavior predicted by the power-law model, which shows a decrease in viscosity with increasing shear stress. The exact graphs are not presented here to maintain the

confidentiality of the material properties. From these graphs, by normalizing the data using a logarithmic transformation, the values for K and n were determined.

Determination of Administration Velocities

A key factor in conducting the simulation was identifying realistic flow velocities. To achieve this, publicly available videos of intra-articular HA viscosupplementation procedures were analyzed. From these videos, application times (Δt) were measured, and with knowledge of the applied volume, the lengths (Δs) corresponding to the syringe geometries were determined. Using these values, the average fluid velocity was estimated for each video using the formula:

$$v = \frac{\Delta s}{\Delta t}$$

Velocity values were derived from five videos (Table 1), and all were tested in the simulations. It was anticipated that higher velocities would result in increased shear stress, allowing for the assessment of the impact of flow speed on shear stress levels.

Table 1 - Average velocities obtained from public domain videos during the application of viscosupplementation with HA.

Velocity	Average velocity (m/s)
1	$8,3 \times 10^{-4}$
2	$1,6 \times 10^{-3}$
3	$1,9 \times 10^{-3}$
4	$3,8 \times 10^{-3}$
5	$6,0 \times 10^{-3}$
6	$1,3 \times 10^{-2}$

Determination of shear stress by computer simulation

Simulations were conducted using computational fluid dynamics (CFD) in Ansys/CFX[®] 18.2, which employs the finite volume method to estimate shear stress in different regions of the syringe/needle assembly. The CFD model for non-Newtonian fluids was based on the Ostwald-de Waele power law. The software required input of the following properties for each HA formulation: material density, molar mass, maximum and minimum shear rates, time constants for viscosity curve generation, fluid consistency index ($k=0.2$ Pa.s); and the power-law index ($n=0.0365$).

Once the parameters were configured, the simulations produced plots correlating shear stress with

administration speeds for each HA formulation.

In vitro validation

Cell culture

Human fibroblast cells (GM07492 cell line) were selected for use in this study. The cells were thawed and maintained throughout the experimental phases in flasks containing Dulbecco's Modified Eagle Medium (DMEM, Sigma-Aldrich), supplemented with 10% fetal bovine serum and antibiotics. The culture environment was strictly controlled, with the incubator set to a temperature of 37°C, in a humidified atmosphere containing 5% CO₂.

Cell viability analysis

In this phase of the project, parameters determined during the computational simulation were validated by comparing in vitro cell viability post-loading, using the optimal HA viscosities and administration velocities identified earlier. To achieve this, cultured human fibroblasts were detached from the culture flasks, resuspended in 2 mL of HA (at a concentration of 10⁵ cells/mL), and loaded into syringe/needle sets identical to those used in the simulation phase. The samples were then administered into wells of a 24-well cell culture plate at rates consistent with those used during the simulations. For the control group, a similar procedure was followed, but cells were resuspended in phosphate-buffered saline instead of HA.

Cell viability post-administration was assessed using direct counting methods with trypan blue staining and an automated cell counter (Bio-Rad[®]). Statistical analysis of the results was performed using basic descriptive statistics and a one-way ANOVA test, followed by Tukey's post hoc test. A significance level of 5% was used for all analyses.

Results and Discussion

Determination of Shear Stress by Computer Simulation

The primary goal of creating the computational model was to estimate the shear stress within the syringe/needle assembly, considering different HA formulations and administration velocities. The expectation was that the simulation would help optimize in vitro biological assays by accurately predicting the influence of key variables (viscosity and administration speed) on the mechanical environment to which the cells would be subjected during the injectable administration procedure.

In addition to optimization, it is important to highlight the potential cost reductions offered by computer simulation, also known as in-silico analysis. This approach reduces the need for extensive in vitro experiments by allowing researchers

to focus on the most relevant experimental conditions for the study's objectives. Such benefits are expected to grow even more in future studies, particularly when human mesenchymal stem cells are used. The advantages of computer simulation in various research fields, including chemistry, biology, biotechnology, and medicine, have been widely recognized in recent decades. Huang and colleagues [9] suggested that CFD could serve as a valuable tool for analyzing and visualizing the impact of fluid forces and stresses on cells. Furthermore, they proposed that computational models will be essential for predicting and testing the large number of parameters that influence cell behavior. The properties of synovial fluid and hyaluronic acid, along with their rheological characteristics, have been well documented in the literature, supporting our proposed model.

Despite the challenges still faced in using computer simulation, such as: the need to validate virtual models, improve reproducibility, advance hardware and software technology, and develop calibration methods, the potential of this approach is widely acknowledged. The expectation is that computer simulations will become increasingly integrated into the scientific methodologies of the aforementioned fields[20]. Regarding the next steps of this research, we aim to gather data that will contribute to the validation of the proposed model, allowing for refinements and improvements to the accuracy and precision of the method.

The shear stress was analyzed at the body and tip walls of the syringe and the cannon and needle shaft. Based solely on the geometry of the syringe/needle assembly, we observed a typical pattern: shear stress was higher in regions with abrupt changes in area and smaller dimensions, as expected. It was clear that the regions of highest shear stress, regardless of HA concentration, were located in the segments corresponding to the cannon and the needle shaft, with the latter exhibiting the most critical shear stress levels.

Figure 3A shows the color plot of shear stress within the syringe/needle assembly during the simulation of HA application with a concentration of 15 mg/mL at a velocity of 1.6×10^{-3} m/s. From these results, we identified the needle as the point of greatest risk to cell viability due to the elevated shear stress that could compromise cellular integrity. Figure 3B illustrates the distribution of flow velocity under the same administration conditions, showing an increase in HA flow velocity, in laminar flow, as it moves through the cannon and needle shaft components. Specifically, within the needle shaft, the flow velocity was highest at the center and progressively decreased toward the wall. This behavior was consistent across all HA formulations.

From the compiled simulation data, we were able to establish the relationship between shear stress, HA concentration (viscosity), and administration velocity (Figure 4).

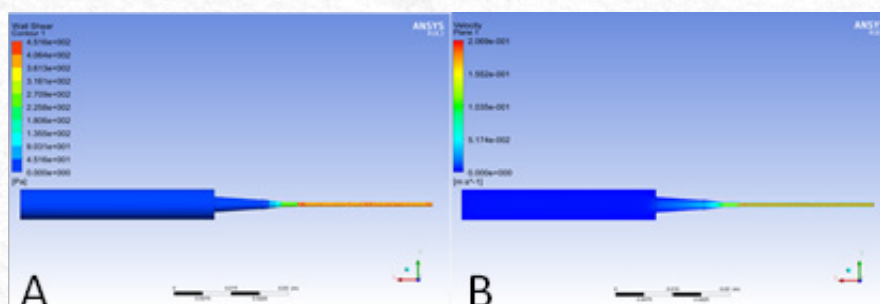


Figure 3 - Shear stress on the wall of the structure and critical points within the needle with higher cellular risk potentials (A) and distribution of flow velocity on a permanent regime (B).

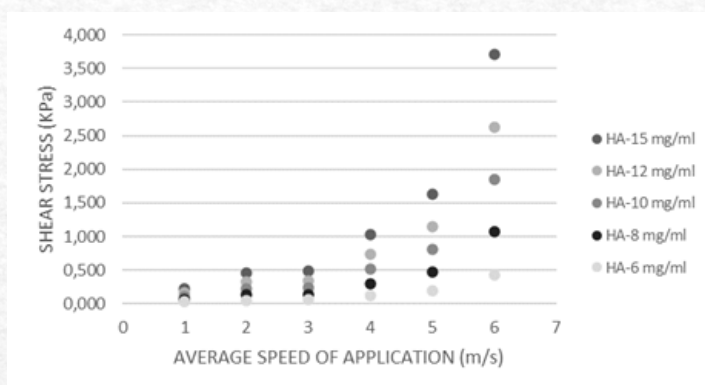


Figure 4 - Variation of shear stress for the 6 values of velocities and 5 values of HA concentration.

A directly proportional relationship between formulation concentration (and thus viscosity) and shear stress was observed when analyzing each velocity separately. It was also evident that the increase in shear stress was more pronounced with higher administration speeds. These results highlight the concentration/viscosity-dependent and velocity-dependent nature of shear stress generated during the injectable administration of HA.

Another important finding is that the formulation with the highest concentration achieved significantly high shear stress values (3.75 kPa) at the highest administration speed, approaching the "critical value" of approximately 4 kPa proposed by Blaeser et al. [21]. In their study, which assessed the risk of cell death during bioprinting procedures, shear stresses near the "critical value" were shown to be sufficient to induce cell death (decreased cell viability) by damaging the structural integrity of the cytoplasmic membrane. This experiment was conducted using fibroblasts embedded in an alginate hydrogel for extrusion in a bioprinter. Factors such as cell type, hydrogel physicochemical properties, and ejection speed may influence the comparison of results. However, it is important to note that, to our knowledge, no scientific publications have specifically addressed injectable administration of cells for regenerative medicine applications. This is why we have compared our findings to the above reference, despite the technical discrepancies.

In vitro validation

To perform the in vitro experiments, the lowest (8.3×10^{-4} m/s) and highest (1.3×10^{-2} m/s) velocity values were selected, corresponding to HA concentrations of 6 mg/mL and 15 mg/mL, respectively. These values were derived from the computational simulation results. As mentioned earlier, the 6 mg/mL concentration resulted in low

shear stress values, regardless of the administration speed. The 15 mg/mL concentration was included in the analysis to assess the real risk of cell death under conditions that produced the highest stress levels. Injectable administration simulations were conducted manually to achieve a higher clinical correlation (hypothetically) for cell therapy administration. The administration time was used as the reference parameter to proportionally infer the administration speed predicted in the simulation.

Data obtained from in vitro experiments enabled the assessment of cell viability, expressed as a percentage, for each experimental group following the simulated administration procedure. These results were subsequently compared to one another and to the control condition (Figure 5).

The control group exhibited cell viability with a mean and standard deviation ($M \pm SD$) of $96.3 \pm 4\%$. These high values are consistent with administration via a liquid vehicle (PBS), which induces minimal shear stress. Values slightly below 100% were expected, reflecting normal cell viability loss associated with standard culture handling procedures. For the HA groups at a concentration of 6 mg/mL administered at low and high speeds, viability was $82.7 \pm 4\%$ and $88.7 \pm 5\%$, respectively. While these means were marginally lower than those of the control group, the differences were not statistically significant ($p \geq 0.05$). In contrast, the HA groups at 15 mg/mL showed viability of $54.7 \pm 8\%$ and $36 \pm 4.6\%$ for the low and high-speed administrations, respectively. Both values were significantly lower ($p < 0.0006$) than those for the control and the HA 6 mg/mL groups, independent of speed. Additionally, a statistically significant difference ($p \leq 0.01$) was observed between the HA 15 mg/mL groups administered at different speeds, with higher speeds resulting in lower viability.

Blaeser et al. [21] investigated cell viability as a

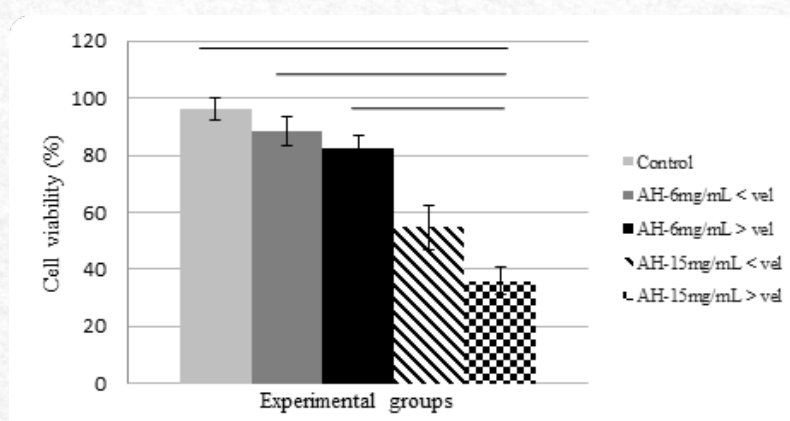


Figure 5 - Mean and standard deviation values of cell viability (human fibroblasts - GM07492) found after injectable administration for the Control, 6 and 15 mg/mL HA groups analyzed (highest and lowest speed) * $p < 0.0006$.

function of shear stress within a 3D printing nozzle, categorizing shear into three groups: <5 kPa, 5-10 kPa, and >10 kPa. They found that cell viability for the <5 kPa group was 96%, indicating preservation of membrane integrity under low shear stress. However, viability significantly declined for groups exposed to >5 kPa shear (91% and 76%, respectively). Notably, their study did not assess the effect of application speed, and since bioprinting typically involves lower velocities than manual administration, it can be inferred that their data align with our findings.

The absence of statistically significant differences in viability among the control, HA-6mg/mL<vel, and HA-6mg/mL>vel groups suggests that cells exhibit a high tolerance to shear stress levels generated during injectable administration, preserving structural integrity. These findings are consistent with low shear stress levels predicted by computational simulations.

In contrast, the significant reduction in viability observed in the HA-15mg/mL<vel and HA-15mg/mL>vel groups suggests that shear stress levels reached thresholds critical to cell integrity during administration. The notably lower viability in the HA-15mg/mL>vel group aligns with high shear stress levels predicted in simulations. Here, cell death reached approximately 65%, which could severely compromise the therapeutic efficacy of the technique, as it relies on maintaining high numbers of viable cells post-administration. Previous studies by Blaeser et al.^[21] and Chang et al.^[22] also reported reduced viability, although with lower percentages of cell death under lower velocity conditions typical of bioprinting.

The significant viability reduction in the HA-15mg/mL<vel group, despite low predicted shear stress levels, suggests that actual shear stress during in vitro experimentation may have been higher than expected. Although this discrepancy was considered during experimental planning, it was deemed a lower priority to more closely mimic real-world injectable administration.

The in vitro viability results of this study support the use of HA at 6 mg/mL concentration as optimal for ensuring high cell viability following injectable administration. However, additional research is needed to explore not only the risk of cell death due to high shear stress but also the potential impact of even low shear levels associated with HA concentration on cell viability.

Kim et al.^[23] demonstrated that shear stress induced by interstitial flow promotes osteogenic differentiation of mesenchymal stem cells via TAZ receptor activation, with calculated shear stress around 0.0135 Pa. This low-level shear stress, achieved experimentally using microchannel flow

systems, could enhance cell differentiation and was reached by all HA formulations even at reduced administration speeds.

The theoretical basis of mechanobiology, initially proposed by Friedrich Pauwels, links mechanical stimuli to cell differentiation processes. This concept strengthens the hypothesis that the mechanical environment during injectable administration may have beneficial effects beyond mere cell viability, potentially enhancing MSC-based therapies ^[4,24]. Further research is warranted to explore the balance between beneficial mechanobiological stimuli and the risk of cell damage, as well as the interaction between HA macromolecules and cells during administration.

Conclusions

The findings of this research provided a detailed characterization of the relationship between shear stress—linked to the viscosity and flow velocity of HA—and cell viability post-administration. The low levels of shear stress predicted by computational simulations, combined with the high cell viability observed in in vitro assays, suggest that a viscosity corresponding to an HA concentration of 6 mg/mL is the most promising for use as a bioink (HA+cells) in bioprinting and for injectable cell therapy applications. Additionally, these results highlight the significant potential of computational simulations as tools for planning and optimizing experimental research in biological sciences, health sciences, and biotechnology. However, further studies are required to fully elucidate the impact of the mechanical environment generated during injectable administration on cellular structural integrity and viability. These efforts are crucial to enhancing the safety and therapeutic efficacy of injectable cell therapies.

Acknowledgements

This article is dedicated to the memory of our dear Jorge Vicente Lopes da Silva, whose vision, dedication, and passion for research were instrumental in the development of this work. His absence is deeply felt, but his legacy will continue to inspire us all. We thank the company DMC Equipamentos LTDA for the technical support and supply of the inputs used in this research.

Funding

This work was financially supported by Fundação de Amparo à Pesquisa do Estado de São Paulo – FAPESP (Processo: 2019/13670-0)

References

[1]. Abatangelo G, Vindigni V, Avruscio G, Pandis L, Brun P.

- Hyaluronic Acid: Redefining Its Role. *Cells* [Internet]. 2020 Jul 1;9(7):1743. Available from: <https://www.mdpi.com/2073-4409/9/7/1743>
- [2]. Sudha PN, Rose MH. Beneficial Effects of Hyaluronic Acid. *Advances in Food and Nutrition Research* [Internet]. 2014;137–76. Available from: <https://www.sciencedirect.com/science/article/pii/B9780128002698000099>
 - [3]. Gallo N, Nasser H, Salvatore L, Natali ML, Campa L, Mahmoud M, et al. Hyaluronic acid for advanced therapies: Promises and challenges. *European Polymer Journal*. 2019 Aug;117:134–47. <https://doi.org/10.1016/j.eurpolymj.2019.05.007>
 - [4]. Wescoe KE, Schugar RC, Chu CR, Deasy BM. The Role of the Biochemical and Biophysical Environment in Chondrogenic Stem Cell Differentiation Assays and Cartilage Tissue Engineering. *Cell Biochemistry and Biophysics*. 2008 Oct 1;52(2):85–102. <https://doi.org/10.1007/s12013-008-9029-0>
 - [5]. Jo CH, Chai JW, Jeong EC, Oh S, Shin JS, Shim H, et al. Intra-articular Injection of Mesenchymal Stem Cells for the Treatment of Osteoarthritis of the Knee: A 2-Year Follow-up Study. *The American journal of sports medicine* [Internet]. 2017;45(12):2774–83. Available from: <https://www.ncbi.nlm.nih.gov/pubmed/28746812>.
 - [6]. Ye H, Zhang R, Zhang C, Xia Y, Jin L. Advances in hyaluronic acid: Bioactivity, complexed biomaterials and biological application: A review. *Asian Journal of Surgery* [Internet]. 2024 Aug 1 [cited 2024 Oct 2]; Available from: <https://www.sciencedirect.com/science/article/pii/S1015958424018414>
 - [7]. Gielen C, Ankone M, Grijpma DW, Poot AA. Hybrid Networks of Hyaluronic Acid and Poly(trimethylene carbonate) for Tissue Regeneration. *Biomacromolecules*. 2022 Nov 23;24(10):4366–74.
 - [8]. Fang Y, Shi L, Duan Z, Rohani S. Hyaluronic acid hydrogels, as a biological macromolecule-based platform for stem cells delivery and their fate control: A review. *International Journal of Biological Macromolecules*. 2021 Oct;189:554–66. <https://doi.org/10.1016/j.ijbiomac.2021.08.140>
 - [9]. Lei Y, Gojgini S, Lam J, Segura T. The spreading, migration and proliferation of mouse mesenchymal stem cells cultured inside hyaluronic acid hydrogels. *Biomaterials*. 2011 Jan;32(1):39–47. <https://doi.org/10.1016/j.biomaterials.2010.08.103>
 - [10]. An C, Li H, Zhao Y, Zhang S, Zhao Y, Zhang Y, et al. Hyaluronic acid-based multifunctional carriers for applications in regenerative medicine: A review. *International Journal of Biological Macromolecules*. 2023 Jan 15;231:123307–7. <https://doi.org/10.1016/j.ijbiomac.2023.123307>
 - [11]. Mao AS, Mooney DJ. Regenerative medicine: Current therapies and future directions. *Proceedings of the National Academy of Sciences*. 2015 Nov 24;112(47):14452–9. <https://doi.org/10.1073/pnas.1508520112>
 - [12]. Yahyazadeh R, Baradaran Rahimi V, Askari VR. Stem cell and exosome therapies for regenerating damaged myocardium in heart failure. *Life Sciences* [Internet]. 2024 Aug 15 [cited 2024 Jul 18];351:122858. Available from: <https://pubmed.ncbi.nlm.nih.gov/38909681/>
 - [13]. Robey PG. *Skeletal Regeneration: Stem Cell Therapy*. Elsevier eBooks. 2020 Jan 1;119–34. <https://doi.org/10.1016/B978-0-12-801238-3.11154-7>
 - [14]. Cruz IBM da, Severo AL, Azzolin VF, Garcia LFM, Kuhn A, Lech O. Regenerative potential of the cartilaginous tissue in mesenchymal stem cells: update, limitations, and challenges. *Revista Brasileira de Ortopedia (English Edition)*. 2017 Jan;52(1):2–10. <http://dx.doi.org/10.1016/j.rboe.2016.11.005>
 - [15]. Boschetti PJ, Pelliccioni O, Mariángel Berroterán, Candal MV, Sabino MA. Fluid flow in a Porous Scaffold for Microtia by Lattice Boltzmann Method. *International Journal of Advances in Medical Biotechnology*. 2019 Mar 1;2(1):46–6.
 - [16]. Ghareh nazifam Z, Dolatabadi R, Baniassadi M, Shahsavari H, Kajbafzadeh AM, Abrinia K, et al. Computational analysis of vincristine loaded silk fibroin hydrogel for sustained drug delivery applications: Multiphysics modeling and experiments. *International Journal of Pharmaceutics*. 2021 Nov;609:121184. <https://doi.org/10.1016/j.ijpharm.2021.121184>.
 - [17]. Gruhn T, Camilo Ortiz Monsalve, Müller C, Heid S, Baccacini AR, Salehi S. Fabrication of Hydrogel-Based Composite Fibers and Computer Simulation of the Filler Dynamics in the Composite Flow. *Bioengineering*. 2023 Apr 6;10(4):448–8. <https://doi.org/10.3390/bioengineering10040448>
 - [18]. Das S, Datta P, Chowdhury AR. Optimizing Cell Deformation in Extrusion-Based Bioprinting Process by Importing Inherent Viscoelasticity Using Computational Fluid Dynamic. *Lecture notes in mechanical engineering*. 2022 Jan 1;337–48 https://doi-org.ez106.periodicos.capes.gov.br/10.1007/978-981-16-6738-1_28
 - [19]. Huang M, Fan S, Xing W, Liu C. Microfluidic cell culture system studies and computational fluid dynamics. *Mathematical and Computer Modelling* [Internet]. 2010 Dec [cited 2019 Dec 12];52(11-12):2036–42. Available from: <https://www.sciencedirect.com/science/article/pii/S0895717710002773>
 - [20]. Choi K, Karr JR, Sauro HM. Status and Challenges of Reproducibility in Computational Systems and Synthetic Biology. Elsevier eBooks. 2019 Dec 26;406–12. <https://doi.org/10.1016/B9780-12-801238-3.11525-9>
 - [21]. Blaeser A, Duarte Campos DF, Puster U, Richtering W, Stevens MM, Fischer H. Controlling Shear Stress in 3D Bioprinting is a Key Factor to Balance Printing Resolution and Stem Cell Integrity. *Advanced Healthcare Materials*. 2015 Dec 2;5(3):326–33. <https://doi.org/10.1002/adhm.201500677>

Terciotti et al.

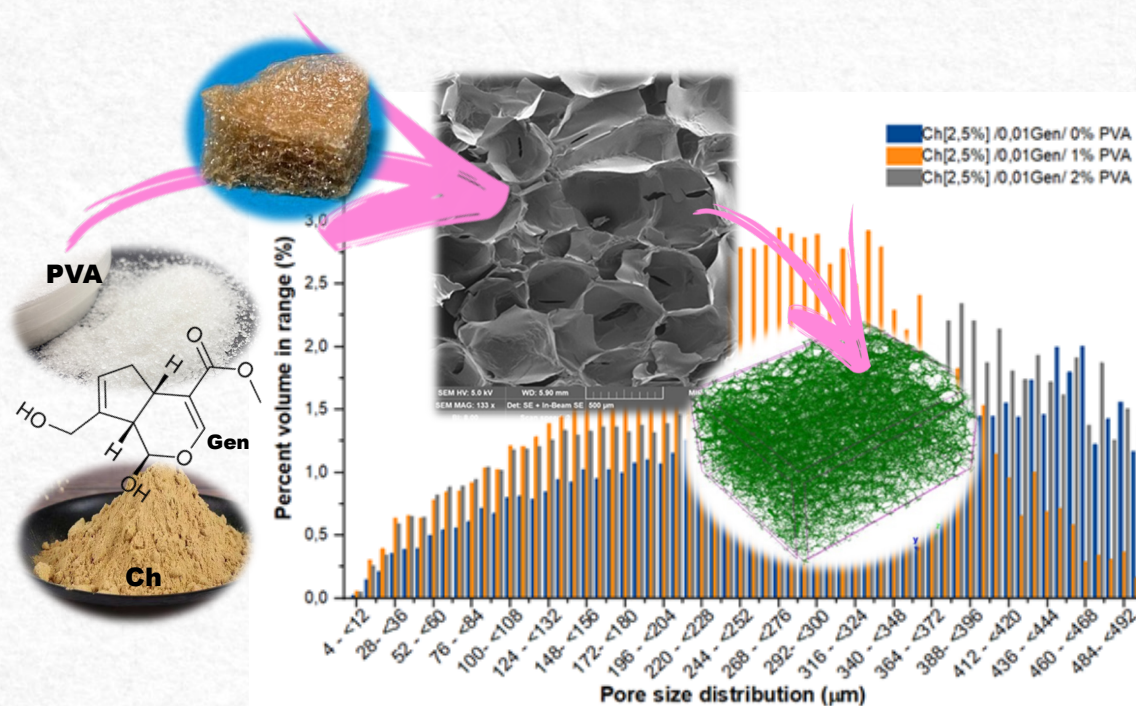
- [22]. Chang R, Nam J, Sun W. Effects of Dispensing Pressure and Nozzle Diameter on Cell Survival from Solid Freeform Fabrication–Based Direct Cell Writing. *Tissue Engineering Part A*. 2008 Jan;14(1):41–8. <https://doi.org/10.1089/ten.a.2007.0004>
- [23]. Kim KM, Choi YJ, Hwang JH, Kim AR, Cho HJ, Hwang ES, et al. Shear Stress Induced by an Interstitial Level of Slow Flow Increases the Osteogenic Differentiation of Mesenchymal Stem Cells through TAZ Activation. Edington DT, editor. *PLoS ONE*. 2014 Mar 21;9(3):e92427. <https://doi.org/10.1371/journal.pone.0092427>
- [24]. Nelson CM, Xiao B, Wickström SA, Dufrêne YF, Cosgrove DJ, Carl-Philipp Heisenberg, et al. Mechanobiology: Shaping the future of cellular form and function. *Cell*. 2024 May 1;187(11):2652–6. <https://doi.org/10.1016/j.cell.2024.04.006>

Morphological analysis reveals the influence of genipin and polyvinyl alcohol on porous morphology on interpenetrated chitosan xerogels

M.V. Guimarães¹; G.H. de Magalhães Gomes^{1,2}; K.F. Santos¹;
J.L. Dávila^{1,3}; L.A. Perdígón³; P.Y. Noritomi¹; M.A. Sabino^{1,3**}

Received: October 2024; Accepted: December 2024.

*Corresponding author: E-mail address: *mvguimaraes@cti.gov.br; **msabino@usb.ve



Abstract: The morphological characterization of xerogels composed of chitosan, genipin, and PVA demonstrates that their porous architecture is essential to their function as scaffolds for tissue engineering, with significant impacts on absorption properties, cell viability, and potential for biomedical application. SEM and microCT analysis confirmed that these xerogels possess a highly porous internal morphology, with interconnected pores forming an interpenetrating polymeric network, free from phase separation between chitosan and PVA. Hemocompatibility assays suggested the non-cytotoxic nature of these materials. Varying genipin concentrations showed that lower concentrations produce more heterogeneous pore sizes, while higher concentrations yield a uniform pore distribution, likely due to the increased availability of crosslinking sites. Additionally, the degree of anisotropy increases with both higher genipin and PVA concentrations, suggesting enhanced alignment within the three-dimensional structure. The total open pore volume, which ranges from 88% to 93%, is modifiable based on the concentrations of genipin and PVA. These insights indicate that these xerogels are viable candidates for clinical applications, particularly as potential substitutes for nucleus pulposus, given their high swelling capacity, porosity, interconnectivity, biocompatibility, and adaptable morphological characteristics.

Keywords: Chitosan. Genipin. Polyvinyl alcohol. SEM. MicroCT. Xerogels.

¹Division DITPS, Renato Archer Center for Information Technology, Campinas, SP, Brazil.

²Federal University of Itajubá, Instituto de Ciências Puras e Aplicadas, Itabira, MG, Brazil.

³Universidad Simón Bolívar, Grupo B5IDA, Dpto. Química. Caracas, Venezuela.

Introduction

Tissue engineering has become a key area of biomedical science, focusing on the repair and regeneration of damaged or diseased tissue. Among the numerous strategies explored, the development of three-dimensional (3D) biopolymer-based scaffolds has shown promise in replicating the architecture of the native extracellular matrix (ECM)^[1].

Chitosan, a chitin-derived biopolymer, has attracted the interest of researchers due to its biocompatibility, biodegradability and versatility in forming gels that can be used as scaffolds for cell culture^[2]. For this reason, this biopolymer can help in the development of various hydrogel formulations with morphological and biomechanical properties that mimic, for example, the morphology of the intervertebral nucleus pulposus^[3]. The nucleus pulposus is an essential component of the intervertebral disc and plays a fundamental role in the biomechanics and functionality of the spine. Its degeneration can lead to painful and debilitating conditions, making it a subject of great interest in traumatology^[4] and the treatment of occupational diseases^[5]. This emphasizes the need to establish effective strategies for its recovery.

Through the use of advanced techniques such as scanning electron microscopy (SEM) and X-ray microtomography (microCT), it is possible to analyze interpenetrating hydrogels and observe how the dispersed phase influences the porous morphology of gels^[6,7] based on a biopolymer matrix such as chitosan^[8]. Interpenetrating gels produced by the mechanical mixing of chitosan with polyvinyl alcohol (PVA) at different concentrations could represent an important advance in the development of scaffolds. They enable new approaches by incorporating dispersed phases, such as PVA, to create new types of interpenetrating gels. An interpenetrating gel consists of two or more polymer networks (of the same or different nature) that chemically or physically interlace but are immiscible^[9]. PVA is a synthetic polymer known for its excellent rheological behavior, hydrophilicity, cell compatibility and ability to improve the mechanical and structural properties of polymer gels^[10]. It is also used in the formulation of ceramic pastes for bioprinting applications^[11].

Some gels need to be crosslinked to achieve the desired behavior. In the context of chitosan, genipin, emerges as one of the most promising agents for crosslinking a natural and non-cytotoxic compound. Being a natural product, it is of great interest for some applications where its solubility in water or in ethanolic solutions at low concentration allows its easy manipulation to be incorporated into biopolymer gels; also providing enhanced structural stability to gels while maintaining their biocompatibility

^[12]. Simple tests, such as hemocompatibility tests, show that the new biomaterial formulations can be safely used in biomedical applications. In addition, international technical standards (ISO and ASTM) define the test protocols for performing this type of evaluation^[13-15].

The rheological, physicochemical, mechanical and bioactive properties of these formulated gels depend directly on their internal morphology. Specialized techniques like scanning electron microscopy (SEM) and microtomography (microCT) are combined to thoroughly analyze the three-dimensional structure of the gel in its dehydrated form, or xerogel.

Scanning electron microscopy (SEM) enables the visualization of surface and internal structures at the microscale and nanoscale^[16]. Microtomography (microCT) uses X-rays to produce 3D images, enabling detailed analysis of pore distribution in materials^[17]. MicroCT provides additional information that cannot be obtained with SEM alone. This combined approach offers a clearer understanding of the morphological properties of the gel and establishes a foundation for future research into applications like tissue regeneration and other biotechnological uses. This is crucial because a well-developed porous structure facilitates nutrient exchange, oxygenation and cell growth within the scaffold^[18]. The interconnection between pores also plays a fundamental role in facilitating adequate blood flow, which is essential for the successful integration of the implant with the surrounding tissue^[19].

This study emphasizes the benefits of using chitosan for scaffolds in tissue engineering and highlights how genipin enhances its formulation by promoting cross-linking, which ensures the dimensional stability of these promising biomaterials. Understanding swelling processes is essential, as they offer valuable insights into the diffusion capacity, fluid absorption, and dimensional stability of materials. Research on biopolymer-based interpenetrating gels offers significant potential for regenerative medicine, particularly in restoring the intervertebral nucleus pulposus.

Therefore, the primary aim of this study is to investigate how the preparation of a chitosan-based gel with different concentrations of PVA impacts not only the physical properties of the gel but also its potential to serve as an effective support for cell growth and tissue regeneration. Furthermore, by altering the concentrations of genipin, this study seeks to elucidate the impact of this variable on essential characteristics, including porosity, pore volume, interconnection density, fractal dimensions, and pore wall thickness. The preliminary results indicate that incorporating PVA as a dispersed and

interpenetrating phase markedly enhances the microarchitecture of the gel, surpassing that of gels composed solely of chitosan and genipin.

Materials and Methods

Preparation of Gel Formulations

The chitin used in this study was extracted from shrimp shells (*Litopenaeus vannamei*) at the B⁵IDA laboratory, and its derivative, chitosan (Ch), was obtained through a standard deacetylation reaction in an alkaline medium at elevated temperatures, resulting in a degree of deacetylation of 79%. This process followed the protocol outlined by Gallardo et al. (2019) [20]. The molecular weight of the Ch was determined using capillary viscometry, yielding a value of 1.04×10^5 g/mol. The synthetic polyvinyl alcohol (PVA) (Himedia, USA) used in the study had a molecular weight of 8×10^4 g/mol. The natural crosslinker, genipin (Gen), was extracted from the fruit of *Genipa americana*, purified in the B⁵IDA laboratory, and characterized following the protocol described by Colmenares et al. (2024) [12].

For the preparation of the interpenetrating network gels, stock solutions were prepared for each polymer, Ch and PVA. The Ch gel was prepared at a [2.5% w/v] concentration using a [1% v/v] acetic acid solution (Fluca Riedel-de Haen, 98%, Spain). The PVA solution was prepared at concentrations of [1% w/v] and [2% w/v] in deionized water. For the crosslinking agent, Gen crystals were dissolved in a 30% ethanol solution to obtain diluted solutions with concentrations of [0.010% w/v] and [0.025% w/v]. Each gel formulation was prepared by mixing equal volumes (1:1:1) of Ch/Gen/PVA, which were combined using a paddle mixer at 200 rpm for 10 minutes at room temperature. The interpenetrated gels formed were thoroughly washed by dialysis, and this procedure was repeated at least 2 times for each formulation before being taken to the lyophilization process (Labconco-Freezone 2.5, -45°C, and 1.5 Torr vacuum for 48 hours). The resulting xerogels, which are the focus of this study, were properly stored in desiccators, and the composition of each formulation is summarized in Table 1.

Table 1 - Composition of each formulation of interpenetrated Ch/Gen/PVA gels.

Gel	F1 (% w/v)	F2 (% w/v)	F3 (% w/v)	F4 (% w/v)	F5 (% w/v)	F6 (% w/v)
Ch	2,5	2,5	2,5	2,5	2,5	2,5
Gen	0,010	0,025	0,010	0,025	0,010	0,025
PVA	0	0	1,0	1,0	2,0	2,0

Morphological characterization of xerogels Microtomography (microCT)

The three-dimensional (3D) morphology of the scaffolds was investigated through microtomography (microCT) analysis. For this, a SkyScan1272 CMOS Edition microCT scanner (Bruker, Kontich, Belgium) was set up with these parameters: 20 kV source voltage, 100 μ A current, 4 μ m pixel size, 0.3° rotation steps from 0 to 180°, no filter, 4-frame averaging, and 2000 ms exposure time per image. The scanning time for each sample was approximately 2 hours.

NRecon software (v2.1.0.1, Bruker, Kontich, Belgium) was used to reconstruct X-ray projections, applying a 4% beam hardening correction, a 2-level ring artifact correction, and no smoothing. The 3D visualizations were generated using the CTvox software (v.3.3.1, Bruker, Kontich, Belgium) (Fig.1). To image analysis, the CTan software (version 1.20.8; 64-bit; Bruker microCT, Kontich, Belgium) was employed, in which the reconstructed images were subjected to binarization utilizing the Otsu 3D automatic segmentation algorithm [21,22]. Additionally, 3D noise removal operations, such as filtering and despeckle, were applied to improve image quality.

Subsequently, a comprehensive 3D morphometric analysis was conducted, which encompassed the evaluation of porosity (both closed and open), pore interconnectivity, degree of anisotropy, fractal dimension, as well as pore size distribution within the volume of interest.

Scanning Electron Microscopy (SEM)

The morphological characteristics of the scaffold surfaces were analyzed using scanning electron microscopy (SEM) on a Tescan MIRA 3 (Korea). For each sample, a cryogenic cross-section was observed to examine the internal morphology of the xerogels and correlate these findings with the results obtained from microCT. Prior to observation, the samples were sputter-coated with gold to ensure adequate conductivity. During SEM imaging, a 15 kV accelerating voltage was applied in the Tescan microscope.

Swelling Assay

Each xerogel sample, shaped as a cylindrical disk, was weighed and then immersed in a phosphate-buffered saline (PBS) solution at 37°C for a period of 36 hours, which is the time required

for all formulations to reach a constant weight and maintain physical stability. The immersion test was carried out in duplicate for each formulation, as well as the weighing was also carried out in duplicate, obtaining the error bars and represented in the result presented.

Based on the weight variation, the swelling ratio (Rh) was calculated using the following equation^[12]:

$$Rh (\%) = [(W_{\text{hydrated}}(t) - W_{\text{xerogel}})] \times 100\% / (W_{\text{xerogel}}) \quad (\text{eq. 1})$$

where: W hydrated represents the weight of the hydrated xerogel as a function of time until equilibrium is reached; W xerogel corresponds to the weight of the dry xerogel (deshydrated gel). The experiment was conducted in triplicate using cylindrical samples to ensure accuracy and reproducibility of the results.

Hemocompatibility

This assay was conducted in accordance with the ISO 10993-4 standard for biological evaluation of medical devices^[23]. The hemolysis test was performed using blood agar, prepared according to the instructions provided by the manufacturer (Merck, Amsterdam). The agar base was cooled to 45 °C and mixed with sterile defibrinated sheep blood (INH Instituto Nacional de Higiene UCV, Caracas) to achieve a final concentration of 5% (v/v). The xerogel samples were sterilized by exposure to UV light for 15 minutes. Subsequently, the prepared blood agar was poured into sterile Petri dishes, and the xerogels were carefully placed onto the solidified agar. The Petri dishes were then incubated in a 5% CO₂/95% air environment at 37°C for 48 hours. Finally, the results were documented photographically.

Results and Discussion

It is well established that the pore architecture in hydrogels is a critical factor in determining their mechanical strength, fluid absorption capacity, and cell viability, while also significantly influencing cellular proliferation and differentiation^[24-26]. Therefore, a thorough understanding of the pore morphology within a 3D structure is crucial, particularly when assessing its potential for biomedical, tissue engineering, and pharmacological applications. The results obtained from advanced techniques, such as SEM combined with microtomography (microCT), provide critical insights into this pore architecture and its degree of interconnectivity. Figure 1 shows representative images of the cross-sectional views of each xerogel, reconstructed using μ CT and further examined transversally via SEM. As illustrated, the chitosan-based xerogels, regardless of the incorporation of genipin as a crosslinking agent or PVA as a dispersed and interpenetrating phase, exhibited a highly porous internal structure characterized by interconnected pores. This interconnected porosity is further confirmed by the

SEM micrographs accompanying the figure. The key microCT-derived parameters are summarized in Table 2.

Upon detailed examination, the morphology resulting from the blending of the natural polymer chitosan with the synthetic PVA showed no evidence of phase separation in any of the prepared formulations. This observation was confirmed through both SEM analysis and microtomography (microCT), which revealed consistent structural integrity across the entire network. Consequently, it can be considered that the hydrogels formed in this study exhibit the characteristics of a fully interpenetrated polymer network (IPN)^[27].

Moreover, when evaluating the effect of genipin concentration on the microstructure of each xerogel formulation, it was observed that lower concentrations of genipin resulted in a broader, more heterogeneous pore size distribution, whereas increasing the concentration of the crosslinking agent led to a narrower, more uniform distribution (Fig. 2). Specifically, at a genipin concentration of 0.010%, the pore sizes ranged from 180–340 μ m and 350–480 μ m, while at 0.025%, the distribution became more homogeneous, ranging from 220–340 μ m. This phenomenon can be attributed to the random nature of the crosslinking reaction: as the genipin concentration increases, the number of effective active crosslinking sites also increases, leading to greater uniformity. Additionally, the higher concentration of the interpenetrating PVA phase appears to further contribute to the improved uniformity in pore size distribution.

These results may be associated with the degree of anisotropy (DA), which appears to increase with higher genipin concentrations and the presence of the interpenetrating PVA phase. According to the literature, DA refers to the measurement of the preferential alignment of solid scaffolds in 3D structures along a particular direction^[28]. In this context, the chitosan/PVA xerogels crosslinked with genipin demonstrated an almost two-fold increase in DA when the genipin concentration was raised. These values are consistent with porous scaffolds exhibiting porosities between 80–95%^[22]. This suggests that genipin, as a crosslinking agent, may promote a more anisotropic properties in these scaffolds^[29].

According to the data presented in Table 2, the open pore volume and the total open pore percentage in the formulations ranged between 88–93%. However, a slight reduction in these percentages was observed as the genipin concentration increased. This result is consistent with the fact that higher genipin concentrations promote more extensive crosslinking reactions, leading to an increase in gel viscosity (hindering the mobility of molecular chains) and a higher crosslinking density, which generates a more stable 3D network.

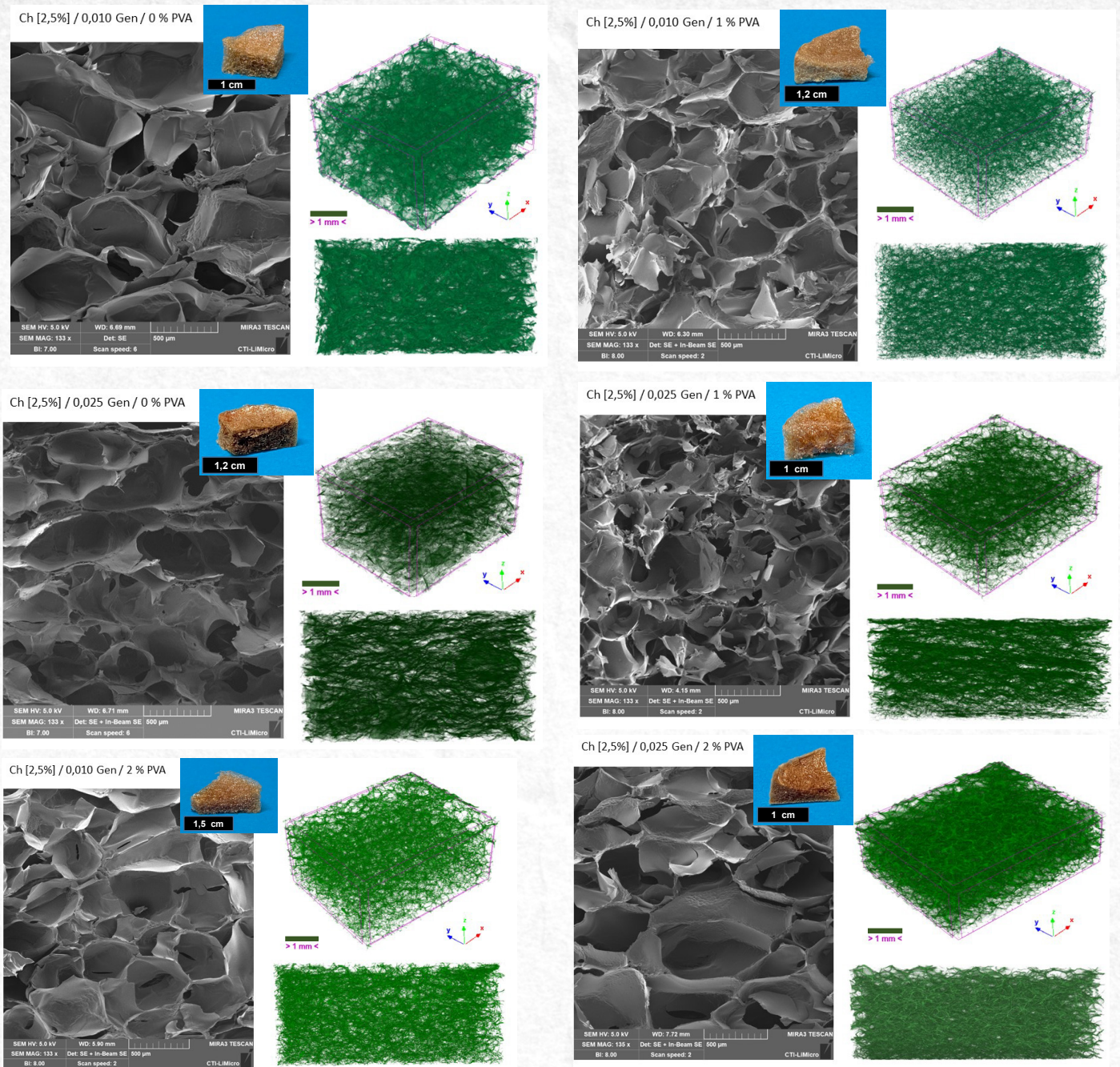


Figure 1 - View of each xerogel and their internal morphology as observed through SEM and X-ray microtomography techniques.

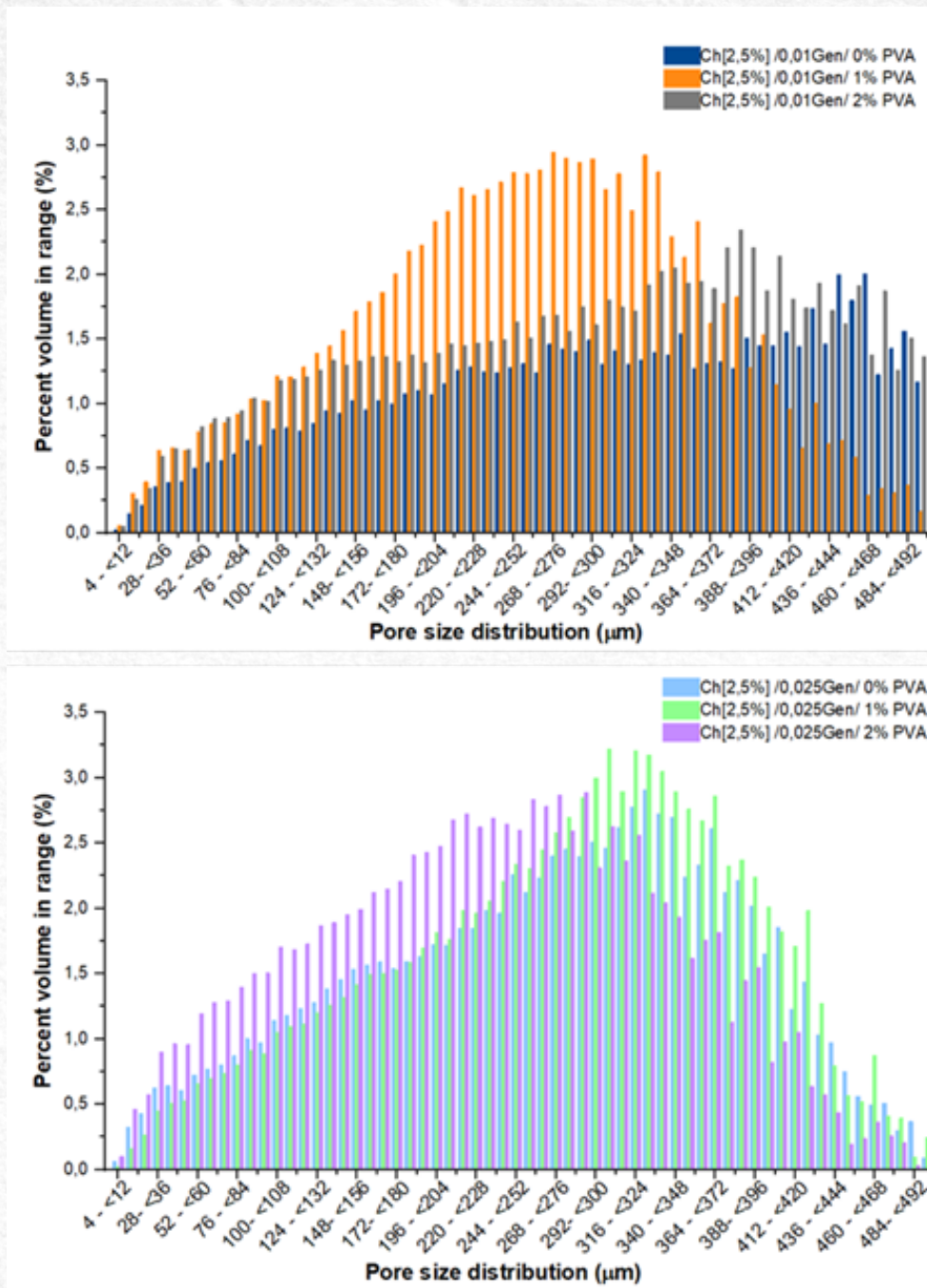


Figure 2 - Pore size distribution of each xerogel sample. Results obtained from microCT analysis.

Table 2 - Morphometric Parameter Assessment. The data are represented for nearly 700-900 slices obtained after MicroCT imaging.

Parameter	Samples					
	F1	F2	F3	F4	F5	F6
Degree of Anisotropy (DA)	1,622	3,182	2,054	3,305	1,754	2,971
Volume of closed pores (mm ³)	0,017	0,012	0,001	0,002	0,000	0,002
Closed porosity (%)	0,114	0,076	0,006	0,019	0,006	0,022
Volume of open pore space (mm ³)	114,281	119,113	107,844	78,723	90,783	72,469
Open porosity (%)	88,743	88,086	92,621	90,911	92,971	89,295
Total volume of pore space (mm ³)	114,298	119,126	107,844	78,725	90,784	72,471
Total porosity (%)	88,756	88,095	92,621	90,913	92,972	89,298
Connectivity	32360	73875	185848	132561	140807	122170
Fractal Dimension	2,472	2,542	2,533	2,464	2,467	2,576

This result is particularly promising, as studies in the field of tissue engineering scaffolds have reported that, in relation to the porous structure of biomaterials, smaller and more regular pore sizes improve the mechanical properties of the gel^[30]. However, the pore size cannot be too small, otherwise it could have restrictions for the diffusion of biomolecules (such as certain proteins, nucleic acids, etc.). Furthermore, the diffusion of macromolecules that may be encapsulated and/or released from such structures is also enhanced^[31]. Considering the use of these materials for cell culture studies, an adequate spatial distribution of cells deposited on the scaffold can be achieved, which facilitates a homogeneous distribution of the extracellular matrix. If the pores are too small, it may make it difficult for these essential elements to pass through, while if they are too large, they may not provide adequate support for cells. According to what the literature has reported, the pore size range is usually between approximately 75 to 500 micrometers^[30-32]. This size allows cells to adhere and migrate through the scaffold, as well as facilitating the diffusion of nutrients and oxygen, as well as the removal of waste. And they should not be less than 20 microns. Consequently, this could initially promote cell proliferation and later differentiation^[32]. Additionally, this ensures the vascularization processes characteristic of tissue regeneration^[33].

Additionally, increasing the proportion of PVA resulted in a decrease in pore size, although the pore size distribution became broader. The higher PVA content, acting as an interpenetrating and dispersed phase within the chitosan matrix, tends to elevate the viscosity of the mixture. This increased viscosity leads to a slower gelation rate, thereby promoting greater solvent evaporation, which indirectly raises the concentration of the solution over time. This

complex process results in the formation of more compact 3D structures, characterized by slightly smaller pores while preserving effective pore interconnectivity.

An important feature of all the xerogels obtained is their pore interconnectivity. The literature reports that such interconnectivity creates free volume, which facilitates cellular migration during the proliferation phase^[34], and thus supports the formation of the extracellular matrix and the movement of fluids, promoting vascularization throughout the molecular network^[35]. Although no significant differences in this parameter were observed with increasing PVA content, the presence of the interpenetrated PVA phase did enhance pore interconnectivity compared to formulations with only the chitosan/genipin phase^[36].

Another critical parameter to evaluate is the fractal dimension (Df) of the hydrogels, a dimensionless index that characterizes the continuous and irregular geometry of three-dimensional networks and quantifies the complexity of their architecture^[22, 37]. Previous studies have indicated that Df can significantly influence cellular behavior and is regarded as a key metric in the design and development of scaffolds for tissue engineering^[22,28]. As shown in Table 2, our analysis revealed that the incorporation of genipin or PVA had no statistically significant effect on the Df of the xerogels, with values remaining similar across all cases, ranging from 2.4 to 2.6. These values can be attributed to the effective crosslinking of the chitosan and PVA polymer chains within the 3D network, despite compositional variations in the formulations. Furthermore, this crosslinking process did not negatively impact the total porosity, which remained at approximately 90%, nor did it compromise the

interconnectivity between pores, both of which are essential for maintaining the functionality of the scaffolds.

Regarding the thickness of pore walls (>80%) in the chitosan xerogels, no significant differences were found, regardless of the incorporation of genipin and PVA. Most pores exhibited a similar wall thickness, ranging from 12–20 μm to 28–36 μm , as shown in Fig. 3. However, when 1% PVA was used, the predominant wall thickness fell within the 12–20 μm range, whereas with 2% PVA, the predominant range expanded to 12–28 μm . This clearly confirms our hypothesis that genipin facilitates crosslinking

between chitosan chains, independent of the presence of an interpenetrated PVA phase, and that this helps improve pore connectivity (as previously demonstrated). This enhanced connectivity could improve fluid transport and enable the generation of three-dimensional structures with walls that ensure dimensional stability. This is an important consideration when developing structures with characteristics that could potentially biomimic those of an intervertebral disc component, specifically the nucleus pulposus, a central, gelatinous, yet mechanically resilient part [38].

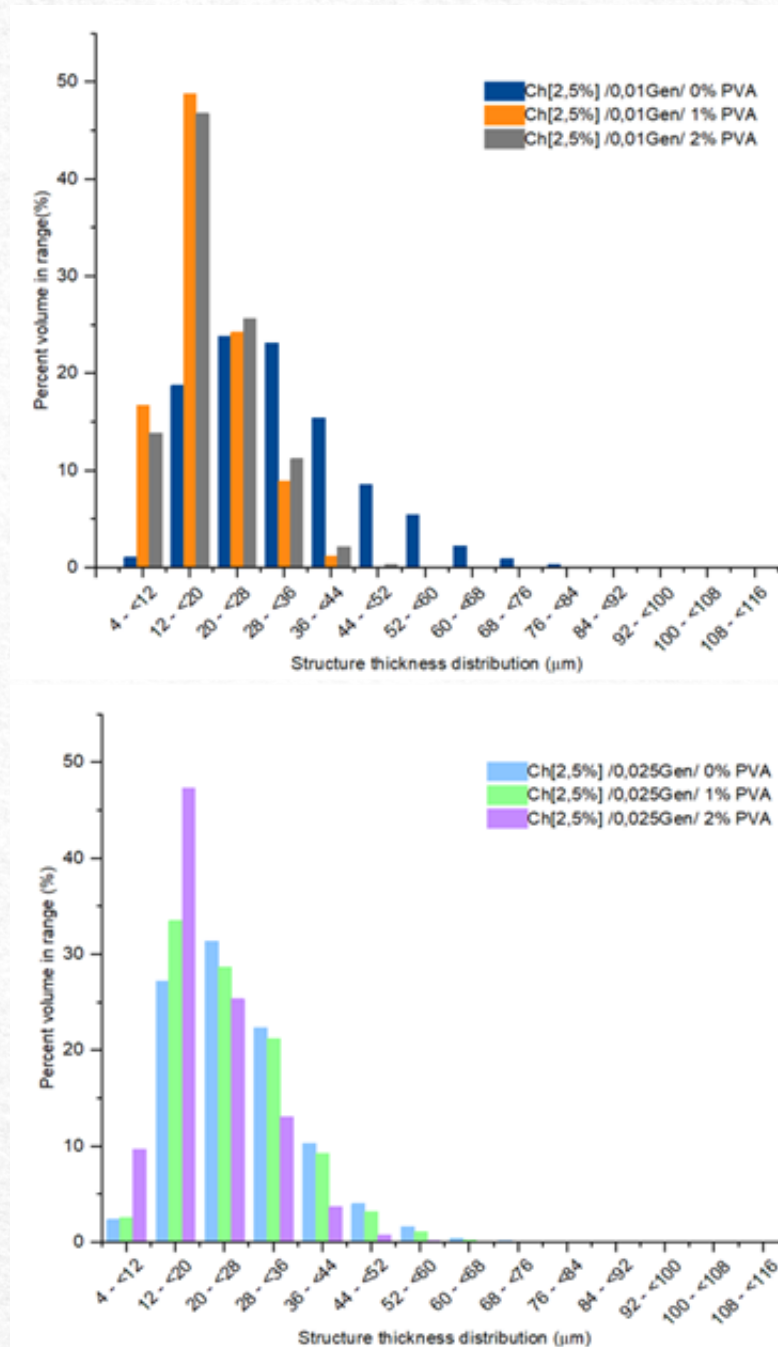


Figure 3 - Effect of genipin and interpenetrated PVA phase in chitosan xerogels on pore wall thickness.

Swelling Assay

At the macroscopic level, the swelling capacity of a hydrogel is determined by the amount of space within the polymer network that can be filled with fluid, the polymer-fluid interaction forces, electrostatic forces, and osmotic forces^[39,40]. The first observation from the results shown in Fig. 4, is that all formulations behave as superabsorbent gels^[40], as in all cases the swelling ratio significantly exceeds 100%, with each sample maintaining its physical and dimensional stability when swollen. In most cases, thermodynamic equilibrium was reached after 28–30 hours, and no further water absorption (gravimetrically) or volume change was observed until the end of the experiment at 36 hours. This process, also known as Donnan equilibrium^[41], correlates the water absorption to the elimination of the osmotic pressure difference between the interior of the polymer network that forms the gel and the external solution in which the hydrogel is immersed^[42,43].

To explain this result, two fluid absorption mechanisms can be considered, both of which may describe the behavior observed in each formulation. The first mechanism is related to polymer-solvent

interactions, specifically the hydroxyl (-OH) groups interactions (from both PVA and chitosan), and the protonated amino groups (-[NH₃]⁺) of chitosan with water molecules. The second mechanism involves the diffusion process through the free volume or space generated by the pores and their interconnectivity, which allows the solvent to permeate these areas, resulting in the relaxation of the Ch/PVA polymer chains that form the crosslinked network^[44-46].

According to the morphologies described in Figures 1–3 and the results summarized in Table 2, among the three components in each formulation, genipin not only acts as a crosslinking agent but also enhances the water absorption capacity, as evidenced by the increase in swelling percentage^[40]. Additionally, the presence of PVA as an interpenetrated phase further supports this process, as these polymer chains not only improve pore interconnectivity but also contribute due to the hydrophilic nature of PVA and its greater elasticity compared to chitosan. This combination promotes better and greater molecular relaxation, allowing a significant amount of water to be retained within the gel without causing a loss of dimensional stability.

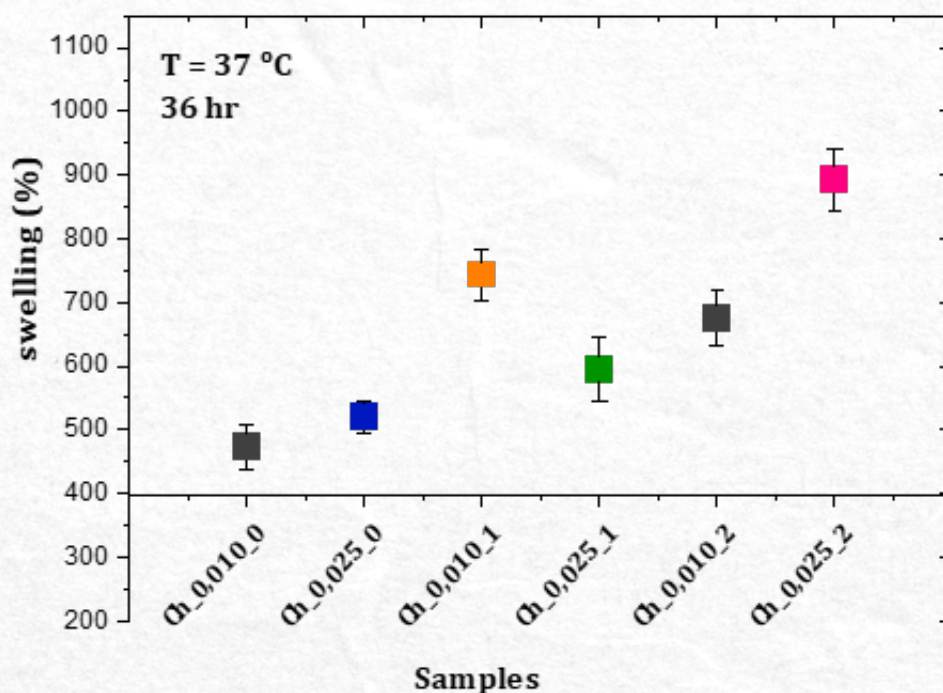


Figure 4 – Swelling assay of xerogels under controlled time and temperature conditions. It is clear from the figure that the swelling behavior is influenced by the presence of the interpenetrated PVA phase in the chitosan matrix. Source: Own authorship, 2024

Hemocompatibility

Among the essential requirements for a material to be used as an implant is biocompatibility, which is evaluated through a variety of experiments standardized by international technical norms (ISO 10993-4) [23]. One such test is the hemocompatibility assay. Hemolysis, or the lysis of blood cells, refers to the rupture of the cell membrane, allowing hemoglobin to be released from erythrocytes. There are three types of hemolysis: alpha, beta, and gamma. In alpha hemolysis, there is a partial breakdown of hemoglobin from erythrocytes. Beta hemolysis involves complete hemoglobin rupture, causing a "clearing" or whitening effect in the agar solution (known as a white halo). Gamma hemolysis, on the other hand, is not technically a hemolytic process but rather an oxidation process of the blood [9].

Figure 5 shows the evaluation of the xerogels in the blood-agar solution (as described in the experimental methodology). As can be seen, regardless of the genipin or PVA concentration within the studied range, no hemolysis was observed—neither alpha nor beta, and even the brown discoloration typical of gamma hemolysis was absent. As reported by Viera et al [9], where acrylamide was used as a positive control, showing a white halo due to hemotoxicity. This indicates that, under the experimental conditions tested, there was no hemolytic effect during the incubation period. In other words, these formulations did not cause the rupture of blood cell membranes, which is a positive indication of the potential of this biomaterial and opens a window for its application in tissue engineering. However, more complex cellular studies are still needed.

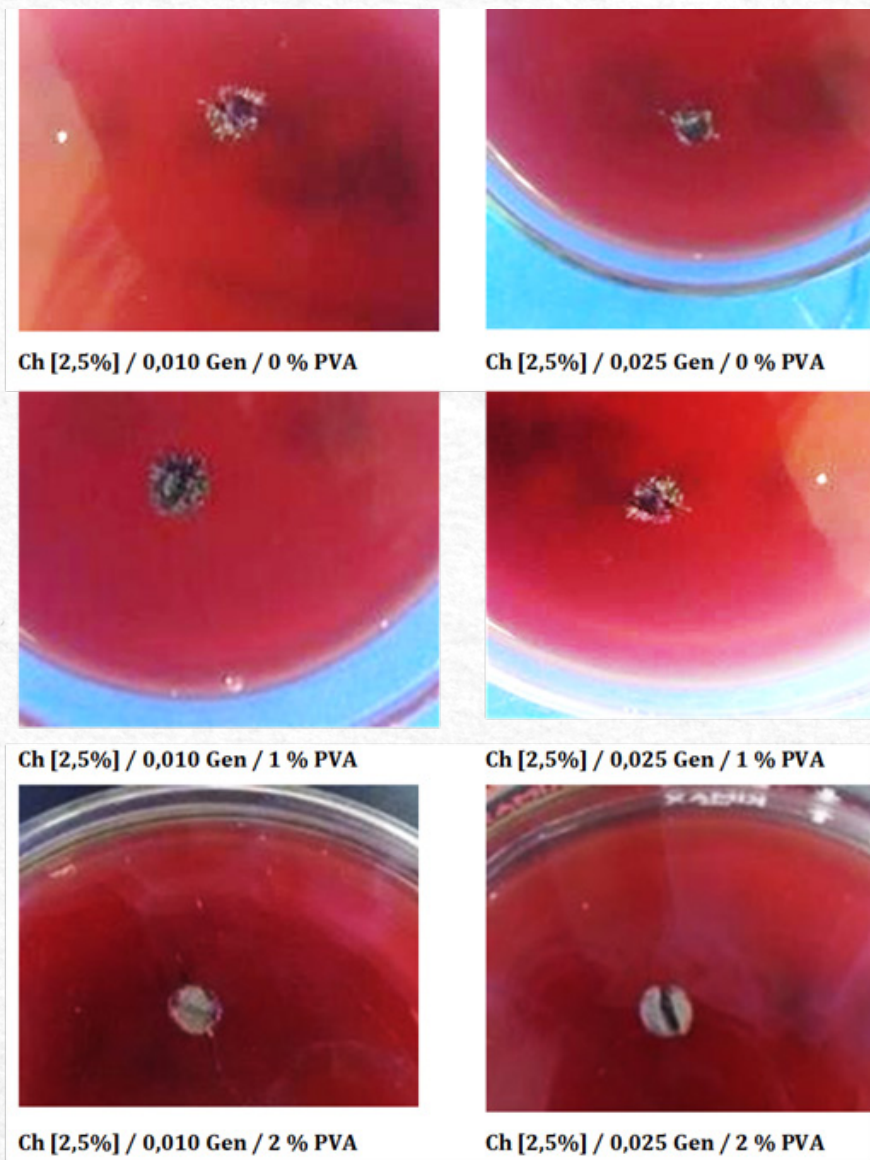


Figure 5 - Agar-blood hemocompatibility assay for the evaluation of the studied xerogels, according to ISO 10993-4 standards. Source: Own authorship, 2024.

This result for the interpenetrated gels is not surprising, as numerous studies have reported that both chitosan (the primary polymer in the xerogels) and PVA (the dispersed phase) are non-toxic and do not elicit allergic or inflammatory responses via any route (implant, ingestion, or topical use)^[47, 48]. Moreover, chitosan has been shown to exhibit antimicrobial, hypocholesterolemic, biodegradable, mucoadhesive and immunostimulant properties, among others^[49]. Many studies have demonstrated its biocompatibility with various types of cells^[49, 51], and this cellular biocompatibility seems to increase with higher degrees of deacetylation. The chitosan used in this work had a degree of deacetylation of 79%. A higher degree of deacetylation means more free amino groups along the polysaccharide chain, which are responsible for promoting cell adhesion and proliferation^[52].

Conclusions

The analysis of interpenetrated xerogels composed of chitosan, genipin, and PVA highlights the crucial influence of pore architecture and interconnectivity on their properties and potential applications. This was demonstrated through the use of innovative techniques, such as X-ray microtomography (microCT), complemented by scanning electron microscopy (SEM) results. It can be concluded that the incorporation of genipin serves as an effective crosslinker, allowing control over pore size distribution, while PVA, as an interpenetrating phase, enhances network interconnectivity, thereby providing a suitable environment for cell growth. These materials exhibit hemocompatibility and superabsorbent behavior. The ability to tune their structural properties further strengthens their potential as scaffolds for use in three-dimensional environments, positioning them as promising candidates for nucleus pulposus replacement in biomedical applications.

Acknowledgment

The authors of this research dedicate it to the memory of Dr. Jorge Vicente Lopes da Silva, a pioneer of additive manufacturing in the Latin American region and the world. Their contribution during his life to our training and professional consolidation is shown in this research.

The authors also are grateful to the CNPq/PCI program (process nos. 301214/2024-7, 300038/2024-0 and 300933/2024-0) for the financial support.

Declarations

Conflict of Interest

All authors declare no conflict of interests.

References

- [1]. Reddy MS, Ponnamma D, Choudhary R, Sadasivuni KK. A comparative review of natural and synthetic biopolymer composite scaffolds. *Polymers*. 2021 Mar 30; 13(7):1105. <https://doi.org/10.3390/polym13071105>
- [2]. Afewerki S, Sheikhi A, Kannan S, Ahadian S, Khademhosseini A. Gelatin-polysaccharide composite scaffolds for 3D cell culture and tissue engineering: towards natural therapeutics. *Bioeng Transl Med*. 2019 Jan; 4(1):96-115. <https://doi.org/10.1002/btm2.10124>
- [3]. Ma T, Liu C, Zhao Q, Zhang Y, Xiao L. Decellularized nucleus pulposus matrix/chitosan hybrid hydrogel combined with nucleus pulposus stem cells and GD-F5-loaded microspheres for intervertebral disc degeneration prevention. *Mol Med*. 2024 Jan 10; 30(1):7. <https://doi.org/10.1186/s10020-024-00777-z>
- [4]. Choi Y, Park MH, Lee K. Tissue engineering strategies for intervertebral disc treatment using functional polymers. *Polymers*. 2019 May 13; 11(5):872. <https://doi.org/10.3390/polym11050872>
- [5]. Santi S, Corridori I, Pugno NM, Motta A, Migliaresi C. Injectable scaffold-systems for the regeneration of spinal cord: advances of the past decade. *ACS Biomater Sci Eng*. 2021 Feb 1; 7(3):983-999. <https://doi.org/10.1021/acsbiomaterials.0c01779>
- [6]. Malaise S, Rami L, Montembault A, Alcouffe P, Burdin B, Bordenave L, Delmond S, David L. Bioresorption mechanisms of chitosan physical hydrogels: a scanning electron microscopy study. *Mater Sci Eng C*. 2014 Sep 1; 42:374-84. <https://doi.org/10.1016/j.msec.2014.04.060>
- [7]. Hildebrand T, Novak J, Nogueira LP, Boccaccini AR, Haugen HJ. Durability assessment of hydrogel mountings for contrast-enhanced micro-ct. *Micron*. 2023 Nov 1; 174:103533. <https://doi.org/10.1016/j.micron.2023.103533>
- [8]. Cui ZK, Kim S, Baljon JJ, Wu BM, Aghaloo T, Lee M. Microporous methacrylated glycol chitosan-montmorillonite nanocomposite hydrogel for bone tissue engineering. *Nat Commun*. 2019 Aug 6; 10(1):3523. <https://doi.org/10.1038/s41467-019-11511-3>
- [9]. Vieira JN, Posada JJ, Rezende RA, Sabino MA. Starch and chitosan oligosaccharides as interpenetrating phases in poly (N-isopropylacrylamide) injectable gels. *Mater Sci Eng C Mater Biol Appl*. 2014 Apr 1; 37:20-7. <https://doi.org/10.1016/j.msec.2013.12.005>
- [10]. Barbon S, Contran M, Stocco E, Todros S, Macchi V,

- Caro RD, Porzionato A. Enhanced biomechanical properties of polyvinyl alcohol-based hybrid scaffolds for cartilage tissue engineering. *Processes*. 2021 Apr 21; 9(5):730. <https://doi.org/10.3390/pr9050730>
- [11]. Romanczuk-Ruszk E, Sztorch B, Pakuła D, Gabriel E, Nowak K, Przekop RE. 3D printing ceramics—materials for direct extrusion process. *Ceramics*. 2023 Feb 1;6(1):364-85. <https://doi.org/10.3390/ceramics6010022>
- [12]. Colmenares LBH, Nejati M, Fang Y, Guo B, Jiménez-Quero A, Capezza AJ, Sabino MA. New sources of genipin-rich substances for crosslinking future manufactured bio-based materials. *RSC Sustain*. 2024;2(1):125-138. <https://doi.org/10.1039/D3SU00303E>
- [13]. Sabino MA, Garcia RA. Synthesis and characterization of S-IPN hydrogels of chitosan/PVA/PNIPAm to be used in the design of nucleus pulposus prosthesis. *Int J Adv Med Biotechnol*. 2020; 3(1):2-15. <https://doi.org/10.25061/ijamb.v3i1.30>
- [14]. ASTM International. Standard Practice for Assessment of Hemolytic Properties of Materials. ASTM F756-17. West Conshohocken, PA: ASTM International; 2017. 6p. <https://doi.org/10.1520/F0756-17>
- [15]. Nalezinková M. In vitro hemocompatibility testing of medical devices. *Thromb Res*. 2020 Nov; 195:146-150. <https://doi.org/10.1016/j.thromres.2020.07.027>
- [16]. Peñaranda JE, Sabino MA. Effect of the presence of lignin or peat in IPN hydrogels on the sorption of heavy metals. *Polym Bull*. 2010; 65:495-508. <https://doi.org/10.1007/s00289-010-0264-3>
- [17]. Ferreira KN, Girón JB, Gomes GH, Rodas AC, da Silva JV, Daguano JK, Sabino MA. Innovative thermosensitive alginate bioink combining cations for enhanced 3D extrusion bioprinting for tissue engineering. *Bioprinting*. 2024 Jun 1; 39: e00340. <https://doi.org/10.1016/j.bprint.2024.e00340>
- [18]. Mukasheva F, Moazzam M, Yernaimanova B, Shehzad A, Zhanbassynova A, Berillo D, Akilbekova D. Design and characterization of 3D printed pore gradient hydrogel scaffold for bone tissue engineering. *Bioprinting*. 2024 Jun 1; 39: e00341. <https://doi.org/10.1016/j.bprint.2024.e00341>
- [19]. Ziaie B, Velay X, Saleem W. Advanced porous hip implants: A comprehensive review. *Heliyon*. 2024 Sep 14;10(18): e37818. <https://doi.org/10.1016/j.heliyon.2024.e37818>
- [20]. Gallardo MGC, Barbosa RC, Fook MVL, Sabino MA. Síntesis y caracterización de un novedoso biomaterial a base de quitosano modificado con aminoácidos. *Matéria (Rio de Janeiro)*. 2019; 24. <https://doi.org/10.1590/S1517-707620190003.0710>
- [21]. Dixit K, Gupta P, Kamle S, Sinha N. Structural analysis of porous bioactive glass scaffolds using micro-computed tomographic images. *J Mater Sci*. 2020 Sep; 55:12705-24. <https://doi.org/10.1007/s10853-020-04850-w>
- [22]. Agarwal G, Agrawal AK, Fatima A, Srivastava A. X-ray tomography analysis reveals the influence of graphene on porous morphology of collagen cryogels. *Micron*. 2021 Nov 1; 150:103127. <https://doi.org/10.1016/j.micron.2021.103127>
- [23]. Nalezinková M. In vitro hemocompatibility testing of medical devices. *Thromb Res*. 2020 Nov 1; 195:146-50. <https://doi.org/10.1016/j.thromres.2020.07.027>
- [24]. Ran J, Xie L, Sun G, Hu J, Chen S, Jiang P, Shen X, Tong H. A facile method for the preparation of chitosan-based scaffolds with anisotropic pores for tissue engineering applications. *Carbohydr Polym*. 2016; 152:615-23. <https://doi.org/10.1016/j.carbpol.2016.07.054>
- [25]. Bi L, Cao Z, Hu Y, Song Y, Yu L, Yang B, Mu J, Huang Z, Han Y. Effects of different cross-linking conditions on the properties of genipin-cross-linked chitosan/collagen scaffolds for cartilage tissue engineering. *J Mater Sci Mater Med*. 2011; 22:51-62. <https://doi.org/10.1007/s10856-010-4177-3>
- [26]. Choi SW, Zhang Y, Xia Y. Three-dimensional scaffolds for tissue engineering: the importance of uniformity in pore size and structure. *Langmuir*. 2010; 26(24):19001-6. <https://doi.org/10.1021/la104206h>
- [27]. Banerjee S, Ray S, Maiti S, Sen KK, Bhattacharyya UK, Kaity S, Ghosh A. Interpenetrating Polymer Network (IPN): a novel biomaterial. *Int J Appl Pharm*. 2010; 2(1):28-33.
- [28]. Ghafar A, Parikka K, Haberthür D, Tenkanen M, Mikkonen KS, Suuronen JP. Synchrotron microtomography reveals the fine three-dimensional porosity of composite polysaccharide aerogels. *Materials*. 2017 Jul 28; 10(8):871. <https://doi.org/10.3390/ma10080871>
- [29]. Murab S, Gupta A, Włodarczyk-Biegun MK, Kumar A, van Rijn P, Whitlock P, Han SS, Agrawal G. Alginate based hydrogel inks for 3D bioprinting of engineered orthopedic tissues. *Carbohydrate Polymers*. 2022 Nov 15; 296:119964. <https://doi.org/10.1016/j.carbpol.2022.119964>

- [30]. Jamali SA, Mohammadi M, Saeed M, Haramshahi SM, Shahmahmoudi Z, Pezeshki-Modaress M. Biomimetic fiber/hydrogel composite scaffolds based on chitosan hydrogel and surface modified PCL chopped-microfibers. *Int J Biol Macromol.* 2024 Oct 1; 278:134936. <https://doi.org/10.1016/j.ijbiomac.2024.134936>
- [31]. Liu B, Chen K. Advances in Hydrogel-Based Drug Delivery Systems. *Gels.* 2024 Apr 13; 10(4):262. <https://doi.org/10.3390/gels10040262>
- [32]. Yin S, Wu H, Huang Y, Lu C, Cui J, Li Y, Xue B, Wu J, Jiang C, Gu X, Wang W. Structurally and mechanically tuned macroporous hydrogels for scalable mesenchymal stem cell-extracellular matrix spheroid production. *Proc Natl Acad Sci U S A.* 2024 Jul 9; 121(28). <https://doi.org/10.1073/pnas.2404210121>
- [33]. Zeltinger J, Sherwood JK, Graham DA, Mueller R, Griffith LG. Effect of pore size and void fraction on cellular adhesion, proliferation, and matrix deposition. *Tissue Eng.* 2001; 7(5):557-72. <https://doi.org/10.1089/107632701753213183>
- [34]. Wu X, Huo Y, Ci Z, Wang Y, Xu W, Bai B, Hao J, Hu G, Yu M, Ren W, Zhang Y. Biomimetic porous hydrogel scaffolds enabled vascular ingrowth and osteogenic differentiation for vascularized tissue-engineered bone regeneration. *Appl Mater Today.* 2022 Jun 1; 27:101478. <https://doi.org/10.1016/j.apmt.2022.101478>
- [35]. Xu Z, Li J, Zhou H, Jiang X, Yang C, Wang F, Pan Y, Li N, Li X, Shi L, Shi X. Morphological and swelling behavior of cellulose nanofiber (CNF)/poly (vinyl alcohol) (PVA) hydrogels: poly(ethylene glycol) (PEG) as porogen. *RSC Adv.* 2016; 6:43626-33. <https://doi.org/10.1039/C6RA03620A>
- [36]. Olăreț E, Stancu IC, Iovu H, Serafim A. Computed tomography as a characterization tool for engineered scaffolds with biomedical applications. *Materials.* 2021 Nov 10; 14(22):6763. <https://doi.org/10.3390/ma14226763>
- [37]. Zoetebier B, Schmitz TC, Ito K, Karperien M, Tryfonidou MA, Paez JI. Injectable hydrogels for articular cartilage and nucleus pulposus repair: status quo and prospects. *Tissue Eng Part A.* 2022 Jun 1; 28(11-12):478-99. <https://doi.org/10.1089/ten.tea.2021.0226>
- [38]. Sabino MA, Garcia RA. Synthesis and characterization of S-IPN hydrogels of chitosan/PVA/PNIPAm to be used in the design of nucleus pulposus prosthesis. *Int J Adv Med Biotechnol.* 2020; 3(1):2-15. <https://doi.org/10.25061/ijamb.v3i1.30>
- [39]. Wang T, Turhan M, Gunasekaran S. Selected properties of pH-sensitive, biodegradable chitosan-poly(vinyl alcohol) hydrogel. *Polym Int.* 2004; 53:911-8. <https://doi.org/10.1002/pi.1461>
- [40]. Baker JP, Stephens DR, Blanch HW, Prausnitz JM. Swelling equilibria for acrylamide-based polyampholyte hydrogels. *Macromolecules.* 1992 Mar; 25(7):1955-8. <https://doi.org/10.1021/ma00033a019>
- [41]. Boyd LM, Carter AJ. Injectable biomaterials and vertebral endplate treatment for repair and regeneration of the intervertebral disc. *Eur Spine J.* 2006 Aug; 15 Suppl 3. <https://doi.org/10.1007/s00586-006-0172-2>
- [42]. Longmi F, Tan YC, Liang HC. In vitro evaluation of a chitosan membrane cross-linked with genipin. *J Biomater Sci Polym Ed.* 2001; 12(8):835-50. <https://doi.org/10.1163/156856201753113051>
- [43]. J. Anderson JM. Biological responses to materials. *Annu Rev Mater Res.* 2001; 31:81-110. <https://doi.org/10.1146/annurev.matsci.31.1.81>
- [44]. Zhang JT, Cheng SX, Zhuo RX. Poly (vinyl alcohol)/poly (N-isopropylacrylamide) semi-interpenetrating polymer network hydrogels with rapid response to temperature changes. *Colloid Polym Sci.* 2003; 281:580-3. <https://doi.org/10.1007/s00396-002-0829-2>
- [45]. Chau M, De France KJ, Kopera B, Machado VR, Rosenfeldt S, Reyes L, et al. Composite hydrogels with tunable anisotropic morphologies and mechanical properties. *ACS Appl Mater Interfaces.* 2016; 28(10):3406-15. <https://doi.org/10.1021/acs.chemmater.6b00792>
- [46]. Wang B, Wu X, Li J, Hao X, Lin J, Cheng D, Lu Y. Thermosensitive behavior and antibacterial activity of cotton fabric modified with a chitosan-poly (N-isopropylacrylamide) interpenetrating polymer network hydrogel. *Polymers.* 2016; 8:1-11. <https://doi.org/10.3390/polym8040110>
- [47]. Desai LS, Lister L. Biocompatibility safety assessment of medical devices: FDA/ISO and Japanese guidelines. *Toxikon Corp.* 2016; 1-19.
- [48]. Sun K, Li ZH. Preparations, properties and applications of chitosan based nanofibers fabricated by electrospinning. *Express Polym Lett.* 2011 Apr 1; 5(4):342-61. <https://doi.org/10.3144/expresspolymlett.2011.34>
- [49]. Mohebbi S, Nezhad MN, Zarrintaj P, Jafari SH, Gholizadeh SS, Saeb MR, Mozafari M. Chitosan in biomedical engineering: a critical review. *Curr Stem Cell Res Ther.* 2019 Feb 1; 14(2):93-116. <https://doi.org/10.2174/1574888X13666180912142028>

- [50]. Qi Y, Jiang X, Meng Z, Wu X. Modified chitosan thermosensitive hydrogel enables sustained and efficient anti-tumor therapy via intratumoral injection. *Carbohydr Polym.* 2016; 144:245-53. <https://doi.org/10.1016/j.carbpol.2016.02.059>
- [51]. Baxter A, Dillon M, Taylor KDA. Improved method for I.R. determination of the degree of N-acetylation of chitosan. *Int J Biol Macromol.* 1992; 14:166-9. [https://doi.org/10.1016/S0141-8130\(05\)80007-8](https://doi.org/10.1016/S0141-8130(05)80007-8)
- [52]. Chiellini F, Ottenbrite RM, Chiellini E, Dash M. Chitosan: a versatile semi-synthetic polymer in biomedical applications. *Prog Polym Sci.* 2011; 36:981-1014. <http://dx.doi.org/10.1016/j.progpolymsci.2011.02.001>

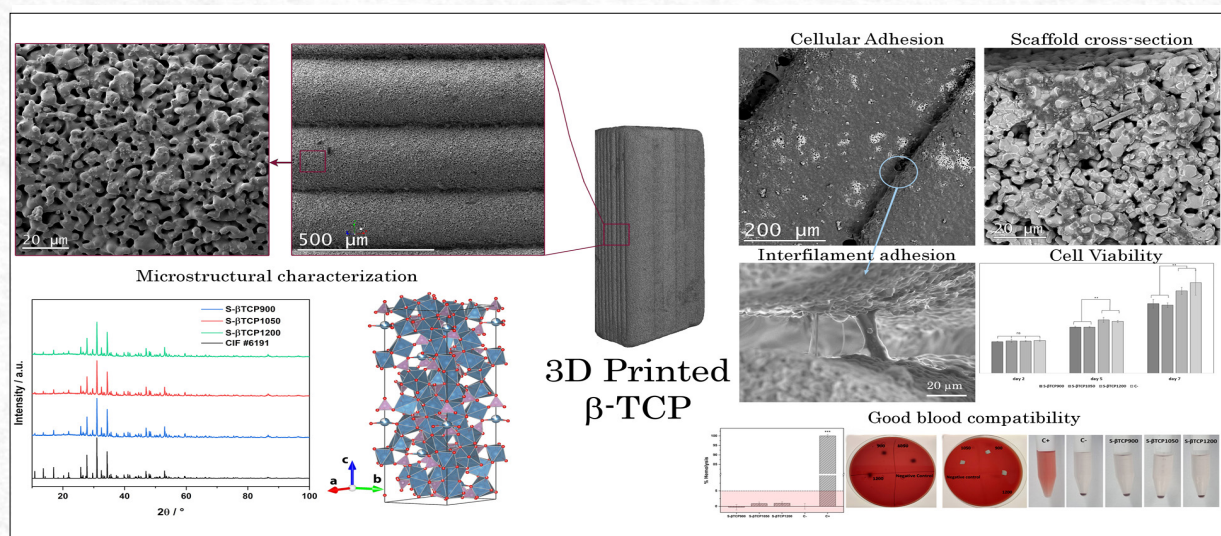


Characterization of 3D-Printed β -TCP Scaffolds with Enhanced Microstructure, Mechanical Properties, and Cell Compatibility

G.H.M. Gomes¹; J. K.M.B. Daguano²; J.G. Bastidas²; K.N. Ferreira³; P.H.J.O. Limirio⁴; P. Dechichi⁴; L.E. Carneiro-Campos⁵

*Corresponding author: E-mail address: gustavohmg@unifei.edu.br

Received: October 2024; Accepted: December 2024.



Abstract: Achieving bone regeneration in large defects caused by trauma, pathology and atrophy is a challenge. Innovative implant materials are emerging as alternatives to autografts in regenerative medicine. 3D-printed β -tricalcium phosphate (β -TCP) scaffolds have emerged as a promising solution for bone tissue replacement, offering patient-specific implants without relying on donors or transplantation. There are many open questions that need to be addressed before they can be used on a large scale. The analysis of sintering temperatures and the different crystalline phases, the in-depth evaluation of the microstructure and its biological response, as well as the assessment of suitable mechanical properties are some of these. The present study carried out a comprehensive characterization of the microstructure of commercial 3D-printed β -TCP using X-ray diffraction coupled with Rietveld refinement, X-ray microtomography and scanning electron microscopy. In addition, blood and cell compatibility tests were carried out using MG63 cells. The imaging techniques revealed the influence of the sintering treatment on the microstructure, resulting in an increase in the average pore size, efficient coalescence between particles and a shrinkage effect at higher temperatures. This behavior had a direct impact on the mechanical properties and cell adhesion behavior. Blood compatibility showed no significant differences between all the samples. However, the material sintered at 1200 °C showed better mechanical properties and a better behavior in the adhesion and proliferation of MG63, which were correlated with a higher density, improved mechanical properties and interconnected porosity, which play a key role in improving osteoblastic function.

Keywords: Tricalcium phosphate. Scaffolds. Additive manufacturing. 3D-printing. Structural characterization.

¹Institute of Pure and Applied Sciences, Federal University of Itajubá, Itabira, MG, Brazil.

²Center of Information Technology Renato Archer, Campinas, SP, Brazil.

³University of São Paulo, Pirassununga, Brazil.

⁴Federal University of Uberlândia, Brazil.

⁵Fluminense Federal University, Innovation Agency, Brazil.

Introduction

Medical complications due to trauma, pathology, and bone atrophy are challenges for surgical reconstructions and tissue recovery in cases of extensive damage (critical-size defects)¹. The need for the development of technologies that can reduce the number of surgeries, morbidity, and cost is still an open question².

For many years, the use of autogenous bone tissue remains as gold standard for cranio-maxillo-facial, orthopedic, and dental implant reconstructions³. However, it is usually associated with morbidity, aesthetic, and functional complications⁴.

Macroscopically, bone tissue is made up of two parts: cortical and cancellous bone. The cortical bone is highly dense and is responsible for providing the primary mechanical properties of bone. Its nutrition is ensured by an intricate number of channels containing blood vessels distributed longitudinally and transversely (Haversian canals and Volkmann canals), connected to the inner and outer surfaces of the cortical structure⁵⁻⁷. Cancellous bone is directly immersed in the bone marrow stroma and is composed of several intertwined trabeculae providing sufficient space for the development of bone cells and vascular networks⁸. Moreover, 80% of the bone remodeling processes during life occur in this region⁹.

In recent decades, interest has arisen in bioengineered implants as reliable alternatives to autografts for the recovery of extensive bone damage. Advances in materials and computerized solutions have made it relatively simple to convert tomographic images into implantable scaffolds for bone reconstruction^{10,11}. The technique enables the precise fabrication of customized patient-specific solutions without relying on donor sites or transplantations¹². In this scenario, synthetic 3D-printed bioceramic scaffolds have emerged as viable solutions due to their osteoconductive capacity for bone engineering. The main advantageous features of these biomaterials are: optimized mechanical properties, plasticity, and controlled degradation. In addition, its alloplastic condition does not demonstrate antigenic effects, the possibility of disease transmission, or any other relevant issue to consider^{13,14}.

To achieve the success of 3D-print scaffolds for bone repair, many factors are required, such as physical and chemical characteristics. In addition, the precision of the manufacturing process to produce robust, high-resolution implants is necessary for the stable formation of the bone-implant interface¹⁵. In order, to obtain an accurate response, the scaffolds must be designed to mimic living tissue, improving blood circulation, and cell

colonization, and facilitating the process of bone formation^{16,17}.

The use of 3-D printing technologies for bones^{18,19} and cartilage regeneration are being approached, with good results, using acellular porous scaffolds that do not seem to induce persistent inflammation or an active immune response²⁰⁻²². Among these materials, ceramic composites are the most studied for the development of biofabricated scaffolds for bone engineering, due to the similarity to natural apatites of bone matrix^{23,24}. Due to its osteoconduction capacity, β -tricalcium phosphate (β -TCP) bioceramic has been widely tested as an option for critical-size bone defects²⁵. Even under these conditions, bone remodeling is known to be a complex and highly regulated process. Different molecular activations that control its initiation, progression, and quiescence are still not fully understood²⁶. To achieve this, inks for 3D printing must align not only with biocompatibility but also with printability, which is not easy. For example, thermoplastic inks' high melting temperatures used in traditional 3D printing are a challenge to overcome²⁷. High temperatures result in the formation of secondary phases and highly crystalline surfaces, while lower temperatures diminish bending strength and the arrangement of the material particles, thereby limiting native cells and local response for bone regeneration^{28,29}. Recognizing the physicochemical processes and their relevance in the crystal arrangement of the biomimetic calcified matrix, transcribing this information to the signaling network of gene activation, and triggering a remodeling process is what is expected when alloplastic graft materials are used³⁰.

Bioceramic inks, incorporating β -TCP and fatty acids, have been successfully used in the development of 3D printing scaffolds. The remodeling capacity and regeneration of native bone have been demonstrated *in vivo* models²⁹. Slots *et al.* showed that these scaffolds retained their pre-sintering shape and chemical composition after sintering, exhibiting clinically relevant mechanical strength³¹. However, dimensional instability caused by sintering shrinkage is a drawback in bioceramics processing, along with limited dissolution in the body environment³².

The interest increases in the β -TCP scaffolds promoted the arising of several commercial companies, commercializing ready-to-use scaffolds for bone regeneration. For example, the product MyBoneR© (CERHUM company) has recently shown improved bone regeneration capability in large animal models employing 3D gyroid-shaped scaffolds, demonstrating the absence of

toxicity and no side effects on the sheep implant in the femur, demonstrating good reliability when compared with Bio-Oss® bovine standard, readily employed in the literature³³. T&R Biofab also produces polycaprolactone and β -TCP scaffolds and has demonstrated efficient biocompatibility, osteoinductivity, and osteoconductivity³⁴. Ossiform® ApS (Denmark) also produces high-quality β -TCP/fatty acid scaffolds, as green pieces. A recent paper by the company shows that 3D-printed β -TCP scaffolds led to the replacement of vascularized compact bone after six months in mini pigs, leading to excellent osteointegration, with no immune reaction³⁵. However, despite the advances, there are still concerns about the microstructure and the functionality of those employed materials, even by commercialized products. A better understanding of the porosity, mass transfer, and how microstructural properties affect their biocompatibility are largely necessary³⁶. A work by Podgórski et al. showed the importance of tailoring the scaffold's porosity, even using fatty acids and organic content that can act as porogenic agents, leading to an internal structure with connected pores³⁷. Another work by Slavin et al. showed that lower sintering temperatures (~ 600 °C) lead to high cellular stress, contrarily, scaffolds sintered at high temperatures (~1100 °C) showed a morphological change in the particle size and porosity, also leading to improved cellular response, showing only a small amount of cellular stress instances. However, the sintering process at higher temperatures also caused crystal phase transformation, probably leading to the observed instances of acute cellular stress³⁸.

In this sense, this work aims to enhance the understanding of how the physicochemical features of β -TCP 3D-printed scaffolds influence the bone microenvironment. The study employs imaging techniques such as scanning electron microscopy (SEM) and X-ray microtomography (μ CT) to understand how the sintering process affects the total porosity, filament thickness, shrinking process, and mineral density of the scaffolds, compared with the performed mechanical analysis. Moreover, hemocompatibility and biocompatibility tests with MG63 were carried out to understand its biological behavior.

Materials and Methods

In this study, fabricated β -Tricalcium Phosphate (β -TCP) Ossiform™ scaffolds, from Odense, Denmark were used. Twelve rectangular bars (25.0 mm long, 2.0 mm wide, and 2.0 mm thick) and twelve gyroid-shaped discs (6.0 mm in diameter and 2.0 mm in width) were checked using a Digimatic caliper (Mitutoyo Absolute Digimatic Caliper,

Tokyo, Japan). The samples were prepared using a β -TCP powder with stearic acid to form a paste, then the ink was transferred to a syringe and the scaffolds were printed using an extrusion process. More information about the methodology used by Ossiform™ can be found in previous papers^{25,31,35}. The pre-sintering stage was carried out for 1 hour at 400 °C, with a cooldown of 2h before sintering. Then, the samples were sintered at 900, 1050, and 1200 °C in triplicate, in atmospheric air, for 16 hours. The samples were named S- β TCP900, S- β TCP1050, and S- β TCP1200, respectively.

X-ray diffraction (XRD) and Rietveld analysis

X-ray diffraction analysis was conducted to determine the crystalline phase of the samples, using a SHIMADZU 7000 with a theta-2theta configuration, Cu radiation ($K\alpha = 1.5406 \text{ \AA}$) with a voltage of 40 kV and a current of 30 mA. A divergence and scatter slit of 1.00° , with a step size of 0.02° , collection time of 1.2s, and a 2θ range of $10^\circ - 100^\circ$. The Rietveld refinement analysis was performed using the GSAS/EXPGUI free software³⁹ and the standard Crystallographic Information File (CIF) from ICSD with code #6191. This analysis aimed to obtain information on the $\text{Ca}_3(\text{PO}_4)_2$ crystal structure, including phase, lattice parameters, calculated density, occupation of Ca(4) site, and position of atoms in the lattice. The VESTA software was used for structure visualization and plotting⁴⁰.

FTIR functional group analysis

The identification of functional groups in the samples was carried out using Fourier transform infrared (FTIR) analysis on a Perkin Elmer Infrared Spectrometer Spectrum 100. The FTIR scans covered a range of 400-4000 cm^{-1} wavenumber, and an average of 16 scans were recorded with a spectral resolution of 4 cm^{-1} , using attenuated total reflectance (ATR) mode. This method allowed for the precise identification of functional groups present in the samples.

Scanning electron microscopy (SEM)

The scanning electron microscopy (SEM) analysis was carried out in a FEG-SEM TESCAN MIRA3 XMU equipment employing the secondary electron (SE) detector at an acceleration voltage of 1.5 kV, with a spot size of 5.2 nm, and ultra-high vacuum (UHV). The tree samples in the study were analyzed on a top view of the printed filament, a close view of the particles on the top, and the fracture of the materials. All the samples were coated with gold nanoparticles to avoid charging effects. The equipment employed for the gold coating is a Sputter Coater from BALTEC, model BALZERS – SCD 050, with the

parameters of 50 mA of current, sputtering time of 30 seconds, and 0.05 mbar of working pressure, leading to a 10 nm gold deposition film.

X-Ray microtomography

To investigate the sintering process of 3D-printed scaffolds and determine porosity parameters, X-ray microtomography (μ CT) was employed. The SKYSCAN 1272 CMOS Edition from Bruker was used for all sample imaging, and images were acquired under consistent conditions. The acquisition parameters for the 2048 x 2048 pixel image included flat field correction, a 6 μ m pixel size, a Cu 0.11 mm filter, a 16-megapixel camera detector, random movement of 50 pixels, an exposure time of 1073 ms, a voltage of 100 kV, a current of 100 μ A, four-frame averaging, and a rotation step of 0.4° with a half-rotation of 180°. Standard procedures were followed to obtain images free of digital artifacts. Reconstruction and visualization of the 3D images were performed using NRecon and CTvox software provided by Bruker. The Results and Discussion section provides further details regarding the reconstruction methodology. The porosity, pore size distribution, and filament thickness values were obtained using the CTan software. The methodology employed the following steps: Filtering with Anisotropic diffusion in the 2D space with 10 iterations and 15 of gradient threshold, thresholding the images from 66 to 255 gray scale, ROI-shrink-wrap to obtain a region of interest (ROI) that contains all the sample, despeckle to remove black speckles with size lower than 64 voxels, and performing the 3D analysis.

Mechanical Analysis

Uniaxial compression and diametral testing were carried out on an Instron ElectroPuls E3000 testing machine (Instron, Norwood, USA), in ambient conditions, with gyroid-shaped disc designs. The loading rate was 0.5 mm/min until the occurrence of failure. A 5kN load cell was used. Compressive strength values (kgf/cm^2) were calculated by dividing the fracture load (F) by the cross-sectional area and converted into MPa. Diametral tensile strength values (kgf/cm^2) were calculated using the equation:

$$DTS = \frac{2F}{\pi dt}$$

where d is the specimen diameter, and t is the height of the specimen. DTS values were converted in MPa.

Three-point bending test was carried out on an Instron ElectroPuls E3000 testing machine (Instron, Norwood, USA), in ambient conditions. Rectan-

gular bars were checked using a Digimatic caliper (Mitutoyo Absolute Digimatic Caliper, Tokyo, Japan). The bars were placed over two rods approximately 2.0 mm in diameter, with a 16.0-mm span length. A compressive force of 20 kgF load cell was applied in the center of the bars using a piston with 2.0 mm in diameter at a 0.5 mm/min crosshead speed to fracture. The flexural strength was measured as previously cited by Tavares *et al.*⁴¹.

Blood compatibility test

To analyze the compatibility of the biomaterials with blood, the hemolysis assay was performed in duplicate as in previous studies^{29,20}. First, 4 ml of anticoagulated sheep blood was diluted with 5 ml of normal saline 0.9%. For the positive and negative controls, 5 ml of Milli-Q water and 5 ml of normal saline 0.9% were used respectively. Biomaterials of the same size were submerged in tubes with 5 ml of normal saline. Then, 100 μ l of diluted blood was added to each group and incubated at 37 °C for 60 min, followed by centrifugation at 1800 rpm for 10 min. Subsequently, the absorbance of the supernatant was taken at 540 nm in a spectrophotometer (Loccus LMR-96, Brazil). The hemolysis percentage was calculated as follows:

$$\% \text{ Hemolysis} = \frac{A_s - A_{nc}}{A_{pc} - A_{nc}} \times 100\%$$

where A_s is the absorbance of the sample, A_{nc} is the absorbance of the negative control, and A_{pc} is the absorbance of the positive control.

Additionally, the results were confirmed with the hemolysis assay on blood agar, in which blood base media was prepared according to fabricant instructions (HIMEDIA, Ref. MI58-500G). The agar base was cooled to 45 °C and mixed gently with sterile defibrinated sheep blood in a final concentration of 5% (vol/vol). Blood agar was poured into sterile Petri dishes and the scaffold samples were placed on solid agar and incubated at 37 °C for 24 and 48 hours.

Cell adhesion and viability

Scaffold samples were sterilized with 70% alcohol followed by UV light for 30 min at each site in a laminar flow. Then, the scaffolds were placed into 24 well plates, and MG63 cells (human osteosarcoma cell line) were seeded on the sample's upper surface at a cell density of 3500 cells/cm². Cells were cultured in Dulbecco's Modified Eagle's Medium (DMEM, Vitrocell, Ref D0025) supplemented with 10% fetal bovine serum (Vitrocell, Ref S0011), 1% penicillin/streptomycin (Vitrocell) and incubated at 37 °C with 5% CO₂. For assessment of cell adhesion,

the presence of attached cells on the samples was analyzed by SEM 24h after seeding. Then, the samples were washed with phosphate-buffered saline (PBS, pH 7.4), fixed in 10% formaldehyde for 30 min, rinsed in PBS, and dehydrated in ethanol series. The dried samples were metalized with a thin layer of gold. Images were acquired using TESCAN MIRA3 XMU equipment, see section 2.4.

Cell viability was examined with a resazurin-based assay (Sigma, Ref. 263-718-5) in triplicate and following the manufacturer's protocol on days 2, 5, and 7. Cells cultured directly on the 24-well cell culture plate (Kasvi, Ref. K12-O24) were taken as the negative control.

Results and Discussion

Structural and chemical analysis

Figure 1(a) presents the XRD diffractograms for the three scaffolds, and it shows that all samples crystallized in the beta-phase of calcium phosphate without the presence of contaminants (β -TCP or β - $\text{Ca}_3(\text{PO}_4)_2$), independently of the temperature. This behavior is corroborated by a previous study by Jensen *et al.*⁴². Also, the scaffolds indicate a trigonal crystal system with a rhombohedral lattice, space group R3c, and international number 161. The atoms occupy the 6a and 18b Wyckoff positions, with different occupancy for some Ca, O, and P

atoms. Figure 1(b) shows the crystalline structure of the material, with Ca^{2+} atoms in disordered octahedrons sharing an oxygen atom with PO_4^{3-} tetrahedral groups in the polyhedral corner. It is known that the partial occupancy and distortions of Ca^{2+} sites alter the occupancy and position of the phosphate groups, thus, altering the densification and properties of the material⁴³. It is also known that β -TCP has five distinct Ca atoms, where the Ca(1), Ca(2), Ca(3), and Ca(5) are been discovered to be fully occupied with one Ca atom (occupancy factor of 1.0), meanwhile, the Ca(4) presents a three-fold coordination with oxygen atoms, leading to tetrahedral coordination, and it also presents a lower occupancy factor around 0.5⁴³. Recently, Sblendorio *et al.* published a paper regarding the structural features of the β -TCP employing atomistic simulation, emphasizing the role of the Ca(4) atoms in the crystal structure. They presented that β -TCP could have seven different unit cell types, varying how many Ca(4) are occupied in the crystal structure⁴⁴. This behavior showed that β -TCP can have a ratio of $\text{Ca}/\text{P} \neq 1.5$, where values above 1.5 mean a higher occupancy of Ca(4) atomic sites, leading to an occupancy above 0.5. To obtain more information about the crystal structure, Rietveld refinement was performed in all the scaffolds. Figures 1(c,d,e) show the Rietveld refinement graphs

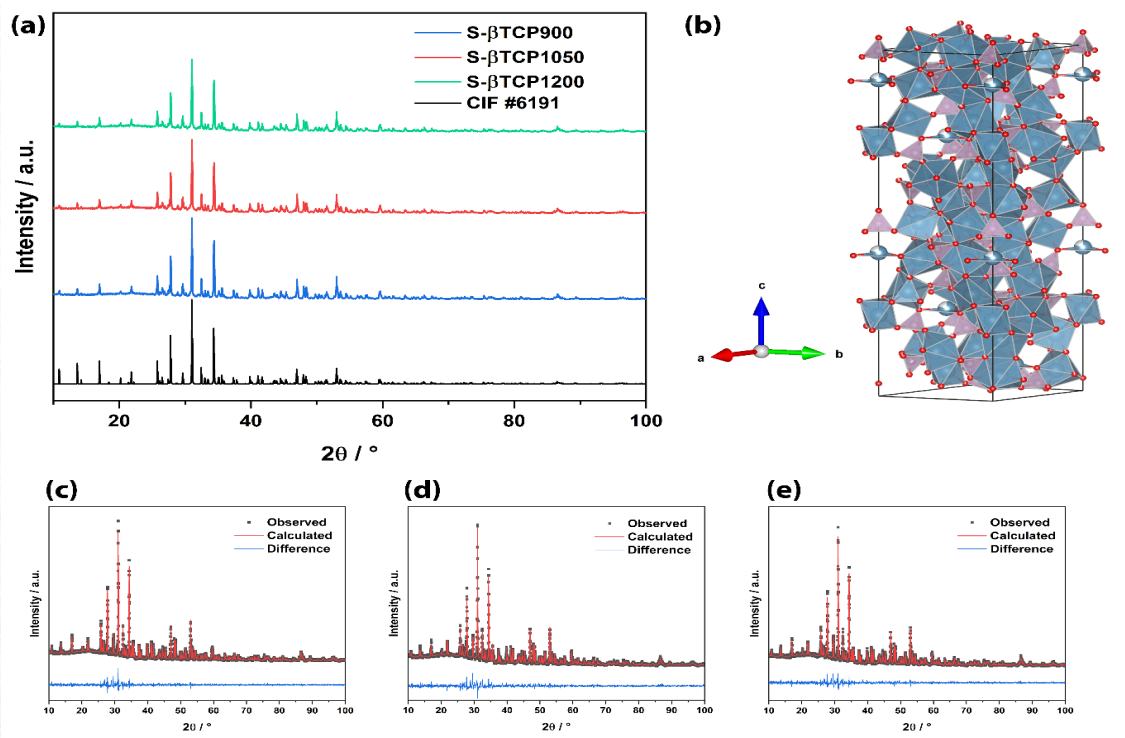


Figure 1 - (a) XRD data from scaffolds and the (b) crystal structure of the Calcium Phosphate - Rietveld refinement graphs of (c) S- β TCP900, (d) S- β TCP1050, and (e) S- β TCP1200 samples.

obtained for the S- β TCP900, S- β TCP1050, and S- β TCP1200 samples, respectively.

The difference curve between the experimental and calculated model shows good confidence in the Rietveld analysis since it appears almost flat for the samples in all the diffractogram regions. Table 1 shows quantitative data obtained through the refinement process, showing values for statistical R coefficients, where all samples presented $X^2 < 2.700$, indicating that the refinement process has chemical and physical meaning⁴⁵. The Rietveld Refinement Data are presented in Supplementary Information. Interestingly, there are no major changes in the lattice parameters, however, it is noticeable significant changes in the Ca(4) occupancy as the sintering temperature increases.

The S- β TCP900 presented a lower Ca(4) occupancy of 0.5942, close to the standard CIF, which led to a Ca/P ratio of 1.513. Meanwhile, the S- β TCP1050 and S- β TCP1200 presented a sharp increase in the Ca(4) occupancy, leading to a higher Ca/P ratio of 1.531 and 1.542, respectively. Sblendorio *et al.* show that a Ca/P ratio higher than 1.500 means that there are more filled Ca(4) sites and the β -TCP has a supercell that is consistent with building blocks of several unit cells with different Ca(4) occupancy, leading to different crystalline structures that can affect its biochemical behavior⁴⁴. Taking this information into account, the S- β TCP900 supercell may be composed of building blocks of three and four filled Ca(4) atomics sites, while the S- β TCP1050 and S- β TCP1200 can be composed of

Table 1 - Quantitative data from the Rietveld refinement of the samples and the standard CIF for comparison.

Sample	Lattice Parameters / Å	Ca(4) occupancy	Ca/P Ratio	Density / g.cm ⁻³	R _F / %	R _p / %	R _{wp} / %	X ²
S- β TCP900	a = b = 10.4231(7) c = 37.360(2)	0.5942	1.513	3.088	8.44	7.85	8.38	2.618
S- β TCP1050	a = b = 10.4196(1) c = 37.350(5)	0.7157	1.531	3.105	8.21	7.47	9.15	2.464
S- β TCP1200	a = b = 10.4233(5) c = 37.36(3)	0.7954	1.542	3.120	8.15	6.61	8.39	2.010
Standard CIF - ICSD #6191	a = b = 10.439(0) c = 37.37(5)	0.4910	1.5000	3.140				

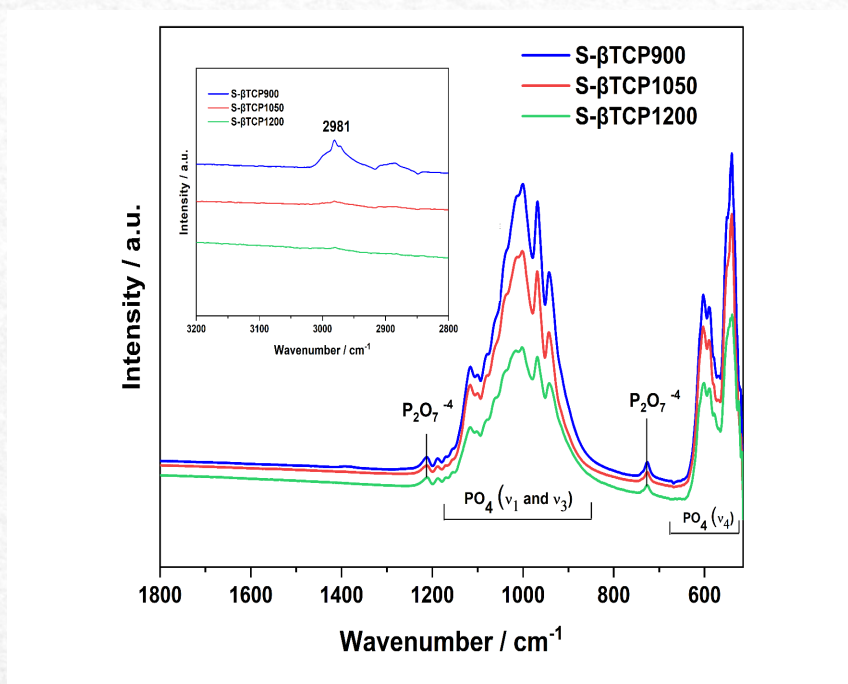


Figure 2 - FTIR spectra of the β -TCP scaffolds.

building blocks of four or five filled Ca(4) sites. These behaviors are closely related to the density of the material and its final structure. It is worth mentioning that this behavior is still undergoing investigation in the literature, and the characteristics of the Ca(4) site cannot be accounted for by employing only one unit cell, but a combination of the seven types found in Sblendorio's work, which could lead to errors in the analysis.

Figure 2 shows the functional groups present in the scaffolds, identified using Fourier-transform infrared (FTIR) spectroscopy. The spectra of the samples exhibited similarities in the functional groups. The ν_3 vibrational mode of the PO_4^{3-} ion was attributed to stretching peaks observed at 1008, 1015, 1080, 1100, and 1115 cm^{-1} . The ν_1 - PO_4 mode was observed at 945 and 970 cm^{-1} , while the ν_4 - PO_4 mode was observed at 605, 592, 552, and 540 cm^{-1} . Changes in the intensity of the stretching peaks were noted with variations in the sintering temperature, consistent with previous findings⁴⁶. Furthermore, less intense peaks were observed at 726 and 1212 cm^{-1} , characteristic of the pyrophosphate group ($\text{P}_2\text{O}_7^{4-}$ species). This observation may be attributed to a non-stoichiometric balance between Ca/P ions in the crystalline structure, which can be related to the Ca(4) atomic site⁴⁷, consistent with the

results obtained from XRD and Rietveld refinement analyses. It is worth mentioning that there is no observation of carbonyl peaks around 1680 cm^{-1} . However, the inset inside Figure 2 presents small intensity vibrations around 2981, 2950, and 2910 cm^{-1} for the S- β TCP900, attributed to the stearic acid of the initial ink. This shows that the initial ink was fully removed during the sintering process of the S- β TCP1050 and S- β TCP1200 samples⁴⁸.

Figure 3 shows the SEM images obtained for the scaffolds. It is clear the changes in the morphology and texture of the 3D-printed scaffolds when the sintering temperature increases, with a smoothing process of the particles on the top of the scaffold filament. It is noticeable that the scaffold filament size shrinks with the thermal treatment, going to 322 ± 14 , 275 ± 13 , and 251 ± 15 μm for the S- β TCP900, S- β TCP1050, and S- β TCP1200 samples, respectively. This information is also presented in Table 2, for comparison purposes of the measured filament size between SEM and μCT analysis. This behavior occurs due to the sintering process and the coalescence between particles, which can be seen in Figures 3(b,e,h), where the S- β TCP900 sample presents detached particles on the surface with a granular morphology, creating a loosely porous network that occurs between

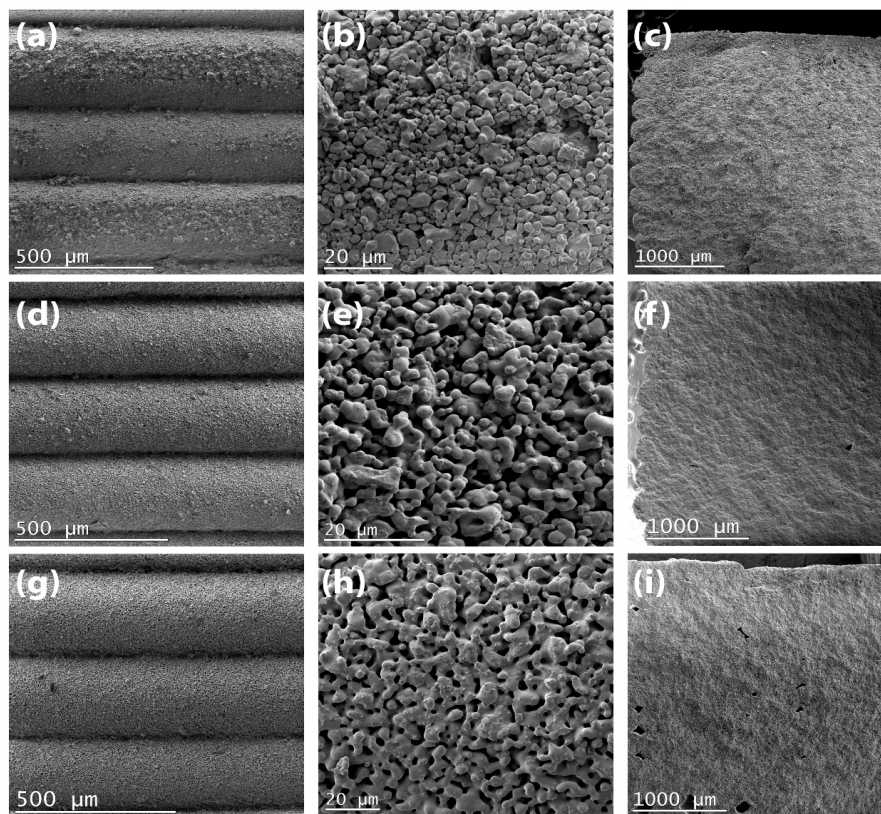


Figure 3 - SEM images of the (a,b,c) S- β TCP900, (d,e,f) S- β TCP1050, and (g,h,i) S- β TCP1200 samples showing the filament top view, filament top view at higher magnification, and side fracture of the scaffolds, respectively.

particles, which do not have strong interaction and coalescence. Meanwhile, the S- β TCP1050 sample presents fewer detached particles and the beginning of coalescence between particles, showing a more efficient sintering process with less granular regions, which directly impacts the mechanical properties, pore size distribution, surface morphology, and cell adhesion and viability properties⁴⁹. Finally, the S- β TCP1200 sample shows a complete coalescence between particles and an optimal sintering process, where the particles are completely connected and it creates a small porous network, with some pores ranging between 1 and 30 μm . However, Figures 3(c, f, i) shows the side view of the scaffold fracture, presenting an interesting behavior. The sintering temperature increase caused the formation of big pores around 100 – 300 μm inside the structure, correlated with the coalescence between particles, that start to bind together, creating empty spaces in the 3D printed structure. This behavior is very important for biomaterial, where a previous study shows the importance of a range of pore sizes to improve cell growth on 3D printed scaffolds, where small pores (1 – 30 μm) are important for mass and nutrient transfer, and bigger pores are good for cell attachment⁵⁰.

To study the sintering process using the μCT technique, it is necessary to follow a strict method of reconstruction due to the lack of information about this methodology in the literature⁵¹. A work by Cengiz *et al.* shows the importance of giving the most information possible to reproduce μCT analysis, and that there is a small number of papers reporting the mineral density of ceramic materials⁵². However, past works presented a way to obtain information about the mean values of greyscale pixels for the volumetric reconstruction, showing the possibilities of obtaining information about the densification of biomaterials⁵³. In this sense, we used the same histogram start and end points of the 16-bit TIFF grayscale images to select the same pixels for all scaffolds during the NRecon reconstruction, ranging the attenuation coefficient from 0.013647 to 0.034850, and the same parameters for smoothing (value = 3), beam-hardening correction (10%), a rectangular region of interest (ROI), and image rotation when needed. This gave us the confidence to analyze the materials in the same pixel density and range, between 0 to 65434 gray levels (0 the pure black and 65434 pure white color), thus providing confidence in analyzing and comparing the materials in this study. We filtered the transfer function in the opacity channel to show only the pixels with grayscale values between 45200 – 65434, and applied it to all analyses, providing information about the dense

regions in the scaffolds.

Figure 4 presents the volumetric reconstruction of the scaffolds, showing the whole sample (Figures 4(a,d,g)) with no transfer function editing, and the transversal and longitudinal view of the samples with the applied transfer function mentioned before. The S- β TCP1200 and S- β TCP1050 possess more dense regions than S- β TCP900, which is correlated to the sintering process of the materials. The S- β TCP900 presents dense regions around the edges of the piece, showing that the sintering process was not that efficient, and the dense regions respect the usual heat flow during the sintering process, coming out of the edges into the core of the sample, and it is clear in Figures 4(b,c) that in the center of the sample, there are no dense particles. Meanwhile, the samples S- β TCP1050 and S- β TCP1200 present more dense particles, thus showing that the sintering process is more efficient at temperatures higher than 1050 $^{\circ}\text{C}$, corroborating SEM images.

Table 2 presents the results of the quantitative analysis conducted using μCT . It was observed that the filament size decreased with increasing sintering temperature, indicating a tendency for contraction of the β -TCP ceramic. The porosity is also affected by the sintering process, showing a decrease in the total porosity. The S- β TCP900 shows the highest porosity values, with a small value of mean pore size. The closure of some of those pores occurs for the S- β TCP1050 and S- β TCP1200 samples, leading to a sharp increase in the mean pore size.

To further assess the behavior of pore size increase, Figure 5 illustrates the pore size distribution derived from quantitative analysis using micro-CT data. The S- β TCP900 sample exhibits over 50% of its pores within the range of 6 to 30 μm . This range corresponds to the gaps observed between granular particles on the material's surface, as depicted in Figure 3(b, e, h). It is noteworthy that the frequency of smaller pore sizes decreases with the rise in sintering temperature. Specifically, the percentage of pores ranging from 6 to 30 μm decreases to approximately 13% for S- β TCP1050 and 8% for S- β TCP1200. The emergence of larger pores contributes to a more uniform distribution of pore sizes. Figures 5(b, c) illustrate a higher frequency of pores with sizes exceeding 100 μm . Interestingly, S- β TCP1200 is the sole sample surpassing the small porosity region, featuring two distinct regions with a Gaussian behavior labeled as Region 1 (red) and Region 2 (green). These regions significantly contribute to the mean pore size compared to the region of pores < 30 μm . This behavior is associated with the formation of larger pores observed in Figures 3(c, f, i). The formation of larger pores can be

attributed to the removal of stearic acid, as shown in Figure 2, during the S- β TCP1050 and S- β TCP1200 sintering processes. This removal process may act as a porogen agent^{54,55}, creating a macroporous structure and different porous regions, which can be beneficial for cell adhesion and proliferation³¹.

Recently, a work by Ossiform[®] also showed a microstructural evaluation of 3D-printed β -TCP scaffolds, corroborating the results presented in our work, such as small pores generated by the sintering process and variations depending on the thermal treatment of the samples⁵⁶.

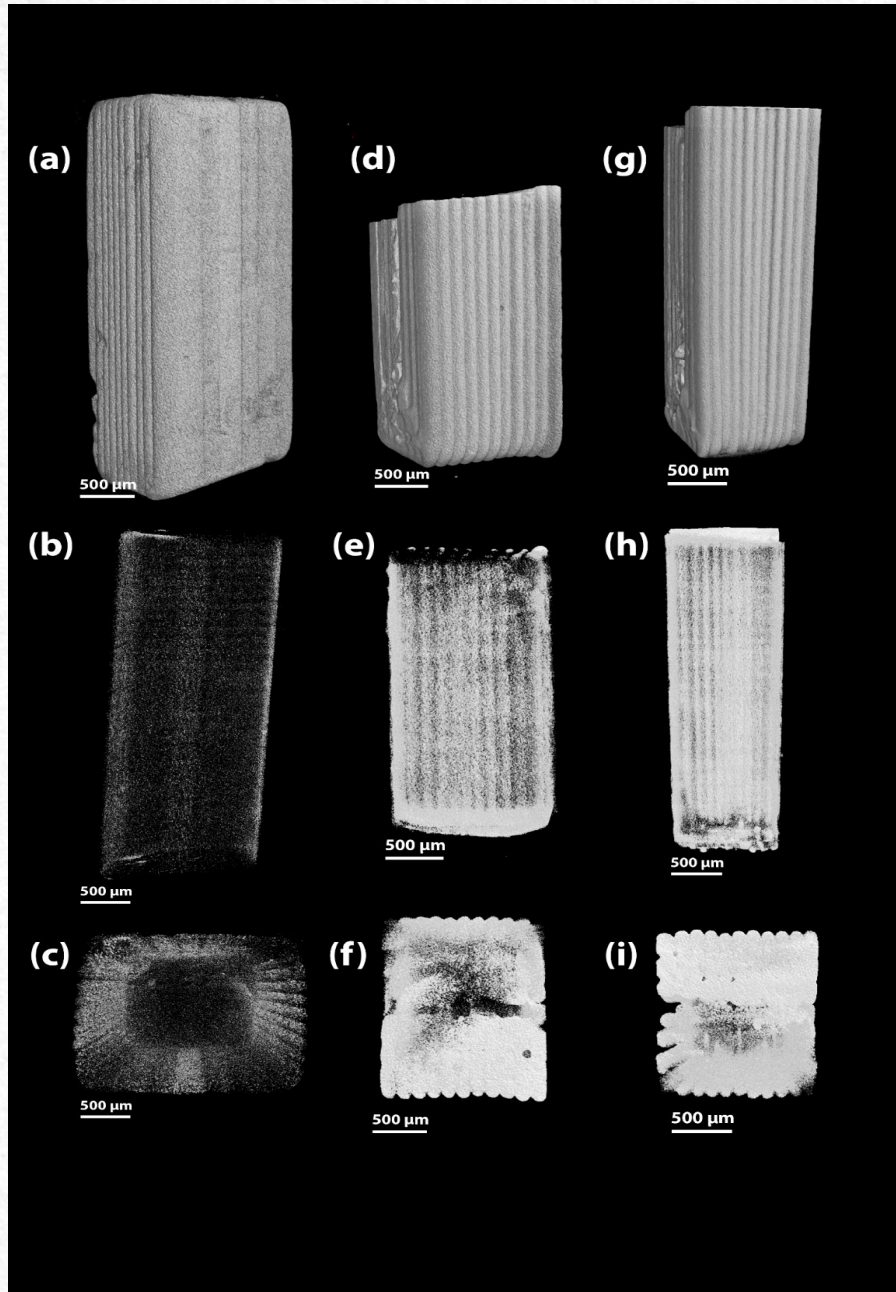


Figure 4 - X-ray μ CT reconstructed images showing the whole piece for (a) S- β TCP900, (d) S- β TCP1050, and (g) S- β TCP1200 samples. Images of the transversal and longitudinal directions, respectively, of the transfer function-filtered scaffolds for the (b,c) S- β TCP900, (e,f) S- β TCP1050, and (h, i) S- β TCP1200.

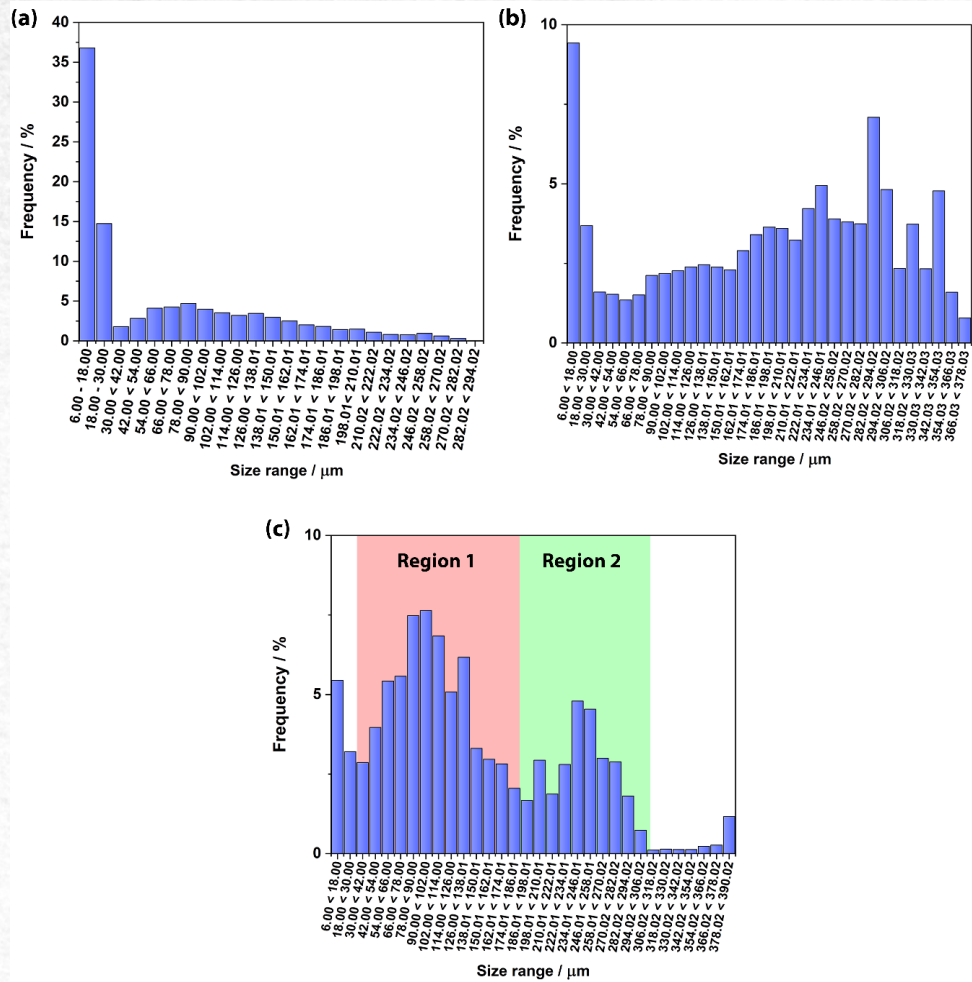


Figure 5 - Pore size distribution of the (a) S- β TCP900, (b) S- β TCP1050, and (c) S- β TCP1200. The quantitative data was obtained through microCT analysis.

Mechanical Analysis

The S- β TCP1200 presented the highest flexural strength values (22.2 ± 4.2 MPa) when evaluated in the three-point bending test, followed by the S- β TCP1050 (10.8 ± 0.6) and then the S- β TCP900 (1.6 ± 1.9) ($p < 0.001$), Figure 6. Regarding the axial compressive test, the same behavior was observed. The S- β TCP1200 (46.0 ± 4.8 MPa) showed higher strength when compared to S- β TCP1050 (13.8 ± 1.7) and S- β TCP900 (2.9 ± 1.0) ($p < 0.001$). These results can be influenced by micropores contained in scaffolds, with a total porosity varying from ~17% (for S- β TCP900) to ~3% (for S- β TCP1200) (Table 2).

The values are comparable with those achieved with 3D printed TCP sintered at 1100°C (11.6 ± 2.1 MPa). However, it is important to highlight that because of an increase of 100°C in sintering temperature, we found the average strength of the sintered samples to be 46 MPa (S- β TCP1200), this was significantly higher than the 11 MPa found in a previously published report for the same material⁵⁷.

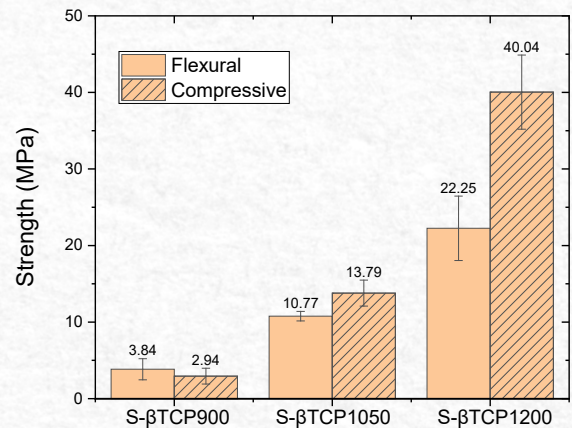


Figure 6 - (a) Flexural strength and (b) axial compressive for S- β TCP900, S- β TCP1050, and S- β TCP1200. Graphs show average values \pm standard deviation.

Table 2 - Porosity parameters and filament thickness measurements obtained by μ CT analysis for β -TCP scaffolds sintered at different temperatures.

Sample	Filament thickness ¹ / μm	Filament thickness ² / μm	Open Porosity / %	Closed Porosity / %	Total Porosity / %	Mean Pore size / μm
S- β TCP900	300 \pm 23	322 \pm 14	14.64	2.31	16.95	17 \pm 7
S- β TCP1050	269 \pm 17	275 \pm 13	3.66	0.53	4.19	196 \pm 107
S- β TCP1200	225 \pm 23	251 \pm 15	2.44	0.39	2.83	139 \pm 86

Blood compatibility tests

The hemolysis test is based on the degree of erythrocyte lysis when the biomaterial comes into contact with these cells *in vitro*. Then, a lower hemolysis percentage suggests good blood compatibility. Figure 7a illustrates the hemolysis percentage of the biomaterials. As expected, the biomaterials had a hemolysis percentage similar to the negative control, suggesting that these were highly hemocompatible (Figure 7b). Also, no hemolysis halo was detected on blood agar after 24 and 48 hours (see Figure 7 c-d), confirming the previous results. Then, the sintering temperature of 3D biomaterials did not interfere with the scaffolds' blood compatibility.

Cell adhesion and viability

The SEM analysis was performed 24h after cell seeding to verify adhesion on the scaffolds and employing the backscattered electron (BSE) detector, where regions with higher atomic numbers (such as calcium and phosphorous) will appear brighter, while a lower atomic number appears darker in the image (such as cell-matrix). Figure 8(a-f) shows that cells were able to adhere to the scaffold's surface. Also, a higher cell density was seen on the S- β TCP1200 (Figure 8f), suggesting an excellent interaction between cells and scaffolds. Moreover, MG63 cells presented a typical morphology with elongated cell processes in the S- β TCP1200, while S- β TCP900 and S- β TCP1050

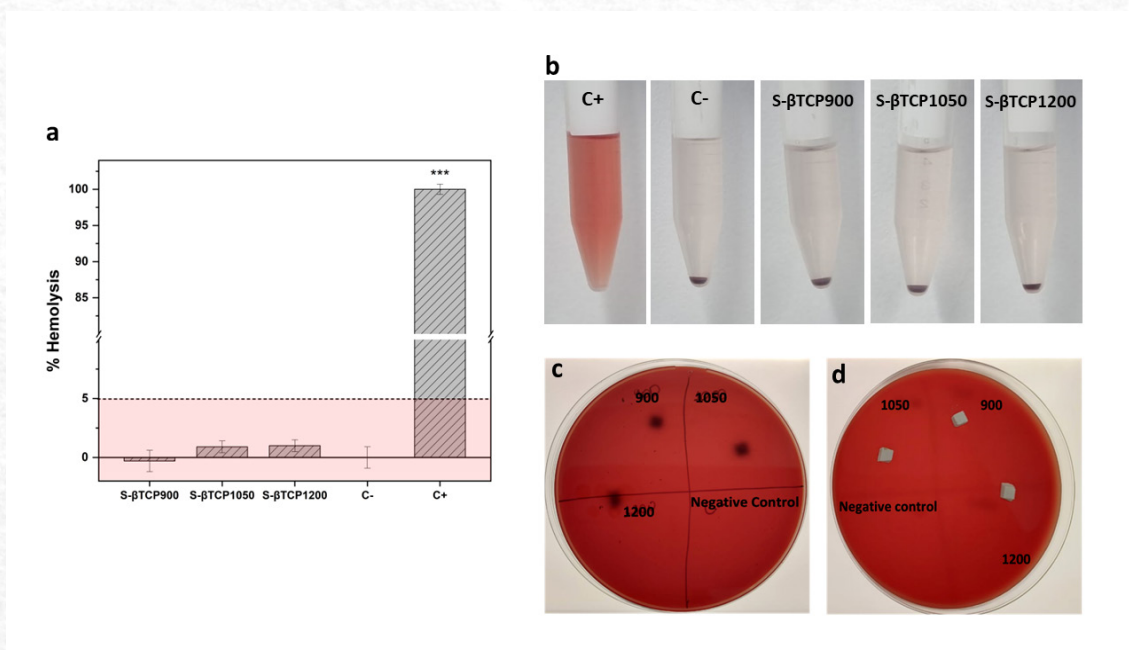


Figure 7 - Blood compatibility test. (a) Hemolysis percentage of scaffolds. (b) Illustration of hemolysis assay. (c) Hemolysis on blood agar after 24h, back of the Petry dish. (d) Hemolysis on blood agar after 48h, front of the Petry dish.

exhibited rounded morphology. Mealy *et al.* found that sintering temperatures are associated with surface topography, described as wavelength (λ), thereby higher sintering temperatures providing a larger basal contact area with more adhesion sites for cells⁵⁸. Conversely, they suggested that the granular surface topography obtained at low sintering temperatures provides insufficient contact area for cell attachment. Similarly, Dulgar *et al.*⁵⁷ suggested that ceramics with higher grain sizes obtained at higher sintering temperatures led to enhanced cell adhesion and proliferation. Then, in our study, the coalescence between particles in S- β TCP1200 could explain better cell adhesion due to the presence of a larger basal contact area for cells.

Regarding cell viability, Figure 9 shows no difference between the S- β TCP1200 group and the negative control at each time. However, a significant difference between the both groups and, S- β TCP900 and S- β TCP1050 was seen on days 5 and 7. These results could be explained due to reduced cell adhesion observed on S- β TCP900 since cell adhesion is crucial for subsequent cell functions such as proliferation, and protein synthesis. Additionally, the improved mechanical properties with higher scaffold density and strength in the S- β TCP1200 may contribute to these differences. Previous studies showed that higher mechanical properties enhance osteoblastic function^{52,53}. This enhancement could be attributed to the cells' ability to sense their extracellular

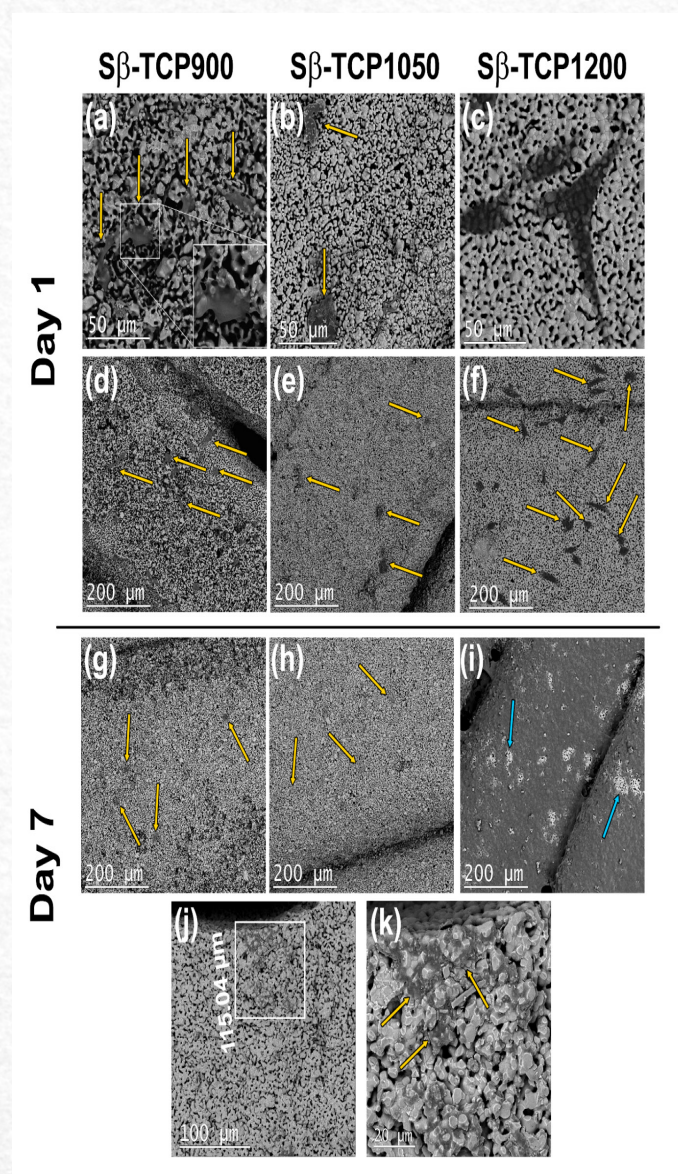


Figure 8 - Backscattered Electron - SEM images of the top view of scaffolds (S- β TCP900, S- β TCP1050 and S- β TCP1200) cultivated with cells at (a-f) day 1 and (g-i) day 7. The (j) cross-section cut of the S- β TCP1200 and (k) a higher magnification of the squared region of (j). Yellow arrows indicate the cells and blue arrows indicate details of the material without cells.

environment mechanosensitive and modulate cell attachment, proliferation, and differentiation based on substrate stiffness^{61,62}. This implies that cells can respond to the mechanical properties of the scaffolds by rearranging cytoskeletal elements and activating mechanotransduction signaling pathways⁶³. Figure 8(g-i) shows SEM images of the scaffolds on day 7, where is possible to see a layer of MG63 cells (dark gray) coating the surface of the scaffold in S- β TCP1200 (Figure 8i), and the blue arrows indicate the areas without cells in light grey. In the rest of the scaffolds, the formation of cell layers was not evident on day 7. Moreover, S- β TCP1200 presented some areas of cell infiltration into the scaffold (around 115 μ m) as is shown in Figure 8 (j-k), probably due to the higher pore size of the scaffold facilitating cell migration. Future studies will explore the impact of different scaffold geometries on the structural and biological properties of 3D-printed β -TCP scaffolds. Additionally, microCT imaging will be employed to analyze in vivo assays, providing detailed insights into scaffold integration and performance in bone regeneration.

Conclusion

In summary, this study evaluated the influence of the sintering process on the microstructure, cell, and blood compatibility of 3D-printed β -TCP scaffolds. Sintering temperatures above 1050 °C showed higher densification with improved mechanical properties, with no detached particles on the surface. Interestingly, during the sintering process of the scaffolds, bigger pores emerged inside the structure, and the filament had a size shrinkage due to the coalescence between particles, but kept its final structure intact. These characteristics produced scaffolds with enhanced mechanical properties and allowed MG63 osteoblast-like cells to penetrate the scaffold and proliferate on the top of the scaffold and inter filaments. These findings show that tailoring the sintering process of 3D-printed β -TCP scaffolds can modulate its structural properties maintaining good cell viability, making the materials a good choice for clinical trials analyzing its performance in regenerating different bone regions.

Acknowledgments

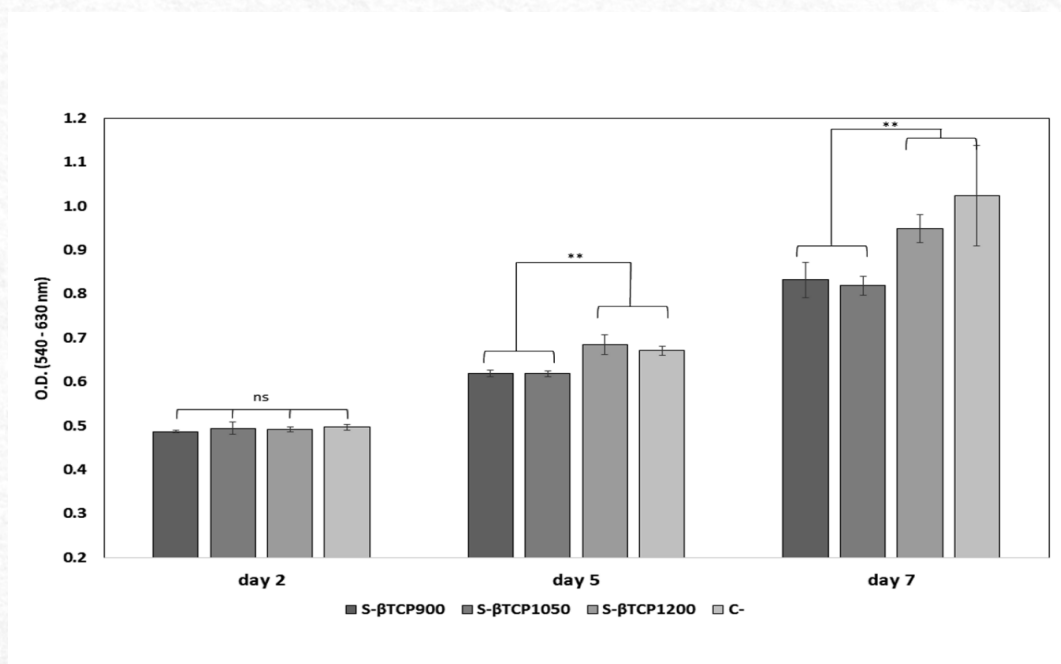


Figure 9 - Cell viability after 2, 5, and 7 days of culture in the scaffolds. Data expressed as the mean \pm SD. * $P \leq 0.05$ and ** $P \leq 0.01$ indicates significance between groups and "ns" no significance by one-way ANOVA followed by Tukey HSD post hoc test ($n=3$). Negative control: cell culture plate. O.D.: Optical density.

First, we honor and express our heartfelt gratitude in memory of Jorge Vicente Lopes da Silva for his unwavering dedication to science and society. As a founding member of the 3D technology and Biofabrication Group at the CTI Renato Archer, he made a significant impact on Brazilian science and society as a researcher and humanitarian person. His passion and commitment to advancing knowledge will continue to inspire generations to come. Thank you.

This work was supported by the National Council for Scientific and Technological Development (CNPq - 312216/2017-3, 444303/2018-9 and 407680/2021-7), and the Coordination for Improvement of Higher Education Personnel - Brazil (CAPES) - Funding Code 001. K. N. Ferreira thanks FAPESP for the financial support (2024/06681-4). L.E. Carneiro-Campos thanks Ossiform® (Denmark), for the collaboration for the development of new technologies for bone tissue repair, and Prof. C. J. Soares, P. D. Barbar, and the postgraduate program in dentistry at the Federal University of Uberlandia (Brazil) for the support received by the biomechanical analysis laboratory. We would like to thank FINEP for the financial support of the EMITUSAÚDE (01.18.0027.01) project on the acquisition of the X-ray microtomography equipment. J. Daguano thanks COLAB, open facilities of CTI Renato Archer.

References

- [1]. Hu J, Zhou Y, Huang L, Liu J, Lu H. Effect of nano-hydroxyapatite coating on the osteoinductivity of porous biphasic calcium phosphate ceramics. *BMC Musculoskelet Disord.* 2014 Apr 1;15:114. <https://link.springer.com/article/10.1186/1471-2474-15-114>
- [2]. Fardin AC, Jardim ECG, Pereira FC, Guskuma MH, Aranega AM, Garcia Júnior IR. Bone graft in dentistry: review of literature. *Innovations Implant Journal.* 2010 Dec;5(3):48–52. http://revodontobvsalud.org/scielo.php?pid=S1984-596020100003000106&script=sci_arttext&lng=en
- [3]. Giannoudis PV, Dinopoulos H, Tsiridis E. Bone substitutes: an update. *Injury.* 2005 Nov;36 Suppl 3. <https://doi.org/10.1016/j.injury.2005.07.029>
- [4]. Horta R, Frias F, Jarnalo M, Teixeira S, Silva P, Oliveira I, Silva A. Facial Reconstruction Based on Combined Three-Dimensional Printing and Microsurgical Free Transfer. *The Journal of Craniofacial Surgery.* 2020 June;31(4). <https://doi.org/10.1097/scs.00000000000006559>
- [5]. Chang B, Liu X. Osteon: structure, turnover, and regeneration. *Tissue Eng., Part B.* 2022;28(2):261–278. <https://doi.org/10.1089/ten.teb.2020.0322>
- [6]. Qin Q, Lee S, Patel N, et al. Neurovascular coupling in bone regeneration. *Exp. Mol. Med.* 2022;54(11):1844–1849. <https://www.nature.com/articles/s12276-022-00899-6>
- [7]. Sparks DS, Savi FM, Dlaska CE, et al. Convergence of scaffold-guided bone regeneration principles and microvascular tissue transfer surgery. *Sci. Adv.* 2023;9(18). <https://pubmed.ncbi.nlm.nih.gov/37146134/>
- [8]. Megías R, Vercher-Martínez A, Belda R, et al. Numerical modelling of cancellous bone damage using an orthotropic failure criterion and tissue elastic properties as a function of the mineral content and microporosity. *Comput. Methods Progr. Biomed.* 2022;219:106764. <https://doi.org/10.1016/j.cmpb.2022.106764>
- [9]. Langdahl B, Ferrari S, Dempster DW. Bone modeling and remodeling: potential as therapeutic targets for the treatment of osteoporosis. *Ther. Adv. Musculoskelet. Dis.* 2016;8(6):225–235. <https://pubmed.ncbi.nlm.nih.gov/28255336/>
- [10]. Dixit K, Gupta P, Kamle S, et al. Structural analysis of porous bioactive glass scaffolds using micro-computed tomographic images. *J Mater Sci.* 2020;55:12705–12724. <https://doi.org/10.1007/s10853-020-04850-w>
- [11]. Rajagopalan S, Lu L, Yaszemski MJ, et al. Optimal segmentation of microcomputed tomographic images of porous tissue-engineering scaffolds. *J Biomed Mater Res A.* 2005;75A:877–887. <https://doi.org/10.1002/jbm.a.30498>
- [12]. Bohner M, Santoni BLG, Döbelin N. β -tricalcium phosphate for bone substitution: Synthesis and properties. *Acta Biomater.* 2020;113:23–41. <https://doi.org/10.1016/j.actbio.2020.06.022>
- [13]. Causa F, Netti PA, Ambrosio L, et al. Poly- ϵ -caprolactone/hydroxyapatite composites for bone regeneration: in vitro characterization and human osteoblast response. *J Biomed Mater Res.* 2006;76:151e62. <https://doi.org/10.1002/jbm.a.30528>
- [14]. Chuenjitkuntaworn B, Inrung W, Damrongsri D, et al. Polycaprolactone/hydroxyapatite composite scaffolds: preparation, characterization, and in vitro and in vivo biological responses of human primary bone cells. *J Biomed Mater Res.* 2010;94:241e51. <https://doi.org/10.1002/jbm.a.32657>
- [15]. Decante G, Costa JB, Silva-Correia J, et al. Engineering bioinks for 3D bioprinting. *Biofabrication.* 2021;13:032001. <https://doi.org/10.1088/1758-5090/abec2c>
- [16]. Chavez T, Gerecht S. Engineering of the microenvironment to accelerate vascular regeneration. *Trends Mol. Med.* 2023;29(1):35–47. <https://doi.org/10.1016/j.molmed.2022.10.005>
- [17]. Ma Y, Lin M, Huang G, et al. 3D spatiotemporal mechanical microenvironment: a hydrogel-based platform for guiding stem cell fate. *Adv. Mater.* 2018;30(49) <https://doi.org/10.1002/adma.201705911>

- [18]. Sherwood JK, Riley SL, Palazzolo R, et al. A three-dimensional osteochondral composite scaffold for articular cartilage repair. *Biomaterials*. 2002;23:4739e51. [https://doi.org/10.1016/s0142-9612\(02\)00223-5](https://doi.org/10.1016/s0142-9612(02)00223-5)
- [19]. Hutmacher DW, Schantz T, Zein I, et al. Mechanical properties and cell cultural response of polycaprolactone scaffolds designed and fabricated via fused deposition modeling. *J Biomed Mater Res*. 2001;55:203e16. [https://doi.org/10.1002/1097-4636\(200105\)55:2%3C203::AID-JBIM1007%3E3.O.CO;2-7](https://doi.org/10.1002/1097-4636(200105)55:2%3C203::AID-JBIM1007%3E3.O.CO;2-7)
- [20]. Sadtler K, Wolf MT, Ganguly S, et al. Divergent immune responses to synthetic and biological scaffolds. *Biomaterials*. 2019;192:405e15. <https://doi.org/10.1016/j.biomaterials.2018.11.002>
- [21]. Zhang S, Hu B, Liu W, et al. Articular cartilage regeneration: the role of endogenous mesenchymal stem/progenitor cell; recruitment and migration. *Semin Arthritis Rheum*. 2020;50:198e208. <https://doi.org/10.1016/j.semarthrit.2019.11.001>
- [22]. Im G-I. Endogenous cartilage repair by recruitment of stem cells. *Tissue Eng Part B*. 2016;22:160e71. <https://doi.org/10.1089/ten.teb.2015.0438>
- [23]. Bigi A, Boanini E. Functionalized biomimetic calcium phosphates for bone tissue repair. *J Appl Biomater Funct Mater*. 2017 Nov 10;15(4). <https://doi.org/10.5301/jabfm.5000367>
- [24]. Posner AS, Beebe RA. The surface chemistry of bone mineral and related calcium phosphates. *Semin Arthritis Rheum*. 1975 Feb;4(3):267–91. [https://doi.org/10.1016/0049-0172\(75\)90013-X](https://doi.org/10.1016/0049-0172(75)90013-X)
- [25]. Jensen MB, Slots C, Ditzel N, et al. Treating mouse skull defects with 3D-printed fatty acid and tricalcium phosphate implants. *J Tissue Eng Regen Med*. 2020 Dec;14(12):1858–68. <https://doi.org/10.1002/term.3146>
- [26]. Boyce BF, Xing L. Biology of RANK, RANKL, and osteoprotegerin. *Arthritis Res Ther*. 2007;9 Suppl 1. <https://doi.org/10.1186/ar2165>
- [27]. Vanden Berg-Foels WS. In situ tissue regeneration: chemoattractants for endogenous stem cell recruitment. *Tissue Eng Part B*. 2014;20:28e39. <https://www.liebertpub.com/doi/abs/10.1089/ten.teb.2013.0100>
- [28]. Indurkar A, Choudhary R, Rubenis K, et al. Advances in sintering techniques for calcium phosphates ceramics. *Mater*. 2021;14(10). <https://doi.org/10.3390/ma14206133>
- [29]. Umemoto S, Furusawa T, Unuma H, et al. In vivo bioresorbability and bone formation ability of sintered highly pure calcium carbonate granules. *Dent Mater J*. 2021;40:1202–1207. <https://doi.org/10.4012/dmj.2020-254>
- [30]. Bolander J, Chai YC, Geris L, et al. Early BMP, Wnt and Ca²⁺/PKC pathway activation predicts the bone forming capacity of periosteal cells in combination with calcium phosphates. *Biomater*. 2016;86:106–118. <https://doi.org/10.1016/j.biomaterials.2016.01.059>
- [31]. Slots C, Jensen MB, Ditzel N, et al. Simple additive manufacturing of an osteoconductive ceramic using suspension melt extrusion. *Dent Mater*. 2017;33:198–208. <https://doi.org/10.1016/j.dental.2016.11.012>
- [32]. Montelongo SA, Chiou G, et al. Development of biinks for 3D printing microporous, sintered calcium phosphate scaffolds. *J Mater Sci Mater Med*. 2021;32:943–16. DOI: 10.1007/s10856-021-06569-9. <https://doi.org/10.1007/s10856-021-06569-9>
- [33]. Bouakaz, I., Drouet, C., Grossin, D., Cobraiville, E., & Nolens, G. (2023). Hydroxyapatite 3D-printed scaffolds with Gyroid-Triply periodic minimal surface porous structure: Fabrication and an in vivo pilot study in sheep. *Acta Biomaterialia*, 170, 580–595. <https://doi.org/10.1016/j.actbio.2023.08.041>
- [34]. Budharaju, H., Suresh, S., Sekar, M. P., de Vega, B., Sethuraman, S., Sundaramurthi, D., & Kalaskar, D. M. (2023). Ceramic materials for 3D printing of biomimetic bone scaffolds – Current state-of-the-art & future perspectives. *Materials & Design*, 231, 112064. <https://doi.org/10.1016/J.MATDES.2023.112064>
- [35]. Thygesen, T., Slots, C., Jensen, M. B., Ditzel, N., Kassem, M., Langhorn, L., & Andersen, M. (2022). Comparison of off-the-shelf β -tricalcium phosphate implants with novel resorbable 3D printed implants in mandible ramus of pigs. *Bone*, 159, 116370. <https://doi.org/10.1016/J.BONE.2022.116370>
- [36]. Zhao, X., Li, N., Zhang, Z., Hong, J., Zhang, X., Hao, Y., Wang, J., Xie, Q., Zhang, Y., Li, H., Liu, M., Zhang, P., Ren, X., & Wang, X. (2024). Beyond hype: unveiling the Real challenges in clinical translation of 3D printed bone scaffolds and the fresh prospects of bioprinted organoids. *Journal of Nanobiotechnology*, 22(1). <https://doi.org/10.1186/S12951-024-02759-Z>
- [37]. Podgórski, R., Wojasiński, M., Małolepszy, A., Jaroszewicz, J., & Ciach, T. (2024). Fabrication of 3D-Printed Scaffolds with Multiscale Porosity. *ACS Omega*, 9(27), 29186–29204. https://doi.org/10.1021/ACSSOMEGA.3C09035/ASSET/IMAGES/LARGE/AO3C09035_0012.JPEG
- [38]. Slavin, B. v., Mirsky, N. A., Stauber, Z. M., Nayak, V. V., Smay, J. E., Rivera, C. F., Mijares, D. Q., Coelho, P. G., Cronstein, B. N., Tovar, N., & Witek, L. (2024). 3D printed β -tricalcium phosphate versus synthetic bone mineral scaffolds: A comparative in vitro study of biocompatibility. *Bio-Medical Materials and Engineering*, 35(4), 365–375. <https://doi.org/10.3233/BME-230214>
- [39]. Toby BH. EXPGUI, a graphical user interface for GSAS. *J Appl Crystallogr* 2001; 34: 210–213. DOI: 10.1107/S0021889801002242
- [40]. Momma K, Izumi F. VESTA 3 for three-dimensional visualization of crystal, volumetric and morphology data. *J Appl Crystallogr* 2011; 44: 1272–1276. <https://doi.org/10.1107/S0021889811038970>

- [41].Tavares LN, Zancopé K, Silva ACA, et al. Microstructural and mechanical analysis of two CAD-CAM lithium disilicate glass-reinforced ceramics. *Braz Oral Res* 2020; 31:34 e004. <https://doi.org/10.1590/1807-3107bor-2020.vol34.0004>
- [42].Wang L, Nancollas GH. Calcium orthophosphates: Crystallization and Dissolution. *Chem Rev* 2008; 108: 4628–4669. <https://doi.org/10.1021/cr0782574>
- [43].Yashima M, Sakai A, Kamiyama T, et al. Crystal structure analysis of β -tricalcium phosphate $\text{Ca}_3(\text{PO}_4)_2$ by neutron powder diffraction. *J Solid State Chem* 2003; 175: 272–277. [https://doi.org/10.1016/S0022-4596\(03\)00279-2](https://doi.org/10.1016/S0022-4596(03)00279-2)
- [44].Sblendorio GA, Le Gars Santoni B, Alexander DTL, et al. Towards an improved understanding of the β -TCP crystal structure by means of "checkerboard" atomistic simulations. *J Eur Ceram Soc* 2023; 43: 3746–3754. <https://doi.org/10.1016/j.jeurceramsoc.2023.02.036>
- [45].Toby BH. R factors in Rietveld analysis: How good is good enough? *Powder Diffr* 2006; 21: 67–70. <https://doi.org/10.1154/1.2179804>
- [46].Gibson IR, Rehman I, Best SM, et al. Characterization of the transformation from calcium-deficient apatite to β -tricalcium phosphate. *J Mater Sci Mater Med* 2000; 11: 799–804. <https://doi.org/10.1023/A:1008905613182>
- [47].Theophanides T, Theophanides T. Introduction to Infrared Spectroscopy. *Infrared Spectroscopy - Materials Science, Engineering and Technology*. Epub ahead of print 25 April 2012. DOI: 10.5772/49106.
- [48].Mao C, Lu J, Xu Q, et al. FTIR study of hydrogen bonding of stearic acid with ethanol, dimethyl sulfoxide, and acetonitrile in supercritical CO_2 . *Chin J Chem* 1999; 17: 223–230. <https://doi.org/10.1002/cjoc.19990170304>
- [49].Cun X, Hosta-Rigau L. Topography: A Biophysical Approach to Direct the Fate of Mesenchymal Stem Cells in Tissue Engineering Applications. *Nanomater* 2020; 10(10): 2070. <https://doi.org/10.3390/nano10102070>
- [50].Han Y, Lian M, Wu Q, et al. Effect of Pore Size on Cell Behavior Using Melt Electrowritten Scaffolds. *Front Bioeng Biotechnol* 2021; 9: 629270. <https://doi.org/10.3389/fbioe.2021.629270>
- [51].Ho ST, Hutmacher DW. A comparison of micro CT with other techniques used in the characterization of scaffolds. *Biomater* 2006; 27: 1362–1376. <https://doi.org/10.1016/j.biomaterials.2005.08.035>
- [52].Cengiz IF, Oliveira JM, Reis RL. Micro-CT – a digital 3D microstructural voyage into scaffolds: a systematic review of the reported methods and results. *Biomater Res* 2018; 22: 1–11. <https://doi.org/10.1186/s40824-018-0136-8>
- [53].Keklikoglou K, Arvanitidis C, Chatzigeorgiou G, et al. Micro-CT for Biological and Biomedical Studies: A Comparison of Imaging Techniques. *J Imaging* 2021; 7: 172. <https://doi.org/10.3390/jimaging7090172>
- [54].de Lima IR, Costa AM, Bastos IN, et al. Development and characterization of 5% mol Zn bioceramic in granular form. *Mater Res* 2006; 9: 399–403. <https://doi.org/10.1590/S1516-14392006000400010>
- [55].Yang Y, Yu H, Zhou X, et al. Shallow porous microsphere carriers with core-shell structure based on glass beads cross-linking chitosan for immobilizing inulinase. *Mol Catal* 2020; 486: 110871. <https://doi.org/10.1016/j.mcat.2020.110871>
- [56].Senck, S., Glinz, J., Heupl, S., Kastner, J., Trieb, K., Scheithauer, U., Dahl, S. S., & Jensen, M. B. (2024). Ceramic additive manufacturing and microstructural analysis of tricalcium phosphate implants using X-ray micro-computed tomography. *Open Ceramics*, 19, 100628. <https://doi.org/10.1016/J.OCERAM.2024.100628>
- [57].Dulgar-Tulloch AJ, Bizios R, Siegel RW. Human mesenchymal stem cell adhesion and proliferation in response to ceramic chemistry and nanoscale topography. *J Biomed Mater Res A* 2009; 90A: 586–594. <https://doi.org/10.1002/jbm.a.32116>
- [58].Mealy J, O'Kelly K. Cell response to hydroxyapatite surface topography modulated by sintering temperature. *J Biomed Mater Res A* 2015; 103: 3533–3538. <https://doi.org/10.1016/j.dental.2016.11.012>
- [59].Swain SK, Gotman I, Unger R, et al. Microstructure, mechanical characteristics and cell compatibility of β -tricalcium phosphate reinforced with biodegradable Fe-Mg metal phase. Epub ahead of print 2015. <https://doi.org/10.1016/j.jmbbm.2015.09.002>
- [60].Kang Y, Scully A, Young DA, et al. Enhanced mechanical performance and biological evaluation of a PLGA coated β -TCP composite scaffold for load-bearing applications. *Eur Polym J* 2011; 47: 1569–1577. <https://doi.org/10.1016/j.eurpolymj.2011.05.004>
- [61].Khatriwala CB, Peyton SR, Metzke M, et al. The regulation of osteogenesis by ECM rigidity in MC3T3-E1 cells requires MAPK activation. *J Cell Physiol* 2007; 211: 661–672. <https://doi.org/10.1002/jcp.20974>
- [62].Tsai SW, Liou HM, Lin CJ, et al. MG63 Osteoblast-Like Cells Exhibit Different Behavior when Grown on Electrospun Collagen Matrix versus Electrospun Gelatin Matrix. *PLoS One* 2012; 7: e31200. <https://doi.org/10.1371/journal.pone.0031200>
- [63].Navarrete RO, Lee EM, Smith K, et al. Substrate Stiffness Controls Osteoblastic and Chondrocytic Differentiation of Mesenchymal Stem Cells without Exogenous Stimuli. *PLoS One* 2017; 12: e0170312. <https://doi.org/10.1371/journal.pone.0170312>

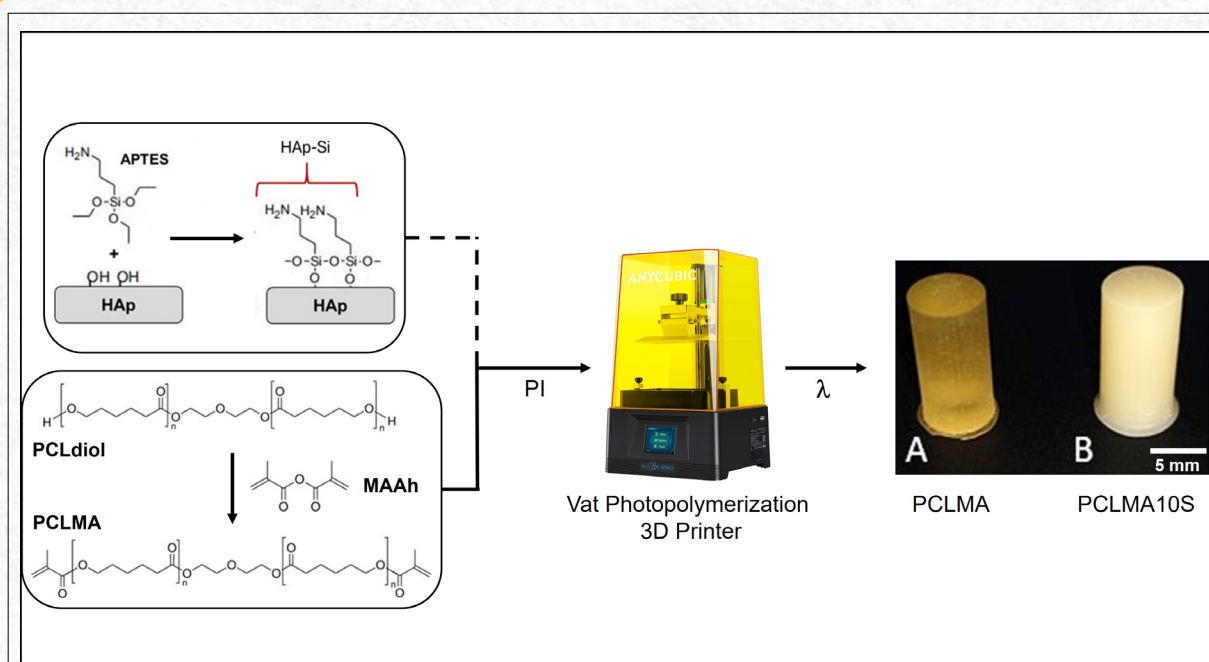


Development of PCLMA/HAp-Si composite resin for vat photopolymerization 3D printing

T. N. Palhares^{1,2,3*}; J. F. Parreira Lovó⁴; G. Costa Rodrigues¹; A. Lima Poli¹; M.A. Sabino^{2,5}; R. Rozental^{3,6,7}; C.C. Schmitt^{1*}

*Corresponding author: E-mail address: thiagonup@gmail.com

Received: October 2024; Accepted: December 2024.



Abstract: The development of bioactive materials for 3D printing has faced significant challenges, particularly in achieving compatibility between organic polymer matrices and inorganic fillers, which is critical for structural stability and biological applications. In this study, a photopolymerizable composite resin based on polycaprolactone methacrylate (PCLMA) was developed, incorporating functionalized hydroxyapatite (HAp-Si) to enhance the phase affinity between the polymer matrix and the inorganic filler. This approach addresses the bottleneck of poor dispersion and weak interfacial interactions commonly reported in the literature for similar systems. Hydroxyapatite was functionalized with 3-aminopropyltrimethoxysilane (APTES), as confirmed by X-ray Diffraction (XRD) and Fourier Transform Infrared Spectroscopy (FTIR), while polycaprolactone diol (PCLdiol) was successfully modified into PCLMA, introducing methacrylate groups and increasing the number-average molecular weight (M_n), also confirmed by FTIR. Scanning Electron Microscopy (SEM) revealed well-dispersed HAp-Si particles, highlighting the improved compatibility and distribution achieved through functionalization. The developed resin exhibited excellent dimensional fidelity during 3D printing of cylindrical samples measuring 6.35×12.70 mm. These findings suggest that PCLMA-based composite resins hold promise for advanced vat photopolymerization applications, particularly in tissue engineering and bioactive implant development.

Keywords: Poly(ϵ -caprolactone) methacrylate. Functionalized hydroxyapatite. Composite resin. Vat photopolymerization. 3D printing

¹Institute of Chemistry of São Carlos, University of São Paulo (USP), São Carlos, SP, Brazil.

²Renato Archer Information Technology Center, Campinas, SP, Brazil.

³Technological Development in Health Center, Oswaldo Cruz Institute, Oswaldo Cruz Foundation (FIOCRUZ), Rio de Janeiro, RJ, Brazil.

⁴University Hospital of UFSCar (Ebserh), Federal University of São Carlos, São Carlos, SP, Brazil.

⁵Department of Chemistry, B5IDA Research Group, Simón Bolívar University (USB), Caracas, Venezuela.

⁶Institute of Biomedical Sciences, Federal University of Rio de Janeiro (UFRJ), Rio de Janeiro, RJ, Brazil.

⁷Department of Neuroscience, Albert Einstein College of Medicine, New York, USA.

Introduction

Among several 3D printing approaches, vat photopolymerization stands out as one of the most precise processes within Additive Manufacturing (AM). This technique enables the production of solid prototypes or end-use objects with high resolution, surface quality, and intricate geometries, using layer heights as fine as 15 to 50 μm . Vat photopolymerization involves curing a photosensitive liquid resin—typically composed of functionalized monomers or oligomers—using a light source in the UV/Vis range (350 to 430 nm), converting the resin into a solid polymer layer by layer^(1–3).

The properties and performance of printed objects are directly linked to the composition of the resin. These resins must meet specific physicochemical and mechanical criteria, such as appropriate viscosity for smooth layer deposition, low shrinkage during curing to ensure dimensional stability, and mechanical robustness to withstand the intended application. The fraction of each component, including fillers, significantly influences these properties. Resins used for vat photopolymerization typically consist of monomeric or oligomeric materials—either natural or synthetic—combined with a photoinitiator. They may also include solvents, fillers, light-absorbing dyes, and curing inhibitors to optimize their functionality and achieve the desired performance characteristics^(2–7).

The molar mass of a polymer directly influences the printing process, as polymers are frequently functionalized through acrylation or methacrylation of their chains. Typically, a higher degree of crosslinking is achieved with shorter chain lengths, whereas longer chains can lead to reduced crosslinking. On one hand, highly dense crosslinked networks enhance print resolution. On the other hand, an increased molar mass raises the viscosity of the resin, causing difficulties in the 3D printing process. This often necessitates elevated temperatures in the vat or the incorporation of organic solvents, which can introduce challenges such as toxicity, difficulties in complete removal, and contraction of the printed models^(8,9).

The polymer/bioceramic composite enhances the properties of both phases and emerges as a promising new material. The effective incorporation of the filler into the polymeric matrix has been the focus of extensive research on composites⁽¹⁰⁾. Several studies in the literature investigate the mixture of poly(ϵ -caprolactone) (PCL) and hydroxyapatite (HAp), despite the low phase compatibility between these materials^(11,12), particularly when PCL is in the solid state.

PCL is a well-established synthetic polymer with a long history of diverse applications. One of its key advantages is its biocompatibility, characterized by

its non-toxic, non-immunogenic nature and low inflammatory response. Another significant benefit is its biodegradability. In vivo, PCL undergoes hydrolytic degradation, producing metabolites such as 6-hydroxyhexanoic acid, CO_2 , and H_2O , which are easily eliminated via the respiratory and urinary systems. Its degradation rate ranges from 2 to 4 years, making it a highly promising material for 3D-printed scaffolds. Additionally, PCL is notable for its favorable mechanical properties, ease of processing, and compatibility with other polymeric and ceramic materials^(13–15).

Hydroxyapatite (HAp) is classified as a calcium phosphate bioceramic, with a structure and functionality comparable to those found in bone and dental tissues. Due to its inherent biocompatibility and bioactivity, HAp is widely used as an implant material and has the property to induce osteogenic differentiation^(16–19).

The stoichiometry of hydroxyapatite (HAp) is commonly represented as $\text{Ca}_5(\text{PO}_4)_3\text{OH}$ or, considering its crystallographic unit cell, $\text{Ca}_{10}(\text{PO}_4)_6(\text{OH})_2$ corresponding to a theoretical Ca/P ratio of 1.67 for stoichiometric HAp. However, in practical terms, HAp can exhibit a variable gram atom Ca/P ratio, ranging from 1.5 (tricalcium phosphate, $\text{Ca}_3(\text{PO}_4)_2$) to 2.0 (tetracalcium phosphate, $\text{Ca}_4(\text{PO}_4)_2\text{CaO}$) as observed in calcium phosphate phase diagrams. This variability reflects the compositional and structural changes that can occur during synthesis or processing^(20–22).

This underscores the importance of improving the affinity of the ceramic filler to the polymeric matrix through surface modification processes, such as silanization. This process involves coating a hydroxylated surface with a silane to alter its properties. For example, 3-aminopropyltrimethoxysilane (APTES) can be used to modify HAp by hydrolyzing the ethoxy groups and forming a siloxane layer on its surface^(23,24). Additionally, the aminopropyl group present on the surface of HAp promotes interactions with polymeric matrices when combined⁽¹¹⁾.

The functionalization of hydroxyapatite (HAp) is a well-established strategy to enhance its integration into composite materials, particularly in improving its compatibility with polymer matrices. Among various functionalization methods, the use of 3-aminopropyltrimethoxysilane (APTES) offers notable advantages. One key benefit of silanizing HAp with APTES is the enhancement of its biocompatibility. While HAp is inherently biocompatible, the introduction of amine ($-\text{NH}_2$) groups reduces its surface energy, increasing compatibility with cellular wall proteins. This improvement facilitates better cell adhesion, proliferation, and differentiation—critical factors for tissue regeneration. Additionally, the formation of polysiloxanes on the HAp surface contributes to increased hardness, strength, and stability, further reinforcing its mecha-

nical properties. The aminopropyl groups present on the silanized HAp surface also promote interaction with polymer matrices, ensuring improved dispersion and physical integrity of the composite scaffolds. These advantages highlight the versatility of APTES functionalization in creating advanced materials for biomedical applications^(23–25).

The literature indicates that even at low filler content, photocurable resin systems mixed with HAp can exhibit poor dispersion and agglomeration⁽²⁶⁾, which is undesirable for vat photopolymerization processes. Conversely, adding filler percentages above 20% can also pose challenges, as it may affect the performance of the 3D printing machine, particularly if it is an LCD-type printer⁽²⁷⁾. This is especially true unless dispersing agents or rheological processing aids are employed, which can subsequently interfere with optimal polymerization.

In this context, the present study developed a composite resin for 3D printing via photopolymerization. The research focused on formulating a composite resin using poly(ϵ -caprolactone) methacrylate (PCLMA) as the matrix, incorporating either silanized hydroxyapatite (HAp-Si) functionalized with APTES or hydroxyapatite (HAp) as fillers. Poly(ϵ -caprolactone) (PCL) is widely recognized for its biocompatibility, biodegradability, and suitability for biomedical applications, particularly in tissue engineering, due to its ability to support cell adhesion and proliferation. Similarly, hydroxyapatite (HAp) is a well-established biomaterial, known for its osteoconductive and bioactive properties, which mimic the mineral component of bone tissue, making it ideal for bone regeneration applications. By combining these intrinsic properties with tailored functionalization, this study aims to develop a potentially biocompatible material that exhibits enhanced phase affinity, mechanical stability, and suitability for complex 3D-printed structures in biomedical applications.

Methodology

Synthesis of hydroxyapatite

Hydroxyapatite (HAp) was synthesized using a wet precipitation method, maintaining a theoretical ion ratio of $[\text{Ca}]^{2+}/[\text{PO}_4]^{3-} = 1.67$. A solution of diammonium hydrogen phosphate ($(\text{NH}_4)_2\text{HPO}_4$) (purity $\geq 99.0\%$, Sigma-Aldrich, Saint Louis, United States) was slowly added to a calcium nitrate solution ($\text{Ca}(\text{NO}_3)_2 \cdot 4\text{H}_2\text{O}$) (purity $\geq 99.0\%$, Sigma-Aldrich, Saint Louis, United States) under constant stirring and heating at 90°C . After the complete addition of the phosphate solution, the pH of the reaction was kept between 10 and 11 by the controlled addition of concentrated ammonium hydroxide (NH_4OH) (purity $\geq 99.0\%$, Sigma-Aldrich, Saint Louis, United States)^(28–30).

The mixture was then vacuum filtered using a Büchner funnel. The resulting solid was washed with ultrapure water until the filtrate reached a neutral pH. The solid was subsequently lyophilized, ground into a powder, and sieved through a $90\ \mu\text{m}$ mesh before being stored in a desiccator.

Functionalization of HAp via silanization with 3-Aminopropyltriethoxysilane (APTES)

The silanization reaction was performed to modify the surface of the hydroxyapatite (HAp). Approximately 1 g of HAp was added to an aqueous solution containing 40 ml of ethanol (P.A.) (purity $>96\%$, Êxodo Científica, Sumaré, Brazil) and 10 ml of distilled water, then sonicated for 2 hours at 60°C to initiate the hydrolysis of alkoxy groups and to deagglomerate the particles. Subsequently, 2.21 g of 3-aminopropyltriethoxysilane (APTES) (purity $\geq 99.0\%$, Sigma-Aldrich, Saint Louis, United States) was dissolved in 50 ml of ethanol (P.A.) and stirred for 30 minutes. This solution was then added to the HAp mixture and stirred for an additional 3 hours. The pH was adjusted to 9–10 with ammonium hydroxide (NH_4OH) (purity $\geq 99.0\%$, Sigma-Aldrich, Saint Louis, United States), and the reaction was allowed to continue for another 3 hours. After filtering the mixture through filter paper, the powder was initially dried at room temperature and then cured at 130°C to strengthen the silane coating by forming a polysiloxane network structure^(24,31–33). Figure S1 illustrates this reaction.

Finally, the product was washed repeatedly until the filtrate reached a neutral pH. The solid was then lyophilized, ground into a powder, and sieved through a $90\text{--}100\ \mu\text{m}$ mesh before being stored in a desiccator. The silanized hydroxyapatite is hereafter referred to as HAp-Si.

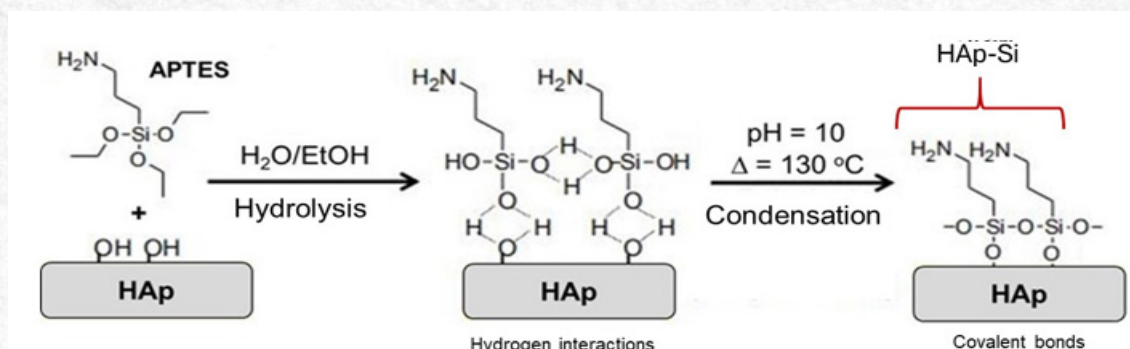


Figure S1 - Silanization functionalization reaction of APTES on HAp Surface
 Source: adapted from Kataoka, Shiba, Tagaya, 2019(17))

Methacrylation of poly(ε-caprolactone) diol

The methacrylation of poly(ε-caprolactone) diol oligomer (PCLdiol) (purity >97%, Sigma-Aldrich, Saint Louis, United States) was achieved through a reaction with methacrylic anhydride (MAAh) (purity ≥94.0%, Sigma-Aldrich, Saint Louis, United States), following methods described in the literature(8,34). Figure S2 illustrates the methacrylation reaction scheme.

The following protocol was employed: The oligomer was dissolved in dichloromethane (DCM) (purity ≥99.8%, Êxodo Científica, Sumaré, Brazil) at 100% of its weight. A 30% molar excess of MAAh and a 30% molar amount of triethylamine (TEA)

(purity ≥99.0%, Êxodo Científica, Sumaré, Brazil) per hydroxyl terminal group were added, with TEA serving to neutralize the methacrylic acid formed during the reaction. The methacrylation was carried out at room temperature under a nitrogen atmosphere for 24 hours. After the reaction was complete, DCM, excess MAAh, TEA, and the methacrylic acid formed were removed by precipitating the methacrylated oligomer in cold isopropanol (purity ≥99.0%, Êxodo Científica, Sumaré, Brazil). The methacrylated oligomer was then centrifuged, washed with distilled water, separated, and lyophilized. The resulting methacrylated product was identified as poly(ε-caprolactone) dimethacrylate resin (PCLMA).

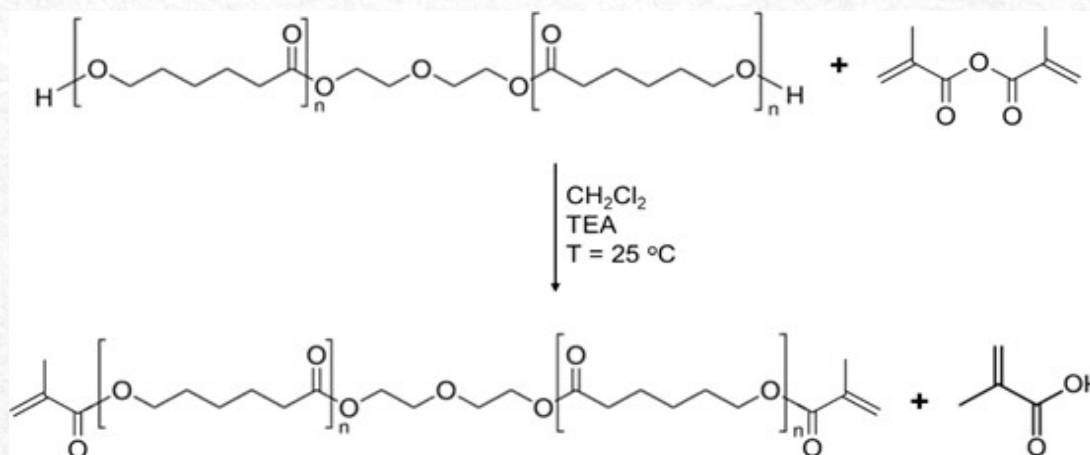


Figure S2 - Methacrylation reaction of PCLdiol to modify and obtain PCLMA.

X-ray Diffraction (XRD) of HAp and HAp-Si

XRD analysis was performed on both HAp and HAp-Si to identify their crystalline structures and assess any modifications resulting from the silanization process. The powder samples were re-sieved to prevent agglomeration. XRD patterns were obtained using a BRUKER APEX II Duo diffractometer with $\text{CuK}\alpha$ radiation ($\lambda = 1.5418 \text{ \AA}$) at room temperature, over a 2θ range of 10° to 70° .

Fourier Transform Infrared Spectroscopy (FTIR)

Transmission-mode FTIR was performed to identify structural changes resulting from the chemical modifications of both HAp and PCLdiol. Fourier Transform Infrared (FTIR) spectroscopy was conducted over a wavenumber range of 4000 to 400 cm^{-1} at room temperature, using KBr in a 1:100 ratio. Data acquisition was carried out on a Shimadzu IR Affinity 1 spectrophotometer, utilizing 32 scans and a resolution of 4 cm^{-1} .

Determination of average molar mass by Gel Permeation Chromatography (GPC) of PCLdiol and PCLMA

The molar mass of PCLdiol and PCLMA was determined using gel permeation chromatography to compare the increase in molar mass resulting from the modification of the polymer matrix. This technique provided values for the number-average molar mass (M_n), weight-average molar mass (M_w), and polydispersity (\mathcal{D}), where $\mathcal{D} = M_w/M_n$.

The analyses were conducted using a Shimadzu chromatograph equipped with LC-20AD pumps, a CBM-20A controller, a CTO-20A oven, and an RID-10A detector. The analytical conditions included a flow rate of 1 mL/min , a temperature of $35 \text{ }^\circ\text{C}$, a duration of 50 minutes, and tetrahydrofuran (THF) (Sigma-Aldrich, Saint Louis, United States) as the mobile phase, with sample injection concentrations of 10 mg/mL . The stationary phase consisted of four Waters Styragel columns in series (HR 4E and HR 5E) with rigid particles of poly(styrene-co-divinylbenzene) copolymer. A standard calibration curve was created to quantify the molar mass as a function of elution time, using poly(methyl methacrylate) and polystyrene standards, with injection concentrations of 5 mg/mL .

Preparation of photocurable composites of PCLMA and HAp-Si

PCLMA was utilized as the polymer matrix to prepare composite samples mixed with either HAp or HAp-Si as fillers. The materials were weighed in the different mass proportions and sonicated for 30 minutes. Subsequently, the photoinitiator Irgacure 369 (purity $>97\%$, Sigma-Aldrich, Saint Louis, United

States) was added at 3 wt% of PCLMA and stirred for 12 hours using a magnetic stirrer to ensure the dispersion and homogeneity of the samples. These mixtures were stored in amber vials, kept in the dark, and away from any light sources to prevent unwanted premature polymerization. This process resulted in a viscous liquid photocurable resin, which serves as the input for 3D printing via photopolymerization.

Based on these considerations, this research prepared photocurable composites with only 10% inorganic filler (either HAp or HAp-Si) as a first approximation. These composites were identified as follows: dimethacrylated PCL (PCLMA), PCLMA + 10% HAp (w/w) (PCLMA10), and PCLMA + 10% HAp-Si (w/w) (PCLMA10S).

Rheology of PCLMA resins and composites PCLMA10 and PCLMA10S

The viscosity of the resins is a crucial parameter for ensuring good printability. Viscosity measurements ($\text{Pa}\cdot\text{s}$) were conducted as a function of shear rate ($1/\text{s}$) on samples of PCLMA and its composites, PCLMA10 and PCLMA10S. Additionally, a commercial resin (Anycubic/Standard Clear Resin), which is from the same brand as the 3D LCD printer used in this study, was included for comparison. The experiments were performed using a TA Instruments DHR-2 rheometer with a parallel plate of 25 mm diameter and 0.5 mm spacing at $25 \text{ }^\circ\text{C}$.

Scanning Electron Microscopy with Energy Dispersive X-ray Spectroscopy (SEM-EDX) of PCLMA and Composites PCLMA10 and PCLMA10S

Scanning Electron Microscopy (SEM) analyses with Energy Dispersive X-ray Spectroscopy (EDX) were conducted using a JEOL JSM-7200F microscope to verify the dispersion, morphology, and size of the filler particles within the polymer matrix. EDX was specifically employed to identify the composition of the inorganic filler and confirm the presence of HAp. The cured materials were frozen in liquid nitrogen and then fractured. They were subsequently affixed to the surface of metallic stubs using carbon tape, which possesses both adhesive and conductive properties. The stubs containing the samples were coated with carbon to enhance conductivity for image acquisition. Images of the samples were obtained using a secondary electron detector, with a potential difference of 15 kV applied for electron acceleration.

Thermogravimetric Analysis / Derivative Thermogravimetric Analysis (TG/DTG) of PCLMA and composites PCLMA10 and PCLMA10S

This analysis was performed to confirm the

addition of filler and to identify the mass value present in each composite formulation. TG/DTG measurements were obtained using a TA Instruments TGA Q50 thermogravimetric analyzer, with approximately 10 to 15 mg of sample in the heating range from 25 to 1000 °C, at a heating rate of 10 °C/min under a nitrogen atmosphere at a flow rate of 50 mL/min

3D printing process by photopolymerization of cylindrical samples

Cylindrical samples with a height (H) of 12.70 mm and a diameter (D) of 6.35 mm were prepared in triplicates. The commercial 3D printer Anycubic Photon Mono was utilized for the subsequent tests in this study. The 3D printing process was conducted through photopolymerization using the Liquid Crystal Display (LCD) technique, employing an LED projector with a nominal wavelength of 405 nm, a resolution of 2560 x 1620 pixels (2K; XY: 0.051 mm; Z: 0.01 mm), a nominal power of 45 W, and a print envelope of 130 x 80 x 165 mm.

The basic printing parameters included a layer height of 0.03 mm (30 micrometers) and a curing time per layer of 6 seconds. Upon completion, the printed models were washed with isopropanol, dried, and subjected to a UV bath using the Anycubic Wash&Cure 2.0 equipment for 1 minute to finalize the curing of residual oligomers. An analysis of variance (ANOVA) with Tukey's test ($\alpha = 0.05$) was performed using OriginLab software to evaluate and compare the grouping of the obtained means.

Results and Discussion

X-ray Diffraction (XRD) Analysis of HAp and

HAp-Si

The XRD diffractogram presented in Figure 1 exhibits well-defined peaks, identifying the primary crystalline phases of hydroxyapatite (HAp) at $2\theta = 25.89^\circ$ (002); 28.18° (102); 28.96° (210); 31.84° (211); 32.90° (112); 34.07° (300); 35.46° (202); 39.27° (212); and 39.80° (310). These findings corroborate those reported in the literature(35,36).

Additionally, the results for HAp-Si indicate that silanization did not alter the crystalline structure of the material(30,37). This observation can be attributed to the degree of grafting, which occurred primarily on the surface of the inorganic particles, as illustrated in Figure S1.

Infrared Spectroscopy by Fourier Transform (FTIR) HAp, HAp-Si, and APTES

The FTIR spectra of HAp, HAp-Si, and APTES are depicted in Figure 2. The functional group bands characteristic of HAp and APTES are evident in HAp-Si, aligning with those reported in the literature. The bands identified in HAp correspond to $-\text{PO}_4^{3-}$ (565 , 605 , 875 , 962 , and 1033 cm^{-1}) and $-\text{OH}$ (3570 cm^{-1}). For APTES, the prominent bands include C-N (1589 cm^{-1}), $-\text{CH}_2-$ (2930 cm^{-1}), and $-\text{NH}_2$ (3372 cm^{-1})(23,38,39).

Although the Si-O-C (1107 cm^{-1}) and Si-O-Si (1080 cm^{-1}) bands are strong and predominant in APTES, they were overshadowed by the $-\text{PO}_4^{3-}$ bands of HAp due to the lower concentration of the silane in the material. Analysis of the HAp-Si spectrum revealed the presence of the primary bands from both materials, as previously mentioned. This observation suggests that the silanization reaction of the HAp surface facilitated by APTES has indeed occurred, a finding that will be further corroborated by the forthcoming.

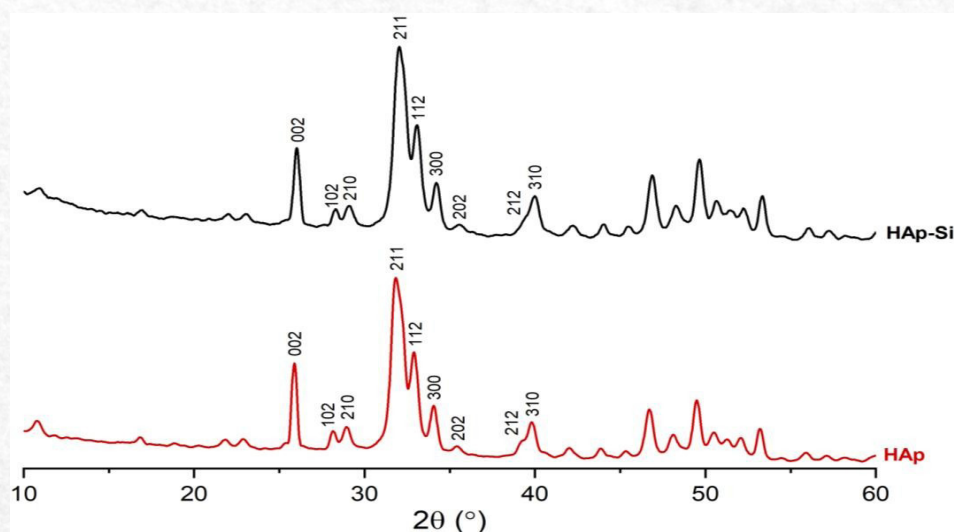


Figure 1 - X-ray Diffraction (XRD) analysis of HAp and HAp-Si.

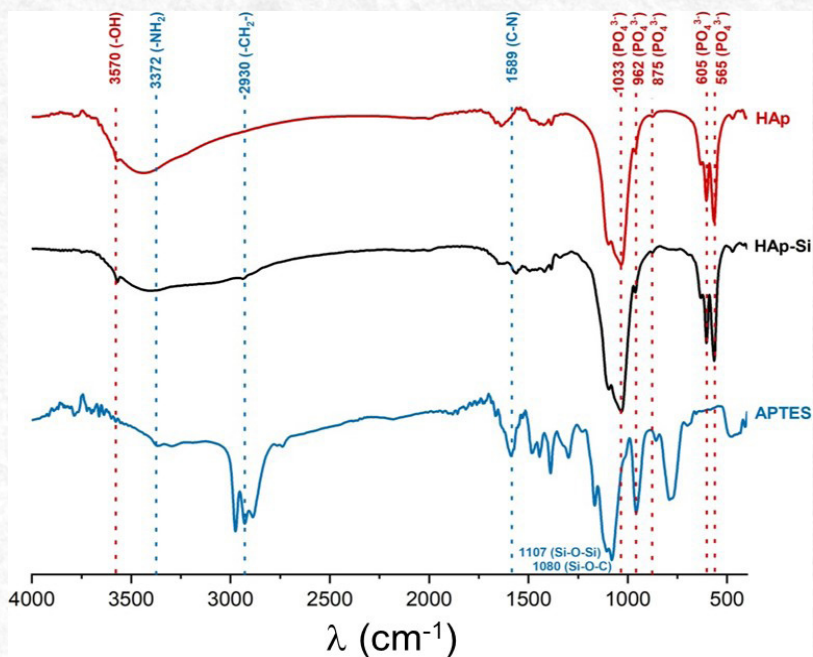


Figure 2 - FTIR Spectra of HAp, HAp-Si, and APTES

MAAh, PCLMA, and PCLdiol

In Figure 3, the absorption band at 1635 cm⁻¹ in the PCLMA spectrum corresponds to the vinyl group (H₂C=CH-) introduced during the methacrylation of PCLdiol with methacrylic anhydride (MAAh). Ad-

ditionally, the hydroxyl (-OH) absorption band, observed around 3500 cm⁻¹ in the PCLdiol spectrum, shows a significant reduction in the PCLMA spectrum due to the substitution of hydroxyl groups during the methacrylation process^(37,40).

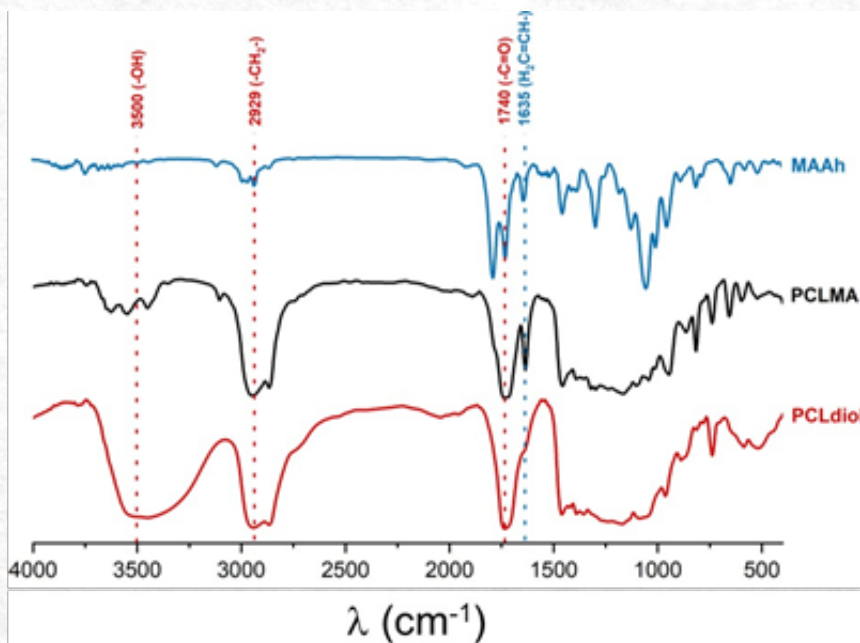


Figure 3 - Fourier Transform Infrared (FTIR) Spectroscopy of PCLdiol, PCLMA, and MAAh Resin.

Molar mass by gel permeation chromatography (GPC) of PCLdiol and PCLMA Resin

The molar mass values were determined to elucidate the variation in the distribution of the PCLdiol resin and its functionalized counterpart, PCLMA. The results for the number-average molar mass (M_n), weight-average molar mass (M_w), and polydispersity (\mathcal{D}), as determined by Gel Permeation Chromatography (GPC), are presented in Table 1. The M_n of PCLdiol was measured at 668 g/mol, aligning reasonably well with the nominal value of 530 g/mol reported by the manufacturer.

It is important to emphasize that organic synthesis, particularly polymerization reactions, inherently produces a distribution of molecular weights described by a normal distribution curve, rather than a single exact value. The reported M_n represents the average of this distribution, explaining the slight deviation from the manufacturer's specification. For PCLMA, the M_n increased to 826 g/mol, confirming the successful substitution of hydrogen atoms in the terminal hydroxyl groups with methacrylate groups.

The polydispersity index (\mathcal{D}) for PCLMA was determined to be 1.47, which is comparable to the \mathcal{D}

value of 1.71 for PCLdiol. A dispersity index close to 1 reflects favorable properties such as improved uniformity of polymer chains, enhanced processability, and better overall material performance. These characteristics are particularly advantageous for polymers designed for advanced applications, including additive manufacturing technologies⁽⁴¹⁾.

Thermogravimetric Analysis (TGA) and Differential Thermogravimetry (DTG) of PCLMA resins and composites PCLMA10 and PCLMA10S

Thermal analysis by TGA was employed to characterize the thermal decomposition profile of the PCLMA resin and its composites, PCLMA10 and PCLMA10S, as illustrated by the curves in Figure 4. This analysis also aimed to estimate the inorganic residue content to evaluate the filler proportion in each resin aliquot and to compare it with the intended theoretical composition.

The residual content values provide estimates of the inorganic filler, specifically the HAp phase, in the PCLMA10 and PCLMA10S composites. In all samples, the curves exhibited a single stage of thermal degradation commencing at temperatures above

Table 1 - Values of Number-Average Molar Mass (M_n), Weight-Average Molar Mass (M_w), and polydispersity (\mathcal{D}).

Sample	M_n (g/mol)	M_w (g/mol)	\mathcal{D}
PCLdiol	668.0	1148.0	1.71
PCLMA	826.0	1214.0	1.47

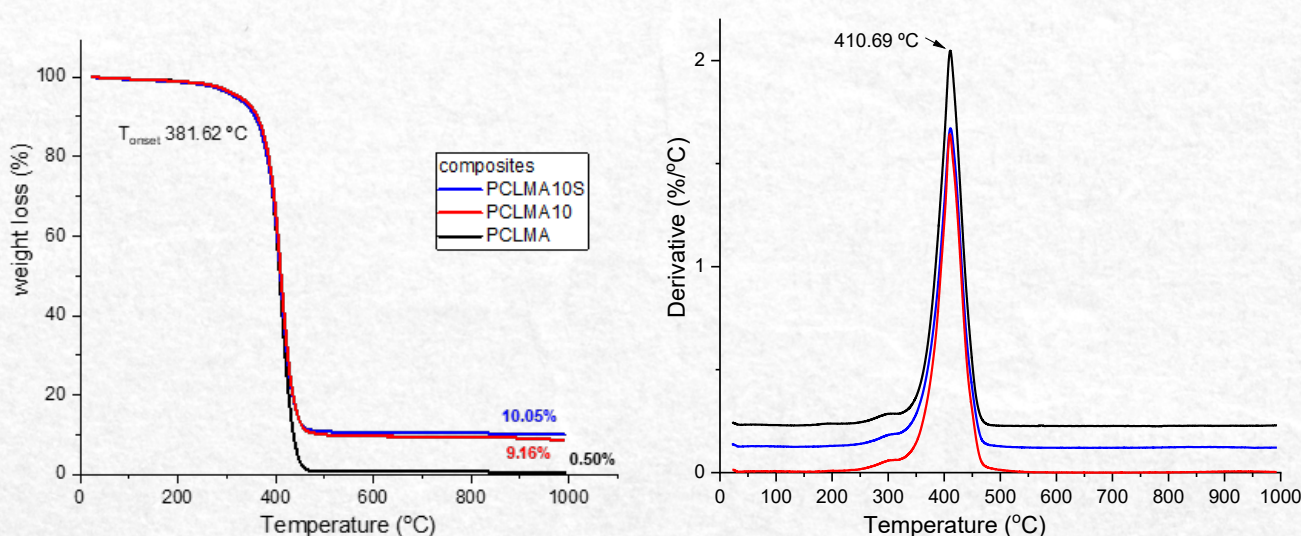


Figure 4 - TGA and DTG Curves of PCLMA Resin and Composites PCLMA10 and PCLMA10S

250 °C, which corresponds to the decomposition of the polymer matrix. A second degradation phase was noted just above 400 °C, confirming the presence of a binary composite with only the filler incorporated in the PCLMA polymer matrix. The onset temperature, indicating the estimated temperature at which material degradation begins, was approximately 381.6 °C for all samples.

The theoretical filler values in the samples reflect the fraction of each sample, indicating variability in filler dispersion and homogeneity throughout the polymer phase. The values in parentheses presented at the end of the curves represent the residual filler content related to the mass loss of HAp (~9.16%) and HAp-Si (~10.1%). The DTG curve indicates that the maximum degradation rate occurs at approximately 410 °C for all samples. Notably, the addition of HAp or HAp-Si did not influence the thermal degradation rate of the polymer matrix.

Rheology of PCLMA resins and composites (PCL-

MA10 and PCLMA10S)

Viscosity is a critical parameter for 3D resin printing through photopolymerization. During printing, the resins need to continuously fill the voids formed by the platform displacement in each layer. Several factors influence high-resolution 3D printing by photopolymerization. Generally, the resin viscosity must be low enough, depending on the molar mass of the monomer/oligomer, to allow detachment of the cured layers from the printing vat. It's also important for the resin to maintain certain pseudoplasticity required for forming a dimensionally stable 3D piece with adequate elastic-plastic behavior⁽⁴²⁾. Otherwise, adhesive forces from the process will cause delamination between the cured layers of the printed object. Additionally, low viscosity resins may allow for higher printing speeds, which could be necessary for small dimensions or high productivity pieces^(9,43).

The viscosity as a function of shear rate for PCLMA resins and the composites PCLMA10

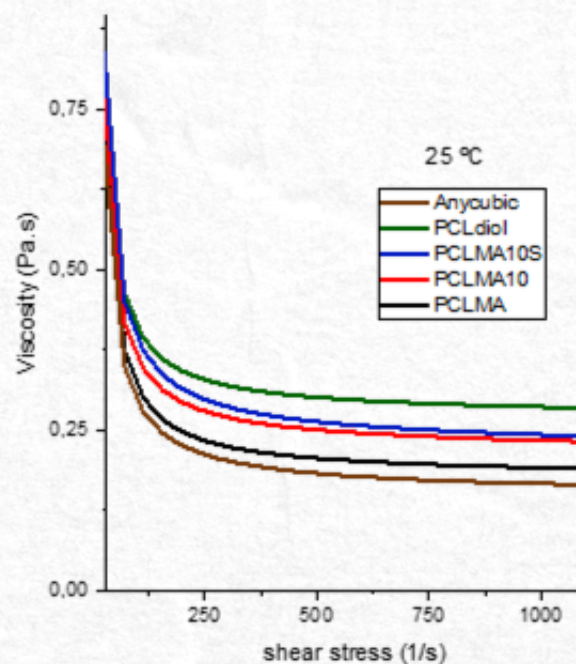


Figure 5 - Viscosity as a function of shear rate for PCLMA resins and PCLMA10 and PCLMA10S composites.

and PCLMA10S was measured at 25°C and is presented in Figure 5. The rheological curves for PCLdiol, PCLMA, PCLMA10, and PCLMA10S resins, along with the commercial Anycubic resin at room temperature (~25°C), demonstrate a viscous fluid behavior. Specifically, the viscosity of PCLdiol, PCLMA, PCLMA10, and PCLMA10S samples reaches a plateau at shear rates between 500 and 1000 s⁻¹, indicating that they behave as Newtonian fluids with constant viscosity as the shear rate

varies. At lower shear rates, ranging from 0 to 500 s⁻¹, the samples exhibit pseudoplastic behavior, which is essential for printing processes to ensure good shape fidelity⁽⁴⁴⁾.

Scanning Electron Microscopy with Energy Dispersive Spectroscopy (SEM-EDX) of the composites

Scanning Electron Microscopy (SEM-EDX) was employed to investigate the morphology of HAp

and HAp-Si fillers dispersed within the PCLMA matrix. This analysis aimed to measure the area of the agglomerates and individual particles, as well as to map and chemically identify the presence of fillers by detecting carbon (C), oxygen (O), calcium (Ca), and phosphorus (P).

Figure 6 presents a cross-sectional view obtained through cryogenic fracture of the cylindrical samples. For the matrix of modified PCLMA, certain marks are observed on the surface of the cryogenic cut, which could also be related to some brittleness induced by the modification made, given that it is known that PCL is a polymer with ductile behavior. At higher magnifications, the presence of inorganic fillers in the composite samples PCLMA10 e PCLMA10S is evident, for magnifications of 200X and 1500X, the presence of the hydroxyapatite phase is evident as dispersed inorganic particles are observed in the polymeric matrix. It is also evident that the fracture propagation pattern for the PCLMA10 composite is different, as a distinct pattern of cryogenic fracture propagation is observed, possibly inducing a certain brittleness to the material.

From Figure 6, it is evident that filler agglomerates formed and coalesced, exhibiting different shapes and sizes, which resulted PCLMA10 in a heterogeneous material. However, in the PCLMA10S sample containing modified hydroxyapatite (HAp-Si), the dispersion process proved to be more effective, demonstrating good distribution of the particles within the PCLMA polymer matrix. This suggests a reduction in interfacial tension between the organic and inorganic phases⁽⁴⁵⁾, indicating

enhanced compatibility that could improve the printability of 3D structures and possibly improve their mechanical performance⁽⁴⁶⁾.

Crosby and Lee (2007) assert that mixing polymers with fillers introduces significant complexities regarding their form. Achieving homogeneous composites with good dispersion and distribution remains a formidable challenge. The addition of excess filler reduces the average distance between particles, thereby increasing the likelihood of collisions and the formation of micrometer-scale aggregates. This phenomenon can result in a loss of the characteristic properties of the material and an increase in its dimensions^(47,48).

Figure 7 presents the EDX analysis conducted at a magnification of 6,500x, focusing on specific points to confirm that the particles observed in the SEM images are indeed hydroxyapatite (HAp). This is evidenced by the detection of calcium (Ca) and phosphorus (P) in their composition. In the case of PCLMA10S, the detection of silicon (Si) further corroborates the successful functionalization of the HAp with APTES.

The HAp used was not subjected to thermal treatment via sintering, which typically promotes crystalline organization and adjusts the composition toward the stoichiometric Ca/P ratio of 1.67. Instead, the synthesized HAp retained a less crystalline and more amorphous structure, leading to a Ca/P ratio of 1.79, as determined by EDX analysis. This deviation from stoichiometry can arise from residual amorphous calcium phosphate phases or an excess of calcium ions incorporated during synthesis.

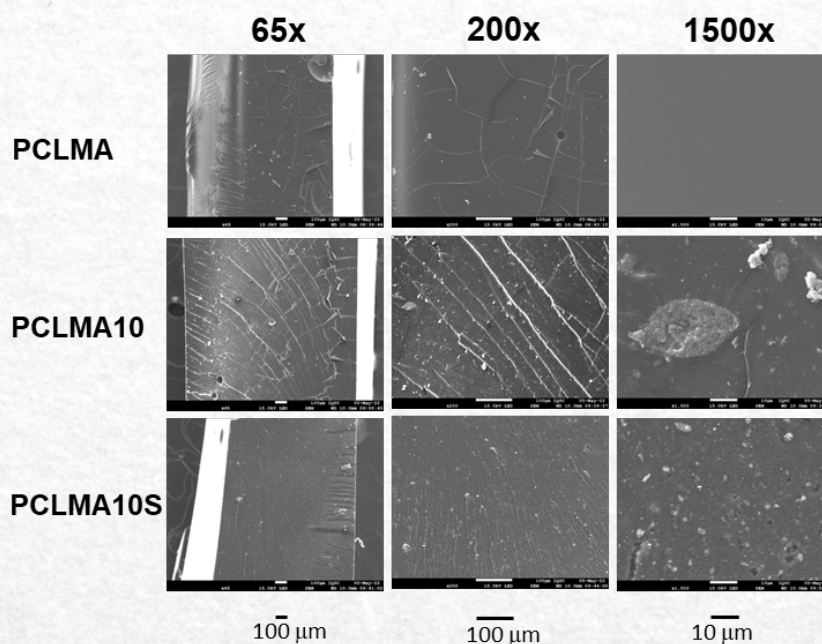


Figure 6 - SEM of fractured cross-section of composites with and without fillers

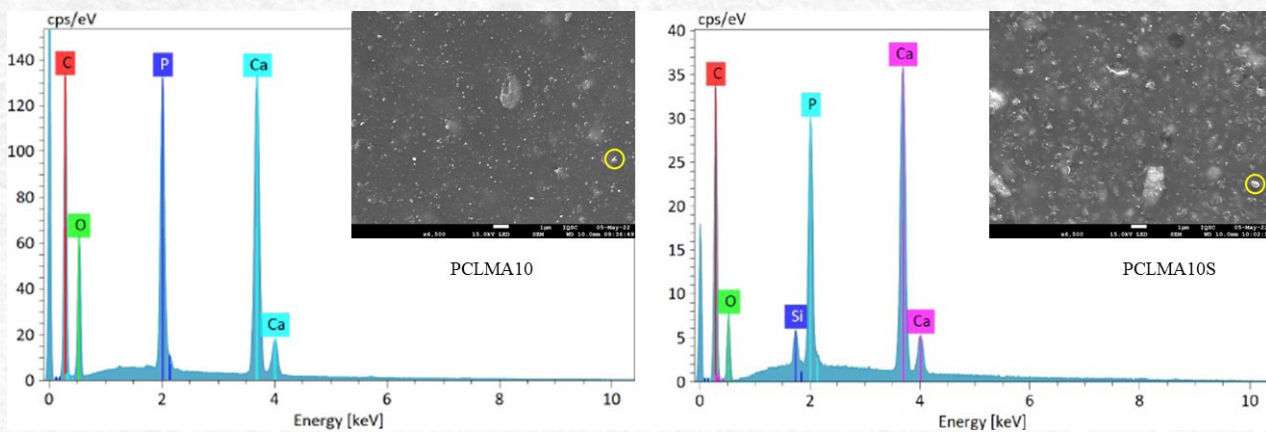


Figure 7 - EDX analysis at 6500x magnification of fractured samples of PCLMA, PCLMA10, and PCLMAIOS.

3D Printing process by photopolymerization

Printing tests were conducted to validate the feasibility of printing solid cylindrical structures. As shown in Figure 8, for comparative purposes, the printing was carried out for the PCLMA resin (A) and the composite PCLMAIOS (B), as the composite with HAp-Si exhibited favorable rheological behavior and good morphology between the phases. It can be observed that for a simple cylindrical geometry, the process of 3D structure formation demon-

strates efficiency.

The color differences observed in the samples are notable. The PCLMA resin exhibited a translucent yellow/golden hue, while the PCLMAIOS composite presented an opaque, milky appearance, visually confirming the dispersion of the filler (HAp-Si) throughout the polymer matrix. This contrast underscores the impact of the inorganic filler on the optical characteristics of the composite.

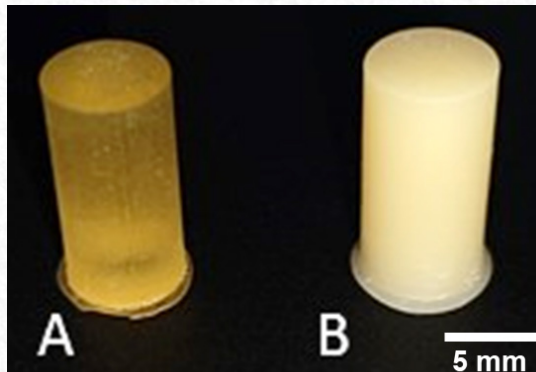


Figure 8 - 3D printing of cylindrical samples of a) PCLMA and b) PCLMAIOS.

Accuracy evaluation of 3D printing cylindrical samples

3D printing resins and materials must possess the necessary precision to match the dimensions of the planned 3D model. The designed samples, with a height (H) of 12.70 mm and a diameter (D) of 6.35 mm, were printed and subsequently compared. The average error (e) was calculated using Equations 2 and 3⁽⁴⁹⁾.

$$e_D = D - d \quad (\text{Eq. 2})$$

$$e_H = H - h \quad (\text{Eq. 3})$$

Where, e_D = average diameter error (mm);

e_D = average diameter error (mm);

D = 3D model diameter (mm);

d = 3D printed sample diameter;

e_H = average height error (mm);

H = 3D model height (mm);

h = 3D printed sample height (mm)..

Table 2 presents the measured diameters and heights of the compression test samples, along

with their respective associated errors.

The results indicate effective light penetration through the subsequent layers of all test samples. Furthermore, the average height for each sample was adequate for them to be categorized in the same group ("a") according to ANOVA analysis.

Regarding the diameter measurements, the test samples made from the PCLMA resin exhibited the

most significant deviation from the designed dimensions, thus belonging to group "A" in the ANOVA analysis. In contrast, the average diameters of the PCLMAIOS and PCLMAIO samples were closer to the intended 6.35 mm, placing them in group "B." Based on the previously observed results, dimensional fidelity in printing was confirmed.

Table 2 - Average diameter and height of compression test samples and associated error.

Sample	Average Diameter (mm)	e_D (mm)	Average Height (mm)	e_H (mm)
PCLMA	6.180 ± 0.045 A*	-0.170 (-2.68 %)	12.678 ± 0.005 a*	-0.022 (-0.04 %)
PCLMAIOS	6.384 ± 0.022 B	+0.034 (+0.54 %)	12.672 ± 0.005 a	-0.028 (-0.04 %)
PCLMAIO	6.396 ± 0.009 B	+0.046 (+0.72 %)	12.678 ± 0.014 a	-0.022 (-0.11 %)

Conclusions

This study demonstrated the successful synthesis of hydroxyapatite (HAp) and its functionalization with APTES to form HAp-Si, as confirmed by X-ray Diffraction (XRD) and Fourier Transform Infrared Spectroscopy (FTIR). The efficient conversion of PCLdiol into polycaprolactone methacrylate (PCLMA) was also verified through FTIR, with the introduction of methacrylate groups enabling photopolymerization via Irgacure 369.

Scanning Electron Microscopy (SEM) revealed dispersed HAp agglomerates, and Energy-Dispersive X-ray Spectroscopy (EDX) indicated a Ca/P ratio of 1.79, slightly deviating from the stoichiometric value due to the absence of post-sinterization treatment. Functionalization improved filler dispersion and its interaction with the polymer matrix.

Cylindrical 3D-printed PCLMA composite samples were fabricated successfully, demonstrating the potential of PCLMA-based photopolymerizable resins for advanced applications. Future studies should further investigate mechanical properties, biocompatibility, and the suitability of complex structures for clinical use, particularly in tissue engineering and bioactive implant development.

Acknowledgements

To the esteemed Dr. Jorge Vicente Lopes da Silva, who is regarded as an exemplary professional and a person of indisputable character. We are profoundly grateful for the opportunities and the freedom you granted us to explore 3D printing. Your legacy continues to inspire, and you will always be remembered

with deep admiration and respect.

Fundação Oswaldo Cruz (Fiocruz) - Processo Fiocruz nº 25380.002400/2021-96 and INOVA PRODUCTS (grant #6320360368) and to the esteemed Rodrigo Correa (VPPIS-Fiocruz) in association with the Brazilian Ministry of Health; São Paulo Research Foundation (FAPESP – grant #2023/14057-6, grant # 2022/15211-6, and grant #2021/13949-5); and Program CNPq (grant # 301211/2024-8 and grant # 311184/2022-7).

References

- [1]. Quan H, Zhang T, Xu H, Luo S, Nie J, Zhu X. Photo-curing 3D printing technique and its challenges. *Bioact Mater.* 2020 Mar;5(1):110–5.
- [2]. Ressler A, Zakeri S, Konnunaho P, Schwentenwein M, Levänen E, Frankberg EJ. Cleaning strategies for 3D-printed porous scaffolds used for bone regeneration fabricated via ceramic vat photopolymerization. *Ceram Int.* 2024 Oct;
- [3]. Enayati-Gerdoodbar A, Khayati A, Ahmadi M, Pourabbas B, Ali Aboudzadeh M, Salami-Kalajahi M. An overview on potential of novel photoinitiators for vat photopolymerization-based 3D/4D printing formulations. *Eur Polym J.* 2024 Dec;221:113552.
- [4]. Bao Y, Paunović N, Leroux J. Challenges and Opportunities in 3D Printing of Biodegradable Medical Devices by Emerging Photopolymerization Techniques. *Adv Funct Mater.* 2022 Apr 19;32(15).
- [5]. Paunović N, Bao Y, Coulter FB, Masania K, Geks AK, Klein K, et al. Digital light 3D printing of customized bioresorbable airway stents with elastomeric properties. *Sci Adv.* 2021 Feb 5;7(6).

- [6]. She Y, Fan Z, Wang L, Li Y, Sun W, Tang H, et al. 3D Printed Biomimetic PCL Scaffold as Framework Interspersed With Collagen for Long Segment Tracheal Replacement. *Front Cell Dev Biol.* 2021 Jan 21;9.
- [7]. Ding Y, Ikura R, Yamaoka K, Nishida K, Sugawara A, Uyama H, et al. Reinforcement and Controlling the Stability of Poly(ϵ -caprolactone)-Based Polymeric Materials via Reversible and Movable Cross-Links Employing Cyclic Polyphenylene Sulfide. *ACS Macro Lett.* 2024 Oct 15;13(10):1265–71.
- [8]. Green BJ, Worthington KS, Thompson JR, Bunn SJ, Rethwisch M, Kaalberg EE, et al. Effect of Molecular Weight and Functionality on Acrylated Poly(caprolactone) for Stereolithography and Biomedical Applications. *Biomacromolecules.* 2018 Sep 10;19(9):3682–92.
- [9]. van Bochove B, Hannink G, Buma P, Grijpma DW. Preparation of Designed Poly(trimethylene carbonate) Meniscus Implants by Stereolithography: Challenges in Stereolithography. *Macromol Biosci.* 2016 Dec 17;16(12):1853–63.
- [10]. Palhares TN, Menezes LR de, Kronemberger GS, Borchio PG de M, Baptista LS, Pereira L da CB, et al. Production and Characterization of Poly (Lactic Acid)/Nanostructured Carboapatite for 3D Printing of Bioactive Scaffolds for Bone Tissue Engineering. *3D Print Addit Manuf.* 2021 Aug 1;8(4):227–37.
- [11]. Biggemann J, Müller P, Köllner D, Simon S, Hoffmann P, Heik P, et al. Hierarchical Surface Texturing of Hydroxyapatite Ceramics: Influence on the Adhesive Bonding Strength of Polymeric Polycaprolactone. *J Funct Biomater.* 2020 Oct 3;11(4):73.
- [12]. Aminatun, Sujak M. K. A, Izak R. D, Hadi S, Sari YW, Gunawarman, et al. Fabrication and biocompatibility evaluation of hydroxyapatite–polycaprolactone–gelatin composite nanofibers as a bone scaffold. *RSC Adv.* 2024;14(34):24815–27.
- [13]. Thijssen Q, Cornelis K, Alkaisy R, Locs J, Damme L Van, Schaubroeck D, et al. Tough Photo-Cross-Linked PCL-Hydroxyapatite Composites for Bone Tissue Engineering. *Biomacromolecules.* 2022 Mar 14;23(3):1366–75.
- [14]. Shah SR, Modi CD, Singh S, Mori DD, Soniwala MM, Prajapati BG. Recent Advances in Additive Manufacturing of Polycaprolactone-Based Scaffolds for Tissue Engineering Applications: A Comprehensive Review. *Regen Eng Transl Med.* 2024 Sep 18;
- [15]. La Fuente CIA, Maniglia BC, Tadini CC. Biodegradable polymers: A review about biodegradation and its implications and applications. *Packaging Technology and Science.* 2023 Feb 26;36(2):81–95.
- [16]. Balasooriya IL, Chen J, Korale Gedara SM, Han Y, Wickramaratne MN. Applications of Nano Hydroxyapatite as Adsorbents: A Review. *Nanomaterials.* 2022 Jul 6;12(14):2324.
- [17]. Baptista LS, Kronemberger GS, Côrtes I, Charelli LE, Matsui RAM, Palhares TN, et al. Adult Stem Cells Spheroids to Optimize Cell Colonization in Scaffolds for Cartilage and Bone Tissue Engineering. *Int J Mol Sci.* 2018 Apr 25;19(5):1285.
- [18]. Kronemberger GS, Palhares TN, Rossi AM, Verçosa BRF, Sartoretto SC, Resende R, et al. A Synergic Strategy: Adipose-Derived Stem Cell Spheroids Seeded on 3D-Printed PLA/CHA Scaffolds Implanted in a Bone Critical-Size Defect Model. *J Funct Biomater.* 2023 Nov 21;14(12):555.
- [19]. Dornelas J, Dornelas G, Rossi A, Piattelli A, Di Pietro N, Romasco T, et al. The Incorporation of Zinc into Hydroxyapatite and Its Influence on the Cellular Response to Biomaterials: A Systematic Review. *J Funct Biomater.* 2024 Jun 28;15(7):178.
- [20]. Wopenka B, Pasteris JD. A mineralogical perspective on the apatite in bone. *Materials Science and Engineering: C.* 2005 Apr;25(2):131–43.
- [21]. Omelon SJ, Grynpas MD. Relationships between Polyphosphate Chemistry, Biochemistry and Apatite Biomineralization. *Chem Rev.* 2008 Nov 12;108(11):4694–715.
- [22]. Narasaraju TSB, Phebe DE. Some physico-chemical aspects of hydroxylapatite. *J Mater Sci.* 1996;31(1):1–21.
- [23]. Marycz K, Kornicka-Garbowska K, Patej A, Sobierajska P, Kotela A, Turlej E, et al. Aminopropyltriethoxysilane (APTES)-Modified Nanohydroxyapatite (nHAp) Incorporated with Iron Oxide (IO) Nanoparticles Promotes Early Osteogenesis, Reduces Inflammation and Inhibits Osteoclast Activity. *Materials.* 2022 Mar 11;15(6):2095.
- [24]. Kataoka T, Shiba K, Tagaya M. Design of Hydroxyapatite-Based Multifunctional Nanoparticles for Cell Labelling and Cell Growth Inhibition. *Regen Med Front.* 2019;2(1).
- [25]. Sypabekova M, Hagemann A, Rho D, Kim S. Review: 3-Aminopropyltriethoxysilane (APTES) Deposition Methods on Oxide Surfaces in Solution and Vapor Phases for Biosensing Applications. *Biosensors (Basel).* 2022 Dec 27;13(1):36.
- [26]. Kennedy BM, De Barra E, Hampshire S, Kelleher MC. Investigation of oleic acid as a dispersant for hydroxyapatite powders for use in ceramic filled photo-curable resins for stereolithography. *J Eur Ceram Soc.* 2023 Dec;43(15):7146–66.
- [27]. Yao Y, Sha N, Zhao Z. Highly Concentrated Hydroxyapatite Suspension for DLP Printing. *IOP Conf Ser Mater Sci Eng.* 2019 Nov 1;678(1):012016.
- [28]. de Oliveira Lomelino R, Castro-Silva II, Linhares ABR, Alves GG, de Albuquerque Santos SR, Gameiro VS, et al. The association of human primary bone cells with biphasic calcium phosphate (β TCP/HA 70:30) granules increases bone repair. *J Mater Sci Mater Med.* 2012 Mar 27;23(3):781–8.
- [29]. Gasperini FM, Calasans-Maia MD, Resende RFB,

- Granjeiro JM, Rossi AM, Lopes RT, et al. Bone-nanohydroxyapatite spheres interface evaluation by synchrotron radiation X-ray microfluorescence. *X-Ray Spectrometry*. 2012 Jan 21;41(1):6–11.
- [30]. Michelot A, Sarda S, Audin C, Deydier E, Manoury E, Poli R, et al. Spectroscopic characterisation of hydroxyapatite and nanocrystalline apatite with grafted aminopropyltriethoxysilane: nature of silane–surface interaction. *J Mater Sci*. 2015 Sep 5;50(17):5746–57.
- [31]. Atak BH, Buyuk B, Huysal M, Isik S, Senel M, Metzger W, et al. Preparation and characterization of amine functional nano-hydroxyapatite/chitosan bionanocomposite for bone tissue engineering applications. *Carbohydr Polym*. 2017 May;164:200–13.
- [32]. Goonasekera CS, Jack KS, Cooper-White JJ, Grøndahl L. Attachment of poly(acrylic acid) to 3-aminopropyltriethoxysilane surface-modified hydroxyapatite. *J Mater Chem B*. 2013;(42):5842.
- [33]. Russo L, Taraballi F, Lupo C, Poveda A, Jiménez-Barbero J, Sandri M, et al. Carbonate hydroxyapatite functionalization: a comparative study towards (bio)molecules fixation. *Interface Focus*. 2014 Feb 6;4(1):20130040.
- [34]. Elomaa L, Teixeira S, Hakala R, Korhonen H, Grijpma DW, Seppälä J V. Preparation of poly(ϵ -caprolactone)-based tissue engineering scaffolds by stereolithography. *Acta Biomater*. 2011 Nov;7(11):3850–6.
- [35]. Nejati E, Mirzadeh H, Zandi M. Synthesis and characterization of nano-hydroxyapatite rods/poly(L-lactide acid) composite scaffolds for bone tissue engineering. *Compos Part A Appl Sci Manuf*. 2008 Oct;39(10):1589–96.
- [36]. Tian G, Zhu G, Xu S, Ren T. A novel shape memory poly(ϵ -caprolactone)/hydroxyapatite nanoparticle networks for potential biomedical applications. *J Solid State Chem*. 2019 Apr;272:78–86.
- [37]. Cai L, Wang S. Poly(ϵ -caprolactone) acrylates synthesized using a facile method for fabricating networks to achieve controllable physicochemical properties and tunable cell responses. *Polymer (Guildf)*. 2010 Jan;51(1):164–77.
- [38]. Lucia A, Bacher M, van Herwijnen HWG, Rosenau T. A Direct Silanization Protocol for Dialdehyde Cellulose. *Molecules*. 2020 May 25;25(10):2458.
- [39]. Salim SA, Loutfy SA, El-Fakharany EM, Taha TH, Husien Y, Kamoun EA. Influence of chitosan and hydroxyapatite incorporation on properties of electrospun PVA/HA nanofibrous mats for bone tissue regeneration: Nanofibers optimization and in-vitro assessment. *J Drug Deliv Sci Technol*. 2021 Apr;62:102417.
- [40]. Risangud N, Jiraborvornpongsa N, Pasee S, Kaewkong P, Kunkit N, Sungkhaphan P, et al. Poly(ester-co-glycidyl methacrylate) for digital light processing in biomedical applications. *J Appl Polym Sci*. 2021 Sep 10;138(42).
- [41]. Zhu Y, Ramadani E, Egap E. Thiol ligand capped quantum dot as an efficient and oxygen tolerance photoinitiator for aqueous phase radical polymerization and 3D printing under visible light. *Polym Chem*. 2021;12(35):5106–16.
- [42]. Peñas MI, Calafel MI, Aguirresarobe RH, Tierno M, Conde JJ, Pascual B, et al. How Is Rheology Involved in 3D Printing of Phase-Separated PVC-Acrylate Copolymers Obtained by Free Radical Polymerization. *Polymers (Basel)*. 2020 Sep 12;12(9):2070.
- [43]. Murphy CA, Lim KS, Woodfield TBF. Next Evolution in Organ-Scale Biofabrication: Bioresin Design for Rapid High-Resolution Vat Polymerization. *Advanced Materials*. 2022 May 24;34(20).
- [44]. Kuang X, Zhao Z, Chen K, Fang D, Kang G, Qi HJ. High-Speed 3D Printing of High-Performance Thermosetting Polymers via Two-Stage Curing. *Macromol Rapid Commun*. 2018 Apr 31;39(7).
- [45]. Goonasekera CS, Jack KS, Cooper-White JJ, Grøndahl L. Dispersion of hydroxyapatite nanoparticles in solution and in polycaprolactone composite scaffolds. *J Mater Chem B*. 2016;4(3):409–21.
- [46]. Šupová M. Problem of hydroxyapatite dispersion in polymer matrices: a review. *J Mater Sci Mater Med*. 2009 Jun 20;20(6):1201–13.
- [47]. Crosby AJ, Lee J. Polymer Nanocomposites: The "Nano" Effect on Mechanical Properties. *Polymer Reviews*. 2007 Apr;47(2):217–29.
- [48]. Lee JY, Zhang Q, Emrick T, Crosby AJ. Nanoparticle Alignment and Repulsion during Failure of Glassy Polymer Nanocomposites. *Macromolecules*. 2006 Oct 1;39(21):7392–6.
- [49]. Lee JS, Park HS, Jung H, Lee H, Hong H, Lee YJ, et al. 3D-printable photocurable bioink for cartilage regeneration of tonsil-derived mesenchymal stem cells. *Addit Manuf*. 2020 May;33:101136.

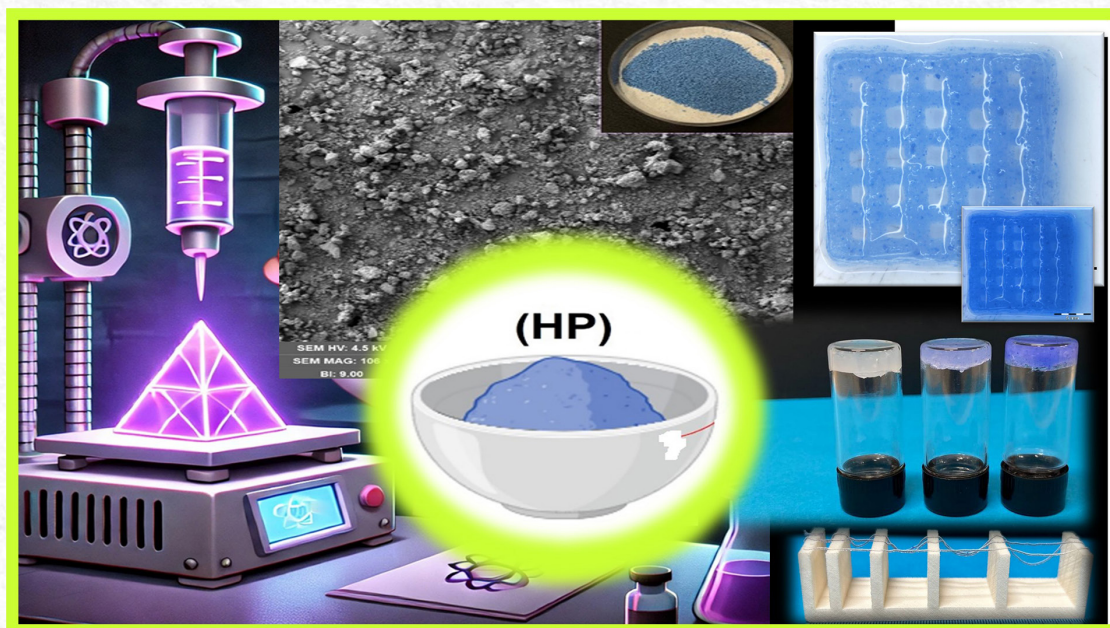


Photoluminescent gels based on han purple: new frontiers in biotechnology

K.F. Santos^{1,2}; C.Y. Morassutia^{1*}; D.A. Ribeiro²; K.V.S. Carvalho¹;
M.A. Sabino^{1,2}; J.V.L Silva¹; J.K.M.B. Daguano^{1,3}

*Corresponding author: E-mail address: claudio.morassuti@cti.gov.br

Received: October 2024; Accepted: December 2024.



Abstract: As a result of the increasing need for new biocompatible materials, polymer-based gels have become promising options. Lately, photoluminescent gels have shown potential for applications in biotechnology and non-invasive tracking due to their ability to emit light when temperature changes occur. This research investigates the incorporation of Han Purple (HP) pigment into a polyethylene glycol/Laponite matrix [92,5/7,5%] (P7LHPO%) to produce a 3D-printed gel. The gels were examined for possible use as smart sensors, focusing on their optical and thermal characteristics. Formulations with HP concentrations of 0.0%, 0.5%, and 2.0% were prepared, followed by extrusion-based 3D printing. Characterization techniques included FTIR, SEM, and optical analyses (emission and excitation spectra). The findings showed 3D structures with good shape fidelity while FTIR indicated suitable compatibility between HP and the matrix. Optical analysis revealed fluorescence with an excitation band between 400 and 700 nm, with a maximum at 620 nm, and an emission band at 830 - 1000 nm with a peak at 925 nm. This study highlights the potential of HP as a promising material for fluorescent gels in 3D printing, creating new opportunities for biotechnology applications.

Keywords: Han Purple. Fluorescence. Responsive gels. Optical sensors. 3D printing. Biotechnology.

¹Renato Archer Information Technology Center, Campinas, SP, Brazil.

² Chemistry Department, Research Group B5IDA, Simon Bolivar University, 8900, Caracas, Venezuela

³Federal University of ABC (UFABC), Center for Engineering, Modeling and Applied Social Sciences (CECS), São Bernardo do Campo, SP, Brazil.

Introduction

The search for materials with innovative properties is crucial for the progress of science and technology, especially in areas such as biotechnology, biomedicine, and pharmacology^[1]. Han Purple (HP), a pigment with both historical significance and promising functional characteristics, has recently sparked interest. Originally developed in ancient China around 700 BCE, HP exhibits a purple color and was widely used in embellishing various artifacts, including vases, bricks, and walls. However, beyond its artistic value, the physical and chemical characteristics of HP make it an appealing candidate for modern technological applications^[2].

The chemical formula of HP is predominantly $\text{BaCuSi}_2\text{O}_6$, and it stands out not only for its relatively straightforward synthesis but also for its fluorescent properties, attributed to the presence of Cu^{2+} ions within its structure^[2]. The synthesis process involves the combination of precursors such as barium carbonate (BaCO_3), silicon dioxide (SiO_2), and copper oxide (CuO) under precise thermal control^[3,4]. These unique characteristics allow HP to emit fluorescence within the near-infrared spectrum (NIR), unlocking new possibilities for its application in biomedical sensors, fluorescent markers, and infrared imaging techniques^[2,5].

In parallel, hydrogel-based biomaterials have become essential in tissue engineering due to their ability to absorb large volumes of water and simulate the conditions of the cellular environment. The development of three-dimensional scaffolds using additive manufacturing techniques, such as 3D printing, has facilitated the reproduction of complex structures that mimic the behavior of natural tissues.

Polyethylene glycol (PEG) stands out as a prominent polymer in this area due to its biocompatibility and versatility. Nevertheless, PEG by itself does not possess the necessary rheological properties to satisfy the requirements of 3D printing, limiting its direct applicability^[6]. To overcome these limitations, rheological modifiers like Laponite XLG—a nanosilicate—are incorporated into the PEG matrix, forming a three-dimensional network that maintains structural integrity during the printing process^[7,8]. This PEG/Laponite combination results in rheologically stable gels, ideal for fabricating complex structures suitable for a wide range of biomedical applications^[9].

The current study aims to synthesize and characterize HP and incorporate it into gels based on a PEG/Laponite matrix, to create a NIR fluorescence and printable gel and explore the HP emissions in response to temperature variations^[9,10]. By integrating this purple pigment into hydrogels, this research not only seeks to expand the understanding of

fluorescent material functionalization but also aims to open new opportunities for its application in biotechnology and regenerative medicine.

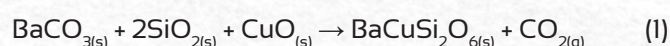
Experimental

Materials

This study utilized Polyethylene glycol-400 (PEG) with a molecular weight range of 380–420 $\text{g}\cdot\text{mol}^{-1}$ (Dinâmica) and Laponite XLG (Colormix). The reagents for the synthesis of Han Purple (HP) included barium carbonate (BaCO_3), silicon dioxide (SiO_2), and copper oxide (CuO), all sourced from Dinâmica.

Synthesis of HP

The HP pigment was produced by combining barium carbonate (BaCO_3), silicon dioxide (SiO_2), and copper oxide (CuO) in a 1:2:1 molar ratio, following the procedure described by McDaniel et al. (2014)^[4]. The components were homogenized using a high-speed mixer (SpeedMixer™ - Hauschild DAC 250), at 1100 rpm for 5 minutes. After homogenization, the carbonate-silica-oxide mixture was subjected to thermal sintering cycles. At first, the mixture was heated to 1000°C at a heating rate of 7°C/min. Following this step, the powder was deagglomerated and exposed to a second thermal cycle at 1050°C with a heating rate of 5°C/min. After high-temperature processing, the material gradually cooled to room temperature (25°C)^[4]. The overall equation (Eq. 1) describing the chemical reaction involves the decomposition of BaCO_3 and the subsequent formation of the fluorescent $\text{BaCuSi}_2\text{O}_6$ phase of HP:



X-ray Diffraction (XRD)

X-ray diffraction measurements were performed using a Rigaku Miniflex 600. The X-ray source was set to 40 kV and 15 mA, employing the $K\alpha$ (Cu) line. The setup included a Soller slit (inc) of 5.0°, IHS of 5.0 mm, SS of 1.250°, DS of 1.250°, and RS of 0.3 mm. Data acquisition was carried out at a scanning rate of 1.5°/min with a step size of 0.02°.

Scanning Electron Microscopy (SEM)

The synthesized HP powder was characterized using scanning electron microscopy (SEM) with a FEG-MIRA 3 (TESCAN) instrument to assess its superficial morphology. The samples were coated with a 10 nm gold-layer to ensure conductivity and were analyzed at a voltage of 4.5 kV.

Optical Characterizations

Optical Absorption

Optical absorption was measured at room temperature using a Perkin Elmer Lambda 1050

spectrophotometer. The spectra were recorded over the range of 300 to 1500 nm. Diffuse reflectance measurements of powder samples were conducted using a 150 mm integrating sphere accessory.

Temperature-Dependent Emission Spectra

Emission spectra as a function of temperature were collected using an Ocean Optics Maya Pro 2000 spectrometer connected via an optical fiber. Measurements were conducted over the range of 200 to 1100 nm. The samples were excited by a rhodamine 6G dye laser at 612.76 nm with a power output of 2.0 ± 0.2 mW. To eliminate excitation interference, a 650 nm long-pass filter was used during emission data collection. The sample temperature was controlled between 293 K and 343 K using a REX C100 controller and a type-K thermocouple.

Excitation-Emission Mapping

Excitation-emission maps were generated using a Horiba Instruments Duetta spectrometer. To acquire the emission spectra, excitation wavelengths ranging from 400 to 700 nm with an increment of 5 nm were used. The integration time for emission signal acquisition was 4 seconds and excitation and emission slit widths were both set at 5 nm. Emission spectra were recorded from 715 nm to 1000 nm, with a 715 nm long-pass filter placed at the emission collection port to exclude excitation line interference.

Chemical Composition Analysis

The chemical composition of the gels was evaluated using a Perkin Elmer Spectrum 100 in attenuated total reflection (ATR) mode. Spectra were acquired over the range of 450 to 4500 cm^{-1} with a resolution of 4 cm^{-1} , and each spectrum is an average of 16 consecutive acquisitions of the same sample.

VIS/NIR Microscopy

A HiView digital microscope was employed for optical imaging. The built-in microscope illumination was used to acquire visible images. For red excitation imaging, a 620 nm LED source (50.0 ± 0.5 mW) was applied. In near-infrared (NIR) imaging, only the 620 nm excitation was maintained, with a 715 nm long-pass filter placed at the microscope port to ensure that only the emission radiation from HP contributed to NIR image formation.

Preparation of HP-doped gels

The preparation of PEG-Laponite gels with 7.5 wt% nanosilicate (referred to as P7L^{HP0%}) followed the method described by Santos et al. (2022)^[7]. Initially, a 44 vol% PEG solution was mixed with Laponite using the SpeedMixer™ at a speed of 1000-1200 rpm for 2 minutes^[7]. The resulting gel was stored at 4-8°C for

48 hours for the aging process.

After preparing the base P7L^{HP0%} gel, Han Purple (HP) was incorporated at concentrations of 0%, 0.5%, and 2% (w/w), resulting in the formulations named P7L^{HP0%}, P7L^{HP0.5%}, and P7L^{HP2%} respectively, based on the total gel mass.

To ensure optimal dispersion of HP particles, the gels were further homogenized in the SpeedMixer™ at 1000-1200 rpm for an additional 2-5 minutes. This ensured the thorough integration of HP into the P7L^{HP0%} gel matrix. Figure 1 illustrates the entire process, from the synthesis of the pigment to its application in PEG-Laponite-based gels.

Qualitative Analysis of the Gels Before 3D Printing

Subsequently, the gels were kept refrigerated (6.0 ± 2.0 °C) until the 3D printing stage. Before printing tests, discs (2.5 ± 0.1 mm in height and 9.5 ± 0.1 mm in diameter) were prepared and examined under an Olympus SZX16 stereomicroscope to verify the homogeneous dispersion of HP in the P7L^{HP0%} matrix.

Although the properties of the P7L^{HP0%} gels have been reported in previous studies, the addition of HP required a new qualitative analysis to assess potential changes in rheological properties, particularly those related to 3D printing. A platform model with known distances, ranging from (0.5, 1.5, 2.0, and 2.5) cm, was used to evaluate the collapse of filaments. Additionally, the sol-gel transition over time was observed through the inversion test.

Printing of Scaffold

The *BioScaffold v. 2.0* software was used to generate printing data for scaffolds with dimensions of 10 mm × 10 mm × 2 mm, consisting of 10 layers. The printing speed was set to 12 mm/s, and a 410 μm diameter nozzle (20G) was employed. The scaffolds were printed using a 593iCAN printer, equipped with a dual extrusion head system^[11]. The whole process was carried out at room temperature (25°C). After printing, the scaffolds were photographed with a stereomicroscope.

The printability (Pr) index was calculated to assess the shape fidelity of the printed scaffolds. This helps evaluate how accurately the produced structures align with the intended design. The calculation follows Eq. 2^[12,13].

$$Pr = \frac{L^2}{16A} \quad (2)$$

Where: (A) is the pore area, (L) is the pore perimeter, and (Pr) is the printability index.

Results and Discussion

Analysis of Synthesized HP Powder

Figure 1 presents the micrograph of the HP powder following synthesis. Figure 2(a) confirms that the HP powder was successfully obtained, exhibiting the expected purple coloration, a characteristic attributed to the presence of barium carbonate in its composition^[14]. The analysis of Figures 2(b) and 2(c) reveals that the particle distribution in the sample was less homogeneous than anticipated for this pigment. The images highlight that the HP particles display irregular shapes, and many aggregates were observed due to the absence of conventional treatment steps^[3]. Furthermore, the thermal treatments applied resulted in larger particle sizes, indicating that high temperatures promoted stronger bonding between the particles, resulting in a more elongated shape^[3,4].

In Figure 3, the synthesized HP powder exhibits purple coloration. The X-ray diffraction (XRD) pattern confirms the presence of the fluorescent phase associated with HP, with the molecular formula BaCuSi₂O₆. This phase exhibits fluorescence emission when excited in the red/NIR region^[3,4]. Both the excitation and emission bands fall within the first transparency window of biological tissues, which enhances the potential of HP for non-invasive biomedical imaging applications^[3].

From the synthesis of HP, it is difficult to predict the size of the formed inorganic particles, but it can be noted from the observations made by SEM that the distribution and morphological characteristics of the photoluminescent pigment have been verified and match the expected proportions. Can be observed in Figure 2(c) is that HP particles appear as agglomerates, which may obscure some phases that are by products of the synthesis, in this sense SEM micrographs only can show the orientation of the particles, while the XRD provides information about the preferred orientation of the crystals of this material. In the XRD diffractogram, there is no evidence indicating an additional phase or an alteration in the crystal structure; only the characteristic bands of HP are present in Figure 3.

Figure 4 presents the absorbance spectrum of the sintered HP powder over the range of 430 to 1200 nm. Two main absorption peaks are observed in the UV-VIS-NIR region: one at 580 nm (a) and the other at 765 nm (b), with the maximum absorption occurring at 580 nm. These absorption bands correspond to the ²B_{1g} → ²E_g and ²B_{1g} → ²B_{2g} transitions of Cu²⁺ ions present in the crystalline structure of the BaCuSi₂O₆ phase^[1, 2, 14]. Therefore, laser excitation of the sample can be effectively performed using wavelengths near the maximum absorption, such as at 612.76 nm.

The emission spectra of HP at different tempe-

ratures, from 293 to 343 K, are shown in Figure 5, covering wavelengths from 750 to 1100 nm. Under excitation at 612.76 nm, an emission band in the near-infrared (NIR) region of 800 to 1100 nm (²B_{2g} → ²B_{1g} transition) is detected. As the temperature increases, a suppression of fluorescence occurs due to the rise in the non-radiative decay rate of the ²B_{2g} emitting level. It is crucial to mention that the presence of two convoluted emission bands in the emission profile is due to the spectrometer's spectral response^[15]. This phenomenon is valuable for developing intensity ratio-based fluorescent temperature sensors. Figure 6 illustrates the ratio of emission areas at 893 nm and 985 nm, which is useful for precise temperature monitoring.

The intensity ratio (I_{893}/I_{985}) decreases nearly linearly as temperature increases. This behavior demonstrates that the system has the potential to be used as an optical temperature sensor with the Fluorescence Intensity Ratio (FIR) technique. To evaluate the sensor's sensitivity, the data were fitted according to the FIR theory^[16,17], which Δ represents the intensity ratio. The theoretical framework is described in Eq. 3.

$$\Delta = \frac{I_{2j}}{I_{1j}} = \frac{g_2 \sigma_{2j} \omega_{2j}}{g_1 \sigma_{1j} \omega_{1j}} e^{\left[\frac{-\Delta E}{k_B T}\right]} = B e^{\left[\frac{-\Delta E}{k_B T}\right]} \quad (3)$$

In FIR theory, I_i and I_j represent the emission intensities of two energy levels of the ion of interest, g_{ij} is the degeneracy of the emitting level, σ_{ij} is the emission cross-section, and ω_{ij} is the angular frequency of the fluorescence transition from the higher level ($i=2$) to the lower level ($i=1$). Additionally, ΔE represents the energy difference between the thermally coupled levels, and k_B is the Boltzmann constant. For thermometric applications, it is crucial to calculate the sensitivity parameter of the technique for the levels being utilized. This sensitivity reflects how the fluorescence intensity ratio responds to changes in temperature Eq. 4 presents the relative sensitivity parameter (S_r)^[18]:

$$S_r = \frac{1}{\Delta} \frac{d\Delta}{dT} = \left[\frac{\Delta E}{k_B T^2} \right] 100 \quad (4)$$

The absolute sensitivity is calculated as the first-order derivative of Δ with respect to temperature. However, to enable the comparison between different materials, the relative sensitivity (Eq. 4) is presented. In this case, S_r is the derivative of Eq. 3, which is normalized by the function Δ itself and multiplied by 100 to express the values in [%/K] units. Figure 7 shows the relative sensitivity calculated from the data presented in Figure 5 for the same temperature range.

In Figure 7, it can be observed that sensitivity

decreases with increasing temperature, which is expected for FIR thermometers. The maximum sensitivity at 293 K was 0.3%/K. Although this sensitivity is considered low in the literature^[19,20], it should be noted that both the excitation and emission wavelengths fall within the first transparency window of biological tissues^[21], making

it particularly attractive for biomedical applications. Another aspect of potential investigation in future research is the addition of impurities to enhance the fluorescence quenching effect. These impurities would aim to increase the phonon energy, further improving the material's performance.

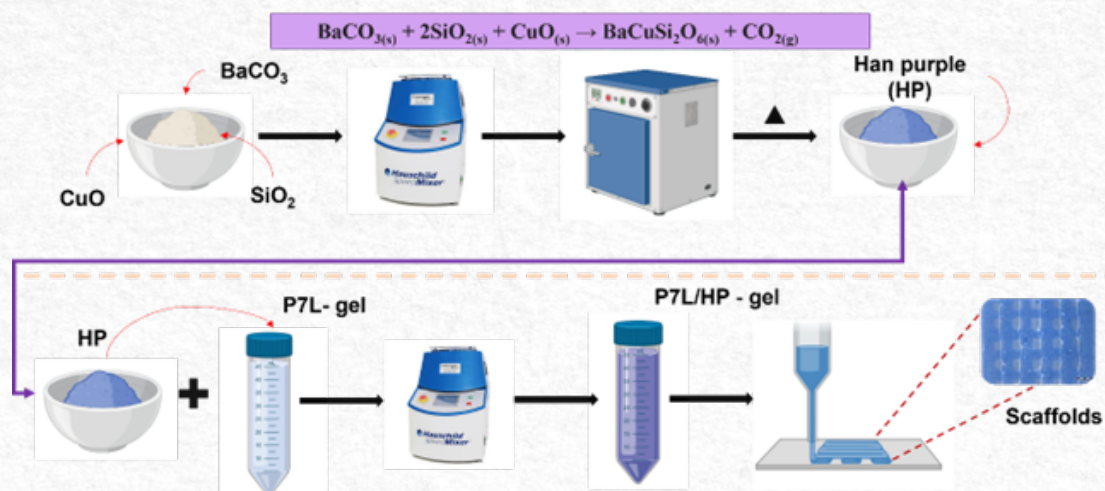


Figure 1 - Illustration of the pigment synthesis process, gel preparation, and sample printing. The images were created using the BioRender® visual tool. Source: Santos et al.

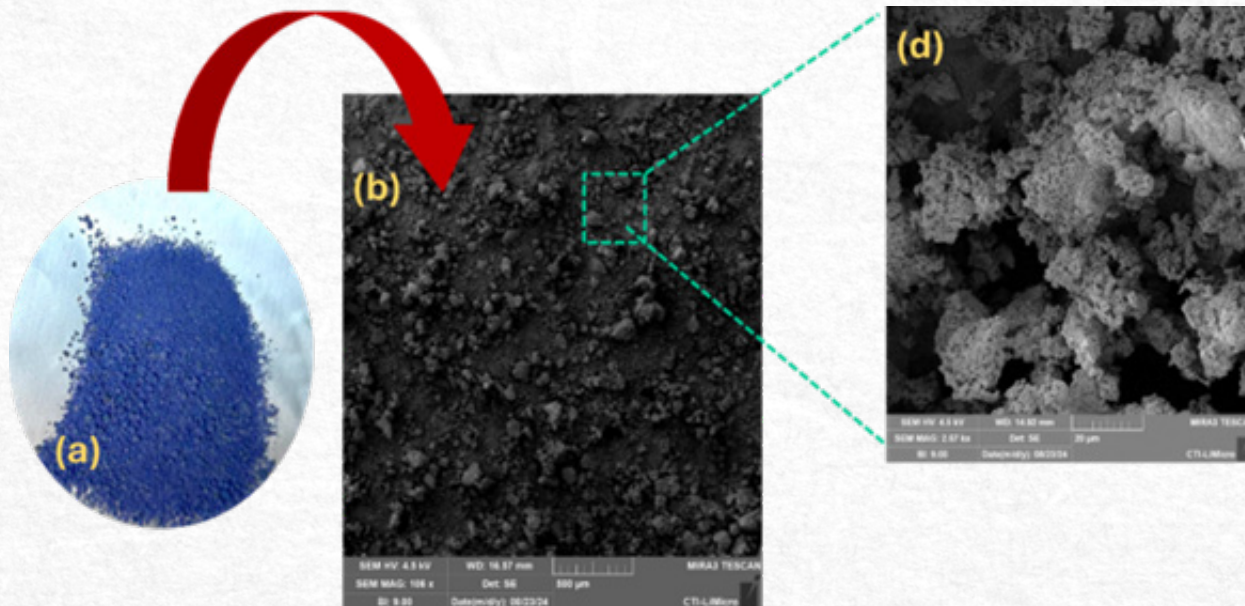


Figure 2 - Micrograph of HP powder after synthesis and morphology of its particles. Where (a) post-sintering powders and (b and c) correspond to powder morphology. Source: Santos et al.

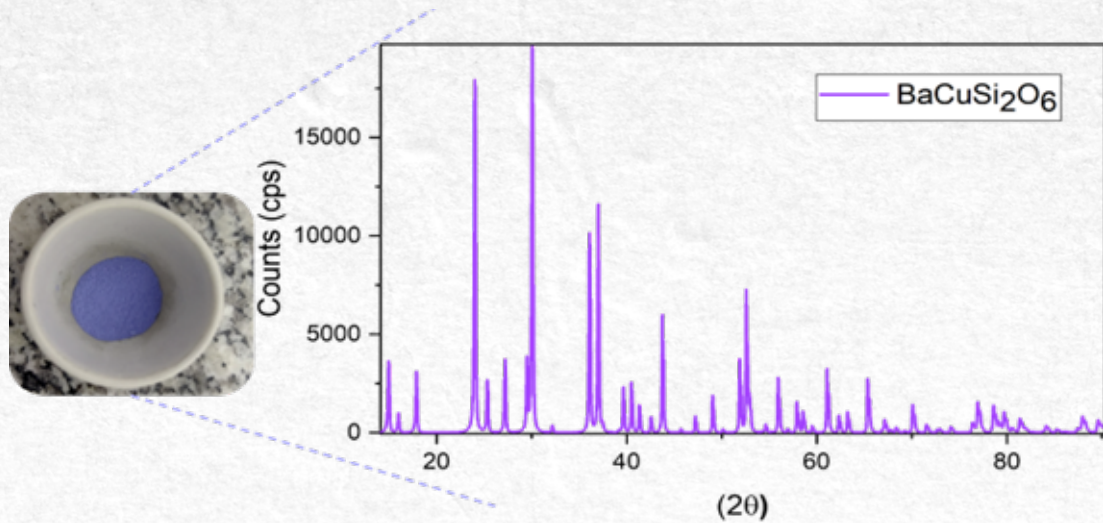


Figure 3 - Diffractogram of the synthesized sample; peaks are characteristics of HP pigment. Source: Santos et al.

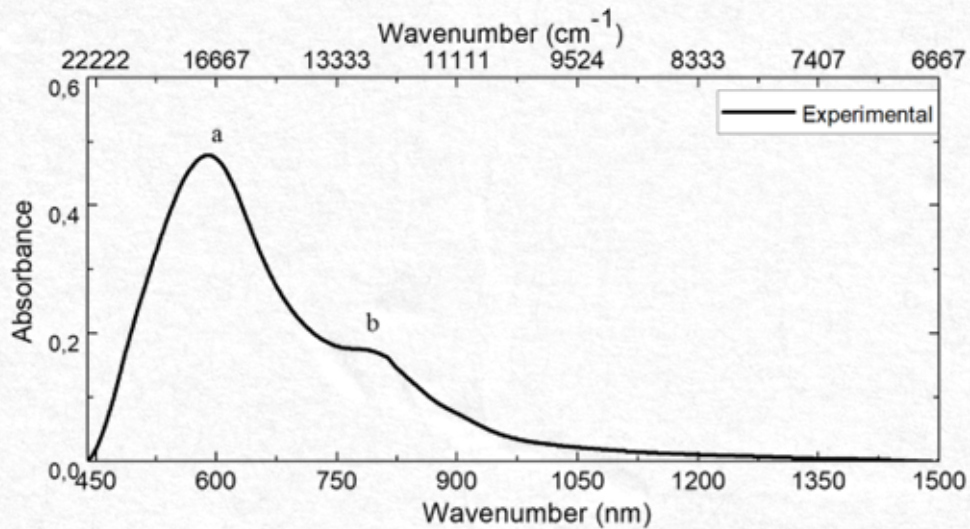


Figure 4 - Absorbance spectrum in the UV-VIS-NIR region for the synthesized HP sample. Source: Santos et al.

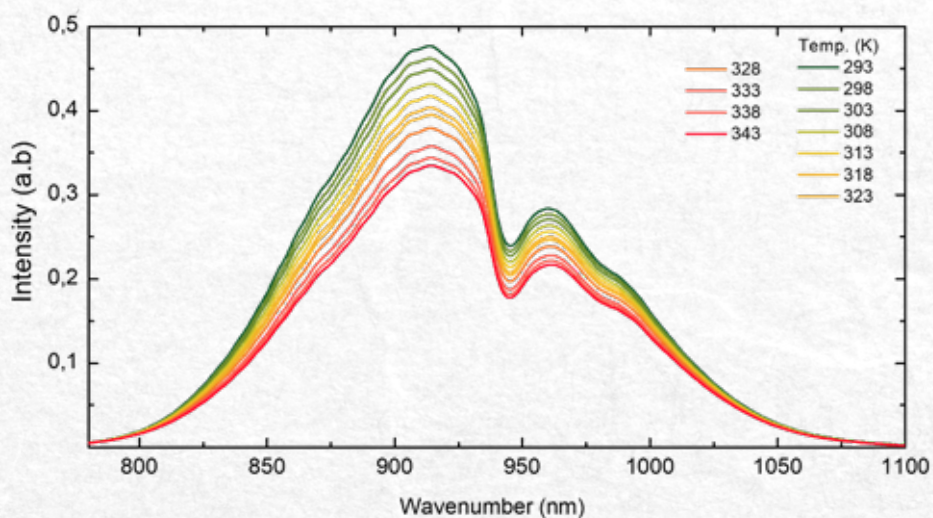


Figure 5 - HP emission at different temperatures, in the range of 293 to 343 K. Source: Santos et al.

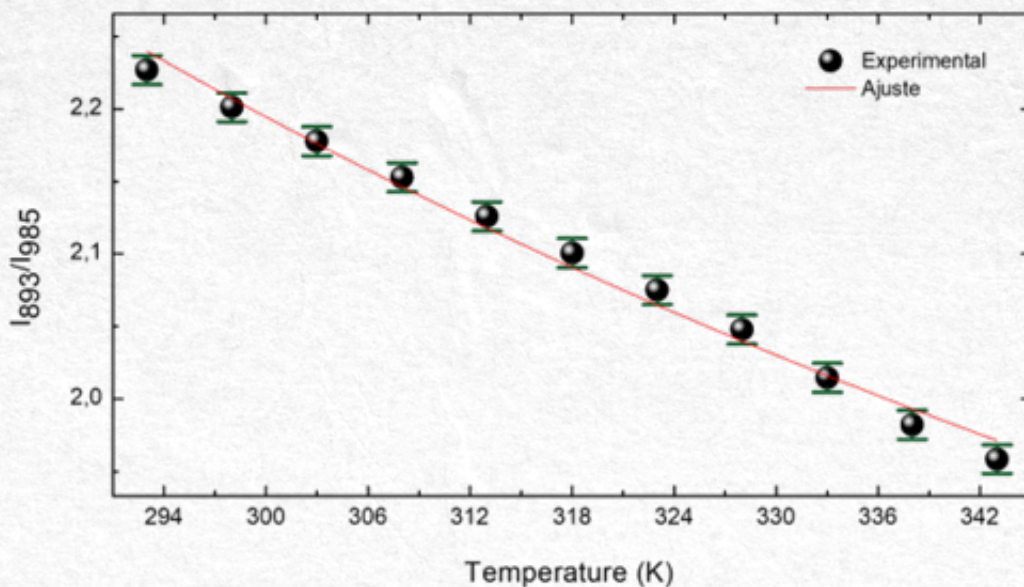


Figure 6 - Intensity ratio for emissions centered at 893 and 985 nm (I_{893}/I_{985}). Source: Santos et al.

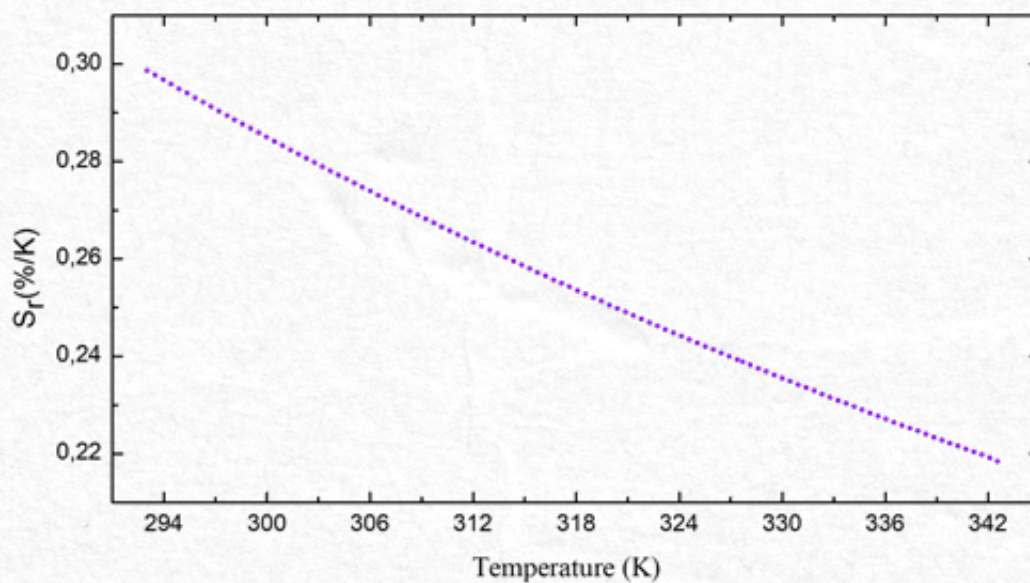


Figure 7 - Relative sensitivity (S_r) in the range of 293 to 343 K. Source: Santos et al.

Analysis of HP-Doped Gels

To investigate the compositional details of the gels produced with and without the incorporation of the HP pigment, the compositions were analyzed using Fourier Transform Infrared Spectroscopy (FTIR), as shown in Figure 8. It is observed that all the curves in Figure 8 exhibit similarities, with slight differences compared to the precursor gel P7L^{HP0%}. The peaks corresponding to the P7L^{HP0%} formulation was previously described by Daguano et al. (2022)^[7]. The bands in the 3677–3012 cm⁻¹ region in the P7L^{HP0.5%} and P7L^{HP2%} compositions are linked to the O-H stretching, which comes from the PEG precursor solution. The peaks at 2963 cm⁻¹ and 2870 cm⁻¹ correspond to the C-H methylene stretching from the PEG precursor. Additionally, the peaks at 1532 cm⁻¹, 1463 cm⁻¹, and 1246 cm⁻¹ are associated with C-H stretching from methyl groups^[22].

The peaks at 994 and 980 cm⁻¹ can be attributed to the Si-O and Si-O-C bonds, respectively, due to the adsorption of the nanosilicate Laponite and silica present in HP, also detectable in the gel base^[7,9]. The characteristic HP peaks (BaCuSi₂O₆), observed at 800 and 1100 cm⁻¹, are associated with Si-O antisymmetric stretching. It is suggested that the peaks in the 670 cm⁻¹ region correspond to the Cu-O

group, although they may be overlapping due to the presence of Laponite nanosilicates and HP silica. Finally, the formation of new peaks in the regions of 1645 and 845 cm⁻¹ is observed in the compositions P7L^{HP0.5%} and P7L^{HP2%}. The peak at 845 cm⁻¹ can be attributed to the Cu-O group^[2]. The peak at 1645 cm⁻¹ is related to the vibrations of the carbonyl group C=O which may be produced in the PEG polymer chain through oxidation, a structural change possibly induced by HP presence. When the PEG gel is mixed with the inorganic HP and, if the photoluminescent compound could act as a photoactivator (generating free radicals) when exposed to UV/Vis light, these radicals can attack the PEG bonds and cause its photo-oxidation, generating carbonyl groups, as evidenced in the FTIR spectrum (peak at 1645 cm⁻¹) of the gels doped with HP^[23]. This phenomenon appears to be independent of the HP concentration within the gel, relying instead on the mere presence of the photoluminescent compound. As illustrated in Figure 10(c), the photoactivation of HP particles by visible light suggests that this process is more likely to occur in environments where the preparation or use of these gels involves oxygen and intense light exposure, or during their storage.

To assess the dispersion of HP particles, discs

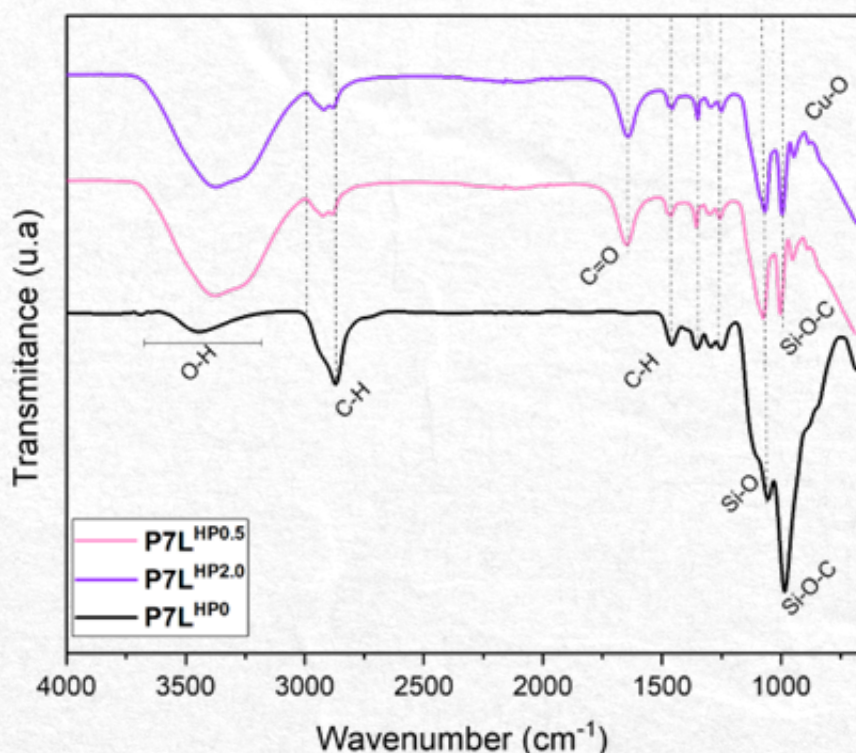


Figure 8 - FTIR analysis of P7LHP0.5% and P7LHP2% gels with HP content of 0.5 and 2% respectively. The P7LHP0% gel was used as a control due to the absence of pigments. Source: Santos et al.

with a 10 mm-diameter were produced, as illustrated in Figure 9. The addition of HP resulted in a color shift toward a bluish hue, with pigmentation intensity increasing proportionally to the HP concentration. Particle dispersion was considered satisfactory in all formulations; however, the P7L^{HP2%} sample exhibited a more homogeneous distribution of particles. In the 0.5% HP formulation, some noticeable particle agglomerations were observed, more prominent than in the 2% HP discs.

Preliminary qualitative tests were carried out to assess the suitability of the photoluminescent gels for printing, as shown in Figure 10. In Figure 10(a),

the gel-filled tubes were kept upside down for 24 hours without any movement observed, indicating sufficient stability for the printing process. Previous studies by Santos and Daguano provided a detailed description of the rheological properties of the base gel PEG/Laponite (PL), offering a solid understanding of the rheological properties of this gel [7,9]. In the case of gel formulations with HP, given their low percentage, it is possible that this does not generate substantial changes in its rheological behavior. These tests also contributed to a better understanding of the gelation process, confirming promising characteristics for printing [24,25]

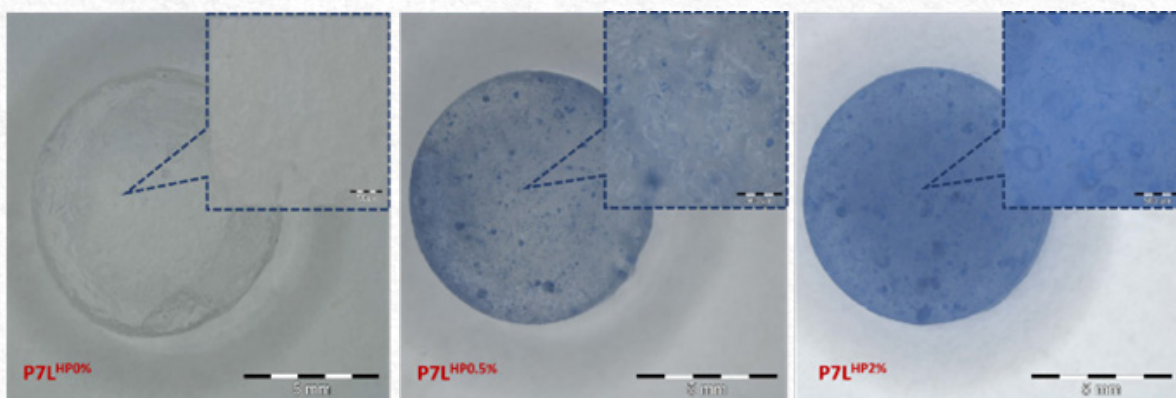


Figure 9 - Tablets made from gels formulated with doping concentrations of: 0%, 0.5%, and 2% HP. Source: Santos et al.

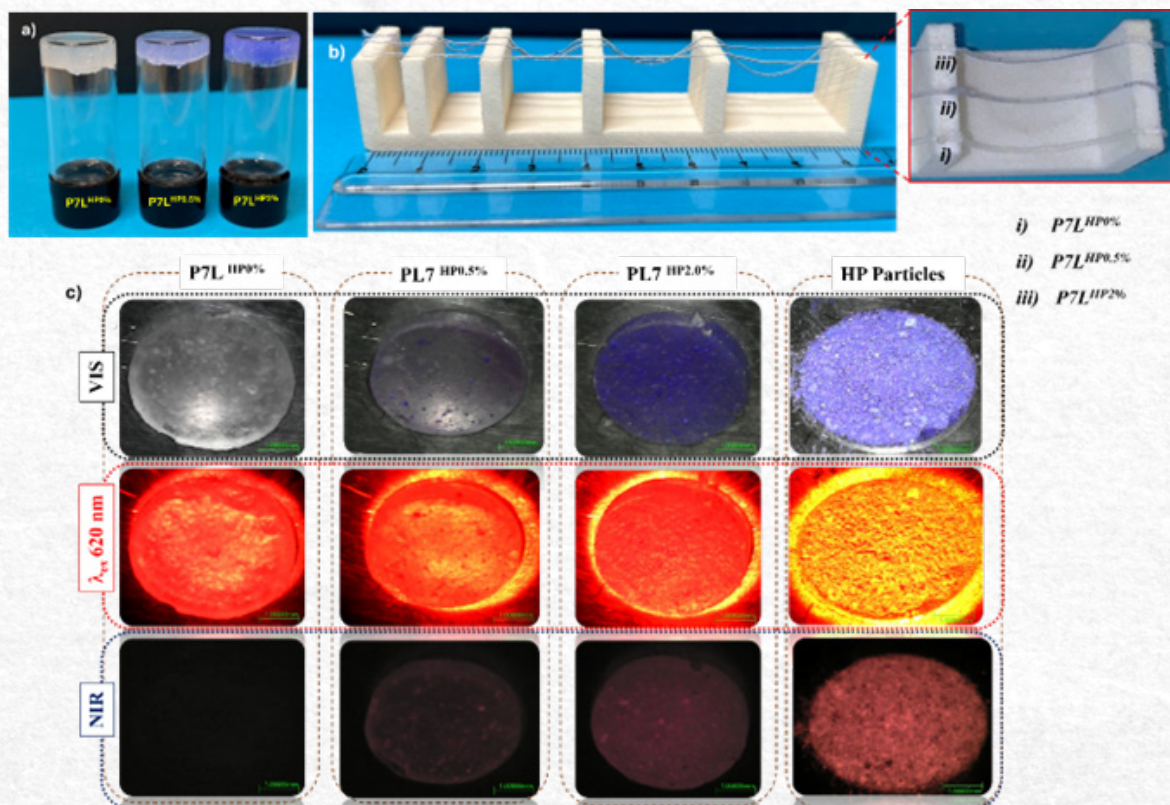


Figure 10 - (a) The sol-gel transition of gels over time through inversion test (after 24 hr); (b) Filament collapse testing and (c) Images of the samples at visible light (VIS), under excitation with red light (λ_{exc} 620 nm), and the fluorescence NIR image (NIR). Source: Santos et al.

In the initial assessment, a manual extrusion pre-test of the gel filaments was carried out, depicted in Figure 10(b). This basic test aimed to evaluate how well the material can be printed and how filaments are formed [26,27]. After pushing the gels onto a surface, uninterrupted rods were created. Nevertheless, a significant deflection of the rods was observed due to the weight of the material, its viscosity, rheological characteristics, gravity's influence, and manual extrusion force. Despite this pronounced deflection, particularly over distances around 2.5 cm, no filament rupture occurred, ensuring that the material exhibited adequate elasticity and stability for subsequent gel printing.

In Figure 10(c), discs were molded from the gels to evaluate their luminescent properties. The samples were excited with monochromatic light at a central wavelength of 620 nm, close to the reported excitation maximum for HP [3]. The P7L^{HP0.5%} and P7L^{HP2%} gels exhibited fluorescence, attributed exclusively to the presence of the HP pigment, as illustrated in the image. Furthermore, the intensity of the NIR light emitted increased proportionally with the HP concentration in the discs. In contrast, the dark-field image reveals

that the disc without HP (P7L^{HP0%}) did not exhibit NIR fluorescence, demonstrating that the base gel alone lacks photoluminescent properties, which are entirely dependent on the presence of HP [2,28].

Following the preliminary tests conducted with the gels, the extrusion-printed scaffolds are presented in Figure 11. During the printing process, the samples containing 2% HP particles encountered significant challenges compared to the gels with 0.5% HP. These difficulties can be attributed to the high particle concentration and irregular morphology, which resulted in flow issues during printing. The irregularity of the particles led to the formation of aggregates, hindering the flow of the gel through the 410 μm diameter syringe nozzle, complicating the extrusion of gels with higher pigment concentration. However, this issue could be mitigated by using nozzles with larger diameters. Despite these challenges, as illustrated in Figure 11, the printed scaffolds exhibited good shape fidelity, with Pr values of 0.92 ± 0.06, 0.87 ± 0.01, and 0.89 ± 0.03 for the P7L^{HP0%}, P7L^{HP0.5%}, and P7L^{HP2%} gels, respectively. These findings suggest that the scaffolds closely resemble the intended design [26,27].

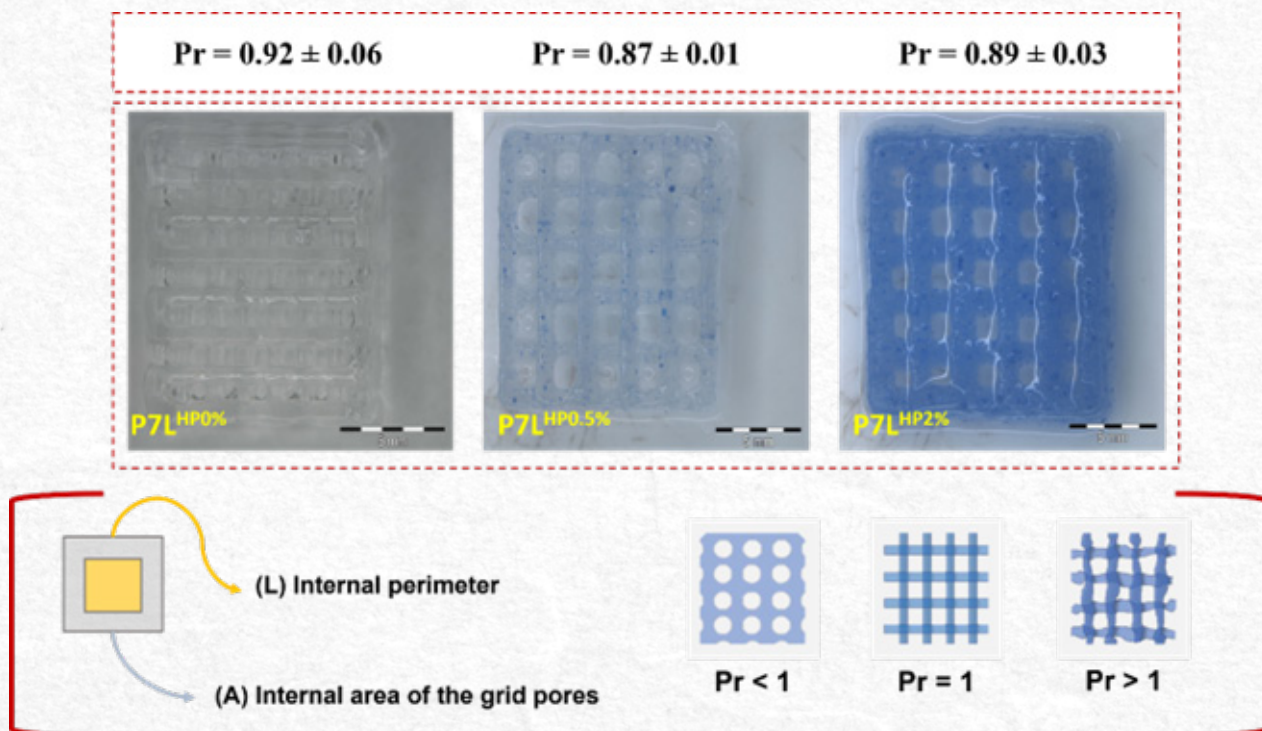


Figure 11 - Scaffolds obtained after printing gels containing HP at levels of 0.5% and 2% in their composition. Source: Santos et al.

Excitation and Emission Spectroscopy – Map of Printed Gels

As demonstrated in Figures 8 and 10, the dispersion of HP pigment was more efficient at the 2% concentration. For this reason, the intensity map of the scaffold was analyzed for this gel, as shown in Figure 12.

The excitation and emission map of the P7L^{HP2%} sample displays a maximum emission photoluminescence at 925 nm and maximum excitation at 625

nm, which are values consistent with those reported in the literature^[2,21]. This is likely due to the energy levels of copper (Cu^{2+}), with the transitions selected for this optical thermometry analysis, indicating a potential application of this material in optical thermometry. However, it was also observed that the fluorescence of the material could be affected by the lack of particle treatment, as is typically performed with Egyptian Blue (EB), a pigment like HP^[4].

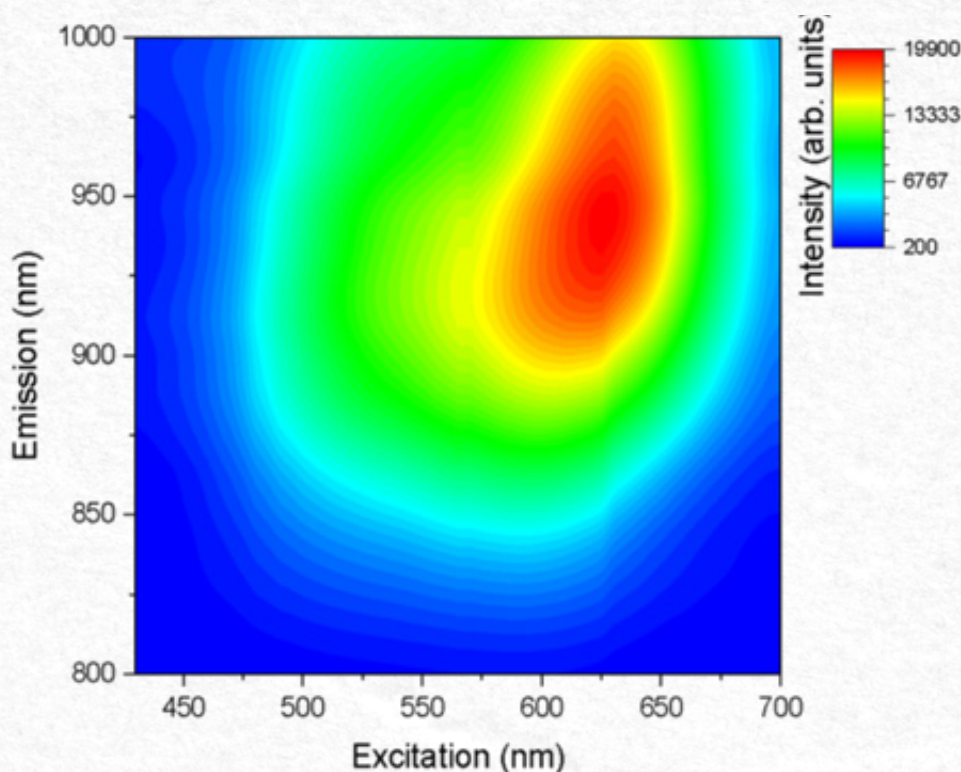


Figure 12 - Excitation versus emission map of the Scaffold produced with the P7LHP2% gel. Source: Santos et al.

Conclusion

In this study, we synthesized the HP pigment and explored its application in PEG-Laponite-based gels with concentrations of 0.5% and 2%. The resulting formulations exhibited luminescent properties and demonstrated good feasibility for constructing three-dimensional structures. Characterization of the synthesized compound confirmed the successful production of HP, which appeared as elongated particles with heterogeneous distribution. Furthermore, the incorporation of HP at the tested concentrations resulted in adequate dispersion within the gel network, as evidenced by photographic images. FTIR analysis verified the interactions between the PEG-Laponite phases and HP, identifying both physical interactions and the formation of new functional groups. Even when dispersed in the polymer matrix, HP retained its fluorescent properties, albeit with reduced intensity. In addition, the formulations exhibited

favorable extrusion characteristics during 3D printing, culminating in the successful fabrication of scaffolds with high shape fidelity. These findings indicate that the use of HP as a dispersed phase in polymeric gels offers a promising innovation, with potential applications in biotechnology, such as in temperature sensors, near-infrared (NIR) imaging, and photothermal applications.

Acknowledgments

This paper is dedicated to the memory of Dr. Jorge V. Lopes da Silva. Sadly, he passed away before the submission of this study. We want to recognize not only his contribution to the conceptualization of this interesting line of research, but also his unconditional support for all of us during our careers as researchers.

We are grateful to Igor Leandro de Oliveira (CTI Renato Archer) for the mechanical technical support in the temperature-dependent emission experiments.

The authors would like to thank FINEP for

funding the EMUTISAÚDE project (grant no. 01.18.0027.00), and the CNPq/PCI program (process nos. 301583/2023-4, 300038/2024-0, and 300933/2024-0) for the financial support. This work was also supported by the National Council for Scientific and Technological Development (CNPq) (grant nos. 312216/2017-3 and 407680/2021-7), and the São Paulo Research Foundation (FAPESP) (process no. 2019/11950-6).

References

- [1]. Bhatia SK, Bhatia S, Inda-Webb ME, Kourmentza K, Moon TS, Singh V, et al. Biotechnology for sustainable materials: innovating today for a greener tomorrow. *Biotechnology for Sustainable Materials* 2024;1(1).
- [2]. Chen Y, Zhang Y, Feng S. Hydrothermal synthesis and properties of pigments Chinese purple BaCu-Si₂O₆ and dark blue BaCu₂Si₂O₇. *Dyes and Pigments* 2014;105:167–73.
- [3]. Pozza G, Ajò D, Chiari G, De Zuane F, Favaro M. Photoluminescence of the inorganic pigments Egyptian blue, Han blue and Han purple. *J Cult Herit* 2000;1(4):393–8.
- [4]. Johnson-McDaniel D, Salguero TT. Exfoliation of Egyptian blue and han blue, two Alkali earth copper silicate-based pigments. *Journal of Visualized Experiments* 2014;(86):1–10.
- [5]. Johnson-McDaniel D, Barrett CA, Sharafi A, Salguero TT. Nanoscience of an ancient pigment. *J Am Chem Soc* 2013;135(5):1677–9.
- [6]. Iguchi M, Hiraga Y, Kasuya K, Aida TM, Watanabe M, Sato Y, et al. Viscosity and density of poly(ethylene glycol) and its solution with carbon dioxide at 353.2K and 373.2K at pressures up to 15MPa. *J Supercrit Fluids* [Internet] 2015; 97:63–73. Available from: <https://www.sciencedirect.com/science/article/pii/S0896844614003490>
- [7]. Daguano JKMB, Giora FC, Santos KF, Pereira ABGC, Souza MT, Dávila JL, et al. Shear-thinning sacrificial ink for fabrication of Biosilicate® osteoconductive scaffolds by material extrusion 3D printing. *Mater Chem Phys* 2022;287.
- [8]. Davern JW, Hipwood L, Bray LJ, Meinert C, Klein TJ. Addition of Laponite to gelatin methacryloyl bioinks improves the rheological properties and printability to create mechanically tailorable cell culture matrices. *APL Bioeng* 2024;8(1).
- [9]. Santos KF, Dávila JL, D'ávila MA, Rodas ACD, da Silva JVL, Daguano JKMB. Rheological study of PEG-Laponite-alginate composite hydrogels aiming 3D extrusion-based printing. *Revista Materia* 2022;27(2).
- [10]. Brunchi CE, Morariu S. Laponite®—From Dispersion to Gel—Structure, Properties, and Applications. *Molecules* 2024;29(12).
- [11]. Dávila JL, Manzini BM, Lopes da Fonsêca JH, Mancilla Corzo IJ, Neto PI, Aparecida de Lima Montalvão S, et al. A parameterized g-code compiler for scaffolds 3D bioprinting. *Bioprinting* [Internet] 2022; 27: e 00222. Available from: <https://www.sciencedirect.com/science/article/pii/S240588662200032X>
- [12]. Jongprasitkul H, Turunen S, Parihar VS, Kellomäki M. Two-step crosslinking to enhance the printability of methacrylated gellan gum biomaterial ink for extrusion-based 3D bioprinting. *Bioprinting* 2022;25.
- [13]. Fu Z, Naghieh S, Xu C, Wang C, Sun W, Chen X. Printability in extrusion bioprinting. *Biofabrication* 2021;13(3).
- [14]. Zhang Z, Ma Q, Berke H. Man-made blue and purple barium copper silicate pigments and the pabstite (BaSnSi₃O₉) mystery of ancient Chinese wall paintings from Luoyang. *Herit Sci* 2019;7(1).
- [15]. Binet L, Lizion J, Bertaina S, Gourier D. Magnetic and New Optical Properties in the UV-visible Range of the Egyptian Blue Pigment Cuprorivaite CaCuSi₄O₁₀. *Journal of Physical Chemistry C* 2021;125(45):25189–96.
- [16]. Wade SA, Collins SF, Baxter GW. Fluorescence intensity ratio technique for optical fiber point temperature sensing. *J Appl Phys* [Internet] 2003;94(8):4743–56. Available from: <https://pubs.aip.org/jap/article/94/8/4743/471248/Fluorescence-intensity-ratio-technique-for-optical>.
- [17]. Morassuti CY, Nunes LAO, Lima SM, Andrade LHC. Eu³⁺ - doped alumino-phosphate glass for ratiometric thermometer based on the excited state absorption. *J Lumin* 2018;193(August 2017):39–43.
- [18]. Morassuti CY, Finoto S, Silva JR, Lima SM, Andrade LH da C. A Novel Route for a Fluorescent Temperature Sensor Based on the Reabsorption Process in Sm²⁺-Doped KCl. *Phys Status Solidi B Basic Res* 2020;257(8):1–6.
- [19]. Lalla EA, León-Luis SF, Monteseuro V, Pérez-Rodríguez C, Cáceres JM, Lavín V, et al. Optical temperature sensor based on the Nd³⁺ infrared thermalized emissions in a fluorotellurite glass. *J Lumin* [Internet] 2015; 166:209–14. Available from: <http://www.sciencedirect.com/science/article/pii/S0022231315002768>
- [20]. Morassuti CY, L Silva AP, Nunes LAO, Lima SM, Andrade LHC. Effect of radiative loss mechanisms on FIR thermometric parameters of Nd³⁺-doped lithium tellurite glasses. *Journal of Rare Earths* [Internet] 2023 Available from: <https://linkinghub.elsevier.com/retrieve/pii/S1002072123001539>.
- [21]. Smith AM, Mancini MC, Nie S. Second window for in vivo imaging. *Nat Nanotechnol* [Internet] 2009;4(11):710–1. Available from: <http://dx.doi.org/10.1038/nnano.2009.326>
- [22]. Lin-Vien D, Colthup NB, Fateley WG, Grasselli JG (Professor). *The Handbook of infrared and raman*

- characteristic frequencies of organic molecules. Academic Press 1991.
- [23]. Fortunato G, Tatsi E, Corsini F, Turri S, Griffini G. Stimuli-Responsive Luminescent Solar Concentrators Based on Photoreversible Polymeric Systems. *ACS Appl Polym Mater* 2020;2(9):3828–39.
- [24]. Rafael D, Andrade F, Martinez-Trucharte F, Basas J, Seras-Franzoso J, Palau M, et al. Sterilization procedure for temperature-sensitive hydrogels loaded with silver nanoparticles for clinical applications. *Nanomaterials* 2019;9(3).
- [25]. Dessì M, Borzacchiello A, Mohamed THA, Abdel-Fattah WI, Ambrosio L. Novel biomimetic thermo-sensitive β -tricalcium phosphate/chitosan-based hydrogels for bone tissue engineering. *J Biomed Mater Res A* 2013;101(10):2984–93.
- [26]. Ren H, Liu Y, Zhang R, Zheng Y, Zhao T, Han J, et al. Near-infrared carbon quantum dots from PEG-based deep eutectic solvents for high-accuracy quantitative analysis of naphthenic acids in wastewater. *J Environ Chem Eng* 2023;11:109988.
- [27]. Temirel M, Dabbagh SR, Tasoglu S. Shape Fidelity Evaluation of Alginate-Based Hydrogels through Extrusion-Based Bioprinting. *J Funct Biomater* 2022;13(4).
- [28]. Naghieh S, Chen X. Printability—A key issue in extrusion-based bioprinting. *J Pharm Anal* 2021;11(5):564–79.

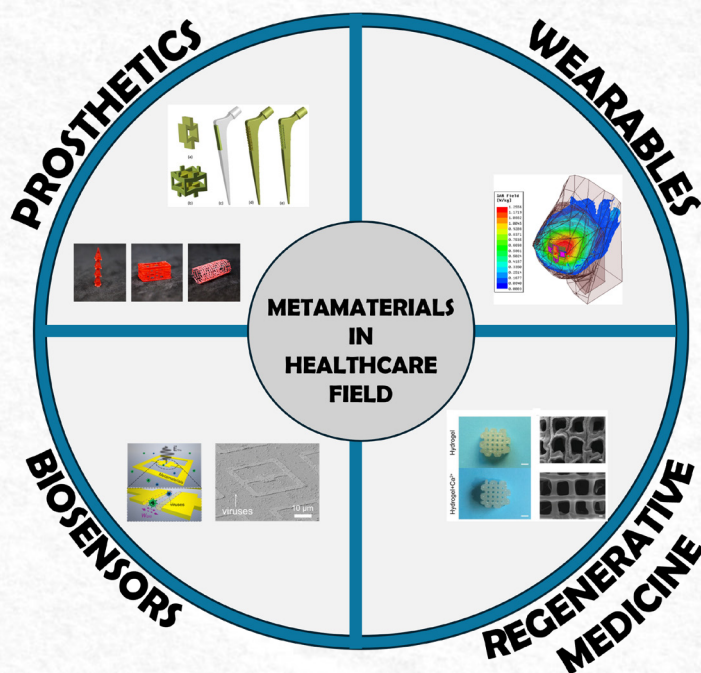


A Brief review on metamaterials applied to the healthcare field

L.M.R. Machado^{1*}; P.Y.Noritomi¹; M.A.Davila²

*Corresponding author: E-mail address: leonardo.machado@cti.gov.br

Received: October 2024; Accepted: December 2024.



Abstract: Metamaterials refer to any modification of the physical behavior of an existing material through the structured arrangement of repetitive patterns, procedurally generated, which can directly influence its response to deformation, thermal dissipation, and vibrational control. This creates possibilities for solutions that were previously difficult to achieve using conventional materials such as metals, ceramics, polymers, and their composites. The use of this technology has gained momentum with the advent of 3D printing, which has made it possible to apply and create these structures for practical validation. The first structures were modeled at the beginning of the last century, such as the creation of patterns to generate anomalous properties, with diverse applications in fields like optics, thermodynamics, and mechanics, as it allows for material design tailored to specific applications. As a result, applications have expanded to various scales, from millimeter-engineered materials to the nanoscale, drawing the attention of researchers from different fields, including healthcare. This interest stems from the vast array of possibilities and innovations driven by advancements in materials and additive manufacturing, combining these fields to generate increasingly adaptive solutions. In this paper, the concept of metamaterials will be introduced, followed by an exploration of various applications of this technology, including medical equipment, devices, prosthetics, orthotics, and implants, as well as potential future applications of this technology in healthcare.

Keywords: Metamaterials. 3D Printing. Advanced Healthcare. Advanced Materials.

¹Division DITPS, Renato Archer Center for Information Technology, Campinas, SP, Brazil.

² State University of Campinas, Faculty of Mechanical Engineering, Campinas, SP, Brazil.

Introduction

Metamaterials can be characterized as artificial materials with distinct properties not found in conventional materials, specifically designed to perform targeted functions⁽¹⁾. The first documented study on the development of this type of material was conducted in 1898 by Jagadis Chunder Bose, a physicist researching electromagnetism. Bose proposed the creation of a material with repetitive helix-shaped structures that could modify the behavior of microwaves⁽²⁾. This theory laid the foundation for the basic concept of characterizing a metamaterial: the presence of a repetitive structure with a unitary geometry, arranged throughout the model, specifically designed to alter the behavior of a physical property.

Following these theories, new applications emerged, gradually attracting researchers from various fields of physics, who applied the principles of structured materials to phenomena such as deformation control and the manipulation of other types of waves, such as light, sound, and thermal flows⁽³⁾. However, the complexity of these structures made them difficult to manufacture, which delayed the practical application of metamaterials until the early 21st century. The resurgence was driven by the advent and popularization of 3D printing, which allowed for greater design freedom, enabling the first metamaterial cells to move from theoretical models to physical prototypes, validated through practical testing.

General Classification of Metamaterial

Metamaterials can be subdivided according to their application⁽⁴⁾, including thermal, electromagnetic, mechanical, and acoustic categories. In general, their properties involve generating a response characterized by negative coefficients, leading to unnatural behaviors.

An example is auxetic materials, which expand along multiple axes without a reduction in cross-section, due to the distribution of deformation through specifically designed cells within the material⁽⁵⁾⁽⁶⁾.

Another fundamental classification pertains to the number of axes in which the unit cell is present in the material⁽⁷⁾ which can be in two-dimensional (planar), or three-dimensional (Figure 1).

For electromagnetic metamaterials, also could be classified by Permittivity (ϵ) a fundamental electrical property that describes a material's ability to polarize in response to an applied electric field. Simply put, this property indicates how easily a material can be polarized, leading to the formation of electric dipoles and by magnetic permeability (μ), a magnetic property that defines a material's ability to magnetize under the influence of an applied magnetic field. This characteristic reflects the ease with which magnetic dipoles can form within the material⁽⁸⁾

The combined analysis of ϵ and μ enables the classification of materials into four distinct categories, represented by quadrants in a Cartesian graph⁽⁹⁾. In this context, the values of ϵ and μ define the electromagnetic properties and specific behaviors of each class:

Quadrant I ($\epsilon > 0, \mu > 0$): Represents conventional materials, encompassing most naturally occurring substances.

Quadrant II ($\epsilon < 0, \mu > 0$): Includes metamaterials with a negative refractive index, known for unique phenomena such as negative refraction and perfect focusing.

Quadrant III ($\epsilon < 0, \mu < 0$): Comprises another type of metamaterial with a negative refractive index, exhibiting properties similar to those in Quadrant II.

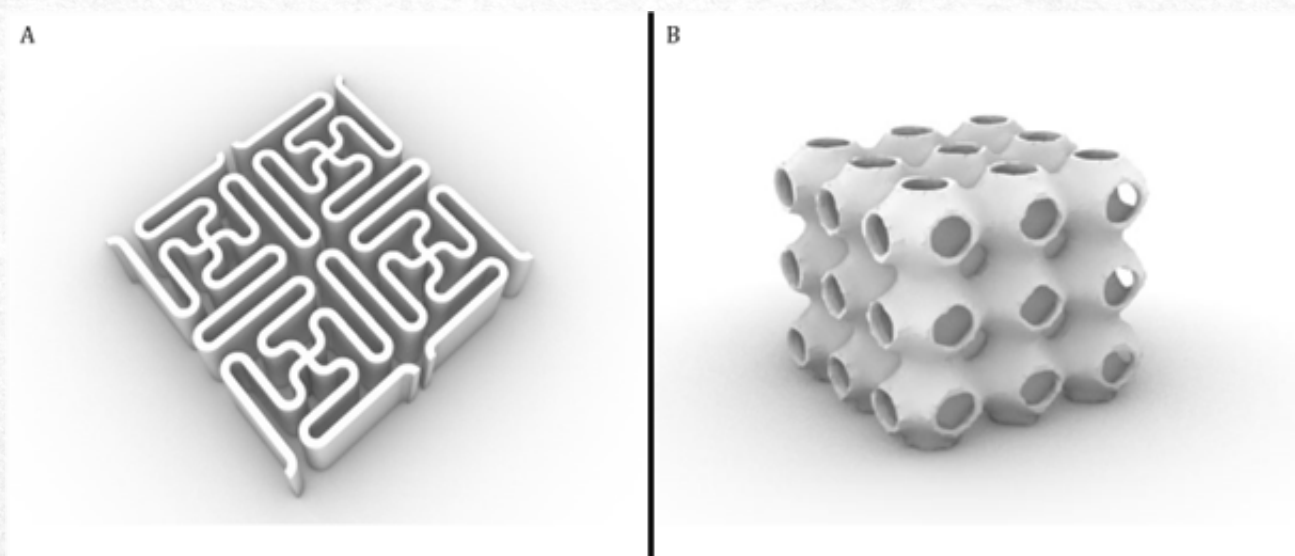


Figure 1 - Representation of different cellular configuration types, A planar cell and B a 3D cell.

Source: Author

Quadrant IV ($\epsilon > 0$, $\mu < 0$): Contains metamaterials that are less explored but show significant potential for specific applications.

In addition to classifying materials, the values of ϵ and μ are directly related to various physical quantities that influence the behavior of electromagnetic waves. For instance, the refractive index of a material is determined by these two parameters, with metamaterials located in Quadrants II and III exhibiting a negative refractive index, enabling phenomena such as anomalous refraction⁽¹⁰⁾. The impedance of a material, which establishes the relationship between the electric and magnetic fields of an electromagnetic wave, is also significantly influenced by ϵ and μ . Furthermore, the phase velocity of an electromagnetic wave in a medium depends directly on these values. In metamaterials with a negative refractive index, the phase velocity may become negative, resulting in counterintuitive properties.

This framework for classification and analysis provides a robust theoretical basis for studying and developing advanced materials with engineered electromagnetic properties. Metamaterials have revolutionized fields such as optics, telecommunications, and energy, enabling the emergence of innovative applications and cutting-edge technologies⁽¹¹⁾

Thermal Metamaterials

Natural materials typically exhibit isotropic properties regarding their thermal dissipation behavior⁽¹²⁾, meaning that all portions of a material dissipate thermal energy uniformly throughout its volume. Thermal metamaterials are designed to modify this isotropic behavior into a controlled anisotropic response⁽¹³⁾, enabling the internal heat flow of a piece to be altered through the arrangement of the material's internal structures, such as the behavior seen in carbon nanotubes.

Examples of functionalities for this type of material include thermal filters⁽¹⁴⁾, structures that facilitate the flow of specific bands of thermal radiation through an insulating medium, enhancing the efficiency of thermosensitive devices such as certain categories of solar panels. These structures typically consist of stacked plates made from two or more materials, creating patterns that, under the effect of heating, allow the selection of the wavelength spectrum that can pass through the assembly.

Other possibilities include flow control structures⁽¹⁵⁾, which regulate thermal dissipation to maintain the functionality of temperature-sensitive components, such as electronic or optical devices⁽¹⁶⁾, preventing overheating or enabling their use in harsh conditions.

Lastly, there are metamaterials with shape memory properties, where heat alters their structure. An example is engineered polymers, which deliberately change their form to selectively modify the behavior of lenses⁽¹⁷⁾.

Electromagnetic Metamaterials

The primary function of electromagnetic metamaterials is to modify behaviors related to electromagnetism, enabling the alteration of electromagnetic fields and wave behavior by manipulating two fundamental physical principles: electromagnetic permittivity and permeability⁽¹⁸⁾. These properties describe how a material is affected by an electromagnetic field and how it responds to magnetization. Such control allows the replication of the functionality of well-known devices, such as antennas and satellites, at much smaller scales, reducing the number of components required for their operation⁽¹⁹⁾.

Among the applications are electromagnetic filters⁽²⁰⁾, which block the propagation of specific wave sizes, thereby enhancing the efficiency of sensors and electromagnetic induction devices, such as fast-charging batteries. In addition to filters, metamaterials can be designed to absorb⁽²¹⁾ or reflect electromagnetic fields⁽²²⁾, making them useful in creating barriers and protective shields, especially for high-power field applications, such as MRI machines and other medical imaging devices.

Optical Metamaterials

Optical metamaterials can be considered a variation of electromagnetic metamaterials, as they fundamentally aim to alter the natural behavior of materials concerning their interaction with waves. However, in this case, the waves pertain to light and its emission spectra, such as infrared, ultraviolet, and others⁽²³⁾. To achieve this, the refractive and absorption coefficients of the material are manipulated.

Applications in this category include the selective variation of focal points⁽²⁴⁾, which allows for the creation of multifocal or controlled monofocal points, even in flat lenses. This technology can produce more effective and compact lasers, color filters⁽²⁵⁾ that block specific light spectra to reduce interference in optical sensors, and cloaking cells⁽²⁶⁾, which are designed to deform light projected onto an object. These cells function as a form of camouflage by bending light to create an illusion of transparency, preventing direct interaction with the light and allowing visibility of what lies behind the object.

Mechanical Metamaterials

Mechanical metamaterials exhibit significant variation from the principles of operation of other metamaterials, as they generally work with structures at the millimeter scale. This is because they aim to modify properties more related to material deformation and stiffness⁽²⁷⁾, thus, their unit cells do not need to be as small as those of other metamaterials, which must be produced at the same scale as the phenomena they are designed to interact with⁽²⁸⁾.

Among the applications are auxetic cells(29), which alter deformation behavior, create impact-resistant structures⁽³⁰⁾, controlled points of elastic deformation for the generation of hinges, and adaptive structures⁽³¹⁾ that facilitate the biomechanical interaction of prosthetics and orthotics⁽³²⁾.

In addition to auxetic properties, these materials can exhibit other interesting behaviors, such as shape memory⁽³³⁾, which allows for the creation of predetermined patterns that change in response to applied forces. This capability enables the development of self-compensating structures and stress converters that, like auxetics, manipulate the forces acting on the material to cancel stress dissipation through inversion. This is achieved by employing structures with variable stiffness points through the combination of independent plates⁽³⁴⁾.

Acoustic Metamaterials

Similar to mechanical metamaterials, this category operates on the principle of varying responses to deformation and stiffness⁽³⁵⁾. However, the application of their cells focuses on the control, modulation, cancellation, and amplification of sound waves, utilizing variations in the vibration patterns of the components to manipulate sound wave propagation in space⁽³⁶⁾. This capability allows for directing sound toward a specific point or altering its amplitude to change the frequency through the vibrations of the metamaterial cell itself, as well as isolating frequencies to prevent distortion in sensors.

Examples of applications include acoustic lenses⁽³⁷⁾,

which can generate directed pulses of vibration to focus the action of sound waves, much like a lens does for a light beam. This prevents dispersion and enhances precision, and this characteristic can be replicated across various frequency ranges, improving the quality of sensors that utilize sound waves, such as ultrasound machines and echography devices.

In terms of modulation, acoustic metamaterials can produce absorbers and acoustic filters⁽³⁸⁾ that cancel or impede the transmission of noise, reducing interference and enhancing the sensitivity of devices that rely on sound to capture information, such as radars and other echolocation devices.

Metamaterials Applied in the Healthcare Field

As observed, despite the exploratory nature of this research, several interesting applications for this technology can already be identified, particularly in newer areas such as wearables, adaptable and intelligent prosthetics, biosensors, cellular scaffolds, and other implantable devices⁽³⁹⁾.

In the realm of wearables, examples include equipment for real-time monitoring of biological signals⁽⁴⁰⁾. These devices serve to monitor critically ill patients, potentially reducing the response time of medical teams, as well as tracking patients with chronic conditions such as diabetes, arrhythmia, and other diseases requiring continuous treatment, or to detect illness in a more efficient way, like exams breast cancer⁽⁴¹⁾, exemplified in the Figure 2.

This kind of devices present groundbreaking advancements in healthcare and communication

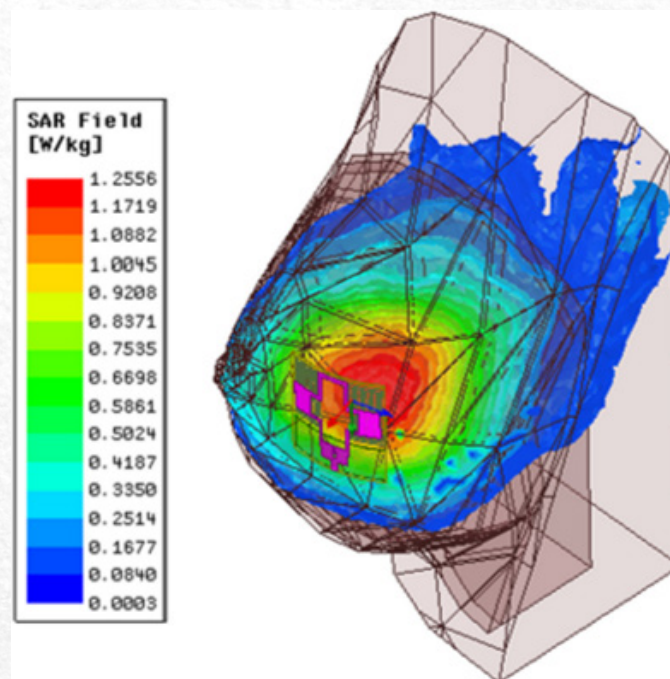


Figure 2 - SAR Field simulation of a bend metamaterial antenna for breast cancer detection. Source:(41)

systems. A notable development, for example, is a wearable pad inspired by metamaterials, designed to enhance the coupling of electromagnetic radiation with biological tissues at 2.4 GHz⁽⁴²⁾. Another application in the safe field is a dielectric metamaterial pad that significantly improves signal penetration in biological tissues, achieving over a 4 dB increase, thus offering a practical solution for diagnostic and therapeutic medical systems.

For transmission specifically, novel metamaterial-based antennas and sensors for 5G, 6G, IoT, and medical devices exhibit compact, broadband, and cost-effective designs⁽⁴³⁾, generating fractal geometries and CSRR structures enhance performance and energy efficiency, highlighting metamaterials' pivotal role in developing eco-friendly, self-powered wearables for advanced healthcare and communication systems.

Besides the studies in the modifications of electromagnetic fields, to improve the efficiency of wearables, the use of artificial intelligence (A.I) was being applied to explore new solutions in the use of metamaterials in this field, for example, using a AI-driven methodologies to optimizes wearable sensors, enabling rapid exploration of design parameters

and enhancing sensitivity, weight, and usability. These approaches facilitate applications in neonatal intensive care, assistive robotics, and personalized medicine⁽⁴⁴⁾.

In terms of applications for prosthetics, metamaterials contribute to the development of prostheses with varied mechanical properties that adapt to the stresses encountered in the model, like natural bone⁽⁴⁵⁾ or improve the comporment of stress distribution⁽⁴⁶⁾, exemplified in Figure 3 and Figure 4 respectively.

This modulation allows for the identification of diverse mechanical properties, minimizing phenomena such as stress shielding⁽⁴⁷⁾, which occurs when metallic materials with higher elastic modulus capture stress on bones, leading to localized bone fragility⁽⁴⁸⁾. Additionally, techniques such as texturing can enhance the integration of the prosthesis with bone⁽⁴⁹⁾, and the incorporation of drug or bioactive material deposition points⁽⁵⁰⁾, can reduce rejection by the immune system and prevent infections⁽⁵¹⁾.

Still in the field of prosthetics, we can highlight more specific applications, like the use of metamaterials to develop biomimetic tendons and other soft tissues⁽⁵²⁾.



Figure 3 - Application of metamaterials in the field of prosthetics and implants. Source: ⁽⁴⁵⁾

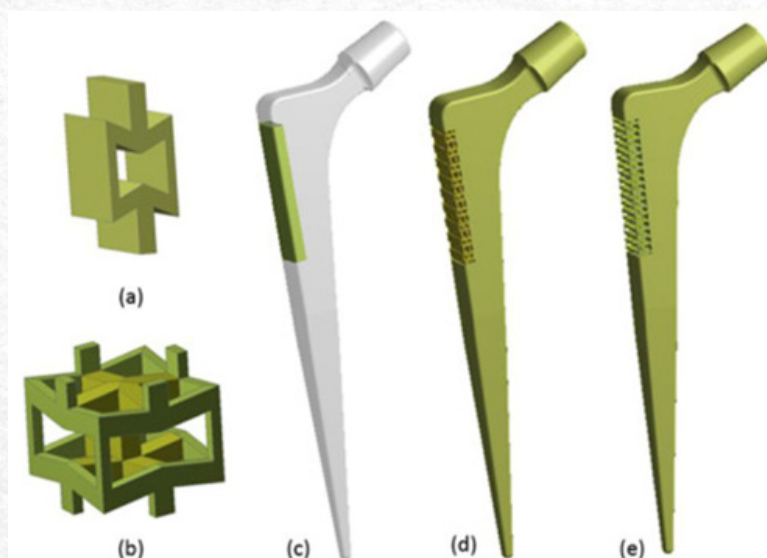


Figure 4 - Application of mechanical metamaterial cell for improving load transfer at proximal-lateral region of the femur. Source: ⁽⁴⁶⁾.

This technology enables the creation of synthetic fibers made from polymers, and through engineered cell design, it alters deformation behavior to closely resemble that of muscular tissue. This capability allows for the replacement of damaged tendons and cartilage, promoting recovery for athletes and accident victims while avoiding the removal of healthy tissue. These synthetic fibers can be implanted alongside the patient's tissue, functioning as grafts.

Focusing on the use of 3D printing, it can be employed for the use of metamaterials for improve the osseointegration in 3D-printed implant screws, which are typically metallic, used frequently in orthopedics⁽⁵³⁾. These screws often cause "stress shielding" and postoperative loosening, impacting long-term fixation⁽⁵⁴⁾. To address these issues, some strategies could be used like voronoi and other lattice structured materials⁽⁵⁵⁾, such as Fischer-Koch S, Octet, Diamond, and Double Gyroid. These porous structures help reduce "stress shielding." Furthermore, bone regeneration on the surface of the screws has increased by a factor of 1 to 50, enhancing the integration between the screw and the bone tissue⁽⁵⁶⁾, Figure 5, show some of the cells applied in the implant.

Other materials, such as polymers, can also be utilized in this prosthetic filed. When combined with techniques like topological optimization, they can create solutions such as the dynamic topological optimization of a transtibial orthopedic implant, 3D printed with adjustable isotropic porous metamaterials, to improve the weight-bearing capacity of the bone structures in the residual limb allowing the implant to withstand varying forces during the gait cycle,

enhancing its functionality and adaptability⁽⁵⁷⁾.

Beside the use for internal prosthetics, the use of metamaterial could be extended to limb substitution, like the use for development of a prosthetic liners for residual limbs to improve comfort and stability, ensuring better load distribution⁽⁵⁸⁾ and the use of cellular auxetic mechanical metamaterials to create flexible joints in soft robotic hands, inspired by human finger joints, offering adjustable stiffness and large bending angles⁽⁵⁹⁾, showed in Figure 6.

In the field of biosensors, metamaterials play a crucial role in developing rapid, compact, and more efficient tests through the creation of nanosensors capable of detecting the presence of specific molecules. These sensors can identify viruses and other pathogenic agents⁽⁶⁰⁾, as well as proteins and enzymes in blood⁽⁶¹⁾. This represents an advancement over conventional tests, as they require significantly smaller quantities of material for detection, making the tests more reliable, quicker, and reducing patient discomfort (Figure 7).

At last, in the field of regenerative medicine, metamaterials are being applied in tissue scaffolds, creating structures that promote tissue differentiation and facilitate interaction and maturation among cells⁽⁶²⁾. Through planned structuring, these scaffolds enable the development of bioabsorbable structures with temporary support, allowing the desired tissue to form. They serve as a framework for spheroids⁽⁶³⁾, which, upon maturation, completely absorb the scaffold, leaving only the newly formed tissue in place (Figure 8).

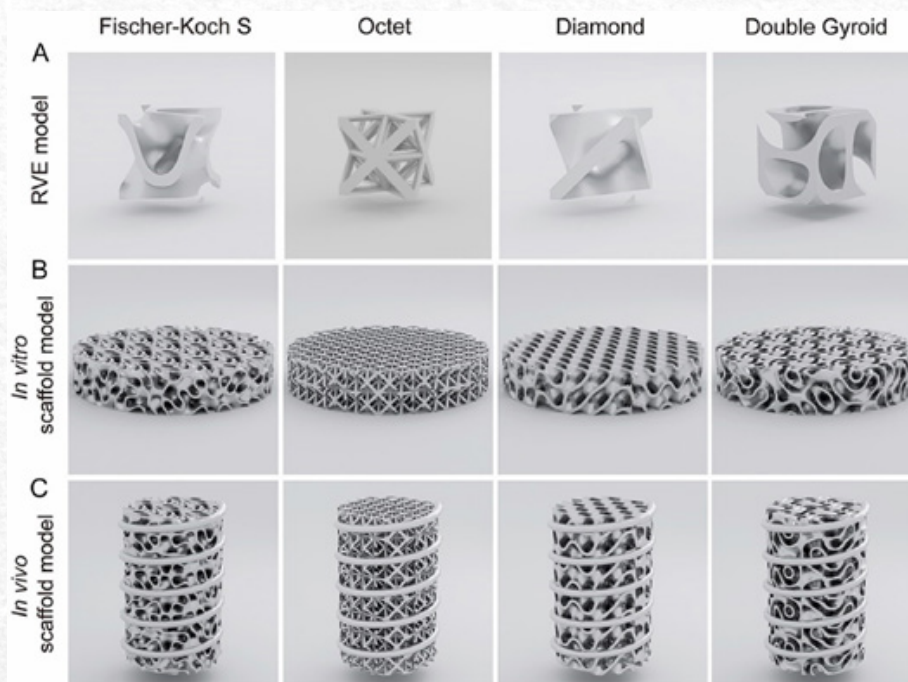


Figure 5 – Mechanical metamaterial cells applied in bone implant to increase osseointegration. Source⁽⁵⁶⁾.

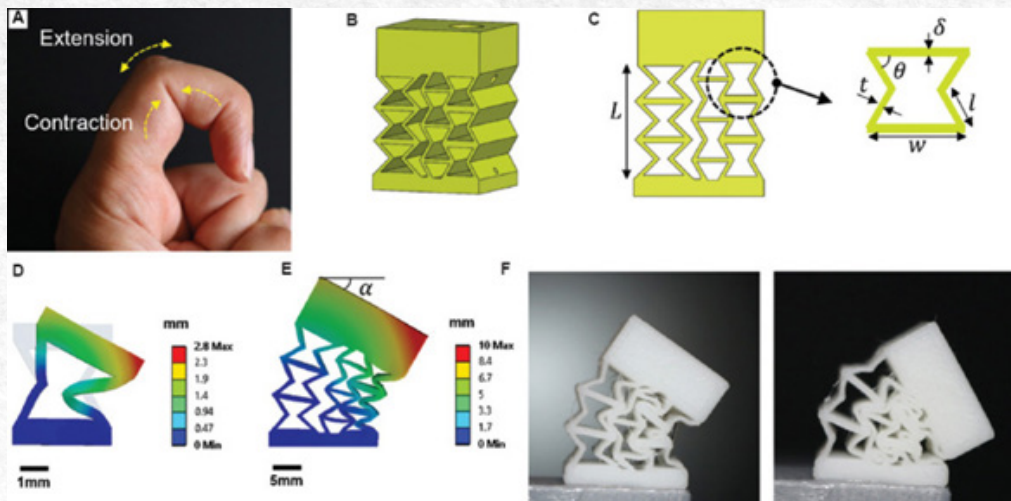


Figure 6 – Metamaterial joint for a soft robot prosthetic hand. Source:⁽⁵⁹⁾

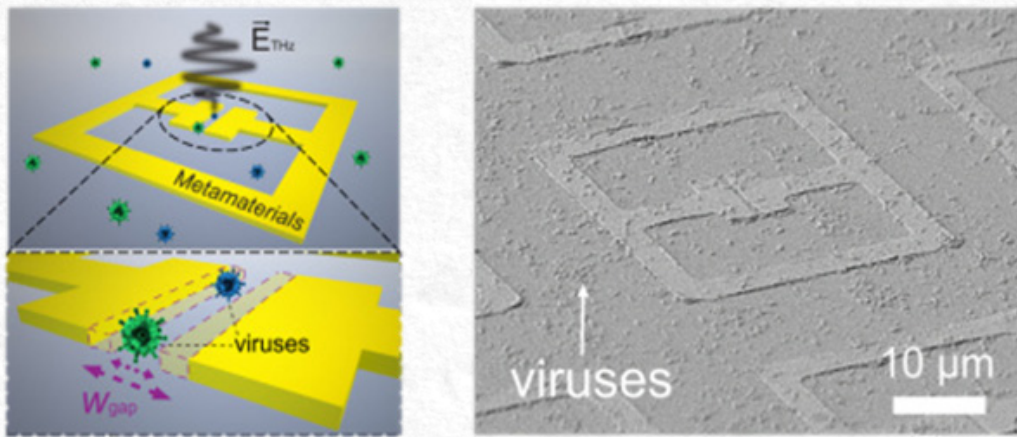


Figure 7 - Application of metamaterials in biosensors virus identification. Source:⁽⁶⁰⁾

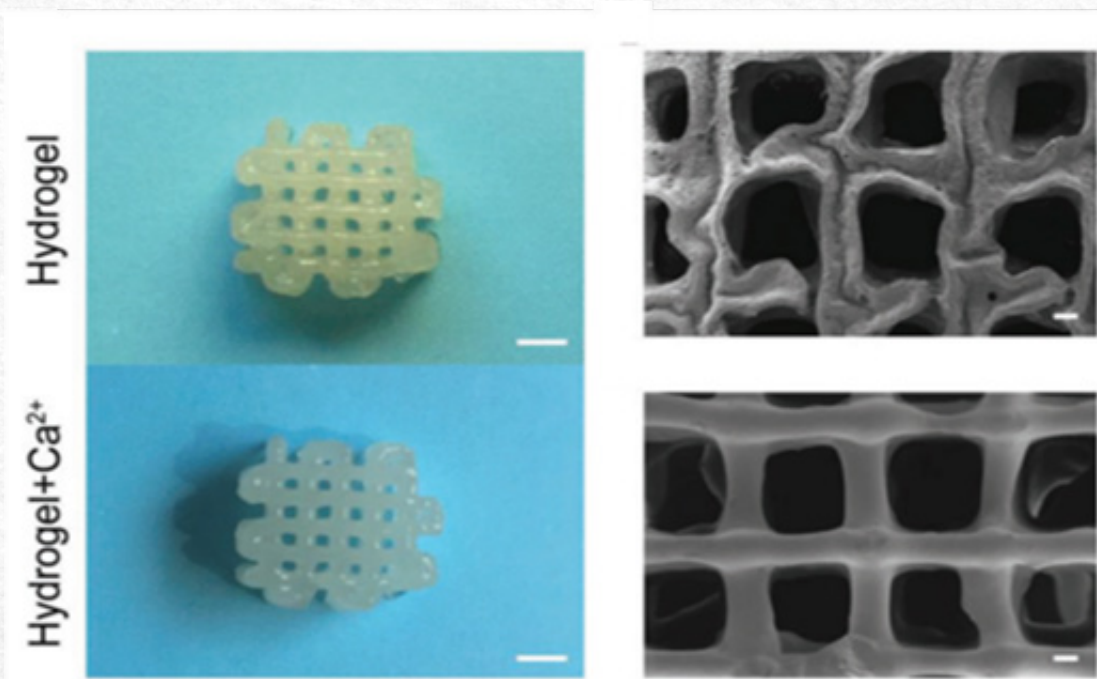


Figure 8 - Application of metamaterials in tissue scaffolds. Source:⁽⁶³⁾

Conclusion

The great potential for advancement in the use of metamaterials is certainly enhanced by the popularization of the use of three-dimensional printing technology, with the healthcare sector being a great entry possibility for this type of technology, largely due to its multidisciplinary nature. The use of metamaterials is undoubtedly transformative, due to its capability to develop personalized solutions and improve the adaptability of materials applications, with lead to a great advantage in detriment of other solutions, in terms modification and adaptability.

However, its widespread adoption faces significant challenges, especially in terms of scalability, due to the manufacturing complexity and costs associated with using disruptive technology such as 3D printing. While these technologies hold immense promise, enabling advancements such as personalized prosthetics, real-time monitoring devices, and rapid pathogen detection, translating them into accessible and economically viable solutions remains a considerable hurdle. Addressing these barriers will require ongoing innovation in manufacturing processes and strategic investment. Despite these challenges, the trajectory of these technologies suggests a future where their integration into healthcare systems becomes not only feasible but indispensable, offering profound improvements in patient care and quality of life.

This progress will enhance our longevity and quality of life, aligning with contemporary measures and the integration of information technology into daily life. It represents a natural evolution of existing equipment, such as probes, smartwatches, rapid tests, and other devices.

Acknowledgment

The authors of this research dedicate it to the memory of Dr. Jorge Vicente Lopes da Silva, a pioneer of additive manufacturing in the Latin American region and worldwide. His invaluable contributions to our training and professional development are reflected in this work.

The authors also extend their gratitude to the Centro de Tecnologia da Informação Renato Archer (CTI) and the Universidade Estadual de Campinas (Unicamp) for their support and collaboration, which were instrumental in enabling the successful completion of this research.

Declarations

Conflict of Interest

All authors declare no conflict of interests.

References

- [1]. Kshetrimayum RS. A brief intro to metamaterials. IEEE Potentials. 2005;23(5):44–6. DOI: 10.1109/MP.2005.1368916
- [2]. Sun M, Hu X, Tian L, Yang X, Min L. Auxetic Biomedical Metamaterials for Orthopedic Surgery Applications: A Comprehensive Review. Orthop Surg. 2024;16(8):1801–15. DOI: 10.1111/os.14142
- [3]. Simovski CR. Material parameters of metamaterials (a Review). Opt Spectrosc. 2009;107(5):726–53. DOI: 10.1134/S0030400X09110101
- [4]. Kadic M, Milton GW, van Hecke M, Wegener M. 3D metamaterials. Nature Reviews Physics. 2019;1(3):198–210. DOI: 10.1038/s42254-018-0018-y
- [5]. Sun Y, Ye W, Chen Y, Fan W, Feng J, Sareh P. Geometric design classification of kirigami-inspired metastructures and metamaterials. Structures. 2021;33:3633–43. DOI: 10.1016/j.istruc.2021.06.072
- [6]. Gibson LJ. Cellular Solids. MRS Bull. 2003;28(4):270–4. DOI: 10.1557/mrs2003.79
- [7]. Sakoda K, editor. Electromagnetic Metamaterials. Vol. 287 Singapore: Springer Singapore; 2019. DOI: 10.1007/978-981-13-8649-7
- [8]. Caloz C, Itoh T. Electromagnetic Metamaterials: Transmission Line Theory and Microwave Applications. Wiley; 2005 Nov 11. DOI: 10.1002/0471754323
- [9]. Smith DR, Pendry JB, Wiltshire MCK. Metamaterials and Negative Refractive Index. Science (1979). 2004;305(5685):788–92. DOI: 10.1126/science.1096796
- [10]. Giri R, Payal R. Negative-Index Metamaterials. In: Electromagnetic Metamaterials. Wiley; 2023. DOI: 10.1002/9781394167074.ch10
- [11]. Lobet M, Kinsey N, Liberal I, Caglayan H, Huidobro PA, Galiffi E, et al. New Horizons in Near-Zero Refractive Index Photonics and Hyperbolic Metamaterials. ACS Photonics. 2023;10(11):3805–20. DOI: 10.1021/acsp Photonics.3c00747
- [12]. Yang F, Zhang Z, Xu L, Liu Z, Jin P, Zhuang P, et al. Controlling mass and energy diffusion with metamaterials. Rev Mod Phys. 2024;96(1):015002. DOI: 10.1103/RevModPhys.96.015002
- [13]. Li Y, Li W, Han T, Zheng X, Li J, Li B, et al. Transforming heat transfer with thermal metamaterials and devices. Nat Rev Mater. 2021;6(6):488–507. DOI: 10.1038/s41578-021-00283-2
- [14]. Dyachenko PN, Molesky S, Petrov AY, Störmer M, Krekelier T, Lang S, et al. Controlling thermal emission with refractory epsilon-near-zero metamaterials via topological transitions. Nat Commun. 2016;7(1):11809. DOI: 10.1038/ncomms11809
- [15]. Han T, Qiu C-W. Transformation Laplacian metamaterials: recent advances in manipulating thermal and dc fields. Journal of Optics. 2016;18(4):044003. DOI: 10.1088/2040-8978/18/4/044003
- [16]. Kim JC, Ren Z, Yuksel A, Dede EM, Bandaru PR, Oh D,

- et al. Recent Advances in Thermal Metamaterials and Their Future Applications for Electronics Packaging. *J Electron Packag.* 2021;143(1). DOI: 10.1115/1.4047414
- [17]. Lee J, Koh CY, Singer JP, Jeon S, Maldovan M, Stein O, et al. 25th Anniversary Article: Ordered Polymer Structures for the Engineering of Photons and Phonons. *Advanced Materials.* 2014;26(4):532–69. DOI: 10.1002/adma.201303456
- [18]. Liu Y, Zhang X. Metamaterials: a new frontier of science and technology. *Chem Soc Rev.* 2011;40(5):2494. DOI: 10.1039/c0cs00184h
- [19]. Capolino F. Capolino F, editor. *Applications of Metamaterials.* CRC Press; 2017 Dec 19. DOI: 10.1201/9781420054248
- [20]. Jorwal S, Dubey A, Gupta R, Agarwal S. A review: Advancement in metamaterial based RF and microwave absorbers. *Sens Actuators A Phys.* 2023;354:114283. DOI: 10.1016/j.sna.2023.114283
- [21]. Khuyen BX, Tung BS, Kim YJ, Hwang JS, Kim KW, Rhee JY, et al. Ultra-subwavelength thickness for dual/triple-band metamaterial absorber at very low frequency. *Sci Rep.* 2018;8(1):11632. DOI: 10.1038/s41598-018-29896-4
- [22]. Zhang T, Duan Y, Liu J, Lei H, Sun J, Pang H, et al. Asymmetric electric field distribution enhanced hierarchical metamaterials for radar-infrared compatible camouflage. *J Mater Sci Technol.* 2023;146:10–8. DOI: 10.1016/j.jmst.2022.10.043
- [23]. Zhang Z, Xu L, Qu T, Lei M, Lin Z-K, Ouyang X, et al. Diffusion metamaterials. *Nature Reviews Physics.* 2023;5(4):218–35. DOI: 10.1038/s42254-023-00565-4
- [24]. Jiang M, Chen ZN, Zhang Y, Hong W, Xuan X. Metamaterial-Based Thin Planar Lens Antenna for Spatial Beamforming and Multibeam Massive MIMO. *IEEE Trans Antennas Propag.* 2017;65(2):464–72. DOI: 10.1109/TAP.2016.2631589
- [25]. Pu M, Ma X, Li X, Guo Y, Luo X. Merging plasmonics and metamaterials by two-dimensional subwavelength structures. *J Mater Chem C Mater.* 2017;5(18):4361–78. DOI: 10.1039/c7tc00440k
- [26]. Balan P M, Mertens A J, Bahubalendruni MVAR. Auxetic mechanical metamaterials and their futuristic developments: A state-of-art review. *Mater Today Commun.* 2023;34:105285. DOI: 10.1016/j.mtcomm.2022.105285
- [27]. Liu Y, Zhao C, Xu C, Ren J, Zhong J. Auxetic metamaterials and their engineering applications: a review. *Engineering Research Express.* 2023;5(4):042003. DOI: 10.1088/2631-8695/ad0eb1
- [28]. Spanos I, Vangelatos Z, Grigoropoulos C, Farsari M. Design and Characterization of Microscale Auxetic and Anisotropic Structures Fabricated by Multiphoton Lithography. *Nanomaterials.* 2021;11(2):446. DOI: 10.3390/nano11020446
- [29]. Fardan MF, Lenggana BW, Ubaidillah U, Choi S-B, Susilo DD, Khan SZ. Revolutionizing Prosthetic Design with Auxetic Metamaterials and Structures: A Review of Mechanical Properties and Limitations. *Micromachines (Basel).* 2023;14(6):1165. DOI: 10.3390/mi14061165
- [30]. Zhang J, Lu G, You Z. Large deformation and energy absorption of additively manufactured auxetic materials and structures: A review. *Compos B Eng.* 2020;201:108340. DOI: 10.1016/j.compositesb.2020.108340
- [31]. Lei M, Hong W, Zhao Z, Hamel C, Chen M, Lu H, et al. 3D Printing of Auxetic Metamaterials with Digitally Reprogrammable Shape. *ACS Appl Mater Interfaces.* 2019;11(25):22768–76. DOI: 10.1021/acsami.9b06081
- [32]. Ren X, Das R, Tran P, Ngo TD, Xie YM. Auxetic metamaterials and structures: a review. *Smart Mater Struct.* 2018;27(2):023001. DOI: 10.1088/1361-665X/aaa61c
- [33]. Bodaghi M, Liao WH. 4D printed tunable mechanical metamaterials with shape memory operations. *Smart Mater Struct.* 2019;28(4):045019. DOI: 10.1088/1361-665X/ab0b6b
- [34]. Tao R, Ji L, Li Y, Wan Z, Hu W, Wu W, et al. 4D printed origami metamaterials with tunable compression twist behavior and stress-strain curves. *Compos B Eng.* 2020;201:108344. DOI: 10.1016/j.compositesb.2020.108344
- [35]. Zhang J, Hu B, Wang S. Review and perspective on acoustic metamaterials: From fundamentals to applications. *Appl Phys Lett.* 2023;123(1). DOI: 10.1063/5.0152099
- [36]. Cummer SA, Christensen J, Alù A. Controlling sound with acoustic metamaterials. *Nat Rev Mater.* 2016;1(3):16001. DOI: 10.1038/natrevmats.2016.1
- [37]. Jackowski-Ashley L, Memoli G, Caleap M, Slack N, Drinkwater BW, Subramanian S. Haptics and Directional Audio Using Acoustic Metasurfaces. In: *Proceedings of the 2017 ACM International Conference on Interactive Surfaces and Spaces.* New York, NY, USA: ACM; 2017. p. 429–33.
- [38]. Arjunan A, Baroutaji A, Robinson J, Vance A, Arafat A. Acoustic metamaterials for sound absorption and insulation in buildings. *Build Environ.* 2024;251:111250. DOI: 10.1016/j.buildenv.2024.111250
- [39]. Khalid MY, Arif ZU, Tariq A, Hossain M, Umer R, Bodaghi M. 3D printing of active mechanical metamaterials: A critical review. *Mater Des.* 2024;246:113305. DOI: 10.1016/j.matdes.2024.113305
- [40]. Sabban A. New Compact Wearable Metamaterials Circular Patch Antennas for IoT, Medical and 5G Applications. *Applied System Innovation.* 2020;3(4):42. DOI: 10.3390/asi3040042
- [41]. Karthikeyan TA, Nesusudha M, Let GS. Investigations on Slotted Metamaterial Backed Wea-

- nable Antenna for Breast Tumor Detection. *Plasmonics*. 2024;19(3):1499–515. DOI: 10.1007/s11468-023-02085-4
- [42].Koutsoupidou M, Tzarouchis DC, Rompolas D, Sotiriou I, Palikaras G, Kosmas P. Wearable Pad for Enhancing EM Coupling with Biological Tissues. *IEEE Trans Antennas Propag*. 2024;1–1. DOI: 10.1109/TAP.2024.3492504
- [43].Sabban A. Novel Meta-Fractal Wearable Sensors and Antennas for Medical, Communication, 5G, and IoT Applications. *Fractal and Fractional*. 2024;8(2):100. DOI: 10.3390/fractalfract8020100
- [44].Yigci D, Ahmadpour A, Tasoglu S. AI-Based Metamaterial Design for Wearables. *Advanced Sensor Research*. 2024;3(3). DOI: 10.1002/adsr.202300109
- [45].Lvov VA, Senatov FS, Veveris AA, Skrybykina VA, Díaz Lantada A. Auxetic Metamaterials for Biomedical Devices: Current Situation, Main Challenges, and Research Trends. *Materials*. 2022;15(4):1439. DOI: 10.3390/ma15041439
- [46].Singh AP, Rana M, Pal B, Datta P, Majumder S, Roychowdhury A. Patient-specific femoral implant design using metamaterials for improving load transfer at proximal-lateral region of the femur. *Med Eng Phys*. 2023;113:103959. DOI: 10.1016/j.medengphy.2023.103959
- [47].Tatullo M, Ambrogio G, Sammartino G. Advances in Dental Implants, Tissue Engineering and Prosthetic Materials. *Materials*. 2023;16(17):5871. DOI: 10.3390/ma16175871
- [48]. Mirzaali MJ, Zadpoor AA. Orthopedic meta-implants. *APL Bioeng*. 2024;8(1). DOI: 10.1063/5.0179908
- [49].Coulais C, Teomy E, de Reus K, Shokef Y, van Hecke M. Combinatorial design of textured mechanical metamaterials. *Nature*. 2016;535(7613):529–32. DOI: 10.1038/nature18960
- [50].Amin Yavari S, Croes M, Akhavan B, Jahanmard F, Eighenhuys CC, Dadbakhsh S, et al. Layer by layer coating for bio-functionalization of additively manufactured meta-biomaterials. *Addit Manuf*. 2020;32:100991. DOI: 10.1016/j.addma.2019.100991
- [51].Wang H, Lyu Y, Bosiakov S, Zhu H, Ren Y. A review on the mechanical metamaterials and their applications in the field of biomedical engineering. *Front Mater*. 2023;10. DOI: 10.3389/fmats.2023.1273961
- [52].Chen J, Wang K, Zhang C, Wang B. An efficient statistical approach to design 3D-printed metamaterials for mimicking mechanical properties of soft biological tissues. *Addit Manuf*. 2018;24:341–52. DOI: 10.1016/j.addma.2018.10.007
- [53].Shirzad M, Zolfagharian A, Bodaghi M, Nam SY. Auxetic metamaterials for bone-implanted medical devices: Recent advances and new perspectives. *European Journal of Mechanics - A/Solids*. 2023;98:104905. DOI: 10.1016/j.euromechsol.2022.104905
- [54].Bandyopadhyay A, Mitra I, Avila JD, Upadhyayula M, Bose S. Porous metal implants: processing, properties, and challenges. *International Journal of Extreme Manufacturing*. 2023;5(3):032014. DOI: 10.1088/2631-7990/acdd35
- [55].Han C, Wang Y, Wang Z, Dong Z, Li K, Song C, et al. Enhancing mechanical properties of additively manufactured voronoi-based architected metamaterials via a lattice-inspired design strategy. *Int J Mach Tools Manuf*. 2024;202:104199. DOI: 10.1016/j.ijmactools.2024.104199
- [56].Luo W, Wang Y, Wang Z, Jiao J, Yu T, Jiang W, et al. Advanced topology of triply periodic minimal surface structure for osteogenic improvement within orthopedic metallic screw. *Mater Today Bio*. 2024;27:101118. DOI: 10.1016/j.mtbio.2024.101118
- [57].García-Ávila J, González-Gallegos CP, Segura-Ibarra V, Vazquez E, García-Lopez E, Rodríguez CA, et al. Dynamic topology optimization of 3D-Printed trans-tibial orthopedic implant using tunable isotropic porous metamaterials. *J Mech Behav Biomed Mater*. 2024;153:106479. DOI: 10.1016/j.jmbbm.2024.106479
- [58].Plessec V, Harih G. Bioinspired Design of 3D-Printed Cellular Metamaterial Prosthetic Liners for Enhanced Comfort and Stability. *Biomimetics*. 2024;9(9):540. DOI: 10.3390/biomimetics9090540
- [59].Mohammadi A, Hajizadeh E, Tan Y, Choong P, Oetomo D. A bioinspired 3D-printable flexure joint with cellular mechanical metamaterial architecture for soft robotic hands. *Int J Bioprint*. 2023;9(3):696. DOI: 10.18063/ijb.696
- [60].Akter N, Hasan M, Pala N. A Review of THz Technologies for Rapid Sensing and Detection of Viruses including SARS-CoV-2. *Biosensors (Basel)*. 2021;11(10):349. DOI: 10.3390/bios11100349
- [61].Yang J, Qi L, Li B, Wu L, Shi D, Ahmed Uqaili J, et al. A terahertz metamaterial sensor used for distinguishing glucose concentration. *Results Phys*. 2021;26:104332. DOI: 10.1016/j.rinp.2021.104332
- [62].Flamourakis G, Spanos I, Vangelatos Z, Manganas P, Papadimitriou L, Grigoropoulos C, et al. Laser-made 3D Auxetic Metamaterial Scaffolds for Tissue Engineering Applications. *Macromol Mater Eng*. 2020;305(7). DOI: 10.1002/mame.202000238
- [63].Che L, Lei Z, Wu P, Song D. A 3D Printable and Bioactive Hydrogel Scaffold to Treat Traumatic Brain Injury. *Adv Funct Mater*. 2019;29(39). DOI: 10.1002/adfm.201904450

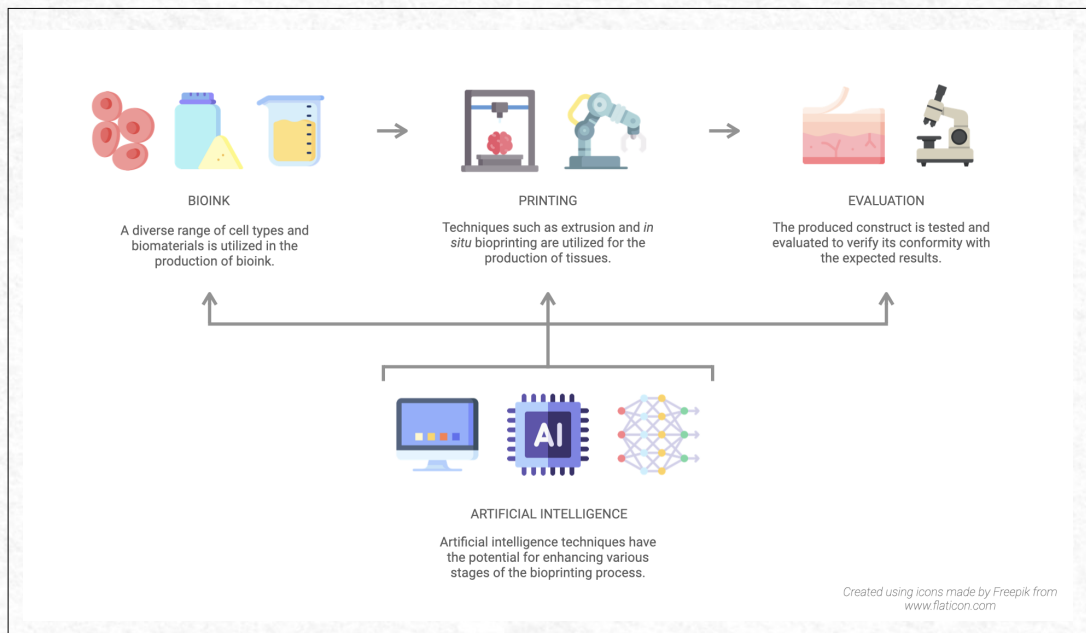


Bioprinting for skin: current approaches, technological advancements and the role of artificial intelligence

V. Castro Thomazi¹; N. Maurmann²; P. Pranke²

*Corresponding author: E-mail address: vcthomazi@gmail.com

Received: October 2024; Accepted: December 2024.



Abstract: Bioprinting is a technique adapted from 3D printing to create biological constructs, including high-quality skin substitutes. It matches or exceeds the quality of traditional fabrication methods, offering precision, consistency and speed, critical attributes for large-scale production. A variety of materials are used, most of them natural, such as alginate, chitosan and gelatin, with cells incorporated into the bioink. These cells may belong to the replicated tissue or include stem cells that can differentiate into the desired cell types. Bioprinting enables precise placement of the skin's layers: hypodermis, dermis and epidermis, allowing for replication of the skin's complex architecture. Notably, bioprinted skin constructs can closely resemble native tissue, even forming structures like hair follicles and glands as the incorporated cells grow, migrate and differentiate. Artificial intelligence (AI) and machine learning (ML) have recently been applied to enhance efficiency, precision and success. AI tools reduce trial and error by optimizing parameters, bioink composition and quality control. This review explores bioprinting methods, materials and advancements, including *in situ* bioprinting, the use of robotic devices and the emerging role of artificial intelligence.

Keywords: Biomaterials. Three-dimensional (3D) culture. Regenerative Medicine. Tissue Engineering.

¹University of Rio Grande do Sul(UFRGS), Brazil.

²Stem Cell Research Institute (Instituto de Pesquisa com Células-tronco), Porto Alegre 90020-010, Brazil.

Introduction

Bioprinting is a promising and rapidly evolving technique capable of assembling high-quality tissue types, including skin substitutes. It is an adaptation of 3D printing to produce biological constructs. It matches the quality of skin constructs built using traditional methods,^[1] and even surpasses them, offering advantages in terms of precision, consistency and speed, key factors for mass production. It has been shown not to affect the capacity for cells growth or the biocompatibility with materials.^[2] Traditional 3D printing uses a variety of materials, with artificial polymers being the most common; however, when printing biological constructs, and especially skin, natural materials such as alginate, chitosan and gelatin are the most frequently chosen. In bioprinting, cells are incorporated into the ink, which is then referred to as bioink.^[3] These cells may be composed of types that belong to the tissue being replicated or not; for example, stem/stromal cells can be used, which differentiate into the desired cell types under the guidance of specific chemical or physical cues.

Moreover, sometimes cells are incorporated not only for their structural role in the tissue, but also for additional benefits in supporting graft maturation.

Skin is a complex organ composed of multiple cell types organized in distinct layers. The structure of skin, with its different layers, is shown in Figure 1. It is the largest human organ and serves various functions, including thermoregulation, immune defense and sensory input. One of the goals of bioprinting skin is to replicate its layers, namely the hypodermis, dermis and epidermis (which are themselves further subdivided), to ensure that specialized cells can perform specific tasks that are highly dependent on the skin's intricate architecture. Bioprinting offers the ability to print each layer of the skin individually in a controlled manner using different materials and cell populations for each layer, thus closely mimicking both the cellular and the architectural makeup of real skin.

It has already been demonstrated that when cells and biomaterials are incorporated in the printing process the cells are able to organize themselves into layers similarly to real skin. More impressively,

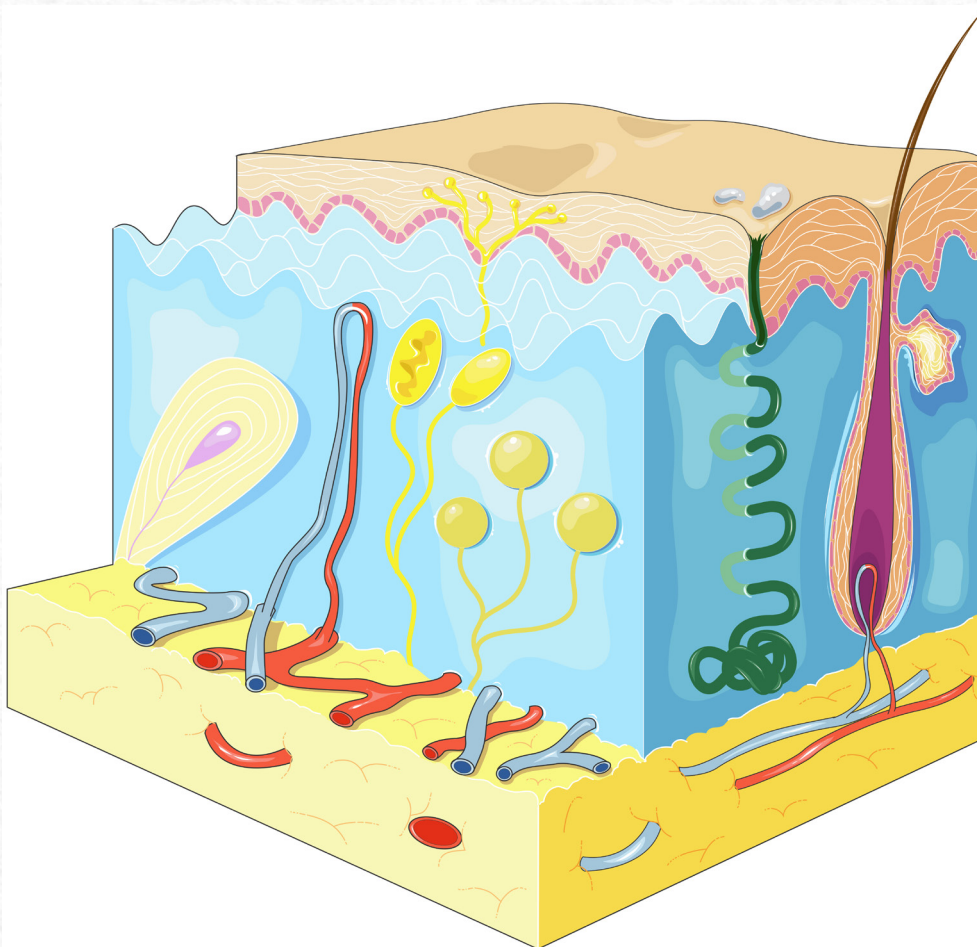


Figure 1 - A representation of skin. Structures shown include a hair follicle, an eccrine sweat gland, cutaneous receptors and the vascular network. Dermis is shown in blue, epidermis is above it, and hypodermis is below it. "Skin icon" by Servier <https://smart.servier.com/> licensed under CC-BY 3.0 Unported <https://creativecommons.org/licenses/by/3.0/>

some bioprinted constructs resemble native tissue to the point of forming specialized structures such as hair follicles and sebaceous glands.^[4-7] This is possible because the cells in the bioink are alive and dynamic. The final product is not fully realized immediately after the printing process; instead, the cells continue to grow, migrate and differentiate over several days, forming new structures and maturing into their final positions and functions.

Recently, artificial intelligence (AI), particularly its subfield of machine learning (ML), has been integrated into bioprinting as a set of tools aimed at enhancing efficiency, precision and overall success. These AI tools, grounded in statistics and linear algebra, have the capacity for handling complex datasets, including those with non-linear and irregular distributions, developing predictive models, classifying data and offering valuable insights. AI can thus help address the multitude of parameters involved in bioprinting, which often necessitate trial-and-error experiments to have their optimal values determined. By reducing the need for extensive experimentation, AI makes the overall process more efficient. Other applications include fine-tuning bioink composition, ensuring quality control, and even enabling fully automated bioprinting. AI tools can also be used alongside bioprinting for applications such as drug discovery, cancer research and cell classification.

This review explores the literature on bioprinting

skin, focusing on the different printing methods, materials and the types of cells incorporated into bioinks. Additionally, it examines recent advances in artificial intelligence and machine learning and their contributions to bioprinting. At the end, there is a selection of the diverse uses of bioprinted skin, which may serve, for example, as a model for basic research or as a transplantable graft.^[8] These new technologies are not only improving the printing process itself but are also transforming the field of biofabrication as a whole.

Bioprinting methods

There are various methods used in bioprinting, most of which are adapted from traditional 3D printing. Setting it apart from other biofabrication methods, bioprinting allows for the construction of printed tissue with all the components (materials, cells and additional factors) in a layer-by-layer fashion, eliminating the need for a prior scaffold to be seeded with the appropriate cells at a different time.

The feasibility of printing skin without a scaffold was demonstrated in a 2017 study with the printing of a construct in the shape of a human ear.^[9] Researchers employed an extrusion method to print a bioink composed of alginate, gelatin and fibrinogen onto a refrigerated support.

An overview of the process of bioprinting is shown in Figure 2.

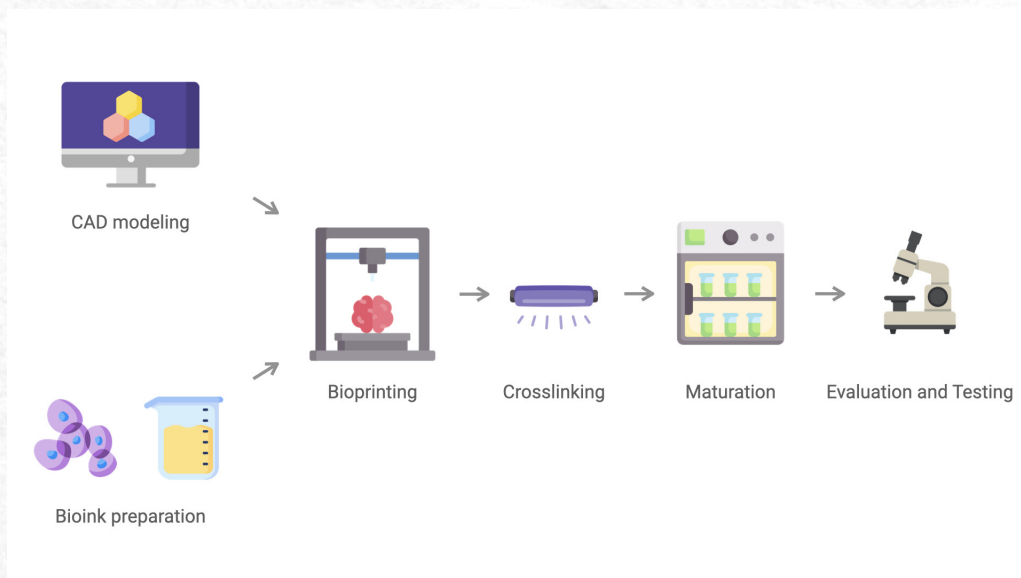


Figure 2 - An overview of bioprinting. First, a computer-aided design (CAD) 3D model is created, and from it, printing instructions are generated for the bioprinter in the form of a G-code. A bioink is prepared by mixing biomaterials and cells. The bioprinter prints using the bioink, following the instructions in the G-code. An optional crosslinking or crosspolymerization step, represented here by an ultraviolet lamp, may follow. The printed construct then undergoes a maturation process, which may last several days. Finally, the construct is evaluated and tested to verify that it has the desired characteristics. Created with icons by Freepik from www.flaticon.com.

Extrusion-based bioprinting

Extrusion is a popular method used in bioprinting and is also one of the most widely employed techniques in 3D printing overall. In this method, the bioink is loaded into a container, such as a cartridge or a syringe, and extruded through a nozzle, often a needle. To propel the bioink through the nozzle, various methods can be applied, including a plunger and air pressure. This versatile technique accommodates a wide range of bioinks, provided they are adequately viscous to be extruded. Precise control over both the extrusion rate and the movement of the nozzle allows for the creation of intricate structures.

Extrusion-based methods have been widely used to bioprint skin constructs. For example, researchers have used extruded bioinks containing fibroblasts and keratinocytes derived from skin biopsies to print bilayer skin substitutes.^[10] One study used extrusion bioprinting to build a scaffold of alginate-gelatin-collagen that had a porous structure to promote perfusion of oxygen and nutrients.^[11] Another group generated an oriented anisotropic microporous structure.^[12] Aligned microarchitectures have an impact on fibroblast-to-myofibroblast transition. The oriented micropores helped with cell spreading and adhesion.

Despite its popularity and versatility, extrusion bioprinting has some limitations. One challenge when bioprinting skin is the difficulty of producing air-exposed cellular monolayers. In traditional extrusion techniques, cells are submerged within the bioink, which may cause an impact on cellular layers. A confluent monolayer of basal keratinocytes, for example, is an important element when mimicking the natural structure of skin. Ongoing advances in extrusion methods are being developed to address this challenge, such as using a sacrificial gelatin, which in one study lead to significant improvements in epidermal differentiation and stratification.^[13]

Drop-on-demand

Drop-on-demand bioprinting uses droplets of the bioink to create complex structures layer-by-layer. The size and placement of the droplets can be precisely tuned, allowing for high resolution of the printed construct and controlled cell placement. A microvalve-based printer, for example, may apply pressure to the printing cartridges and print droplets of the biomaterial onto a receiving surface.^[14]

One of the main goals of skin bioprinting is to promote the organization of specialized cell populations into functional structures. A two-step bioprinting strategy utilizing the drop-on-demand printing method has been employed to emulate epidermal melanin units, which are epidermal

patterns of melanocytes and keratinocytes.^[15]

In one study, piezoelectric inkjet bioprinting was used to bioprint distinct keratinocyte subpopulations within a single skin construct to create a model for studying specific clinical conditions, namely atopic dermatitis and ichthyosis vulgaris.^[16] When exposed to a voltage pulse, a piezoelectric actuator undergoes deformation, creating mechanical stress, and, consequently, pressure, which ejects droplets of the bioink from the printhead nozzle in a very controlled manner.

One group employed droplet-based bioprinting to print full-thickness grafts for skin defects intraoperatively in a rat model.^[7] The bioprinter had three heads, loaded with a dermal bioink, a hypodermal bioink and a crosslinker.

Light-based techniques

Light-based techniques include laser-assisted bioprinting (LaBP) and light-sheet bioprinting.

The LaBP setup consists of two layers of glass, one of them is coated with material able to absorb a laser (e.g. gold) and attached to a layer of biomaterial.^[17] The other one is the receiver glass slide that is mounted below it. The laser goes through the upper glass layer and locally evaporates the laser absorbing layer. The vapor pressure propels the biomaterial to the receiving glass slide. Complex structures can be printed on the receiver glass by changing the relative position between the two glass slides.

Light sheet bioprinting projects the light onto a container of biomaterial that has a photoinitiator, a substance that triggers the solidification or polymerization of the material when exposed to light.^[18] By changing the position of this light sheet in relation to the biomaterial, the structure is gradually built layer-by-layer. Due to the thinness and precision of the light sheet, this method allows for high resolution bioprinting.

A laser-assisted bioprinted method, similar to the ones described above, was employed to create an *in vitro* skin model in one study.^[19] The authors called it four-dimensional due to the addition of time as the fourth dimension, considering here the maturation time of the printed construct an essential part of the process.

Robot-assisted methods and in situ bioprinting

There is a growing interest in developing new, versatile methods of bioprinting which make use of printers with robotic arms, allowing greater range of movements and adaptation to unusual printing surfaces, especially *in vivo*. In addition, a group utilized a robotic system to bioprint pigmented, pre-vascularized dermal-epidermal skin substitutes

as a proof-of-concept for the implementation of an automatized manufacturing process for the production of skin substitutes.^[20]

One approach to uneven surfaces is using a stereotactic technique, which allowed researchers to bioprint a skin substitute *in situ* in mice.^[21] Skin wounds in the animals were scanned and identified with binocular cameras that informed the path for a robotic arm to deposit a bioink directly onto the wounds.

Others have also investigated *in situ* bioprinting. It was used to print with a hydrogel containing amniotic fluid-derived stem (AFS) cells and bone marrow-derived mesenchymal stem cells (BMMSCs).^[22] One group employed an enzyme-free protocol to mechanically extract keratinocytes and fibroblasts from human skin biopsies and produce a bioink for *in situ* printing.^[23]

A mobile printer also printed autologous skin cells *in situ*.^[24] The cells used were human dermal fibroblasts (HDF) and human epidermal keratinocytes (HEK). Immunohistochemistry determined that the cells were present in the wound area up to 6 weeks after printing in nu/nu mice. A further study used *in situ* bioprinting assisted by a robotic printer,^[5] this time using a GelMA hydrogel loaded with epidermal stem cells (Epi-SCs) and skin-derived precursors (SKPs) obtained from 1-3-day-old C57BL/6 mice.

The examples above show that multiple methods are being tested, with none of them being universally preferred, not just in relation to the printer, but also with the utilized cells and materials.

Other methods of printing

In addition to the more popular methods, and also as a complement to them, innovative approaches are being explored to improve precision, efficiency and functionality; and to enable printing with materials that may not be feasible otherwise.

One such method is suspended layer additive manufacturing, which was used in one study to create a continuous tri-layered implant closely resembling human skin.^[25] This method uses a suspension reservoir: a material, typically a fluid gel, that supports each printed layer while being printed. This allows for greater flexibility when choosing bioinks, because they do not need to exhibit high viscosity or rapid curing to support the printed structure as the shape is held in place by the suspension reservoir.

Cryogenic 3D bioprinting using free-form extrusion has also been investigated.^[26] A group used a modified extrusion system paired with a cryogenic platform. The technique consists of extruding the material and quickly cooling it to form porous 3D

structures.

To create a hybrid biomedical and electronic skin construct, one group employed microfluidic-regulated 3D bioprinting (MRBP).^[27] Tri-layer artificial skin patches were built combining a bioprinted layer of polyurethane and bioactive glass (PU-BG) and electrospun layers of polycaprolactone (PCL) and of polyurethane (PU) with polyacrylic acid. A sensing film was also added to the construct. The skin patch was able to sense pressure and, when put on the wrist of a human volunteer, it could detect pulse waves. The tri-layer construct showed faster healing in a mouse model when compared to the controls.

Crosslinking and crosspolymerization

Some bioinks require an additional step after being printed to achieve the necessary rigidity and the desired mechanical properties. Polymerization establishes the chemical bonds necessary for the formation of long polymer chains and, consequently, solidification. Crosslinking links existing polymer chains, also leading to increased rigidity.

One approach involved extruding bioinks containing alginate onto a calcium-containing substrate, which allows gradient secondary crosslinking and a final result that resembles dermal stiffness.^[28] Natural polymers such as gelatin and xanthan gum have been crosslinked with glutaraldehyde.^[29] One study used a hyaluronic acid crosslinker in a thiol-ene hydrogel composed of a dextran-based backbone.^[18]

Another compound that has been used as a crosslinker is genipin, extracted from gardenia fruits.^[30] It is biocompatible and has anti-inflammatory and antibacterial effects. Researchers prepared a hydrogel of chitosan, genipin and polyethylene glycol (PEG), laden with human keratinocytes and dermal fibroblasts, that was used to print layers on a basal layer of alginate. Cell viability in 7 days was over 85% for both cell lines. Other studies also used genipin, producing hydrogels of gelatin combined with polyvinyl alcohol.^[2,31]

Photopolymerization and photocrosslinking are techniques that use light to provide the energy, via photons, required for the reactions. These techniques allow the bioink to remain in a liquid state while being extruded through the printer nozzle but solidify rapidly once printed and exposed to light of adequate wavelength. This helps overcome challenges related to the viscoelastic properties of bioinks, which must be fluid enough to be extruded but capable of forming solid structures upon printing. An example of this approach is a study in which a photopolymerizable bioink was formulated using GelMA, silk fibroin methacrylate, and photoactivated platelet releasate (PPR).^[32] This combination of

components ensured adequate physicochemical and rheological characteristics both for printing and for the formation of a solid structure after polymerization. A research group combined extrusion with a dual-photo source cross-linking technique, enabling the bioink to achieve the desired stiffness soon after extrusion.^[33]

Another method for controlling the rigidity of the final construct is enzyme crosslinking, which employs enzymes as catalysts for the reactions.

One study combined both photocrosslinking and enzyme crosslinking to achieve enhanced mechanical properties.^[34] Tyrosinase was added to a hydrogel of GelMA and collagen for its ability to cross-link collagen and its bioactivity in regeneration. Another study also combined two different methods of crosslinking and polymerization.^[35] Fibrinogen was combined with alginate in a bioink that was enzymatically polymerized by thrombin and ionically crosslinked using calcium. A third example of mixed methods was the coupling of photocrosslinking and thermosensitive crosslinking.^[36] A bioink was prepared using GelMA and hyaluronic acid methacryloyl (HAMA) mixed with decellularized extracellular matrix (dECM), whose thermosensitivity allows crosslinking at 37°C.

Maturation

After the bioprinting, it is crucial to provide the appropriate environment for cells within the construct to mature, migrate and, in the case of stem cells, differentiate. Besides the traditional method of cell culturing in medium in a submerged fashion, others may be employed.

Air-liquid interface (ALI) culture has been used to replicate full-thickness skin.^[37] In this method, skin constructs mature in both culture medium and air at the same time. Usually, the structure is mounted on a permeable membrane that allows the bottom part to be nourished by the culture medium, while exposing the top layer to air. This method is frequently used for culturing epithelia, such as the epidermis, due to superior differentiation results when compared to submerged cultures.^[38]

Defining shape for printing

One of the main advantages of bioprinting is its ability to produce structures with precise shapes. As a result, ensuring that the printer can accurately replicate anatomical shapes is a key aspect of research aimed at improving the technique.

One approach involves the creation of a virtual model of the structure to be printed using medical diagnostic imaging. A research team demonstrated the feasibility of using computed tomography (CT) scans to guide the design of bioprinted skin.^[39] They

printed a skin equivalent in the shape of a human face using a bioink of hyaluronic acid, glycerol, gelatin and fibrinogen with HEKs and HDFs. By using CT scans or other 3D images, it is possible to print structures that accurately replicate the anatomical features of the intended recipient, potentially improving the integration of the bioprinted tissue with the host and leading to more functional outcomes.

Vascularization

When printing complex tissue such as skin, one of the primary challenges is to achieve good vascularization so that the cells within the construct receive adequate nourishment. It is difficult to ensure that the transplanted structure integrates properly with the recipient's vascular network. One method is by establishing a vascular network in the construct prior to transplantation because grafts often fail to integrate due to the absence of a vascular network within the dermis.

It is possible to bioprint a pre-vascularized dermal layer. One group printed sequential layers using two bioinks, laden with HDFs and human umbilical vein endothelial cells (HUVEC), in an alternating pattern.^[32] Immunofluorescence showed the formation of endothelialized microvascular structures in the dermal layer after 14 days. Another approach was used to bioprint a vascularized dermis in a bilayered skin substitute.^[40] The bioink contained human fibroblasts, human endothelial cells and human pericytes. The dermis was printed using two layers of the same bioink intercalated by a sterile polyglycolic acid (PGA) mesh, with the goal of improving mechanical properties.

Endothelial cells (ECs) cultivated from cord blood human endothelial colony-forming cells (HECFCs) can be used for this goal, as shown in another study.^[41] These cells self-assembled into endothelial networks after being transplanted to immunodeficient mice. Vascular structures were observed 4 weeks after the engraftment. Zielinska and colleagues cocultured human dermal microvascular endothelial cells (HDMECs) with human fibroblasts, which lead to the formation of a vascular network of capillaries in two weeks of an *in vitro* culture.^[42] In a rat model, anastomosis between the capillaries of human origin and those from the animal were observed 1 week after engraftment.

Biomaterials used in bioinks

As bioprinting technology advances, researchers continue to develop and optimize bioinks that combine multiple natural and synthetic components. These materials not only provide the structural framework required for skin regeneration but also actively promote cellular processes such as adhe-

sion, proliferation and differentiation, making them essential for creating functional, long-lasting skin constructs. The published literature shows that a wide variety of materials have been employed to create functional constructs that mimic human skin. The combination of different materials within the same structure can provide specialized support for different cell populations.

Biomaterials

Biomaterials are materials designed to interact with biological systems, playing an essential role in tissue engineering. With a diversity spanning from natural materials and synthetic polymers to complex compounds, biomaterials offer tailored solutions for various therapeutic and regenerative needs.

Synthetic polymers are sometimes used in bioprinting skin. They are usually more resistant than biological materials, and can thus enhance the structural integrity and mechanical strength of the printed structures. One study employed a porous PU layer as a wound dressing material to give structural support to the dermal and epidermal layers printed onto it.^[39] Poly(lactic-co-glycolic) acid (PLGA) is another polymer that has been incorporated into the fabrication of skin substitutes.^[43] Patterned nanofibers of polymer films have also been integrated into bioprinted scaffolds to guide

cell behavior, providing biological cues that aid in tissue development. In the study by Bian et al., the films composed of electrospun nanofibers of a combination of PLGA and GelMA were used with this goal in mind.^[44]

Alginate is a biocompatible naturally occurring polymer derived from the cell walls of brown seaweeds. It is a very popular material in bioprinting due to its availability and biochemical and mechanical characteristics, which allow it to form hydrogels and be chemically modified and mixed with many other compounds. Several studies use alginate in the bioink formulation.^[45-49] Figure 3 shows a bioprinter in operation using a hydrogel containing alginate and polyethylene glycol (PEG).

Chitosan is a biocompatible polymer derived from chitin, which is found in the exoskeletons of crustaceans. Characteristics such as its antimicrobial activity and capacity to form hydrogels make it a valuable material in bioprinting. As an alginate, it is also chemically modifiable and blends well with other materials, making it a popular choice for the composition of bioinks.^[50-52]

Gelatin is derived from collagen, commonly obtained from animal connective tissue. Its resemblance to extracellular matrix components makes it an excellent choice in bioprinting applications. Its versatility is similar to that of

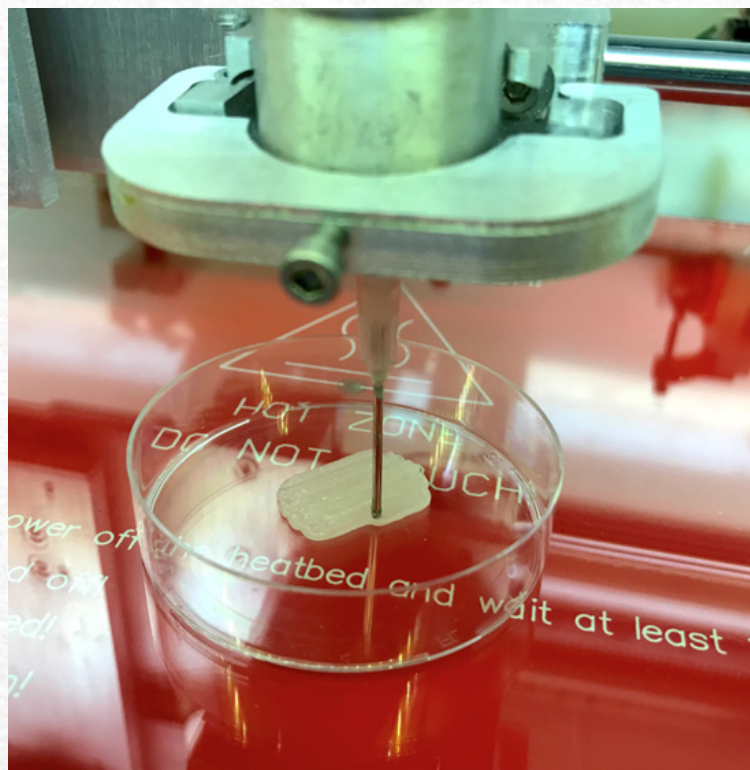


Figure 3 - An extrusion-based bioprinter. The needle extrudes a hydrogel composed of polyethylene glycol (PEG) and alginate into a Petri dish, following a design defined by the researchers. Photograph of the Stem Cell Laboratory, Universidade Federal do Rio Grande do Sul.

alginate and chitosan: it also mixes well with other components and is often subjected to chemical modifications. It provides good support for cell adhesion, proliferation, and differentiation, which explains its high prevalence in bioink formulations.

[2,45,46,48–51]

GelMA is a modified gelatin with added methacrylate groups, which allows it to be crosslinked under UV light. It has been widely used as a bioink base due to its biocompatibility, low immunogenicity and the possibility of adjusting physical and chemical properties through different degrees of methacrylation and concentration.^[53] Recombinant human type III collagen (rhCol3) has been incorporated into a GelMA bioink to support the bioprinting of skin equivalents.^[54] It showed a faster wound healing in a rat model when compared with GelMA alone. GelMA has also been combined with nanocellulose to generate skin constructs with hair follicles and early-stage rete ridge structures.^[55] Nanocellulose has also been added to other materials such as gellan gum (GG) and alginate for the fabrication of skin bioinks.^[56–58] One study mixed GelMA with dermis-derived decellularized extracellular matrix.^[13] GelMA and silk fibroin glycidyl methacrylate (SilMA) were mixed into a bioink that could be photocrosslinked using UV light in one step while combining both materials.^[59]

Pectin can also be methacrylated and used to mimic the mechanical properties of the dermal extracellular matrix, presenting cell-adhesive ligands and protease-sensitive domains for tissue development.^[60]

Some materials are incorporated into bioinks to promote specific effects during the maturation of the construct. For example, one group added phosphosilicate calcium bioglasses, a type of bioactive glass, to a bioink of alginate and GelMA to stimulate angiogenesis in the printed tissue.^[61] Another study developed a salvianolic acid B, alginate and gelatin (SAB-SA-Gel) composite scaffold due to the antioxidant, free-radical scavenging and angiogenic capacities of SAB. These effects were observed when fibroblast-like cells of rat skin (RSI) and HUVECs were cultivated in the scaffolds.^[62] In another work, a bi-layered GelMA-gelatin structure, incorporating keratinocytes for the epidermis and fibroblasts with HUVECs for the dermis, was further enhanced with amniotic membrane extract (AME) to promote angiogenesis.^[63] The effect of AME in angiogenesis is inconclusive.

Human-derived products including plasma and fibrin are also possible biomaterials for skin biofabrication. A plasma-based bioink has been used to print bilayered skin constructs by combining it with human fibroblasts and keratinocytes to treat burns and other types of wounds.^[64] One study used a

blend of fibrin and gelatin to produce a "biopaper", a biomimetic hydrogel to serve as a scaffold for a bioink loaded with fibroblasts.^[65] Fibrinogen, the precursor of fibrin, was also mixed with gelatin and sodium alginate to produce a hydrogel for bioprinting.^[37]

One approach to mimic the extracellular matrix is to create bioinks directly from extracellular matrices, mixing them with hydrogels. For example, one study used microfragmented adipose extracellular matrix (mFAECM) incorporated into a bioink to support skin regeneration.^[66] Other studies also used matrices from sources including the adipose tissue and the skin itself.^[7,13,67,68] Additionally, decellularized matrices from non-human sources, such as fish and pig skin, have been used, retaining key extracellular matrix components that aid in tissue development.^[69,70] One study showed that a fibrinogen hydrogel supplemented with dECM resulted in improved biological, physical and printability properties when compared with unsupplemented hydrogel.^[71] One group built scaffolds of dECM, gelatin, quaternized chitosan (QC) and poly(ionic liquid)s (PILs).^[72] QC has a modified amino group that confers better antibacterial activity when compared to regular chitosan. PILs are made from the polymerization of ionic liquid monomers; they are biocompatible and have an antibacterial effect.

An interesting addition to bioinks are extracellular vesicles, which are small lipid membrane particles that mediate intercellular communication.^[73,74] They are varied and, thus, the composition of the vesicle-loaded bioinks can be tailored to influence diverse local effects.

When creating a bioink, the materials and the cells are usually prepared separately and then mixed. One study developed a novel passive mixing technique to incorporate the cell suspension into highly viscous bioinks.^[75] Greater cell viability was observed with the novel mixing method when compared to traditional ones.

Free radical-copolymerization is another unusual technique that was used to produce a skin bioink. Polyethylene oxide (PEO), chitosan and poly(methylmethacrylic acid) (PMMA) were used.^[76] The mixture was heated and at 65°C, ammonium persulfate (APS) was added to initiate copolymerization by generating sulfate radicals. After temperature reduction, HDFs were incorporated into the bioink.

Cells

Various types of cells are used in bioprinting skin constructs. Approaches often involve using cell populations derived from the skin, such as keratinocytes and fibroblasts, or stem cells that can differentiate into skin cell types. Different types of cells are

often incorporated into the same skin constructs. One study used six different primary human cells to print three layers of skin.^[77]

When using stem cells, one viable source is adipose tissue. Adipose-derived stem cells (ASCs) have been encapsulated in hydrogels to serve as a foundational element in skin regeneration.^[28] Another source of stem cells is human amniotic fluid. Amniotic fluid-derived stem (AFS) cells have shown the ability to modulate immune responses. In one study, these cells were suspended in a fibrin-collagen gel, alongside bone marrow-derived mesenchymal stem cells, and printed directly over wound sites, supporting new tissue formation.^[22] Another study mixed epidermal stem cells and skin-derived precursors from neonatal mice with Matrigel[®], printing them directly onto wounds for skin regeneration.^[21] Human platelet lysate (HPL) was added to a bioink with adipose tissue derived mesenchymal stromal cells to potentially increase cell proliferation and tissue healing.^[53]

Human endothelial cells, fibroblasts, pericytes and keratinocytes are frequently included in bioinks. One research group isolated and expanded these cells from human skin biopsies, combining them with human collagen type I and human plasma fibronectin to form stratified skin grafts.^[40] These grafts exhibited mature epidermal structures in mice models. One study used HDFs in a gelatin-hyaluronan hydrogel, which demonstrated good viability and proliferation.^[44] Another study paired a dermal layer with a keratinocyte-laden bioink to form the epidermal layer, which was then exposed to air-liquid interface to promote maturation and stratification.^[78]

Other human skin cells, including dermal microvascular endothelial cells, have been bioprinted to create multi-layered skin models, in this case in a fibrinogen-based bioink.^[79] Melanocytes have been incorporated into bioinks to produce pigmented bioprinted skin.^[15,34,80]

Human foreskin is also a source of cells. One study used both human foreskin dermal fibroblasts and human foreskin keratinocytes for different layers of skin.^[41] Primary neonatal keratinocytes and immortalized human keratinocytes have been used in the context of toxicology testing.^[81]

HUVEC are sometimes incorporated to promote the formation of a vascular network.^[63,68]

Some skin constructs are developed to study specific conditions and mimic pathological patterns in diseased tissue. To achieve this, specially selected cell populations may be used. In one study, researchers printed keratinocyte subpopulations with down-regulated expression of filaggrin, a structural protein, to model atopic dermatitis and ichthyosis

vulgaris.^[16] Additionally, skin constructs have been developed for cancer research, using bioprinted models of cancerous cells to study tumor growth and treatment responses, such as in the case of squamous cell carcinoma.^[82]

Spheroids

The use of spheroids has emerged as a strategy in bioprinting due to their ability to enhance tissue organization and development. Spheroids are compact clusters of cells that, when incorporated into bioinks, can better replicate the complex interactions between different cell types and promote the maturation of tissue.

In one study, researchers produced skin spherical organoids composed of human keratinocytes, fibroblasts and vascular endothelial cells as an initial step for bioprinting.^[33] These spheroids were then incorporated into a GelMA hydrogel to form a bioink. Subsequently, in a nude mouse model of full-thickness skin wounds, the bioprinted skin spherical organoids promoted faster healing when compared with pure hydrogels and with hydrogels loaded with cell cultures.

In another study, spheroids containing dermal papilla cells (DPCs), HEKs, human epidermal melanocytes (HEMs) and HUVEC in different combinations were evaluated.^[4] DPCs and HUVEC were printed within the dermal layer. Following this, an epidermal layer containing HEKs and HEMs was printed. After maturation, spheroids of DPCs and HUVEC were surrounded by cells that migrated from the epidermal layer, forming hair follicle structures that resembled the native tissue.

Spheroids have also been used to promote the differentiation of hair follicles (HF) alongside sweat glands (SG) within a bioprinted skin construct.^[6] HF spheroids were seeded onto bioprinted SG scaffolds made of alginate-gelatin gel and mesenchymal stem cells cultivated in a medium for SG differentiation. The presence of HF spheroids promoted the differentiation of both HF and SG in the construct.

Artificial intelligence and machine learning AI contributions to printing

Artificial intelligence (AI), particularly its subfield of Machine Learning (ML), encompasses a diverse group of mathematical and computational techniques. Recently, these techniques have been gradually integrated into bioprinting processes to enhance efficiency, precision, parameter optimization and overall outcomes. ML is especially valuable for fine-tuning parameters that traditionally rely on trial-and-error approaches.^[83] However, the applications of AI and ML are much more diverse, ranging from relatively simple predictive models to

robotic automation of bioprinting processes.^[84] A list of the main ML models is presented in Table 1.

The integration of ML within the domain of bioprinting remains at an early stage, with only a limited number of studies available to date. Preliminary studies, comprised mostly of proof-of-concept demonstrations, are primarily focused on constructs other than skin. Notably, a study employed supervised ML algorithms to test scaffold performance for skin tissue engineering, although it employed electrospun scaffolds rather than bioprinted ones.^[85]

The integration of ML within the domain of bioprinting remains at an early stage, with only a limited number of studies available to date. Preliminary studies, comprised mostly of proof-of-concept demonstrations, are primarily focused on constructs other than skin. Notably, a study employed supervised ML algorithms to test scaffold performance for skin tissue engineering, although it employed electrospun scaffolds rather than bioprinted ones.^[85] Despite the lack of studies specifically focused on skin constructs, the procedural framework for bioprinting is generally consistent across tissue types. The advancements discussed henceforth highlight the prospect of leveraging ML to enhance various bioprinting processes, potentially benefiting applications tailored to skin bioprinting.

Bioprinting parameters, for example, have been optimized with ML using data collected from published literature.^[86] A process traditionally dependent on trial-and-error, parameter optimization was demonstrated in a study that used different AI models in the production of 6-thioguanine (6-TG) loaded PLGA microparticles for bioprinting.^[83] Compared to the traditional design of experiments (DoE)

methods, AI models showed superior performance by predicting key formulation parameters, thus increasing efficiency. ML techniques, like support vector machines (SVMs), can assist in selecting printing parameters. In one study, an SVM model was employed to reduce the need for extensive experimentation and improve the printability of pluronic hydrogels.^[87]

One group developed an AI-based model to improve digital light processing-based bioprinting.^[88] This method faces challenges due to light scattering caused by the cells in the bioink, which can disrupt photopolymerization. The developed AI model used data from trial prints to learn and help compensate for these scattering effects, leading to improved consistency and quality in the printed constructs.

Hierarchical machine learning (HML) frameworks have been employed to improve printing fidelity with an alginate hydrogel.^[89] This model includes domain knowledge information about physicochemical relationships. Strategies like Gaussian process modeling have been applied to evaluate nozzle geometries that have an impact on shear stress and, consequently, cell viability.^[90] A computational fluid dynamics (CFD) model was used to calculate shear stress, thus showing how the coupling of different numerical models can improve prediction capacity. In another example, a learning-based cell injection control (LCIC) model that combined CFD and a multilayer perceptron (MLP) network was used with piezoelectric drop-on-demand printing to eliminate satellite droplets, a common issue with this method.^[91]

One of the most interesting applications of artificial intelligence is computer vision (CV). It

Table 1 - Popular ML models. Supervised models are trained using labeled data, that is, they learn to map specific inputs to outputs based on examples. Unsupervised models work with unlabeled data and aim to identify patterns or groupings within the data.

Supervised Learning Models	Unsupervised Learning Models
Linear Regression and Logistic Regression	Hierarchical Clustering
Support Vector Machines	Principal Component Analysis
Neural Networks	Independent Component Analysis
Naive Bayes	K-Means Clustering
Gradient Boosting Machines (e.g. XGB)	Gaussian Mixture Models
Gaussian Processes	Association Rule Learning (Apriori, Eclat)
Decision Trees	Self-Organizing Maps
Random Forests	
K-Nearest Neighbors	

allows for the analysis of images produced by cameras, thus facilitating data extraction and the use of complex data. One group developed an adaptive printing system that integrated real-time feedback control to a robotic printer through a computer vision model.^[84] This setup allowed bioprinting on dynamic freeform surfaces, e.g. a moving hand, enabling more precise and flexible bioprinting. In another study, AI-based control loops, including a convolutional neural network (CNN), were developed to automatically adjust printing parameters and monitor the process in real time, leading to a reduction of material waste.^[92] Other studies have similarly employed computer vision as a means of detecting deviation of the printing trajectory from the reference and correcting it.^[93–95]

Additionally, ML-based anomaly detection systems informed by other sensors are being developed. The CNN in one study was particularly good at detecting nonuniformity.^[96]

AI contributions to bioink fabrication

Besides improving the action of printing itself, AI techniques can assist in identifying and producing the best materials and bioinks for bioprinting. These methods can link bioink characteristics and fabrication parameters with outcomes such as cell viability and the mechanical properties of the final construct. Neural networks (NN), for instance, can integrate data from laboratory experiments and literature to correlate bioink parameters, for example, concentration, with the desired features of bioprinted constructs.^[97] An ML algorithm called extreme gradient boost (XGB) was used to gain insights into how different hydrogel preparation parameters influence stiffness.^[98]

One challenge is predicting and ensuring the correct viscosity of the bioink. Traditional predictive models often fall short in accurately doing this. One study employed Bayesian optimization (BO) to predict viscosity with a relatively small data input, achieving good agreement with empirical knowledge.^[99] Techniques like this can reduce the waste of valuable materials that would otherwise be spent in repetitive trial-and-error experiments to obtain the correct flow properties.

One group established a relationship between rheological properties of bioinks and their printability using AI-driven methods.^[100] They found that a high elastic modulus improves shape fidelity. This finding underscores the potential of AI methods to provide critical insights about the interaction of multiple variables throughout the bioprinting process.

Varied AI contributions

As a collective effort, one of the significant ad-

vances in integrating AI and bioprinting is the development of large, open-source datasets of experimentally tested parameters.^[101] These datasets can be used to train various AI models which can then be fine-tuned for specific applications.

AI is sometimes paired with bioprinting in larger experimental designs, even when the former does not have a direct impact on the latter. One research group combined them for bacterial classification. They employed an acoustic bioprinting technique to produce droplets with a volume of less than 5 picoliters, with only a few cells in them, at a high rate. High-throughput surface-enhanced Raman spectroscopy (SERS) was then employed in each droplet and coupled with a machine-learning classification model.^[102] They were able to achieve highly accurate cell classification.

Still in the realm of high-throughput detection and classification, a study used bioprinted organoids that were imaged using high-speed live cell interferometry (HSLCI); this data was then analyzed using ML algorithms.^[103] This pipeline was used, for example, to quantify drug responses in cancer models.

In another innovative example of integrating AI and bioprinting, one group bioprinted artificial skin to study mosquito biting patterns.^[104] Mosquito feeding platforms mimicking skin were printed using hydrogels perfused with blood. The developed CV model was able to identify the mosquitos' engorged or non-feeding abdomens with good precision.

Tumor treatment responses have been evaluated using bioprinted patient-derived glioma tissues.^[105] Machine learning was able to predict drug efficacy on these constructs.

Uses of bioprinted skin

The main goal of research in skin bioprinting is to produce adequate substitutes for natural tissue that resemble real skin and promote regeneration. However, bioprinted skin constructs have also been used for other applications that are not, at least immediately, related to tissue regeneration; for instance, as an *in vitro* disease model.

Bioprinting was used to create skin models to study aging with a group.^[106] Printed samples included microrelief, a natural surface topography of the skin, present from birth, that has an impact on wrinkling. Constructs with skin textures corresponding to different ages were fabricated. Bioprinted skin can serve to test a variety of chemicals, for example, cosmetic products, potential irritants and drugs.^[19,32] It may serve as a substitute for animal models in certain tests, without the ethical concerns associated with it. It may also be a platform for training artificial intelligence algorithms, as discus-

sed above.

One group used bioprinted skin to test the permeation of nanocapsules containing quinizarin, a candidate for skin inflammation.^[107] Another study combined bioprinting with microfluidic platforms for high-throughput testing of chemicals and drugs on complex skin models.^[108] Bioprinted skin models have been employed for large scale toxicology testing in a high-throughput screening platform.^[81]

In a study outside the area of disease or toxicology research, one group bioprinted skin constructs that mimicked different skin tones across the Fitzpatrick scale by using polydopamine as a "synthetic melanin".^[109] These constructs could be used to study the effect of skin phototypes on biomedical optic devices. As mentioned earlier, bioprinted skin has also been used in mosquito research.^[104] This could contribute to the development of repellents or other more effective methods to protect against mosquito-borne diseases.

Conclusion

Skin bioprinting is rapidly developing, driven by advances in areas that are having an impact on techniques, materials, the availability of cells and other factors, contributing to printed constructs that are complex and effective for a variety of uses. Among the innovations, artificial intelligence is playing an expanding role in several steps crucial to bioprinting.

Acknowledgments

Figure 2 and the visual abstract were created using icons made by Freepik from www.flaticon.com.

Dedication

In memory of Dr. Jorge Vicente Lopes da Silva, whose contributions to the field of 3D printing were invaluable. His dedication and passion for science continue to inspire us all.

Support

The Office of Naval Research Global (ONRG Award N62909-21-1-2026) and National Council of Technological and Scientific Development (Conselho Nacional de Desenvolvimento Científico e Tecnológico, CNPq/Brazil

References

- [1]. Li J, Fu S, Lu KW, Christie O, Gozelski MT, Cottone MC, Cottone P, Kianian S, Feng KC, Simon M, Rafailovich M, Dagum AB and Singh G, Engineering functional skin constructs: A quantitative comparison of three-dimensional bioprinting with traditional methods. *Exp. Dermatol.* 31, (2022). DOI: 10.1111/exd.14488
- [2]. Masri S, Fadilah NIM, Hao LQ, Maarof M, Tabata Y, Hiraoka Y and Fauzi MB, Multifunctionalised skin substitute of hybrid gelatin-polyvinyl alcohol bioinks for chronic wound: injectable vs. 3D bioprinting. *Drug Deliv. Transl. Res.* 14, 1005–1027 (2024). DOI: 10.1007/s13346-023-01447-z
- [3]. Steffens D, Braghirolli DI, Maurmann N and Pranke P, Update on the main use of biomaterials and techniques associated with tissue engineering. *Drug Discov. Today* 23, 1474–1488 (2018). DOI: 10.1016/j.drudis.2018.03.013
- [4]. Motter Catarino C, Cigaran Schuck D, Dechiario L and Karande P, Incorporation of hair follicles in 3D bioprinted models of human skin. *Sci. Adv.* 9, eadg0297 (2023). DOI: 10.1126/sciadv.adg0297
- [5]. Chen H, Ma X, Gao T, Zhao W, Xu T and Liu Z, Robot-assisted in situ bioprinting of gelatin methacrylate hydrogels with stem cells induces hair follicle-inclusive skin regeneration. *Biomed. Pharmacother. Biomedicine Pharmacother.* 158, (2023). DOI: 10.1016/j.biopha.2022.114140
- [6]. Zhang Y, Enhejirigala null, Yao B, Li Z, Song W, Li J, Zhu D, Wang Y, Duan X, Yuan X, Huang S and Fu X, Using bioprinting and spheroid culture to create a skin model with sweat glands and hair follicles. *Burns Trauma* 9, tkab013 (2021). DOI: 10.1093/burnst/tkab013
- [7]. Kang Y, Yeo M, Derman ID, Ravnicek DJ, Singh YP, Alioglu MA, Wu Y, Makkar J, Driskell RR and Ozbolat IT, Intraoperative bioprinting of human adipose-derived stem cells and extra-cellular matrix induces hair follicle-like downgrowths and adipose tissue formation during full-thickness craniomaxillofacial skin reconstruction. *Bioact. Mater.* 33, 114–128 (2024). DOI: 10.1016/j.bioactmat.2023.10.034
- [8]. Cubo-Mateo N and Gelinsky M, Wound and Skin Healing in Space: The 3D Bioprinting Perspective. *Front. Bioeng. Biotechnol.* 9, 720217 (2021). DOI: 10.3389/fbioe.2021.720217
- [9]. Pourchet LJ, Thepot A, Albouy M, Courtial EJ, Boher A, Blum LJ and Marquette CA, Human Skin 3D Bioprinting Using Scaffold-Free Approach. *Adv. Healthc. Mater.* 6, (2017). DOI: 10.1002/adhm.201601101
- [10]. Quílez C, de Aranda Izuzquiza G, García M, López V, Montero A, Valencia L and Velasco D, Bioprinting for Skin. *Methods Mol. Biol.* Clifton NJ 2140, 217–228 (2020). DOI: 10.1007/978-1-0716-0520-2_14
- [11]. Niu C, Wang L, Ji D, Ren M, Ke D, Fu Q, Zhang K and Yang X, Fabrication of SA/Gel/C scaffold with 3D bioprinting to generate micro-nano porosity structure for skin wound healing: a detailed animal in vivo study. *Cell Regen. Lond. Engl.* 11, (2022). DOI: 10.1186/s13619-022-00113-y
- [12]. Shi B, Zhu T, Luo Y, Zhang X, Yao J, Cao X, Zhu Y, Miao H, Li L, Song Q, Zhang H and Xu L, Three-dimensional bioprinted cell-adaptive hydrogel with

- anisotropic micropores for enhancing skin wound healing. *Int. J. Biol. Macromol.* 136106 (2024). doi:10.1016/j.ijbiomac.2024.136106 DOI: 10.1016/j.ijbiomac.2024.136106
- [13].Ahn M, Cho W-W, Lee H, Park W, Lee S-H, Back JW, Gao Q, Gao G, Cho D-W and Kim BS, Engineering of Uniform Epidermal Layers via Sacrificial Gelatin Bioink-Assisted 3D Extrusion Bioprinting of Skin. *Adv. Healthc. Mater.* 12, e2301015 (2023). DOI: 10.1002/adhm.202301015
- [14].Ng WL, Yeong WY and Naing MW, Polyvinylpyrrolidone-Based Bio-Ink Improves Cell Viability and Homogeneity during Drop-On-Demand Printing. *Materials* 10, 190 (2017). DOI: 10.3390/ma10020190
- [15].Ng WL, Qi JTZ, Yeong WY and Naing MW, Proof-of-concept: 3D bioprinting of pigmented human skin constructs. *Biofabrication* 10, 025005 (2018). DOI: 10.1088/1758-5090/aa9ele
- [16].Madiedo-Podvrsan S, Belaïdi JP, Desbouis S, Simonetti L, Ben-Khalifa Y, Collin-Djangone C, Soeur J and Rielland M, Utilization of patterned bioprinting for heterogeneous and physiologically representative reconstructed epidermal skin models. *Sci. Rep.* 11, (2021). DOI: 10.1038/s41598-021-85553-3
- [17].Michael S, Sorg H, Peck C-T, Koch L, Deiwick A, Chichkov B, Vogt PM and Reimers K, Tissue engineered skin substitutes created by laser-assisted bioprinting form skin-like structures in the dorsal skin fold chamber in mice. *PloS One* 8, e57741 (2013). DOI: 10.1371/journal.pone.0057741
- [18].Hafa L, Breideband L, Ramirez Posada L, Torras N, Martinez E, Stelzer EHK and Pampaloni F, Light Sheet-Based Laser Patterning Bioprinting Produces Long-Term Viable Full-Thickness Skin Constructs. *Adv. Mater. Deerfield Beach Fla* 36, e2306258 (2024). DOI: 10.1002/adma.202306258
- [19].Cadau S, Rival D, Andre-Frei V, Chavan M M, Fayol D, Salducci M, Brisson B and Guillemot F, New bioprinted skin, cosmetic in vitro model. *J. Cosmet. Sci.* 68, 85–90 (2017).
- [20].Pontiggia L, Van Hengel IA, Klar A, Rüttsche D, Nanni M, Scheidegger A, Figi S, Reichmann E, Moehrlen U and Biedermann T, Bioprinting and plastic compression of large pigmented and vascularized human dermo-epidermal skin substitutes by means of a new robotic platform. *J. Tissue Eng.* 13, 20417314221088513 (2022). DOI: 10.1177/20417314221088513
- [21].Zhao W, Chen H, Zhang Y, Zhou D, Liang L, Liu B and Xu T, Adaptive multi-degree-of-freedom in situ bioprinting robot for hair-follicle-inclusive skin repair: A preliminary study conducted in mice. *Bioeng. Transl. Med.* 7, e10303 (2022). DOI: 10.1002/btm2.10303
- [22].Skardal A, Mack D, Kapetanovic E, Atala A, Jackson JD, Yoo J and Soker S, Bioprinted amniotic fluid-derived stem cells accelerate healing of large skin wounds. *Stem Cells Transl. Med.* 1, 792–802 (2012). DOI: 10.5966/sctm.2012-0088
- [23].Desanlis A, Albouy M, Rousselle P, Thépot A, Santos MD, Auxenfans C and Marquette C, Validation of an implantable bioink using mechanical extraction of human skin cells: First steps to a 3D bioprinting treatment of deep second degree burn. *J. Tissue Eng. Regen. Med.* 15, 37–48 (2021). DOI: 10.1002/term.3148
- [24].Albanna M, Binder KW, Murphy SV, Kim J, Qasem SA, Zhao W, Tan J, El-Amin IB, Dice DD, Marco J, Green J, Xu T, Skardal A, Holmes JH, Jackson JD, Atala A and Yoo JJ, In Situ Bioprinting of Autologous Skin Cells Accelerates Wound Healing of Extensive Excisional Full-Thickness Wounds. *Sci. Rep.* 9, 1856 (2019). DOI: 10.1038/s41598-018-38366-w
- [25].Moakes RJA, Senior JJ, Robinson TE, Chipara M, Atansov A, Naylor A, Metcalfe AD, Smith AM and Grover LM, A suspended layer additive manufacturing approach to the bioprinting of tri-layered skin equivalents. *APL Bioeng.* 5, 046103 (2021). DOI: 10.1063/5.0061361
- [26].Shi L, Hu Y, Ullah MW, Ullah I, Ou H, Zhang W, Xiong L and Zhang X, Cryogenic free-form extrusion bioprinting of decellularized small intestinal submucosa for potential applications in skin tissue engineering. *Biofabrication* 11, 035023 (2019). DOI: 10.1088/1758-5090/ab15a9
- [27].Dong T, Hu J, Dong Y, Yu Z, Liu C, Wang G and Chen S, Advanced biomedical and electronic dual-function skin patch created through microfluidic-regulated 3D bioprinting. *Bioact. Mater.* 40, 261–274 (2024). DOI: 10.1016/j.bioactmat.2024.06.015
- [28].Ma Y, Wang Y, Chen D, Su T, Chang Q, Huang W and Lu F, 3D bioprinting of a gradient stiffened gelatin-alginate hydrogel with adipose-derived stem cells for full-thickness skin regeneration. *J. Mater. Chem. B* 11, 2989–3000 (2023). DOI: 10.1039/d2tb02200a
- [29].Piola B, Sabbatini M, Gino S, Invernizzi M and Renò F, 3D Bioprinting of Gelatin-Xanthan Gum Composite Hydrogels for Growth of Human Skin Cells. *Int. J. Mol. Sci.* 23, 539 (2022). DOI: 10.3390/ijms23010539
- [30].Hafezi F, Shorter S, Tabriz AG, Hurt A, Elmes V, Boateng J and Douroumis D, Bioprinting and Preliminary Testing of Highly Reproducible Novel Bioink for Potential Skin Regeneration. *Pharmaceutics* 12, 550 (2020). DOI: 10.3390/pharmaceutics12060550
- [31].Masri S, Fauzi FAM, Hasnizam SB, Azhari AS, Lim JEA, Hao LQ, Maarof M, Motta A and Fauzi MB, Engineered-Skin of Single Dermal Layer Containing Printed Hybrid Gelatin-Polyvinyl Alcohol Bioink via 3D-Bioprinting: In Vitro Assessment under Submerged vs. Air-Lifting Models. *Pharm. Basel Switz.* 15, (2022). DOI: 10.3390/ph15111328
- [32].Bhar B, Das E, Manikumar K and Mandal BB, 3D Bioprinted Human Skin Model Recapitulating Native-Like Tissue Maturation and Immunocompetence as an Advanced Platform for Skin Sensitization Assess-

- ment. Adv. Healthc. Mater. 13, e2303312 (2024). DOI: 10.1002/adhm.202303312
- [33]. Zhang T, Sheng S, Cai W, Yang H, Li J, Niu L, Chen W, Zhang X, Zhou Q, Gao C, Li Z, Zhang Y, Wang G, Shen H, Zhang H, Hu Y, Yin Z, Chen X, Liu Y, Cui J and Su J, 3-D bioprinted human-derived skin organoids accelerate full-thickness skin defects repair. *Bioact. Mater.* 42, 257–269 (2024). DOI: 10.1016/j.bioactmat.2024.08.036
- [34]. Shi Y, Xing TL, Zhang HB, Yin RX, Yang SM, Wei J and Zhang WJ, Tyrosinase-doped bioink for 3D bioprinting of living skin constructs. *Biomed. Mater. Bristol Engl.* 13, 035008 (2018). DOI: 10.1088/1748-605X/aaa5b6
- [35]. Cavallo A, Al Kayal T, Mero A, Mezzetta A, Guazzelli L, Soldani G and Losi P, Fibrinogen-Based Bioink for Application in Skin Equivalent 3D Bioprinting. *J. Funct. Biomater.* 14, 459 (2023). DOI: 10.3390/jfb14090459
- [36]. Zhang D, Fu Q, Fu H, Zeng J, Jia L and Chen M, 3D-bioprinted human lipoaspirate-derived cell-laden skin constructs for healing of full-thickness skin defects. *Int. J. Bioprinting* 9, 718 (2023). DOI: 10.18063/ijb.718
- [37]. Liu J, Zhou Z, Zhang M, Song F, Feng C and Liu H, Simple and robust 3D bioprinting of full-thickness human skin tissue. *Bioengineered* 13, 10087–10097 (2022). DOI: 10.1080/21655979.2022.2063651
- [38]. Chen S and Schoen J, Air-liquid interface cell culture: From airway epithelium to the female reproductive tract. *Reprod. Domest. Anim. Zuchtgy.* 54 Suppl 3, 38–45 (2019). DOI: 10.1111/rda.13481
- [39]. Seol Y-J, Lee H, Copus JS, Kang H-W, Cho D-W, Atala A, Lee SJ and Yoo JJ, 3D Bioprinted BioMask for Facial Skin Reconstruction. *Bioprinting Amst. Neth.* 10, e00028 (2018). DOI: 10.1016/j.bprint.2018.e00028
- [40]. Baltazar T, Jiang B, Moncayo A, Merola J, Albanna MZ, Saltzman WM and Pober JS, 3D bioprinting of an implantable xeno-free vascularized human skin graft. *Bioeng. Transl. Med.* 8, e10324 (2023). DOI: 10.1002/btm2.10324
- [41]. Baltazar T, Merola J, Catarino C, Xie CB, Kirkiles-Smith NC, Lee V, Hotta S, Dai G, Xu X, Ferreira FC, Saltzman WM, Pober JS and Karande P, Three Dimensional Bioprinting of a Vascularized and Perfusable Skin Graft Using Human Keratinocytes, Fibroblasts, Pericytes, and Endothelial Cells. *Tissue Eng. Part A* 26, 227–238 (2020). DOI: 10.1089/ten.TEA.2019.0201
- [42]. Zielinska D, Fisch P, Moehrlen U, Finkielstein S, Linder T, Zenobi-Wong M, Biedermann T and Klar AS, Combining bioengineered human skin with bioprinted cartilage for ear reconstruction. *Sci. Adv.* 9, eadh1890 (2023). DOI: 10.1126/sciadv.adh1890
- [43]. Bastidas JG, Maurmann N, da Silveira MR, Ferreira CA and Pranke P, Development of fibrous PLGA/fibrin scaffolds as a potential skin substitute. *Bio- med. Mater. Bristol Engl.* 15, 055014 (2020). DOI: 10.1088/1748-605X/aba086
- [44]. Bian S, Hu X, Zhu H, Du W, Wang C, Wang L, Hao L, Xiang Y, Meng F, Hu C, Wu Z, Wang J, Pan X, Guan M, Lu WW and Zhao X, 3D Bioprinting of Artificial Skin Substitute with Improved Mechanical Property and Regulated Cell Behavior through Integrating Patterned Nanofibrous Films. *ACS Nano* 18, 18503–18521 (2024). DOI: 10.1021/acsnano.4c04088
- [45]. Liu P, Shen H, Zhi Y, Si J, Shi J, Guo L and Shen SG, 3D bioprinting and in vitro study of bilayered membranous construct with human cells-laden alginate/gelatin composite hydrogels. *Colloids Surf. B Biointerfaces* 181, 1026–1034 (2019). DOI: 10.1016/j.colsurfb.2019.06.069
- [46]. Li J, Chi J, Liu J, Gao C, Wang K, Shan T, Li Y, Shang W and Gu F, 3D printed gelatin-alginate bioactive scaffolds combined with mice bone marrow mesenchymal stem cells: a biocompatibility study.
- [47]. Antich C, de Vicente J, Jiménez G, Chocarro C, Carrillo E, Montañez E, Gálvez-Martín P and Marchal JA, Bio-inspired hydrogel composed of hyaluronic acid and alginate as a potential bioink for 3D bioprinting of articular cartilage engineering constructs. *Acta Biomater.* 106, 114–123 (2020). DOI: 10.1016/j.actbio.2020.01.046
- [48]. Ramakrishnan R, Kasoju N, Raju R, Geevarghese R, Gauthaman A and Bhatt A, Exploring the Potential of Alginate-Gelatin-Diethylaminoethyl Cellulose-Fibrinogen based Bioink for 3D Bioprinting of Skin Tissue Constructs. *Carbohydr. Polym. Technol. Appl.* 3, 100184 (2022). DOI: 10.1016/j.carpta.2022.100184
- [49]. Shi L, Xiong L, Hu Y, Li W, Chen Z, Liu K and Zhang X, Three-dimensional printing alginate/gelatin scaffolds as dermal substitutes for skin tissue engineering. *Polym. Eng. Sci.* 58, 1782–1790 (2018). DOI: 10.1002/pen.24779
- [50]. Ng WL, Yeong WY and Naing MW, Development of Polyelectrolyte Chitosan-gelatin Hydrogels for Skin Bioprinting. *Procedia CIRP* 49, 105–112 (2016). DOI: 10.1016/j.procir.2015.09.002
- [51]. Ng WL, Yeong WY and Naing MW, Polyelectrolyte gelatin-chitosan hydrogel optimized for 3D bioprinting in skin tissue engineering. *Int. J. Bioprinting* 2, 53 (2024). DOI: 10.18063/IJB.2016.01.009
- [52]. Azadmanesh F, Pourmadadi M, Zavar Reza J, Yazdian F, Omidi M and Haghrosadat BF, Synthesis of a novel nanocomposite containing chitosan as a three-dimensional printed wound dressing technique: Emphasis on gene expression. *Biotechnol. Prog.* 37, e3132 (2021). DOI: 10.1002/btpr.3132
- [53]. Tanadchangsang N, Pasanaphong K, Tawonsawatruk T, Rattanapinyopituk K, Tangketsarawan B, Rawiwet V, Kongchanagul A, Srikaew N, Yoyruerop T, Panupinthu N, Sangpayap R, Panaksri A, Boonyagul S and Hemstapat R, 3D bioprinting of fish skin-ba-

- sed gelatin methacryloyl (GelMA) bio-ink for use as a potential skin substitute. *Sci. Rep.* 14, 23240 (2024). DOI: 10.1038/s41598-024-73774-1
- [54]. Yang Y, Xu R, Wang C, Guo Y, Sun W and Ouyang L, Recombinant Human Collagen-Based Bioinks for the 3D Bioprinting of Full-thickness Human Skin Equivalent. *Int. J. Bioprinting* 8, 611 (2022). DOI: 10.18063/ijb.v8i4.611
- [55]. Li M, Sun L, Liu Z, Shen Z, Cao Y, Han L, Sang S and Wang J, 3D bioprinting of heterogeneous tissue-engineered skin containing human dermal fibroblasts and keratinocytes. *Biomater. Sci.* 11, 2461–2477 (2023). DOI: 10.1039/d2bm02092k
- [56]. Lameirinhas NS, Teixeira MC, Carvalho JPF, Valente BFA, Pinto RJB, Oliveira H, Luís JL, Pires L, Oliveira JM, Vilela C and Freire CSR, Nanofibrillated cellulose/gellan gum hydrogel-based bioinks for 3D bioprinting of skin cells. *Int. J. Biol. Macromol.* 229, 849–860 (2023). DOI: 10.1016/j.ijbiomac.2022.12.227
- [57]. Apelgren P, Amoroso M, Säljö K, Lindahl A, Branting C, Stridh Orrhult L, Gatenholm P and Kölbly L, Skin Grafting on 3D Bioprinted Cartilage Constructs In Vivo. *Plast. Reconstr. Surg. Glob. Open* 6, e1930 (2018). DOI: 10.1097/GOX.0000000000001930
- [58]. Sever M, Škrinjar D, Maver T, Belak M, Zupanič F, Anžel I and Zidarič T, The Impact of Temperature and the Duration of Freezing on a Hydrogel Used for a 3D-Bioprinted In Vitro Skin Model. *Biomedicines* 12, 2028 (2024). DOI: 10.3390/biomedicines12092028
- [59]. Xu L, Zhang Z, Jorgensen AM, Yang Y, Jin Q, Zhang G, Cao G, Fu Y, Zhao W, Ju J and Hou R, Bioprinting a skin patch with dual-crosslinked gelatin (GelMA) and silk fibroin (SilMA): An approach to accelerating cutaneous wound healing. *Mater. Today Bio* 18, 100550 (2023). DOI: 10.1016/j.mtbio.2023.100550
- [60]. Bebiano LB, Presa R, Vieira F, Lourenço BN and Pereira RF, Bioinspired and Photo-Clickable Thiol-Ene Bioinks for the Extrusion Bioprinting of Mechanically Tunable 3D Skin Models. *Biomim. Basel Switz.* 9, 228 (2024). DOI: 10.3390/biomimetics9040228
- [61]. Liu Y, Liu X, Guo H, Wang X, Li A, Qiu D and Gu Q, 3D bioprinting bioglass to construct vascularized full-thickness skin substitutes for wound healing. *Mater. Today Bio* 24, 100899 (2024). DOI: 10.1016/j.mtbio.2023.100899
- [62]. Lihao Q, Tingting L, Jiawei Z, Yifei B, Zheyu T, Jingyan L, Tongqing X and Zhongzhi J, 3D bioprinting of Salvianolic acid B-sodium alginate-gelatin skin scaffolds promotes diabetic wound repair via antioxidant, anti-inflammatory, and proangiogenic effects. *Biomed. Pharmacother. Biomedicine Pharmacother.* 171, 116168 (2024). DOI: 10.1016/j.biopha.2024.116168
- [63]. Pazhouhnia Z, Noori A, Farzin A, Khoshmaram K, Hoseinpour M, Ai J, Ebrahimi M and Lotfibakhshaiesh N, 3D-bioprinted GelMA/gelatin/amniotic membrane extract (AME) scaffold loaded with keratinocytes, fibroblasts, and endothelial cells for skin tissue engineering. *Sci. Rep.* 14, 12670 (2024). DOI: 10.1038/s41598-024-62926-y
- [64]. Cubo N, Garcia M, Del Cañizo JF, Velasco D and Jorcano JL, 3D bioprinting of functional human skin: production and in vivo analysis. *Biofabrication* 9, 015006 (2016). DOI: 10.1088/1758-5090/9/1/015006
- [65]. Hakam MS, Imani R, Abolfathi N, Fakhrzadeh H and Sharifi AM, Evaluation of fibrin-gelatin hydrogel as biopaper for application in skin bioprinting: An in-vitro study. *Biomed. Mater. Eng.* 27, 669–682 (2016). DOI: 10.3233/BME-161617
- [66]. Zhang D, Lai L, Fu H, Fu Q and Chen M, 3D-Bioprinted Biomimetic Multilayer Implants Comprising Microfragmented Adipose Extracellular Matrix and Cells Improve Wound Healing in a Murine Model of Full-Thickness Skin Defects. *ACS Appl. Mater. Interfaces* 15, 29713–29728 (2023). DOI: 10.1021/acsami.2c21629
- [67]. Jang K-S, Park S-J, Choi J-J, Kim H-N, Shim K-M, Kim M-J, Jang I-H, Jin S-W, Kang S-S, Kim S-E and Moon S-H, Therapeutic Efficacy of Artificial Skin Produced by 3D Bioprinting. *Mater. Basel Switz.* 14, 5177 (2021). DOI: 10.3390/ma14185177
- [68]. Jin R, Cui Y, Chen H, Zhang Z, Weng T, Xia S, Yu M, Zhang W, Shao J, Yang M, Han C and Wang X, Three-dimensional bioprinting of a full-thickness functional skin model using acellular dermal matrix and gelatin methacrylamide bioink. *Acta Biomater.* 131, 248–261 (2021). DOI: 10.1016/j.actbio.2021.07.012
- [69]. Lee H, Chun W and Kim G, Three-Dimensional Artificial Skin Construct Bioprinted with a Marine-Based Biocomposite. *Biomacromolecules* 24, 2864–2878 (2023). DOI: 10.1021/acs.biomac.3c00253
- [70]. Cavallo A, Al Kayal T, Mero A, Mezzetta A, Pisani A, Foffa I, Vecoli C, Buscemi M, Guazzelli L, Soldani G and Losi P, Marine Collagen-Based Bioink for 3D Bioprinting of a Bilayered Skin Model. *Pharmaceutics* 15, 1331 (2023). DOI: 10.3390/pharmaceutics15051331
- [71]. Jorgensen AM, Chou Z, Gillispie G, Lee SJ, Yoo JJ, S S and Atala A, Decellularized Skin Extracellular Matrix (dsECM) Improves the Physical and Biological Properties of Fibrinogen Hydrogel for Skin Bioprinting Applications. *Nanomater. Basel Switz.* 10, (2020). DOI: 10.3390/nano10081484
- [72]. Xu J, Fang H, Su Y, Kang Y, Xu D, Cheng YY, Nie Y, Wang H, Liu T and Song K, A 3D bioprinted decellularized extracellular matrix/gelatin/quaternized chitosan scaffold assembling with poly(ionic liquid)s for skin tissue engineering. *Int. J. Biol. Macromol.* 220, 1253–1266 (2022). DOI: 10.1016/j.ijbiomac.2022.08.149
- [73]. Taghdi MH, Muttiah B, Chan AML, Fauzi MB, Law JX and Lokanathan Y, Exploring Synergistic Effects of Bioprinted Extracellular Vesicles for Skin Regeneration. *Biomedicines* 12, 1605 (2024). DOI: 10.3390/biomedicines12071605

- [74].Girón J, Maurmann N and Pranke P, The role of stem cell-derived exosomes in the repair of cutaneous and bone tissue. *J. Cell. Biochem.* 123, 183–201 (2022). DOI: 10.1002/jcb.30144
- [75].Thayer PS, Orrhult LS and Martínez H, Bioprinting of Cartilage and Skin Tissue Analogs Utilizing a Novel Passive Mixing Unit Technique for Bioink Precellularization. *J. Vis. Exp. JoVE* 56372 (2018). doi:10.3791/56372DOI: 10.3791/56372
- [76].Ullah F, Javed F, Mushtaq I, Rahman L-U, Ahmed N, Din IU, Alotaibi MA, Alharthi AI, Ahmad A, Bakht MA, Khan F and Tasleem S, Development of highly-reproducible hydrogel based bioink for regeneration of skin-tissues via 3-D bioprinting technology. *Int. J. Biol. Macromol.* 230, 123131 (2023). DOI: 10.1016/j.ijbiomac.2022.123131
- [77].Jorgensen AM, Gorkun A, Mahajan N, Willson K, Clouse C, Jeong CG, Varkey M, Wu M, Walker SJ, Molnar JA, Murphy SV, Lee SJ, Yoo JJ, Soker S and Atala A, Multicellular bioprinted skin facilitates human-like skin architecture in vivo. *Sci. Transl. Med.* 15, eadf7547 (2023). DOI: 10.1126/scitranslmed.adf7547
- [78].Lee V, Singh G, Trasatti JP, Bjornsson C, Xu X, Tran TN, Yoo S-S, Dai G and Karande P, Design and fabrication of human skin by three-dimensional bioprinting. *Tissue Eng. Part C Methods* 20, 473–484 (2014). DOI: 10.1089/ten.TEC.2013.0335
- [79].Jorgensen AM, Varkey M, Gorkun A, Clouse C, Xu L, Chou Z, Murphy SV, Molnar J, Lee SJ, Yoo JJ, Soker S and Atala A, Bioprinted Skin Recapitulates Normal Collagen Remodeling in Full-Thickness Wounds. *Tissue Eng. Part A* 26, 512–526 (2020). DOI: 10.1089/ten.TEA.2019.0319
- [80].Min D, Lee W, Bae I-H, Lee TR, Croce P and Yoo S-S, Bioprinting of biomimetic skin containing melanocytes. *Exp. Dermatol.* 27, 453–459 (2018). DOI: 10.1111/exd.13376
- [81].Wei Z, Liu X, Ooka M, Zhang L, Song MJ, Huang R, Kleinstreuer NC, Simeonov A, Xia M and Ferrer M, Two-Dimensional Cellular and Three-Dimensional Bio-Printed Skin Models to Screen Topical-Use Compounds for Irritation Potential. *Front. Bioeng. Biotechnol.* 8, 109 (2020). DOI: 10.3389/fbioe.2020.00109
- [82].Kurzyk A, Szumera-Ciećkiewicz A, Miłoszewska J and Chechlińska M, 3D modeling of normal skin and cutaneous squamous cell carcinoma. A comparative study in 2D cultures, spheroids, and 3D bioprinted systems. *Biofabrication* 16, (2024). DOI: 10.1088/1758-5090/ad2b06
- [83].Wang J, Heshmati Aghda N, Jiang J, Mridula Habib A, Ouyang D and Maniruzzaman M, 3D bioprinted microparticles: Optimizing loading efficiency using advanced DoE technique and machine learning modeling. *Int. J. Pharm.* 628, 122302 (2022). DOI: 10.1016/j.ijpharm.2022.122302
- [84].Zhu Z, Guo S-Z, Hirdler T, Eide C, Fan X, Tolar J and McAlpine MC, 3D Printed Functional and Biological Materials on Moving Freeform Surfaces. *Adv. Mater.* Deerfield Beach Fla 30, e1707495 (2018). DOI: 10.1002/adma.201707495
- [85].Sujeun LY, Goonoo N, Ramphul H, Chummun I, Gimmié F, Baichoo S and Bhaw-Luximon A, Correlating in vitro performance with physico-chemical characteristics of nanofibrous scaffolds for skin tissue engineering using supervised machine learning algorithms. *R. Soc. Open Sci.* 7, 201293 (2020). DOI: 10.1098/rsos.201293
- [86].Tian S, Stevens R, McInnes BT and Lewinski NA, Machine Assisted Experimentation of Extrusion-Based Bioprinting Systems. *Micromachines* 12, 780 (2021). DOI: 10.3390/mi12070780
- [87].Fu Z, Angeline V and Sun W, Evaluation of Printing Parameters on 3D Extrusion Printing of Pluronic Hydrogels and Machine Learning Guided Parameter Recommendation. *Int. J. Bioprinting* 7, 434 (2021). DOI: 10.18063/ijb.v7i4.434
- [88].Guan J, You S, Xiang Y, Schimelman J, Alido J, Ma X, Tang M and Chen S, Compensating the cell-induced light scattering effect in light-based bioprinting using deep learning. *Biofabrication* 14, (2021). DOI: 10.1088/1758-5090/ac3b92
- [89].Bone JM, Childs CM, Menon A, Póczos B, Feinberg AW, LeDuc PR and Washburn NR, Hierarchical Machine Learning for High-Fidelity 3D Printed Biopolymers. *ACS Biomater. Sci. Eng.* 6, 7021–7031 (2020). DOI: 10.1021/acsbomaterials.0c00755
- [90].Reina-Romo E, Mandal S, Amorim P, Bloemen V, Ferraris E and Geris L, Towards the Experimentally-Informed In Silico Nozzle Design Optimization for Extrusion-Based Bioprinting of Shear-Thinning Hydrogels. *Front. Bioeng. Biotechnol.* 9, 701778 (2021). DOI: 10.3389/fbioe.2021.701778
- [91].Shi J, Wu B, Song B, Song J, Li S, Trau D and Lu WF, Learning-Based Cell Injection Control for Precise Drop-on-Demand Cell Printing. *Ann. Biomed. Eng.* 46, 1267–1279 (2018). DOI: 10.1007/s10439-018-2054-2
- [92].Bonatti AF, Vozzi G, Chua CK and Maria CD, A Deep Learning Quality Control Loop of the Extrusion-based Bioprinting Process. *Int. J. Bioprinting* 8, 620 (2022). DOI: 10.18063/ijb.v8i4.620
- [93].Liu C, Liu J, Yang C, Tang Y, Lin Z, Li L, Liang H, Lu W and Wang L, Computer Vision-Aided 2D Error Assessment and Correction for Helix Bioprinting. *Int. J. Bioprinting* 8, 547 (2022). DOI: 10.18063/ijb.v8i2.547
- [94].Liu C, Yang C, Liu J, Tang Y, Lin Z, Li L, Liang H, Lu W and Wang L, Error assessment and correction for extrusion-based bioprinting using computer vision method. *Int. J. Bioprinting* 9, 644 (2023). DOI: 10.18063/ijb.v9i1.644
- [95].Barjuei ES, Shin J, Kim K and Lee J, Precision improvement of robotic bioprinting via vision-based tool path compensation. *Sci. Rep.* 14, 17764 (2024). DOI:

10.1038/s41598-024-68597-z

- [96].Jin Z, Zhang Z, Shao X and Gu GX, Monitoring Anomalies in 3D Bioprinting with Deep Neural Networks. *ACS Biomater. Sci. Eng.* 9, (2023). DOI: 10.1021/acs-biomaterials.0c01761
- [97].Mohammadrezaei D, Podina L, Silva JD and Kohandel M, Cell viability prediction and optimization in extrusion-based bioprinting via neural network-based Bayesian optimization models. *Biofabrication* 16, (2024). DOI: 10.1088/1758-5090/ad17cf
- [98].Ege D and Boccaccini AR, Investigating the Effect of Processing and Material Parameters of Alginate Dialdehyde-Gelatin (ADA-GEL)-Based Hydrogels on Stiffness by XGB Machine Learning Model. *Bioeng. Basel Switz.* 11, 415 (2024). DOI: 10.3390/bioengineering11050415
- [99].Xu Y, Sarah R, Habib A, Liu Y and Khoda B, Constraint based Bayesian optimization of bioink precursor: a machine learning framework. *Biofabrication* 16, (2024). DOI: 10.1088/1758-5090/ad716e
- [100].Lee J, Oh SJ, An SH, Kim W-D and Kim S-H, Machine learning-based design strategy for 3D printable bioink: elastic modulus and yield stress determine printability. *Biofabrication* 12, 035018 (2020). DOI: 10.1088/1758-5090/ab8707
- [101].Rafieyan S, Ansari E and Vasheghani-Farahani E, A practical machine learning approach for predicting the quality of 3D (bio)printed scaffolds. *Biofabrication* 16, (2024). DOI: 10.1088/1758-5090/ad6374
- [102].Safir F, Vu N, Tadesse LF, Firouzi K, Banaei N, Jeffrey SS, Saleh AAE, Khuri-Yakub BPT and Dionne JA, Combining Acoustic Bioprinting with AI-Assisted Raman Spectroscopy for High-Throughput Identification of Bacteria in Blood. *Nano Lett.* 23, 2065–2073 (2023). DOI: 10.1021/acs.nanolett.2c03015
- [103].Tebon PJ, Wang B, Markowitz AL, Davarifar A, Tsai BL, Krawczuk P, Gonzalez AE, Sartini S, Murray GF, Nguyen HTL, Tavanaie N, Nguyen TL, Boutros PC, Teitell MA and Soragni A, Drug screening at single-organoid resolution via bioprinting and interferometry. *Nat. Commun.* 14, 3168 (2023). DOI: 10.1038/s41467-023-38832-8
- [104].Janson KD, Carter BH, Jameson SB, de Verges JE, Dalliance ES, Royse MK, Kim P, Wesson DM and Veiseh O, Development of an automated biomaterial platform to study mosquito feeding behavior. *Front. Bioeng. Biotechnol.* 11, 1103748 (2023). DOI: 10.3389/fbioe.2023.1103748
- [105].Tang M, Jiang S, Huang X, Ji C, Gu Y, Qi Y, Xiang Y, Yao E, Zhang N, Berman E, Yu D, Qu Y, Liu L, Berry D and Yao Y, Integration of 3D bioprinting and multi-algorithm machine learning identified glioma susceptibilities and microenvironment characteristics. *Cell Discov.* 10, 39 (2024). DOI: 10.1038/s41421-024-00650-7
- [106].Sun W, Wang B, Yang T, Yin R, Wang F, Zhang H and Zhang W, Three-Dimensional Bioprinted Skin Micro-relief and Its Role in Skin Aging. *Biomim. Basel Switz.* 9, 366 (2024). DOI: 10.3390/biomimetics9060366
- [107].do Amaral SR, Amantino CF, Atanasov A, Sousa SO, Moakes R, Oliani SM, Grover LM and Primo FL, Photodynamic Therapy as a Novel Therapeutic Modality Applying Quinizarin-Loaded Nanocapsules and 3D Bioprinting Skin Permeation for Inflammation Treatment. *Pharm. Basel Switz.* 17, 1169 (2024). DOI: fa
- [108].Ng WL and Yeong WY, The future of skin toxicology testing - Three-dimensional bioprinting meets microfluidics. *Int. J. Bioprinting* 5, 237 (2019). DOI: 10.18063/ijb.v5i2.1.237
- [109].Yim W, Zhou J, Sasi L, Zhao J, Yeung J, Cheng Y, Jin Z, Johnson W, Xu M, Palma-Chavez J, Fu L, Qi B, Retout M, Shah NJ, Bae J and Jokerst JV, 3D-Bioprinted Phantom with Human Skin Phototypes for Biomedical Optics. *Adv. Mater. Deerfield Beach Fla* 35, e2206385 (2023). DOI: 10.1002/adma.202206385